



# COOL 11

## *Workshop on Beam Cooling and Related Topics*

September 12 - 16, 2011  
Pansionat "Dubna" , Alushta, Ukraine  
hosted by JINR, Dubna  
at support of BINP SB RAS, Novosibirsk and  
Scientific Council of RAS on Charged Particle Accelerators

The workshop on beam cooling and related topics, COOL'11, will highlight the state of the art in the physics and engineering of beam cooling systems and related techniques, including electron, stochastic, laser and muon (ionization) cooling in storage rings and particle traps.

### International Program Committee

I. Meshkov (JINR, Dubna, Russia) –Co-Chair  
A. Skrinsky (BINP, Novosibirsk, Russia) – Co-Chair  
M. Steck (GSI, Darmstadt, Germany) – Co-Chair  
E. Akhmanova (JINR, Dubna, Russia) - secretary  
I. Ben-Zvi (BNL, Brookhaven, USA)  
H. Danared (MSL, Stockholm, Sweden)  
J. Dietrich (IKP FZJ, Jülich, Germany)  
M. Grieser (IMP, Heidelberg, Germany)  
T. Katayama (GSI, Germany)  
D. Möhl (CERN, Switzerland)  
S. Nagaitsev (FNAL, Batavia, USA)  
A. Noda (Kyoto University, Japan)  
V. Parkhomchuk (BINP, Novosibirsk, Russia)  
D. Prasuhn (IKP, Jülich, Germany)  
A. Sessler (LBNL, Berkeley, USA)  
G. Shirkov (JINR, Dubna, Russia)  
G. Tranquille (CERN, Switzerland)  
X. D. Yang (IMP, Lanzhou, China)  
A. Wolf (IMP, Heidelberg, Germany)



### Organizing Committee

G. Shirkov (JINR, Dubna, Russia) – Chair  
I. Meshkov (JINR, Dubna, Russia) – Co-Chair  
G. Trubnikov (JINR, Dubna, Russia) – Co-Chair  
S. Yakovenko (JINR, Dubna, Russia) – Scientific secretary  
E. Akhmanova (JINR, Dubna, Russia) – secretary  
O. Matyukhina (JINR, Dubna, Russia) – secretary  
M. Kuzin (BINP, Novosibirsk, Russia)  
A. Philippov (JINR, Dubna, Russia)  
R. Pivin (JINR, Dubna, Russia)  
K. Zhdanova (JINR, Dubna, Russia)



Email: [cool11@jinr.ru](mailto:cool11@jinr.ru)

Workshop website: <http://cool11.jinr.ru>



## Preface

The Workshop on beam cooling and related topics, COOL'11, was organized by the Joint Institute for Nuclear Research (Dubna, Moscow region) supported by the BINP SB RAS and the Scientific Council of RAS on charged particle accelerators. It was held in the "Pansionat Dubna" located on the shore of the Crimean Peninsula in Alushta, Ukraine, from September 12 to 16, 2011.

About 50 participants from the leading accelerating centers of the world discussed new ideas and trends, new results and new technologies in the field of beam cooling. About 27 contributions were presented in talks and 18 on posters dedicated to various problems of the development and application of cooling methods.

All existing leading projects using methods of cooling, and projects which are in a stage of preparation were presented. Among them - new projects of facilities under development: NICA, FAIR, ELENA at CERN, the Cryogenic Storage Ring at MPI, LEPTA at JINR, EI Collider at Jlab, eRHIC at BNL .

The five days meetings and a poster session included the discussions about novel ideas under development such as coherent electron cooling, frictional cooling and others. A different technique was proposed for future high energy accelerators based on the use of ionization cooling for the cooling of muons, either for highest luminosity in a muon collider or for application in a future neutrino factory. The participants presented the newest results of investigations in the facilities and experiments with the application of cooling all around the World: US – Tevatron (Fermilab), RHIC (BNL), EU – AD: ALPHA, ATRAP, ASACUSA (CERN), COSY (FZJ), ESR & SIS-18 (GSI), TSR (MPI), Japan - S-LSR (Kyoto University), China – CSRM and CSRe (IMP CAS), Russia – LEPTA (JINR).

Traditionally the Program Committee of the Workshop considered proposals for the next workshops. By a close vote, CERN was selected as the organizer of the next workshop in this series in 2013. The expression of interest for hosting COOL in 2015 presented by JLab was met with good acceptance.

The scientific program of the Workshop was complemented by a half day excursion to the city of Yalta which gave the opportunity to enjoy the landscape, historic places and the comfortable weather.

The organizers would like to thank the Joint Institute for Nuclear Research (Dubna), the Budker Institute of Nuclear Physics RAS (Novosibirsk), the Scientific Council of RAS on charged particle accelerators and all employees of the "Pansionat Dubna" for the help and support in the organization of the Workshop.

Great thanks should be given to the members of the Workshop Organizing Committee Grigory Trubnikov, Sergey Yakovenko, Ekaterina Akhmanova, Olga Matyukhina, Alexander Philippov, Roman Pivin and Kristina Zhdanova, who prepared and managed the Workshop with high efficiency and great enthusiasm. The JACoW's responsible person in Russia Maxim Kuzin deserves special the thanks for successfully introducing the Scientific Programme Management System (SPMS) of the Joint Accelerator Conference Website (JACoW) for the processing and publication of the workshop and his editorial work.

Finally, we would like to express our sincere appreciation to all the participants for their active participation in this Workshop.

Co-Chair of the Program  
Committee of COOL'11  
Igor Meshkov  
(JINR, Dubna, Russia)

Co-Chair of the Program  
Committee of COOL'11  
Markus Steck  
(GSI, Darmstadt, Germany)

# Contents

<b>Preface</b>	<b>i</b>
Foreword . . . . .	iii
Contents . . . . .	v
Committees . . . . .	vii
Pictures . . . . .	viii
MOIO01 – Electron Cooling Performance at IMP Facility . . . . .	1
MOIO02 – NICA Project at JINR . . . . .	6
MOIO03 – Current Plans for Beam Cooling at FAIR . . . . .	10
MOIO05 – Status of the 2 MeV Electron Cooler for COSY/HESR . . . . .	15
MOIO06 – Recent Status of Beam Cooling at S-LSR . . . . .	19
MOIO07 – Application of Cooling Methods to NICA Project . . . . .	25
THIOA01 – Ultimate Performance of Relativistic Electron Cooling at Fermilab . . . . .	31
THIOA02 – The First Commission Results of the High Voltage Magnetized Cooler for COSY . . . . .	37
THIOA03 – The Advance Technology Extraction for Therapy Ions Beam from Carbon Storage Ring with Electron Cooling . . . . .	43
THCOB01 – Radiative Recombination of Heavy Bare Nuclei and Ions in Electron Cooling System . . . . .	48
TUIOB01 – Numerical Investigation of Stochastic Cooling at NICA Collider . . . . .	52
TUIOB02 – Simulations of Stochastic Cooling of Antiprotons in the Collector Ring CR . . . . .	58
TUCOB01 – Stochastic Cooling Project at the Experimental Storage Ring, CSRe at IMP . . . . .	64
TUCOA01 – Helical Cooling Channel Developments . . . . .	67
TUIOA01 – MICE step I: First Measurement of Emittance with Particle Physics Detectors . . . . .	71
TUIOA02 – Progress in the Construction of the MICE Cooling Channel . . . . .	75
WECOB01 – Methods for Optimization of the Dynamics of the Storage of Positrons in the Surko Trap . . . . .	81
WEIOA01 – Enhancing Trappable Antiproton Populations Through an Induction Unit Followed by Frictional Cooling . . . . .	85
WECOA01 – Ion Kinetics in the Ultra-low Energy Electrostatic Storage Ring (USR) . . . . .	89
TUPS03 – Closed Orbit Correction in 2 MeV Electron Cooler Section at COSY-Juelich . . . . .	92
TUPS05 – Simulation of High-Energy Electron Cooling at COSY with BETACOOOL Program . . . . .	95
TUPS06 – Electron Gun with Variable Beam Profile for COSY Cooler . . . . .	99
TUPS07 – Electron Collector for 2 MeV Electron Cooler for COSY . . . . .	103
TUPS08 – System for Measurement of Magnetic Field Line Straightness in Solenoid of Electron Cooler for COSY . . . . .	107
TUPS09 – LEPTA Project: Towards Positrons . . . . .	111
TUPS10 – Magnetic System of Electron Cooler for COSY . . . . .	114
TUPS11 – Superconducting Shield for Solenoid of Electron Cooling System . . . . .	118
TUPS12 – Optical Electron Beam Diagnostics for Relativistic Electron Cooling Devices . . . . .	121
TUPS13 – Electron Cooler for NICA Collider . . . . .	125
TUPS15 – The Stochastic Cooling System of HESR . . . . .	129
TUPS16 – An Improved Forward Travelling Wave Structure Design for Stochastic Cooling at Experimental Cooler Storage Ring (CSRe) at the Institute of Modern Physics (IMP) in China . . . . .	132
TUPS19 – Simulation Study of Barrier Bucket Accumulation with Stochastic Cooling at the GSI ESR . . . . .	136
TUPS20 – Demonstration of Longitudinal Stacking in the ESR with Barrier Buckets and Stochastic Cooling . . . . .	140
TUPS21 – The Nonlinear Transformation of a Ions Beam in the Plasma Lens . . . . .	144
TUPS22 – Deceleration of Carbon Ions at the Heavy Ion Storage Ring TSR . . . . .	147
<b>Appendices</b>	<b>151</b>
List of Authors . . . . .	151
Institutes List . . . . .	155
Participants List . . . . .	158

## **International Program Committee**

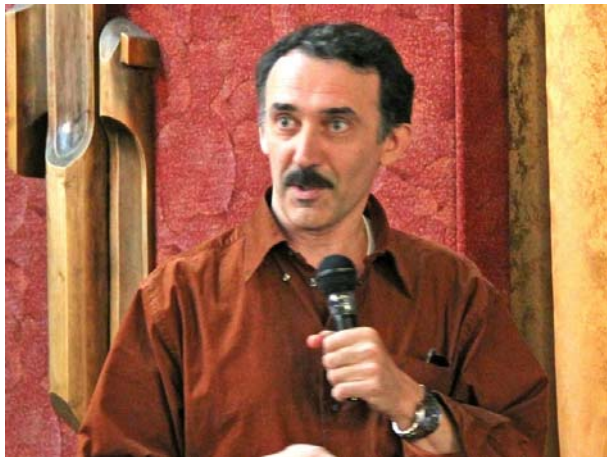
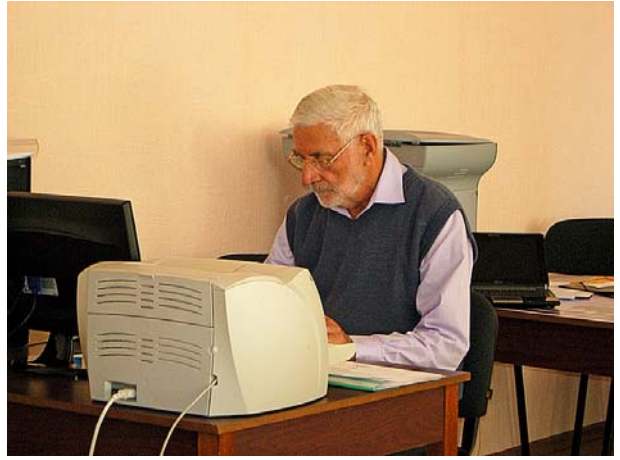
- Igor Meshkov (JINR, Dubna, Russia) – Co-Chair
- Alexander Skrinsky (BINP, Novosibirsk, Russia) – Co-Chair
- Markus Steck (GSI, Darmstadt, Germany) – Co-Chair
- Ekaterina Akhmanova (JINR, Dubna, Russia) - secretary
- Ilan Ben-Zvi (BNL, Brookhaven, USA)
- Hakan Danared (MSL, Stockholm, Sweden)
- Jurgen Dietrich (IKP FZJ, Julich, Germany)
- Manfred Grieser (IMP, Heidelberg, Germany)
- Takeshi Katayama (GSI, Germany)
- Dieter Mohl (CERN, Switzerland)
- Sergei Nagaitsev (FNAL, Batavia, USA)
- Akira Noda (Kyoto University, Japan)
- Vasily Parkhomchuk (BINP, Novosibirsk, Russia)
- Dieter Prasuhn (IKP, Julich, Germany)
- Andrew Sessler (LBNL, Berkeley, USA)
- Grigori Shirkov (JINR, Dubna, Russia)
- Gerard Tranquille (CERN, Switzerland)
- XiaoDong Yang (IMP, Lanzhou, China)
- Andreas Wolf (IMP, Heidelberg, Germany)

## **Local Organizing Committee**

- Grigory Shirkov (JINR, Dubna, Russia) – Chair
- Igor Meshkov (JINR, Dubna, Russia) – Co-Chair
- Grigory Trubnikov (JINR, Dubna, Russia) – Co-Chair
- Sergey Yakovenko (JINR, Dubna, Russia) – Scientific secretary
- Ekaterina Akhmanova (JINR, Dubna, Russia) – secretary
- Olga Matyukhina (JINR, Dubna, Russia) – secretary
- Maxim Kuzin (BINP, Novosibirsk, Russia)
- Alexander Philippov (JINR, Dubna, Russia)
- Roman Pivin (JINR, Dubna, Russia)
- Kristina Zhdanova (JINR, Dubna, Russia)









## ELECTRON COOLING PERFORMANCE AT IMP FACILITY\*

Xiaodong Yang<sup>#</sup>, Jie Li, Lijun Mao, Guohong Li, Xiaoming Ma, Tailai Yan, Mingtao Song, Youjin Yuan, Jiancheng Yang, Ruishi Mao, Tiecheng Zhao, Peng Li, Wei Zhang, Dayu Yin, Weiping Chai, Huan Jia, Wenheng Zheng, Xiaohu Zhang, Institute of Modern Physics, CAS, Lanzhou, 730000, P. R. China

### Abstract

The ion beam of  $^{58}\text{Ni}^{19+}$  with the energy of 6.39MeV/u was accumulated in the main ring of HIRFL-CSR with the help of electron cooling. The related angle between ion and electron beams in the horizontal and vertical planes was intentionally created by the steering coils in the cooling section after maximized the accumulated ion beam in the ring. The radial electron intensity distribution was changed by the ratio of potentials of grid electrode and anode of the electron gun, the different electron beam profiles were formed from solid to hollow in the experiments. In these conditions, the maximum accumulated ion beam intensity in the 10 seconds was measured, the lifetime of ion beam was measured, simultaneously the momentum spread of the ion beam varying with particle number was measured during the ion beam decay, furthermore, and the power coefficient was derived from these data. In additional, the momentum spread in the case of constant particle number was plotted with the angle and electron beam profile. The oscillation and shift of the central frequency of the ion beam were observed during the experiments. The upgrade and improvement in the CSRm cooler and the progress in the CSRc cooler were presented. These results were useful to attempt the crystal beam forming investigation in the CSR.

### MAIN WORKS IN CSR

- $^{209}\text{Bi}^{36+}$  Accumulation and Acceleration in CSRm
- Experiments related to cancer therapy [1]
- Patients treatment
- Mass measurement [2]
- Prophase Experiments on recombination [3]

### Accumulation and acceleration of $^{209}\text{Bi}^{36+}$

A new superconducting ECR ion source SECRAL developed by IMP has started operation to provide high intensity heavier ion beam.  $^{209}\text{Bi}^{36+}$  delivered by the SECRAL was accelerated by smaller cyclotron SFC to 1.877 MeV/u and then injected into CSRm. The average pulse intensity was about 1.8  $\mu\text{A}$  in the injection line. The average pulse particle number of  $^{209}\text{Bi}^{36+}$  was about  $7.3 \times 10^6$  in one standard multi-turn injection. With the help of electron cooling of partially hollow electron beam,  $4.4 \times 10^7$  particles were accumulated in the ring after 67 times injection in 10 seconds, and  $1.3 \times 10^7$  particles were accelerated to the final energy of 170 MeV/u. The DCCT signal of  $^{209}\text{Bi}^{36+}$  beam was displayed in Fig. 1 during accumulation and acceleration with the help of electron cooling.

<sup>#</sup>yangxd@impcas.ac.cn

\*Work supported by The National Natural Science Foundation of China, NSFC(Grant No. 10975166, 10905083, 10921504)

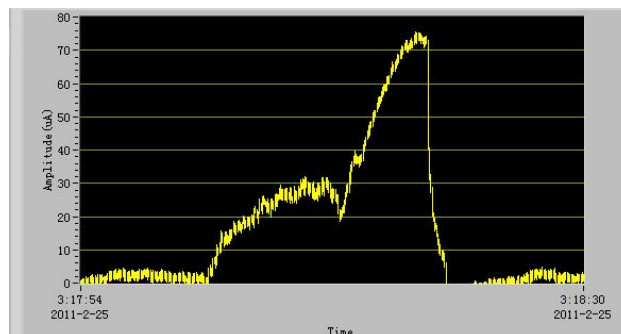


Figure 1: DCCT signal of  $^{209}\text{Bi}^{36+}$  beam accumulation and acceleration with the help of electron cooling, 1.87MeV/u -170MeV/u.

### BEAM ACCUMULATION IN CSR

The main function of electron cooler in CSRm was heavy ion beam accumulation. The accumulation efficiency was related with a lot of parameters of storage ring and electron cooler, such as the work-point setting, closed-orbit, electron density, and angle between electron beam and ion beam. At the beginning, the electron beam alignment was done to maximize the accumulated ion beam intensity. This setting was defined as "0" angle. The related angle between ion and electron beams in the horizontal and vertical planes was intentionally created by the steering coils in the cooling section after maximized the accumulated ion beam in the ring in the case of fixed storage ring parameters setting and electron beam parameters. After ion beam accumulation, the ion beam intensity and longitudinal signal were recorded by the DCCT monitor and Schottky probe during the ion beam decayed, and the maximal accumulated ion beam intensity in the 10 seconds interval was derived from the DCCT signal. The dependence of the ion beam intensity on the related horizontal and vertical angle was presented in the Fig. 2a and 2b. The angle between ion and electron beams reflected the temperature of electron in the system. In the case of the fixed electron beam current, ion encountered different electron temperature. The temperature influenced the cooling force and cooling time. The cooling force varying as the angle was reported in the reference [4]. The cooling force approached to maximal value in the perfect alignment between ion and electron beams, and the cooling time was minimal. One can see the maximal accumulated ion beam intensity was obtained near the zero angles in both panes. Another main parameters was the electron beam profile, the radial electron intensity distribution was changed by the ratio of potentials of grid electrode and anode of the electron gun, in this sense, and the different electron beam profiles were

formed from solid to hollow in the experiments. In these conditions, the maximum accumulated ion beam intensity in the 10 seconds was plotted in Fig. 2c. One can find that the maximal ion intensity attained near  $U_{grid}/U_{anode}=0.2$ , this results was similar as the previous results from CSR [4]. This indicated that the accumulation efficiency approached maximal in the partially hollow electron beam.

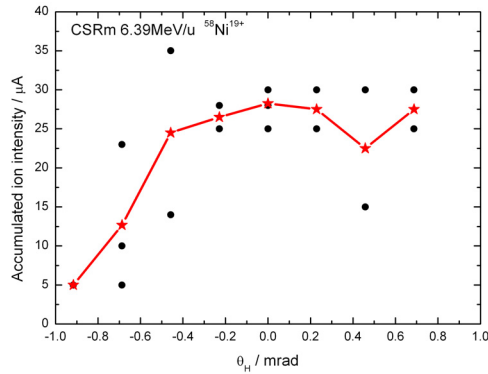


Figure 2a: The dependence of accumulated ion intensity in 10s on the related horizontal angle between ion and electron beams.

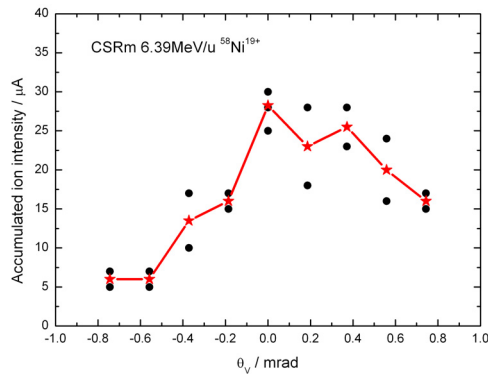


Figure 2b: The dependence of accumulated ion intensity in 10s on the related vertical angle between ion and electron beams.

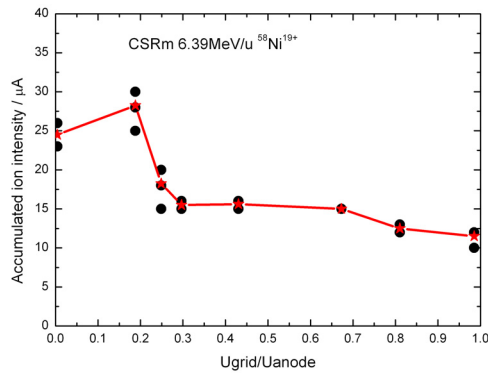


Figure 2c: The dependence of accumulated ion intensity in 10s on the profile of electron beam.

Electron cooling

### EXPONENT

The scaling law of momentum spread varying as the stored particle number was reported in many references [5, 6, 7]. A lot of result was presented from the aspects of

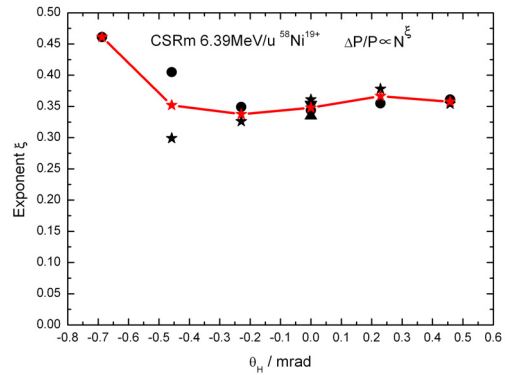


Figure 3a: The power coefficient varies with the related horizontal angle between ion and electron beams. The momentum spread was scaled with the particle number as power law  $\Delta P/P \propto N^\xi$ . The exponent in the figure is the power coefficient  $\xi$ .

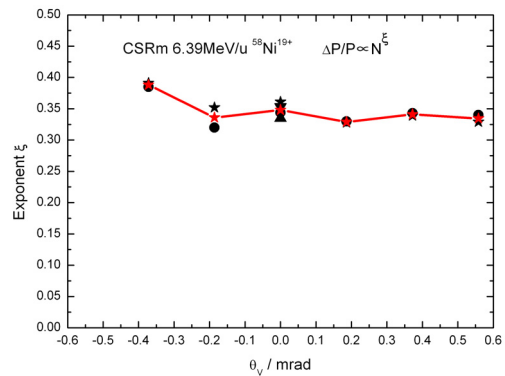


Figure 3b: The power coefficient varies with the related vertical angle between ion and electron beams.

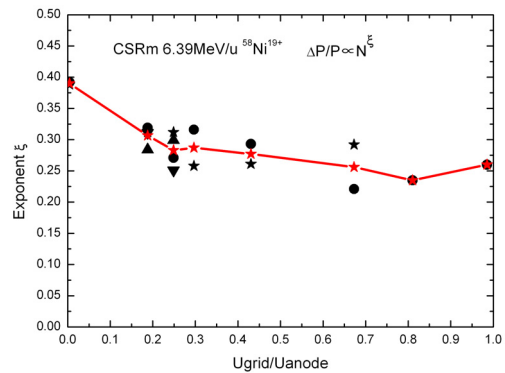


Figure 3c: The power coefficient varies with the profile of electron beam.

theoretical and experimental, in addition, some simulated results was presented. The power coefficient  $\xi$  was derived from the recorded iqt data by the Schottky probe in this experiment. The results were presented in the Fig. 3a and 3b. From the diagram one can see that the power coefficient became bigger in the case of a bigger related angle between ion and electron beams. It was near 0.3 in the smaller angles. These were consistent with the results of the references [7, 8]. When the electron beam was solid, the power coefficient was bigger. For a hollow electron beam it became smaller. The power coefficient as a function of the electron profile was shown in the Fig.3c.

### MOMENTUM SPREAD

The momentum spread of the ion beam after electron cooling was an important parameter in the storage ring. It indicated the minimal value of the ion temperature after the equilibrium. The momentum spread versus the related horizontal and vertical angle between ion and electron beams was illustrated in the Fig. 4a and 4b in the circumstances of fixed particle number. The momentum spread was smaller in the condition of bigger angles, whereas the momentum spread was bigger under the circumstances of smaller angle. These results were good agreement with the reference [5, 7]. In the Fig. 4c, the momentum spread versus the electron beam profile was shown. These results revealed that the momentum spread was smaller in the condition of solid electron beam, and the bigger momentum spread in the case of hollow electron beam. For the same electron current the space potential did not change outside the electron beam, but the potential continuously increased inside for the solid electron beam. The potential was the reason of variation of the ion beam momentum spread with the changing of electron beam profile. When the ratio of  $U_{grid}/U_{anode}$  increased, the profile of the electron beam was close to the hollow beam, the suppression of the electron beam energy decreased.

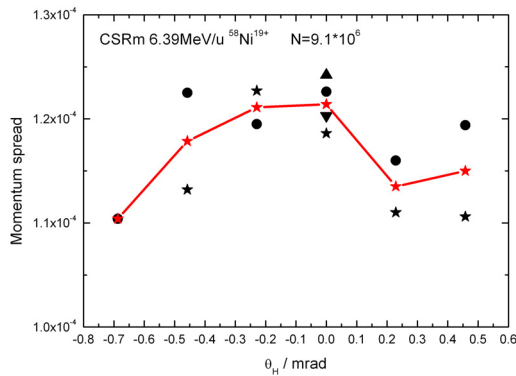


Figure 4a: The momentum spread versus the related horizontal angle between ion and electron beams in the case of fixed particle number  $N=9.1 \cdot 10^6$ .

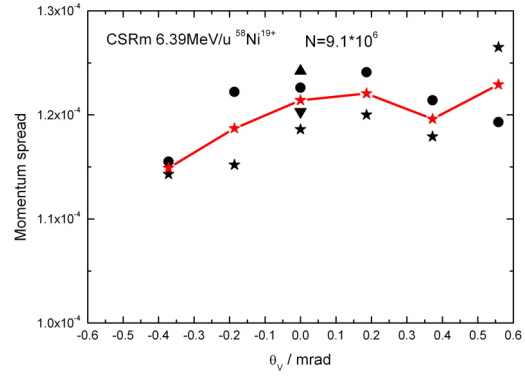


Figure 4b: The momentum spread versus the related vertical angle between ion and electron beams in the case of fixed particle number  $N=9.1 \cdot 10^6$ .

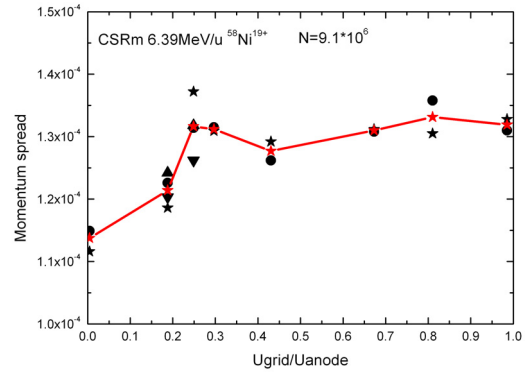


Figure 4c: The momentum spread versus the profile of electron beam in the case of fixed particle number  $N=9.1 \cdot 10^6$ .

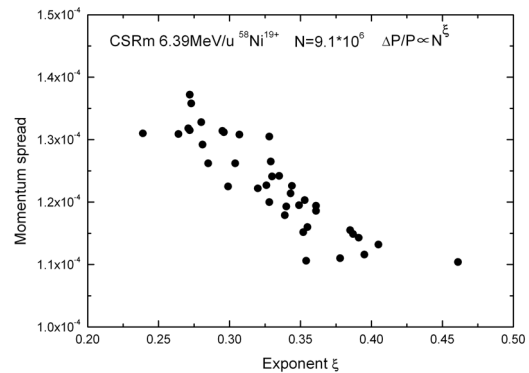


Figure 5: The momentum spread as a function of the exponent (power coefficient) in the case of fixed particle number  $N=9.1 \cdot 10^6$ .

In the Fig. 5, the momentum spread as a function of the exponent (power coefficient  $\xi$ ) was plotted. This result was similar as the reference [7]. The smaller momentum spread emerged in the case of a bigger exponent.

## LIFETIME

The lifetime of stored ion beam was a complicated problem in the storage ring, the factors influenced the lifetime included work-point setting, vacuum, particle species, charge state, especially the electron cooler parameters such as electron density and radial distribution.

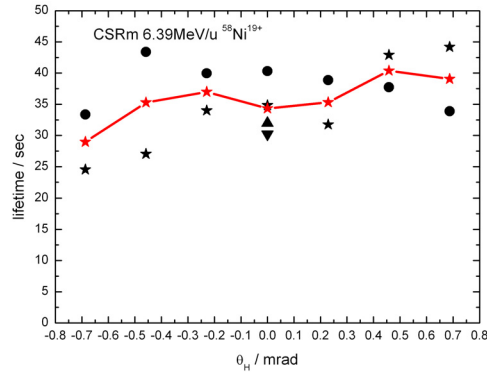


Figure 6a: The lifetime as a function of the related horizontal angle between ion and electron beams. The lifetime of ion beam in the CSM was derived from the signal of DCCT.

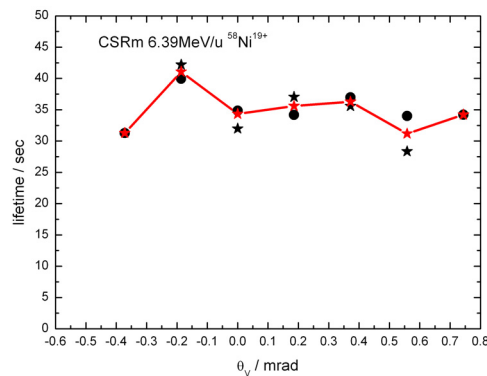


Figure 6b: The lifetime as a function of the related vertical angle between ion and electron beams.

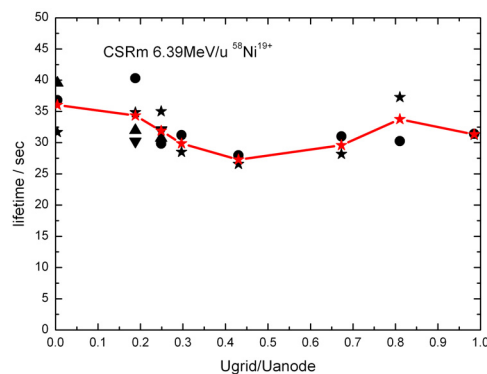


Figure 6c: The lifetime as a function of the profile of electron beam.

Electron cooling

Capturing electron by the ion was the main beam loss way in the present of electron ring cooling and normal operation mode of storage ring. In this case, the temperature of electron was the important parameter. The possibility of capturing increased in the case of the lower related temperature between ions and electrons in the three degree of freedom, and the beam loss become serious, as a consequence the lifetime of ion beam became shorter. Fig 6a and 6b shows the lifetime of ion beam as a function of the related horizontal and vertical angle between ion and electron beams. From these results, the influence of angle on the ion beam lifetime was slight. When the electron moved in the cooler, the temperature was varied in the different situations. The maximal temperature increased when the angle existed, but the lowest temperature was not changed. The ions had their choices when the ion captured the free electron, as a result, no varying in the lifetime. The lifetime as a function of electron beam profile was shown in the Fig. 6c; the lifetime change is not obvious in the case of hollow electron beam as expected. The reason was the energy of electron beam was not perfectly matched in term of the varying of space charge in the different radial electron distribution.

## FREQUENCY SHIFT AND OSCILLATION

A related angle between ion and electron beams in the horizontal and vertical planes was intentionally created by the steering coils in the cooling section. In the vertical direction, the central frequency of ion beam shifted towards the lower side when the angle was bigger than a certain value. There was no obvious frequency shift in the case of smaller angles. In despite of the polarity of angle referenced to the zero, the tendency of central frequency shift was the same as demonstrated in The Fig. 8a. The frequency different is about  $\Delta f/f=9.5 \times 10^{-4}$ . This can be interpreted as that an additional angle was created in the cooling section in the case of the fixed ion energy and dipole field of storage ring. This angle resulted in the increscent of ion beam path length in the vertical direction, in the other hands; the projection of the electron velocity in the ion beam orbit became smaller. The ion beam was drugged to the lower energy level, and the central frequency of ion beam became smaller compared with the situation of better alignment due to the both effects. In the horizontal plane, not only the central frequency of ion beam shifted towards the lower side, but also obvious oscillation appeared when the angle was bigger than a certain value. One conceivable explanation was that the high voltage of cooler was changed due to the electron beam hit in some place of cooler in the case of a bigger misalignment angle. The diameter of electron beam in the cooling section was about 59mm. The energy modulation of electron beam performed the similar behavior in the Schottky signal as exemplified in Fig. 9. The signal of modulation was uniform; the signal of oscillation was random. The different phenomena were observed in negative and positive angle in the horizontal

plane. The central frequency shift and oscillation did not appear in the opposite angle, as shown in the Fig. 8b. The reasonable explanation was not found.

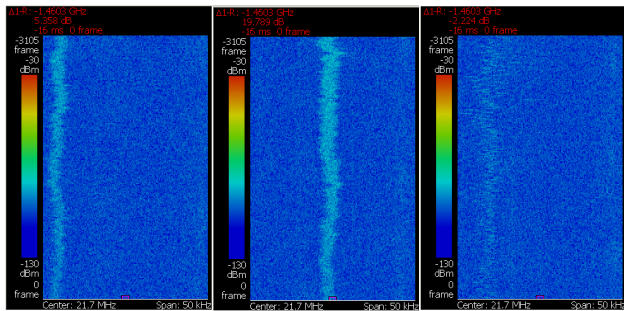


Figure 8a: The Schottky signals at different misalignment angle in the vertical plane (left:  $\theta_v=0.744$ mrad, centre:  $\theta_v=0$ mrad, right:  $\theta_v=-0.744$ mrad). The central frequency of ion beam moves to lower side in the case of a bigger misalignment in two directions. The frequency shift is not symmetrical.

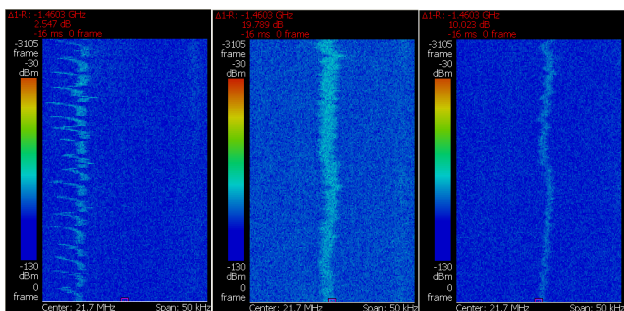


Figure 8b: The Schottky signals at different misalignment angle in the horizontal direction (left:  $\theta_H=0.687$ mrad, centre:  $\theta_H=0$ mrad, right:  $\theta_H=-0.687$ mrad). The central frequency of ion beam move to lower side, and the longitudinal oscillation was observed in the bigger misalignment in the horizontal plane.

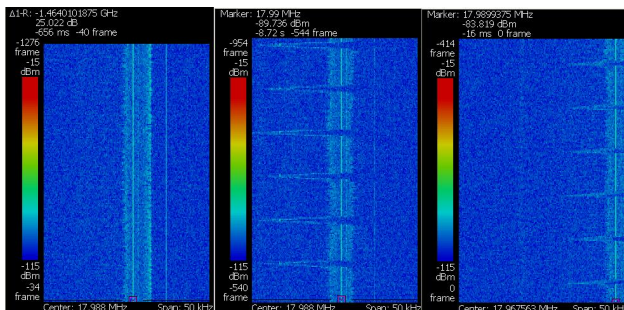


Figure 9: The Schottky signal during the modulation of electron beam energy. (left: no modulation, centre: 10V-100ms-1000ms, right: 20V-100ms-1000ms)

### PROGRESS, UPGRADE AND IMPROVEMENT IN CSR

- Add energy modulation system for CSRm cooler
- Improve the stability of power supply for CSRe dipoles
- Temperature control for 300kV cooler
- High voltage of CSRe cooler approach to 285kV

Electron cooling

- 14 days continuous work at 285kV

### SUMMARY OF CSR STATUS

- The 35kV cooler can work at the lower energy (<1kV).
- The 300kV cooler can work at the higher energy (~285kV, 520MeV/u).
- The oscillation of ion beam was not caused by the instability of high voltage of cooler.
- Partial hollow electron beam is helpful to ion beam accumulation.
- A longitudinal oscillation signal was observed from Schottky probe during experiments.

### REFERENCES

- [1] Qiang Li, Lembit Sihver, “Therapeutic techniques applied in the heavy-ion therapy at IMP”, Nuclear Instruments and Methods in Physics Research B. 269 (2011) 664-670.
- [2] X. L. Tu, H. S. Xu, M. Wang, et al, “Direct Mass Measurements of Short-Lived A=2Z-1 Nuclides  $^{63}\text{Ge}$ ,  $^{65}\text{As}$ ,  $^{67}\text{Se}$ , and  $^{71}\text{Kr}$  and Their Impact on Nucleosynthesis in the rp Process”, Physical Review Letters, 106, 112501 (2011).
- [3] L. J. Meng, X. Ma, H. P. Liu, X. D. Yang, et al, “The first test experiment performed at the electron cooler of storage rings in Lanzhou”, 2009 Journal of Physics: Conference Series (JPCS).163 012031 (2009).
- [4] Xiaodong Yang, Guohong Li, et al, “Electron Cooling Experiments in CSR”, RuPAC’10, Protvino, Russia, 27 September 2010, WECHZ05, p.161 (2010), <http://accelconf.web.cern.ch/AccelConf/r10/papers/w echz05.pdf>.
- [5] R. W. Hasse, O. Boine-Frankenheim, “Scaling laws with current for equilibrium momentum spread and emittances from intrabeam scattering and electron cooling”, Nuclear Instruments and Methods in Physics Research A 532 (2004) 451–453.
- [6] M. Steck, K. Beckert, H. Eickhoff, B. Franzke, F. Nolden, H. Reich, et al, “Lowest Temperatures in Cooled Heavy Ion Beams at the ESR”, EPAC’98, Stockholm, 22 June 1998, THP42G, p. 1064 (1998), <http://accelconf.web.cern.ch/AccelConf/e98/PAPER S/THP42G.PDF>.
- [7] I.Meshkov, A.Sidorin, A.Smirnov, A. Noda, K.Noda, J.Dietrich, et al, “Necessary Condition for Beam Ordering”, COOL’07, Bad Kreuznach, Germany, September 10, 2007, TUA1C03, p. 87 (2007), <http://accelconf.web.cern.ch/AccelConf/cl07/PAPER S/TUA1C03.PDF>.
- [8] M. Steck, K. Beckert, P. Beller, C. Dimopoulou, F. Nolden, “Limitations to the observation of beam ordering”, COOL’07, Bad Kreuznach, Germany, September 10, 2007, THAP22, p. 217 (2007), <http://accelconf.web.cern.ch/AccelConf/cl07/PAPER S/THAP22.PDF>.

## NICA PROJECT AT JINR

V. Kekelidze, R. Lednicky, V. Matveev, I. Meshkov\*,  
A. Sorin, G. Trubnikov, JINR, Russia

### Abstract

The project of Nuclotron-based Ion Collider fAcility NICA/MPD (MultiPurpose Detector) under development at JINR (Dubna) is presented. The general goals of the project are providing of colliding beams for experimental studies of both hot and dense strongly interacting baryonic matter and spin physics (in collisions of polarized protons and deuterons). The first program requires providing of heavy ion collisions in the energy range of  $\sqrt{s_{NN}} = 4\div 11$  GeV at average luminosity of  $L = 1\cdot 10^{27}$  cm<sup>-2</sup>·s<sup>-1</sup> for <sup>197</sup>Au<sup>79+</sup> nuclei. The polarized beams mode is proposed to be used in energy range of  $\sqrt{s_{NN}} = 12\div 27$  GeV (protons at luminosity of  $L \geq 1\cdot 10^{30}$  cm<sup>-2</sup>·s<sup>-1</sup>). The key issue of the Project is application of cooling methods – stochastic and electron ones. The report contains description of the facility scheme and characteristics in heavy ion operation mode, status and plans of the project development.

### NUCLOTRON-M & NICA PROJECT

The Nuclotron-based Ion Collider fAcility (NICA) [1] is a new accelerator complex (Fig. 1) being constructed at JINR. It is aimed to provide collider experiments with:

- heavy ions <sup>197</sup>Au<sup>79+</sup> at  $\sqrt{s_{NN}} = 4\div 11$  GeV (1÷4.5 GeV/u ion kinetic energy) at average luminosity of  $1\cdot 10^{27}$  cm<sup>-2</sup>·s<sup>-1</sup> (at  $\sqrt{s_{NN}} = 9$  GeV);
- light-heavy ions colliding beams of the same energy range and luminosity;
- polarized beams of protons  $\sqrt{s} = 12\div 27$  GeV (5÷12.6 GeV kinetic energy) and deuterons  $\sqrt{s_{NN}} = 4\div 13.8$  GeV (2÷5.9 GeV/u ion kinetic energy) at average luminosity  $\geq 1\cdot 10^{30}$  cm<sup>-2</sup>·s<sup>-1</sup>.

The proposed facility consists of the following elements (Fig. 1):

- “Old” injector (pos. 1): set of light ion sources including source of polarized protons and deuterons and Alvarez-type linac LU-20\*);
- “New” injector (pos. 2, under construction): ESIS-type ion source that provides <sup>197</sup>Au<sup>32+</sup> ions of the intensity of  $2\cdot 10^9$  ions per pulse of about 7 μs duration at repetition rate up to 50 Hz and linear accelerator consisting of RFQ and RFQ Drift Tube Linac (RFQ DTL) sections. The linac accelerates the ions at  $A/q \leq 8$  up to the energy of 6 MeV/u at efficiency not less than 80 %.

- *Booster-synchrotron* housed inside Synchrophasotron yoke (pos. 3). The Booster (pos. 4) has superconducting (SC) magnetic system that provides maximum magnetic rigidity of 25 T·m at the ring circumference of 215 m. It is equipped with electron cooling system that allows to provide cooling of the ion beam in the energy range from injection energy up to 100 MeV/u. The maximum energy of <sup>197</sup>Au<sup>32+</sup> ions accelerated in the Booster is of 600 MeV/u. Stripping foil placed in the transfer line from the Booster to the Nuclotron allows to provide the stripping efficiency at the maximum Booster energy not less than 80 %.

- *Nuclotron* – SC proton synchrotron (pos. 5) has maximum magnetic rigidity of 45 T·m and the circumference of 251.52 m provides the acceleration of completely stripped <sup>197</sup>Au<sup>79+</sup> ions up to the experiment energy in energy range of 1÷4.5 GeV/u and protons up to maximum energy of 12.6 GeV.

- *Transfer line* (pos. 6) transports the particles from Nuclotron to Collider rings.

- *Two SC collider rings* (pos. 8) of racetrack shape have maximum magnetic rigidity of 45 T·m and the circumference of about 400 m. The maximum field of SC dipole magnets is 1.8 T. For luminosity preservation an electron and stochastic cooling systems will be constructed.

- *Two detectors* – MultiPurpose Detector (MPD, pos. 9) and Spin Physics Detector (SPD, pos. 10) are located in opposite straight sections of the racetrack rings.

- *Two transfer lines* transport particle beams extracted from Booster (pos. 11) and Nuclotron (pos. 12) to the new research area, where fixed target experiments both basic and applied character will be placed.

The NICA parameters (Table below) allow us to reach the goals of the project formulated above.

One of NICA accelerators – Nuclotron is used presently for fixed target experiments on extracted beams (Fig. 1, pos. 7).

This program is planned to be developed further and will be complementary to that one to be performed at Collider in heavy ions beam mode operation. The program includes experimental studies on relativistic nuclear physics, spin physics in few body nuclear systems (with polarized deuterons) and physics of flavours. At the same time, the Nuclotron beams are used for research in radiobiology and applied research.

\* Corresponding author: meshkov@jinr.ru

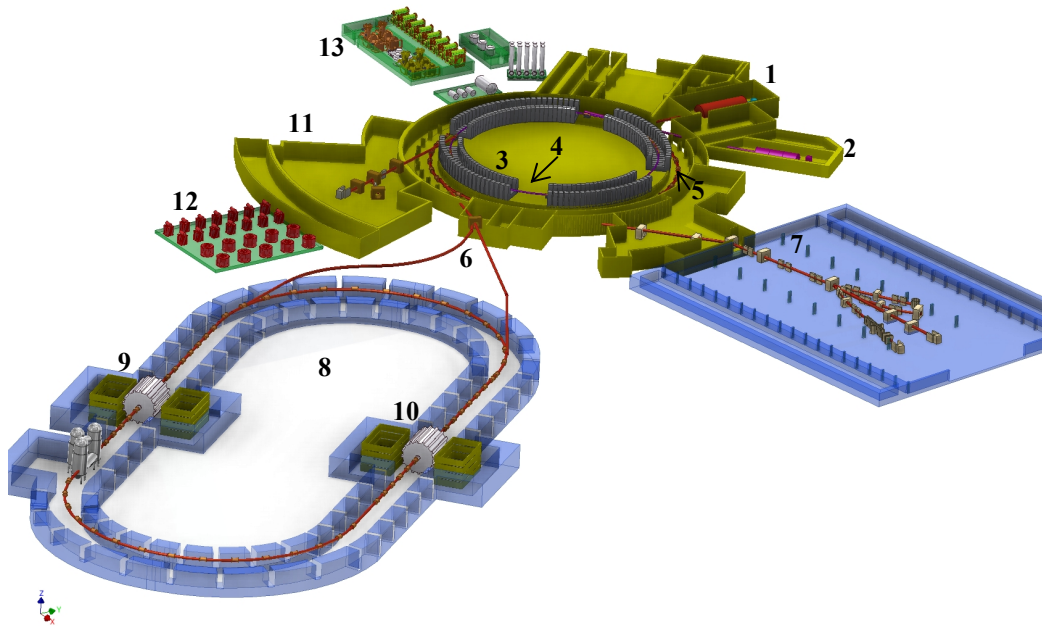


Figure 1: Scheme of NICA facility: 1 – light and polarized ion sources and “old” Alvarez-type linac; 2 – ESIS source and new RFQ linac; 3 – Synchrotron yoke; 4 – Booster; 5 – Nuclotron; 6 – beam transfer lines; 7 – Nuclotron beam lines and fixed target experiments; 8 – Collider; 9 – MPD; 10 – SPD; 11 – new research area, 12 – cryogenic plant, 13 – auxiliary equipment

Table of parameters of NICA accelerators

Acceleration	Booster project	Nuclotron		Collider project
		Project	Status (April 2011)	
1. Circumference, m	212.2	251.5		503.0
2. Max. magn. field, T	2.0	2.0	2.0	1.8
3. Magn. rigidity, T·m	25.0	45	39.5	45
4. Cycle duration, s	4.0	4.02	5.0	≥ 2000
5. B-field ramp, T/s	1.0	1.0	1.0	< 0.1
6. Accelerated/stored particles	$p \div ^{197}\text{Au}^{79+}, p\uparrow, d\uparrow$	$p\text{-Xe}, d\uparrow$		$p \div ^{197}\text{Au}^{79+}, p\uparrow, d\uparrow$
<b>Maximum energy, GeV/u</b>				
Protons	–	12.6	–	12.6
Deuterons	–	5.87	5.1	5.87
Ions, GeV/u	$^{197}\text{Au}^{32+}$ 0.4	$^{197}\text{Au}^{79}$ 4.5	$^{54}\text{Xe}^{24+}$ 1.0	$^{197}\text{Au}^{79}$ 4.5
<b>Intensity, ion number per cycle (bunch)</b>				
protons	$1 \cdot 10^{11}$	$1 \cdot 10^{11}$	$1 \cdot 10^{11}$	$1 \cdot 10^{11}$
deuterons	$1 \cdot 10^{10}$	$1 \cdot 10^{10}$	$1 \cdot 10^{10}$	$1 \cdot 10^{10}$
$^{197}\text{Au}^{79}$	$2 \cdot 10^9$	$2 \cdot 10^9$	$1 \cdot 10^6$ ( $^{54}\text{Xe}^{24+}$ )	$1 \cdot 10^9$

## COLLIDER LUMINOSITY AND COOLING ISSUES

The collider design has to provide the project luminosity and its maintenance during a long time necessary for an experiment performance. That requires, correspondingly:

- 1) formation of ion beams of high intensity and sufficiently low emittance,
- 2) ion beam life time.

Beam intensity is limited, in principle, by beam space charge effects, which can be estimated by so called “tune shift criteria”. *The first one*, and most strong of them usually, is so called betatron oscillation tune shift (or “*The Laslett tune shift*”):

$$\Delta Q = \frac{Z^2}{A} \cdot \frac{r_p N_i}{\beta^2 \gamma^3 4\pi \varepsilon_{geom}} \cdot k_{bunch}, \quad k_{bunch} = \frac{C_{Ring}}{\sqrt{2\pi} \cdot \sigma_s}. \quad (1)$$

Here  $Ze$  and  $A$  are ion charge and mass number,  $r_p$  is proton classic radius,  $N_i$  is ion number per bunch in the bunched ion beam,  $\beta$ ,  $\gamma$  are the ion Lorentz factors,  $k_{bunch}$  is bunch factor,  $C_{Ring}$  is the Collider ring circumference,  $\sigma_s$  is bunch length ( $\sigma$ -value for Gaussian beam),  $\varepsilon_{geom}$  is the ion bunch “geometrical” transverse emittance (do distinguish with “normalized” one  $\varepsilon_{norm}$  used below). *The second criterion* is so called *beam-beam parameter* that describes ion betatron tune shift related to scattering of ion on the electromagnetic field of encountering ion bunch:

$$\xi = \frac{Z^2}{A} \cdot \frac{r_p N_i (1 + \beta^2)}{4\pi \beta^2 \gamma \varepsilon_{geom}} \quad (2)$$

For practical estimates one can use the numerical criterion for beam stability as follows:

$$\Delta Q_{total} \equiv \Delta Q + n_\xi \xi \leq 0.05. \quad (3)$$

$n_\xi$  is number of interaction points.

One of instabilities and major problems of the NICA collider is suppression of intrabeam scattering (IBS) in intense ion bunches. The last one defines mainly the beam life time. For this purpose we have proposed to use both electron cooling [2] and stochastic cooling [3] methods. In the first case we assume achievement of equilibrium between cooling and space charge forces when space charge tune shift  $\Delta Q_{total}$  reaches a resonant value (e. g., 0.05). We call it *space charge dominated regime* (SCD regime). Then using Formulae (1), (2) and well known expression for luminosity of round colliding beams one can derive simple relations between parameters:

$$L \propto \Delta Q_{total}^2 \cdot \varepsilon_{geom} \cdot f_L(E_{ion}) \cdot f_{HG}, \quad (4)$$

$$N_i \propto \Delta Q_{total} \cdot \varepsilon_{geom} \cdot f_N(E_{ion}),$$

where  $E_i$  is ion energy,  $f_L$ ,  $f_n$  are the functions describing energy dependence of parameters,  $f_{HG}$  is hour-glass effect function. We see that maximum luminosity is achieved if beam emittance  $\varepsilon_{geom}$  has maximum, i. e. coincides with the ring acceptance. At some circumstances the luminosity can be limited by “not the beam reasons” (e. q., detector performance). Then one can optimise the SCD regime decreasing equilibrium emittance and  $N_i$  (Fig. 2). Such an optimisation can be done with variation of  $N_i$  number. In the case of limited luminosity one can also avoid SCD regime decreasing ion number and allowing, by weakening cooling force, the beam emittance keeping  $\Delta Q_{total}$  below resonant value. We call it *IBS Dominated regime* (IBS DR) when equilibrium state is provided with equality IBS and cooling rates:

$$R_{IBS} = R_{cool}. \quad (5)$$

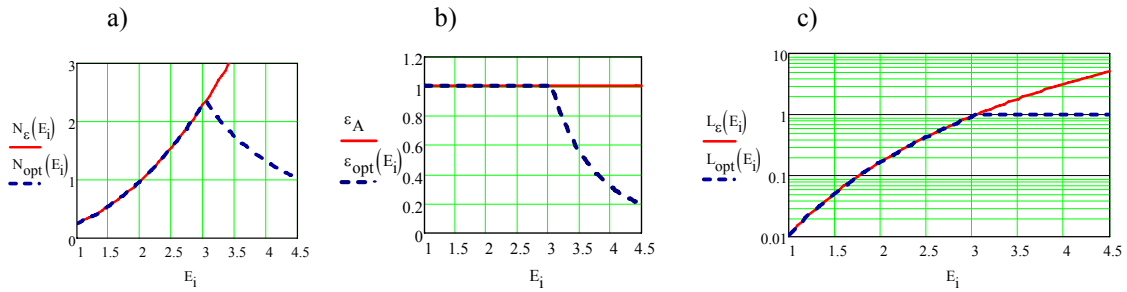


Figure 2: Space charge dominated regime; ion number per bunch (a), beam emittance (b) and luminosity (c) versus ion energy in two cases: full acceptance if filled with ions (red solid curves) and luminosity is limited (blue dash curve); the ring acceptance =  $40 \pi$ -mm-mrad, parameter units:  $[N_i] = 10^9$ ,  $[\varepsilon] = \pi$ -mm-mrad,  $[L] = 10^{27} \text{ cm}^{-2} \cdot \text{s}^{-1}$ .

Then, at fixed luminosity, similar by to Formulae (4) one can write

$$L = \text{const}, \quad N_i \propto \sqrt{L \cdot \varepsilon_{geom}} \cdot \varphi_L(E_i),$$

$$\Delta Q_{total} \propto \sqrt{\frac{L}{\varepsilon_{geom}}} \cdot \psi_L(E_i) < \Delta Q_{max}. \quad (6)$$

As we see, minimum  $\Delta Q_{total}$  corresponds to maximum emittance, i.e. full acceptance filling with ions. Simultaneously, it gives us maximum  $\tau_{IBS}$  at relatively increased ion number (Fig. 3). One should mention that at IBS DR ion number dependence of energy is rather weak – proportional to  $(N_{ion}/C)^{-1/2}$ .

For NICA parameters, as it follows from Fig. 3, IBS DR regime can be used at  $E_i > 3$  GeV/u where  $\Delta Q < 0.05$ . At the same energy range we plan to use stochastic cooling. At lower energy electron cooling application is preferable (if not to say more realizable) [3, 2]. However, then another problem appears: ion recombination with cooling electrons. This effect can be significantly diminished by increase of cooling electrons temperature [4].

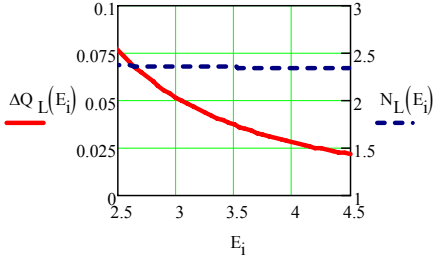


Figure 3: IBS dominated regime; beam tune shift  $\Delta Q_{total}$  (red solid curve) and ion number per bunch  $N_i$  (blue dash

curve) at constant luminosity  $L = 1 \cdot 10^{27} \text{ cm}^{-2} \cdot \text{s}^{-1}$  and beam emittance of  $1.0 \pi \cdot \text{mm} \cdot \text{mrad}$ ;  $[N_i] = 10^9$ .

The described approach (SC and IBS dominated regimes) can be developed even further. One can, for instance, increase luminosity in low energy range (below 3 GeV/u) by enlarging minimum beta-functions in IP area. That will be followed by decrease of beta-functions in the lenses of final focus and lead correspondingly to increase of the ring acceptance. Those steps are planned for future development.

## CONCLUSION

The status main characteristics of NICA project and principle problems related to the NICA collider creation are considered in this report. The NICA project as a whole has passed the phase of concept formulation and is presently under development of the working project, manufacturing and construction of the prototypes.

The project realization plan foresees a staged construction and commissioning of the accelerators that form the facility. The main goal is beginning of the facility commissioning in 2017.

## REFERENCES

- [1] Search for a QCD Mixed Phase at the Nuclotron-based Ion Collider Facility (NICA White Paper), [http://theor.jinr.ru/twiki/pub/NICA/WebHome/WhitePaper\\_5.03.pdf](http://theor.jinr.ru/twiki/pub/NICA/WebHome/WhitePaper_5.03.pdf).
- [2] S. Yakovenko, E. Ahmanova, A. Kobets et al., Cooler for Collider NICA, Proc. of COOL'2011, TUPS13.
- [3] G. Trubnikov, Application of Cooling Methods in the NICA Project, Proc. of COOL'2011, MOIO07.
- [4] A. Philippov, A. Kuznetsov, I. Meshkov, Radioactive Recombination of Bare Nuclei and Ions in Electron Cooling System, Proc. of COOL'2011, THCOB01.

## CURRENT PLANS FOR BEAM COOLING AT FAIR

M. Steck for the 'FAIR Project Team'  
GSI Darmstadt, Germany

### *Abstract*

The accelerators of the international FAIR project are designed to provide stable heavy ion beams, rare isotope beams and antiprotons with high intensity and high beam quality. Beam cooling is indispensable to improve the beam quality of secondary beams produced by bombardment of thick targets. The goals of the project as well as the methods to achieve high intensity and high quality secondary beams will be described. Due to budget constraints the project realization is planned in a staged scenario. The main accelerator systems in the first project stage to provide cooled beams will be the Collector Ring for pre-cooling of secondary beams and the High Energy Storage Ring for experiments with stored cooled antiprotons.

### INTRODUCTION

The international FAIR project will provide heavy ion and proton primary beams over a large range of energies [1]. These beams serve four basic physics programs, research with high energy antiprotons, studies of compressed baryonic matter, nuclear structure and related astrophysics, and atomic and plasma physics and their applications. The use of beam cooling is foreseen for highly charged primary heavy ion beams, for rare isotope beams from the new large acceptance separator SuperFRS and for antiproton beams produced in a dedicated antiproton source with a target and a separator section. A number of storage rings was conceived for various purposes, such as pre-cooling of the hot secondary beams immediately after the production target, for accumulation of the pre-cooled secondary beams and finally storage rings equipped with powerful cooling systems which allow the use of high quality cooled beams in high precision and high luminosity experiments with internal targets [2]. Another option will be the deceleration of cooled secondary beams for experiments at low energy and even after further deceleration in linear decelerators, nearly to rest, for which beam cooling is indispensable. For these purposes mainly four storage rings were designed, the Collector Ring (CR) for the pre-cooling of antiprotons and rare isotopes, the accumulator ring RESR for the accumulation of high intensity antiproton beams by a dedicated stochastic cooling system, the New Experimental Storage Ring (NESR) as a storage ring for internal experiments with heavy ions and rare isotopes and deceleration of cooled beams of ions and antiprotons, and the High Energy Storage Ring (HESR) for experiments with cooled antiprotons using internal hydrogen targets.

Stochastic cooling

These storage rings together with the other new accelerator facilities of the FAIR project were documented in technical design reports [3].

After a revision of the project cost, it was decided that the project will be constructed in a staged manner. The first stage of the project, called Modularized Start Version (MSV), is conceived such that it can serve all four basic pillars of the physics program of FAIR. Due to the limited money available for the first part of the FAIR project, however, the accumulator ring RESR and the ion storage ring NESR had to be postponed to a later stage of the FAIR project and will not be constructed in the frame of the MSV. As a compensation of the lack of stored ion beams in the MSV of FAIR it was decided that the operation of the existing ESR storage ring will be continued.

### FAIR ACCELERATORS OF THE MODULARIZED START VERSION

The MSV is based on the existing linear accelerator UNILAC for heavy ions serving as injector into the existing heavy ion synchrotron SIS18. An extended upgrade program is under way to improve the performance of these injector machines and towards increased intensities and acceleration with higher ramp rate. The MSV now comprises the following new accelerator facilities. A new 70 MeV proton linac as injector in front of the synchrotron SIS18 will provide the high intensity proton beam required for the production of antiprotons, it can fill SIS18 up to the space charge limit. The new synchrotron SIS100 uses the SIS18 as injector for high intensity proton and heavy ion beams. The maximum magnetic rigidity of 100 Tm allows either acceleration to higher energy or the acceleration of low charge states, which provides higher beam intensity as no additional stripping stage in front of SIS18 is needed, thus avoiding the reduction of intensity associated with the use of the stripper foil. The SIS100 design is based on super-ferric magnets allowing fast 4 T/s ramping of the magnetic field which is needed to provide high average beam intensities [4]. The 1080 m circumference ring tunnel of SIS100 will be prepared for the later installation of an additional 300 Tm superconducting synchrotron for the acceleration of heavy ions to correspondingly higher energy or for use as a stretcher ring for slow extraction of 100 Tm beams accelerated in SIS100.

After SIS100 two stations for the production of secondary beams will be constructed. The SuperFRS has a target for the production of rare isotope beams by projectile fragmentation followed by a large acceptance super-

conducting magnetic separator [5]. The fragment beams can be used either for fixed target experiments or for injection into the CR storage ring [6] where phase space reduction by fast stochastic pre-cooling allows the transfer to a subsequent storage ring for internal experiments or deceleration to lower energy. Therefore SIS100 will provide both a slow and a fast extraction mode for heavy ions. The second target station is designed for the production of antiprotons from an intense 50 ns short bunch of 29 GeV protons. A nickel target followed by a magnetic horn and a magnetic separator provides 3 GeV antiprotons for the injection into the CR storage ring. Fast bunch rotation and debunching and subsequent stochastic cooling in the CR prepare the antiprotons for further use.

In the MSV the only user of the pre-cooled secondary beams will be the HESR [7]. The HESR is a storage ring of 50 Tm maximum magnetic rigidity. The 3 GeV antiprotons from the CR will be accumulated at 3 GeV by a combination of an rf system for compression of the circulating beam into a fraction of the storage ring and stochastic cooling. The feasibility of the proposed stacking scheme in the HESR was recently investigated in a proof-of-principle experiment at the ESR [8]. This experiment demonstrated the feasibility of the proposed accumulation scheme and confirmed the predictive power of computer simulations which are used to study and optimize the antiproton accumulation in the HESR [9].

## COLLECTOR RING CR

The Collector Ring CR was from the very beginning of the FAIR project designed as a pre-cooling ring for secondary beams. Both types of secondary beams, antiprotons and rare isotopes are produced in a thick solid target by bombardment with a high intensity primary beam. Consequently, the production of the secondary beam is associated with angular scattering and energy straggling in the target. The secondary beam has large transverse emittance and longitudinal momentum spread. Therefore the main design issue for the storage ring was a large acceptance, transversely and longitudinally. The use of large aperture magnets and a lattice design which considers the higher order components affecting particles with large betatron amplitudes were major design aspects. These aspects did not change in the frame of the MSV. The same is true for the use of fast bunch rotation and adiabatic debunching of the incoming short bunch of secondary particles which requires a dedicated rf system.

In the original full FAIR project the pre-cooled secondary beams from the CR were transferred to another storage ring for accumulation of intense secondary beams, for antiprotons the accumulation was foreseen in the dedicated accumulator ring RESR, for rare isotopes accumulation in the NESR should precede the preparation of the rare isotope beam for the experiment.

After postponing both rings to a phase after the construction of the MSV, the CR design had to be modified for the Stochastic cooling

transfer of the antiproton beam directly to the HESR. The direct connection to the HESR requires the extraction of the beam on the Western side of the ring, compared to the previous location of the extraction point on the Eastern straight section. The basic magnetic structure remained unchanged, but various components had to be rearranged, in addition various technical aspects required an increase of the ring circumference by about 10 m. All this resulted in the latest version of the CR, called CR version 68. The most recent design parameters can be found in Table 1.

Table 1: Parameters of the CR storage ring version 68.

circumference	221.45 m	
maximum bending power	13 Tm	
beam species	ions	antiprotons
energy	740 MeV/u	3 GeV
revolution frequency	1.124 MHz	1.315 MHz
betatron tune $Q_x, Q_y$	3.19, 3.71	4.27, 4.84
transition energy $\gamma_t$	2.82	3.85
momentum slip factor $\eta$	0.186	-0.011
horizontal acceptance	240 $\mu\text{m}$	240 $\mu\text{m}$
vertical acceptance	200 $\mu\text{m}$	200 $\mu\text{m}$
momentum acceptance	$\pm 3.0\%$	$\pm 1.5\%$

The main subsystem of the CR is still after all modifications the stochastic cooling system. It is designed for cooling of both antiprotons and rare isotopes. As both secondary beam species are injected at the maximum magnetic rigidity of the CR of 13 Tm the system must be able to cool particles at different velocities, the relativistic velocity  $\beta$  of rare isotopes of 740 MeV/u kinetic energy is 0.83, for antiprotons of 3 GeV  $\beta$  is 0.97. These two velocities govern the design of all components of the stochastic cooling system, particularly the design of the electrodes used as pickups and kickers of the stochastic cooling system, but also parts of the low level rf components like signal combination and delay lines.

For the ring design the two velocities have resulted in two ion optical modes with different transition energy  $\gamma_t$  and consequently different momentum slip factor  $\eta$ . The momentum slip factor should have a small absolute value, for antiprotons  $\eta$  is -0.011, for rare isotopes it is 0.186. This uses the flexibility of the focussing structure of the CR with 11 independently controlled families of quadrupole magnets. Moreover, 6 families of sextupole magnets are adjusted to achieve maximum acceptance for the large emittance secondary beams. For both secondary beam species the ring will be operated near the maximum magnetic rigidity, which results in small variations of field quality with field level. However, the different ion optical settings for ions and antiprotons and the different polarity will require special care when operating the CR with the two species.

Injection and extraction of antiprotons and ions will be performed along the same beamlines. Nevertheless, the requirements for injection components are different and as

some kicker modules are used for both injection and extraction a bipolar kicker system is required. For the latest version of the ring lattice the main change is caused by the change of the extraction point from one straight section to the other one. A special new requirement comes from the small momentum acceptance of the HESR storage ring which will accumulate the antiprotons. The bunch transferred from CR to HESR should be as long as possible in order to minimize the momentum spread. The bunch length is limited by the rise and fall time of the kicker pulse. As an economic trade off rise and fall times of 200 ns are specified for the large aperture kicker magnets.

A system which was only minutely affected by the recent lattice changes is the bunch rotation rf system. It is located in one of the two dispersion free straight sections of the CR and will provide up to 200 kV rf voltage at the revolution frequency of the particles (1.32 MHz for antiprotons, 1.12 MHz for rare isotopes). Five rf cavities filled with magnetic alloy material have to provide the large rf amplitude over less than 1 ms in order to transform the incoming 50 ns short bunch into a nearly coasting beam by fast change of the bunch phase by 90 degrees. An optimized scenario for the combination of bunch rotation and adiabatic debunching of the incoming antiproton bunch will reduce the momentum spread from  $\pm 3.0\%$  to  $\pm 0.7\%$ . This will result in a minimum cooling time of the stochastic cooling system which is applied after the rf manipulations. For rare isotopes the bunch will be of similar length and the rf manipulation will reduce the momentum spread from  $\pm 1.5\%$  to less than  $\pm 0.4\%$ .

On this nearly coasting beam with reduced momentum spread the stochastic cooling system will act. The stochastic cooling system for the CR has been developed over several years. Changes of the ring design did not influence the major hardware specifications which are determined by the necessity to use the same system for antiprotons and ions. The frequency band of the basic cooling system is 1 - 2 GHz with an option to add cooling systems in the band 2 - 4 GHz. The necessity to cool the different velocities of antiprotons and ions strongly affected the choice of the electrodes and the low level rf system. Due to the low signal to noise ratio of the antiprotons the electrodes are designed for cooling them to 20 K. The electrode structures of slotline type have been designed and studied with model electrodes. Measurements of the properties of these electrodes have been performed and their design was optimized [10]. At present the main task is the manufacturing of the electrodes in an ultrahigh vacuum compatible technology. They should be produced from alumina with UHV compatible metalization. First prototypes are in production and their electromagnetic properties will be measured and optimized.

Further improvement of the electrode sensitivity is achieved by movement of the pick-up electrodes. Special mechanisms have been designed and tested which allow a controlled movement of the electrodes matched to the progress of the transverse cooling process. A proto-

type vacuum chamber with movable electrode mechanisms based on fast moving linear motors has been manufactured. The control of the motors was optimized for fast (cycle times of about 1 s are required for the cooling of rare isotopes) and shock-free motion.

Low level rf in the band 1 - 2 GHz is designed which allows fast changes of delays for the necessary changes between antiproton and ion operation. Many other parameters of the rf components need to be controlled in the course of the cooling process or due to the different beam species.

The use of the three orthogonal cooling systems is presently studied in computer simulations [11]. One aspect is the necessity to specify the parameters of the various stochastic cooling system, another aspect is the definition of an optimum strategy to operate and move the different electrode arrays in order to achieve the required phase space reduction within a minimum cooling time. The results of the simulations will provide the information for the optimum specification and later operation of the different cooling systems. An extension of the longitudinal cooling system to the band 2 - 4 GHz will be studied in the simulations as this is a promising option to both increase the cooling speed and to reduce the momentum spread for better acceptance of the pre-cooled beam by the HESR. Space for the installation of the additional cooling system in the CR straight sections is reserved.

## HIGH ENERGY STORAGE RING HESR

The High Energy Storage Ring HESR has a circumference of 574 m and can be operated up to a magnetic rigidity of 50 Tm. The antiprotons will be injected at an energy of 3 GeV. In the scenario of the MSV the antiprotons will come from the CR and will be accumulated in the HESR, in a later stage the accumulation will be performed in the RESR. After accumulation of a high intensity antiproton beam, the antiprotons are either decelerated or accelerated in the HESR to an energy in the range 0.8 to 14.1 GeV according to the requirements of the internal experiment. The main HESR experiment is focussing on the PANDA detector which is a large  $4\pi$  detector system installed around the interaction point with an internal hydrogen target [12].

Beam cooling in the HESR in the frame of the MSV has two main goals, accumulation of a high intensity antiproton stack and the preparation of best beam quality for experiments with the internal hydrogen target. The operation of the HESR with beam cooling is described in a separate contribution to these proceedings [13]. The stochastic cooling system, which will be available in the MSV, mainly covers the energy range from the injection energy 3 GeV up to the maximum energy of 14.1 GeV, an option to use time of flight cooling instead of filter cooling for lower energies is under investigation [14]. The same system will also be used to provide cooling for the preparation of a stack of up to  $1 \times 10^{10}$  antiprotons. Pre-cooled antiprotons from the CR are accumulated in combination with an rf system which allows compression of the stack into a fraction of

the ring circumference. The rf system will generate barrier buckets which allow a flexible control of the fraction of the ring which is filled by the stack and the fraction which is available for injection of new particles. The barrier bucket system of the HESR was foreseen from the beginning for the compensation of the energy loss during operation of the HESR with an internal target. The optimum strategy for the accumulation in the HESR was studied in computer simulations [15]. It is expected that accumulation of up to  $1 \times 10^{10}$  antiprotons can be performed with an efficiency close to 100 %. In the full version of the FAIR project the stochastic cooling system will support the operation with high intensity stacks, after accumulation in the RESR storage ring, of up to  $1 \times 10^{11}$  antiprotons in a high luminosity mode.

For better beam quality in a high quality mode an electron cooling system was proposed which should at least cover the energy range up to 8 GeV and after an upgrade the full energy range of HESR operation [16]. The high energy electron cooling system, however, is out of the scope of the FAIR project and is an option for a future upgrade. An option for electron cooling in the HESR is still in reach. The 2 MeV electron cooling system for COSY could, after decommissioning of COSY, be transferred to the HESR [17]. It can then cover the lower energy range, approximately the energy range below the injection energy (0.8 to 3 GeV), and provide high quality antiproton beams for internal experiments. Electron cooling in this energy range is expected to be more powerful than the proposed stochastic cooling by the time of flight method.

## EXTENSIONS OF THE MODULARIZED START VERSION

The accelerator sections which were part of the full FAIR project, but are not contained in the Modularized Start Version are planned to be realized as extensions depending on the availability of funding. The largest additional accelerator subproject is the SIS300, a superconducting synchrotron for the acceleration of heavy ions up to a maximum magnetic rigidity of 300 Tm. SIS300 will be installed in the ring tunnel of SIS100 where sufficient space is reserved in the tunnel design of the MSV. Therefore this addition does not require money for the construction of an additional building. Some additional investment will have to go into high energy beamlines and the extension of experimental areas. The main goal is an increase of the energy for heavy ion beams either for low charge states and highest beam intensities or for high charge states and maximum beam energy.

Two extensions are directed towards the improvement of possibilities with cooled beams. These are the construction of the two storage rings RESR and NESR which will provide improved beam quality or higher beam intensities by application of cooling, in particular for the accumulation of secondary beams.

Stochastic cooling

### RESR

The main mission of the RESR storage ring is the accumulation of high intensity antiproton beams [18]. The RESR has the same magnetic rigidity of 13 Tm as the CR, the beams will be transferred to the RESR with the energy which is used for pre-cooling in the CR. The basic ion optical structure of the RESR is fixed, but the ring circumference had to be increased in order to be able to install the RESR in a common tunnel with the CR. The change of the extraction point of the CR also resulted in a corresponding change of the injection point of the RESR. As extraction from the RESR is required in both straight sections of the RESR, in order to serve both HESR and NESR from RESR, the design of the extraction systems remained unchanged.

The ion optical lattice of the RESR offers a large momentum acceptance as required for the proposed accumulation scheme which will follow the procedure formerly used at the AA ring at CERN [19]. It will provide large flexibility to adjust the momentum slip factor which is regarded a key parameter to optimize the stochastic accumulation system. The accumulation procedure has been studied in simulations and the required performance for sufficiently fast accumulation was confirmed [20].

As the RESR is located in a common tunnel with the CR no additional building needs to be constructed. All technical infrastructure and space for the technical subsystems of the RESR is already planned and will be provided in the frame of the MSV. Therefore additional funding is only required for the RESR ring and its technical supply systems.

### NESR

The NESR storage ring has different modes of operation [21]. The standard injection into the NESR will be performed at the maximum magnetic rigidity of 13 Tm, either antiprotons or ions. The pre-cooled secondary beams will come from the CR via the RESR, stable ions will come from either SIS18 or SIS100 via a separate direct beamline. An electron cooling system is foreseen which covers the energy range from the maximum injection energy for ions (740 MeV/u) down to the minimum energy after deceleration (4 MeV/u). Electron cooling will also be crucial for the deceleration of antiprotons from 3 GeV to 30 MeV for experiments with slow antiprotons in the FLAIR facility after the NESR [22].

Electron cooling in the NESR will provide powerful cooling for all experiments with stored ions over a large energy range. The most challenging aspect involving cooling, the accumulation of low intensity rare isotopes has been prepared by experiments in the existing ESR storage ring at GSI [23]. These experiments demonstrated the feasibility of longitudinal accumulation by combination of an rf system which compresses the stack into a fraction of the ring circumference with electron cooling. This scheme is identical with the foreseen accumulation of antiprotons in the HESR, except that electron cooling will be applied instead of stochastic cooling in the HESR. The experiments were

performed with different rf manipulations, fixed barriers, moving barriers and injection onto the unstable fixed point of an harmonic rf operating at harmonic number  $h = 1$ . From the comparison with simulations it can be concluded that the simulation tools have sufficient predictive power to base the design of the NESR systems on the simulations. Another conclusion was that the quality of the technical systems will be crucial for the efficiency of beam accumulation. Particularly the quality of the pulse generated to provide the injection kick for the incoming bunch is of outstanding importance. Short rise and fall times have to match the relatively short revolution time of the beam in the NESR and any ringing of the kicker system after the pulse will unavoidably heat the circulating beam transversely resulting in extended cooling time and additional inefficiency of the accumulation method. The same is true for the control of the rf waveform used to compress the beam and the synchronization of the the incoming bunch with the rf voltage and the kicker pulse. These are very demanding requirements for the control and performance of these accelerator subsystems.

The funding of the NESR is a more critical issue than for the RESR since funding is not only required for the accelerator, but also for additional buildings for the NESR ring, the technical systems and the low energy experimental area after the NESR.

## STATUS AND OUTLOOK

The contracts for the foundation of the FAIR company were signed and the new FAIR company was founded end of 2010. The first partner countries started to transfer their financial contributions. Germany, as the main partner country started to assign funding which is presently used to start the ordering of the most time critical accelerator components. The completion of all documents for the civil construction work for FAIR is a prerequisite for first construction activities. After the building permit by German authorities, the first construction work for FAIR is still expected to start in the fourth quarter of 2011. In parallel the activities to start production of accelerator components will be intensified. A large fraction of the production of components will be supervised by GSI, either as German in-kind contributions to the FAIR project or as orders by the FAIR company based on international cash contributions. The stochastic cooling system of the CR is planned as a major German in-kind contribution provided by GSI. Similarly, most parts of the HESR storage ring, and its beam cooling systems in particular, will be a German in-kind contribution provided by Forschungszentrum Jülich. A general time schedule for the FAIR project based on the present information on the expected resources, financial and man power, is in work. Specifications for all required components are worked out as a basis for the hardware contributions to the FAIR project regarding the general standards of the project.

Stochastic cooling

## REFERENCES

- [1] FAIR Baseline Technical Report. GSI, Darmstadt, 2006, <http://www.gsi.de/fair/reports/btr.html>.
- [2] M. Steck et al., PAC'09. Vancouver, Canada, May 2009, FR1GRI03, <http://www.jacow.org>.
- [3] FAIR Technical Design Reports, GSI, Darmstadt, 2008. <http://indico.gsi.de>.
- [4] P. Spiller et al., EPAC'08, Genoa, Italy, June 2008, MOPC100, <http://www.jacow.org>.
- [5] H. Geissel et al., Nucl. Instr. Meth. B204 (2003) 71.
- [6] A. Dolinskii, F. Nolden, M. Steck, COOL07, Bad Kreuznach, Germany, September 2007, TUA2C08, <http://www.jacow.org>.
- [7] R. Maier et al., PAC'11, New York, USA, March 2011, TUPS20, <http://www.jacow.org>.
- [8] M. Steck et al., contribution to this workshop.
- [9] T. Katayama, et al., contribution to this workshop.
- [10] C. Peschke, U. Jandewerth, F. Nolden, P. Petri, M. Steck, COOL09, Lanzhou, China, September 2009, THPMCP003, <http://www.jacow.gsi.de>.
- [11] C. Dimopoulou et al., contribution to this workshop.
- [12] PANDA - Technical Progress Report, <http://www-panda.gsi.de>.
- [13] D. Prasuhn et al. contribution to this workshop.
- [14] R. Stassen et al., contribution to this workshop.
- [15] H. Stockhorst et al. IPAC'11. San Sebastian, Spain, September 2011, THPS003, <http://www.jacow.org>.
- [16] B. Gålnander, T. Bergmark, S. Johnson, T. Johnson, T. Lofnes, G. Norman, T. Peterson, K. Rathsmann, D. Reistad, EPAC'08, Genoa, Italy, June 2008, THPP049, <http://www.jacow.org>.
- [17] J. Dietrich et al, contribution to this workshop.
- [18] S. Litvinov, A. Dolinskii, O. Gorda, F. Nolden, M. Steck, PAC'09, Vancouver, Canada, May 2009, FR5REP118, <http://www.jacow.org>.
- [19] H. Koziol, S. Maury, CERN-PS 95-15 (AR/BD), 1995.
- [20] M. Steck et al., IPAC'10, Kyoto, Japan, June 2010, TH-PEC038, <http://www.jacow.org>.
- [21] C. Dimopoulou, O. Dolinskyy, R.G. Heine, T. Katayama, U. Laier F. Nolden, G. Schreiber, M. Steck, COOL09, Lanzhou, China, September 2009, THM2MCIO02, <http://www.jacow.gsi.de>.
- [22] E. Widmann et al., Phys. Scr. 72 (2005) C51.
- [23] C. Dimopoulou, B. Franzke, T. Katayama, F. Nolden, G. Schreiber, M. Steck, D. Möhl, EPAC'08, Genoa, Italy, June 2008, THPP048, <http://www.jacow.org>.

## STATUS OF THE 2 MEV ELECTRON COOLER FOR COSY / HESR

J. Dietrich<sup>#</sup>, V. Kamerdzhev, FZJ, Jülich, Germany

M.I. Bryzgunov, A.D. Goncharov, V.M. Panasyuk, V.V. Parkhomchuk, V.B. Reva,  
D.N. Skorobogatov, BINP, Novosibirsk, Russia.

### Abstract

The 2 MeV electron cooling system for COSY-Jülich is being built to boost the luminosity in presence of strong heating effects of high-density internal targets in the entire energy range. The 2 MeV cooler is also well suited in the start up phase of the High Energy Storage Ring (HESR) at FAIR in Darmstadt. It can be used for beam cooling at injection energy and for testing new features of the high energy electron cooler for HESR. The design and construction of the cooler is accomplished in cooperation with the Budker Institute of Nuclear Physics in Novosibirsk, Russia. The infrastructure necessary for the operation of the cooler in the COSY ring (radiation shielding, cabling, water cooling etc.) is established. The electron beam commissioning at BINP Novosibirsk started in May of 2011. First results are reported. Final commissioning at COSY-Jülich is planned for the end of 2011.

### INTRODUCTION

The new generation of particle accelerators operating in the energy range of 1-8 GeV/u for nuclear physics experiments requires very powerful beam cooling to obtain high luminosity. For example the investigation of meson resonances with PANDA detector requires momentum spread in antiproton beam, which must be better than  $10^{-4}$ . To obtain such a momentum spread cooling time in the range of 0.1- 10 s is needed. The 4 MeV electron cooler at the RECYCLER ring (FNAL) [1] achieves cooling time about 1 hour. The new cooler for COSY should provide a few orders of magnitude more powerful longitudinal and transverse cooling which requires new technical solutions. The basic idea of this cooler is to use high magnetic field along the orbit of the electron beam from the electron gun to the electron collector. In this case high enough electron beam density at low effective temperature can be achieved in the cooling section.

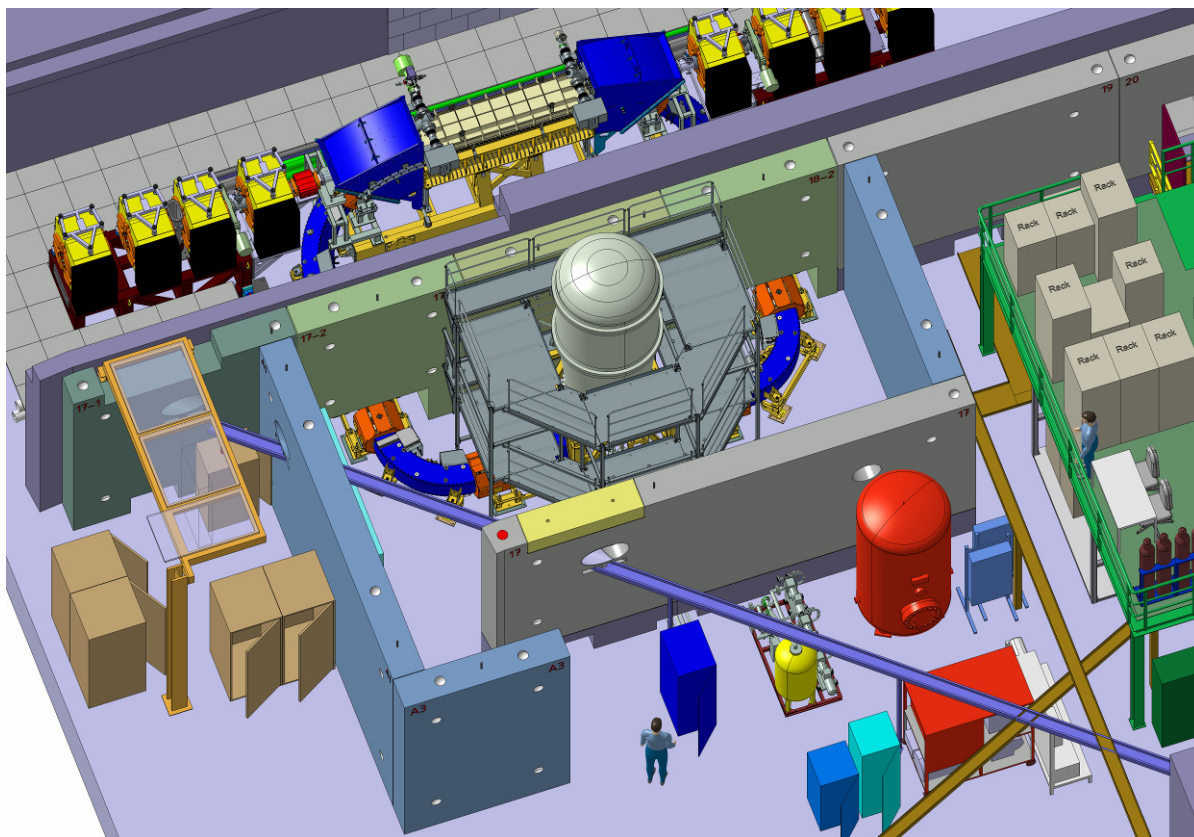


Figure 1: A 3D model of the 2 MeV electron cooler to be installed in COSY.

<sup>#</sup>j.dietrich@fz-juelich.de

## BASIC DESIGN FEATURES

The basic parameters of the COSY cooler are listed in Table 1 [2]. The length of the cooling section is given by the space available in the COSY ring.

Table 1: Basic Parameters of the 2 MeV electron cooler.

Energy Range	0.025 ... 2 MeV
High Voltage Stability	$< 10^{-4}$
Electron Current	0.1 ... 3 A
Electron Beam Diameter	10 ... 30 mm
Length of Cooling Section	2.69 m
Toroid Radius	1.00 m
Magnetic Field (cooling section)	0.5 ... 2 kG
Vacuum at Cooler	$10^{-9}$ ... $10^{-10}$ mbar

In Fig. 1 the layout of the COSY 2 MeV cooler is shown. The main features of the cooler are [2]:

1. The design of the cooling section solenoid is similar to the ones of CSR (IMP) and LEIR (CERN) coolers designed by BINP [3,4]. However, for the 2 MeV cooler the requirement on straightness of magnetic field lines is so high ( $\Delta\theta < 10^{-5}$ ) that a system for control of magnetic field lines in vacuum becomes necessary.

2. For suppression of high energy electron beam losses at IMP and LEIR coolers electrostatic bending was used [5]. The shape of the 2 MeV transport lines, however, dictates a different approach. The collector (inside the HV terminal) will be complemented by a Wien filter to suppress return electron flux.

## STATUS OVERVIEW

Fig. 2 shows the cooler being assembled in Novosibirsk [6]. The electron beam transport channel from the bottom of the high voltage vessel to cooling section and back to the high voltage vessel is assembled and vacuum tested. The leakage rate is better than  $2 \cdot 10^{-9}$  mbar-l/s. The high voltage vessel is not completed yet. The measurements of the magnetic field along the electron beam orbit from gun to collector are finished [7]. An in-vacuum system for measuring magnetic field straightness in the cooling section is installed. The cascade transformer is assembled and the characteristics of the low voltage generator were studied. The ceramic acceleration and deceleration tubes are completed. Electronic components for the high voltage sections are tested on two sections, however production of 33 sets is still in process and should be finished in September 2011. The electron gun and collector with Wien filter are tested on a dedicated test bench, see Fig. 3 [8, 9]. The perveance of the electron gun of  $9.5 \mu\text{A}/\text{V}^{3/2}$  corresponds to the calculation. The Wien filter for suppression of the secondary emission from the collector was tested successfully. Problems with Penning discharges for high voltages were observed. Conditioning under high voltage and vacuum improvements increased discharge threshold. Collector efficiency is better than  $10^{-5}$ . As first stage, the high voltage terminal can be installed in the high voltage vessel.

In the COSY ring the section for installing the cooler is prepared [10]. The position of one bumper is changed. The beam pipe diameter in this section is reduced to 100 mm, the value corresponding to diameter of the vacuum chamber inside the cooling section. Additional steering coils were installed on the quadrupoles for orbit correction [11]. New concrete radiation shielding walls with two large openings for the electron beam transport line are installed. After the summer shutdown COSY is fully operational. The  $\text{SF}_6$  gas system is delivered, the power supplies are ordered.



Figure 2: Assembling the 2 MeV electron cooler at BINP.

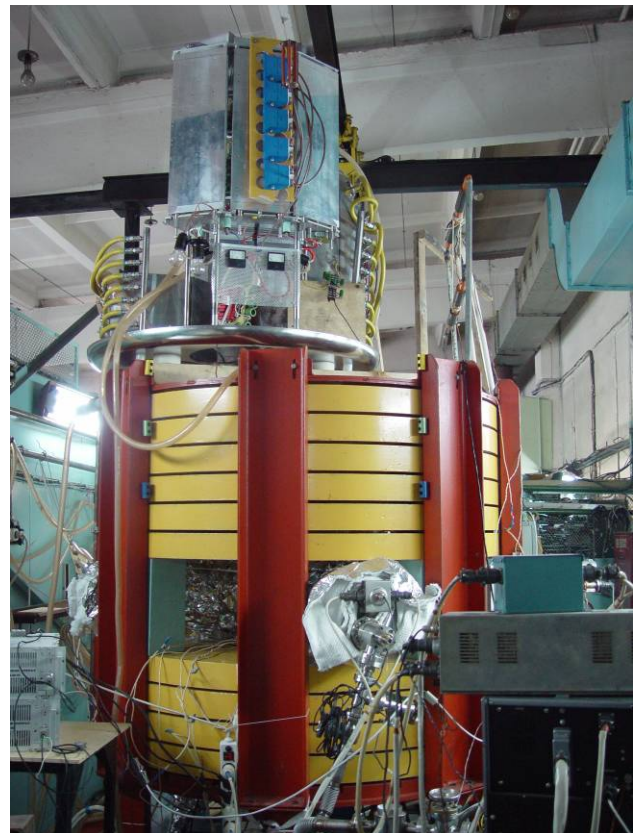


Figure 3: Electron gun and collector test bench at BINP.

## MAIN COMPONENTS

### Magnetic System

The main component of the magnetic system is the cooling solenoid. To satisfy the requirements on straightness of the magnetic field, the cooling solenoid is assembled from numerous short coils. The required field quality is achieved by mechanically adjusting the angles of individual coils.

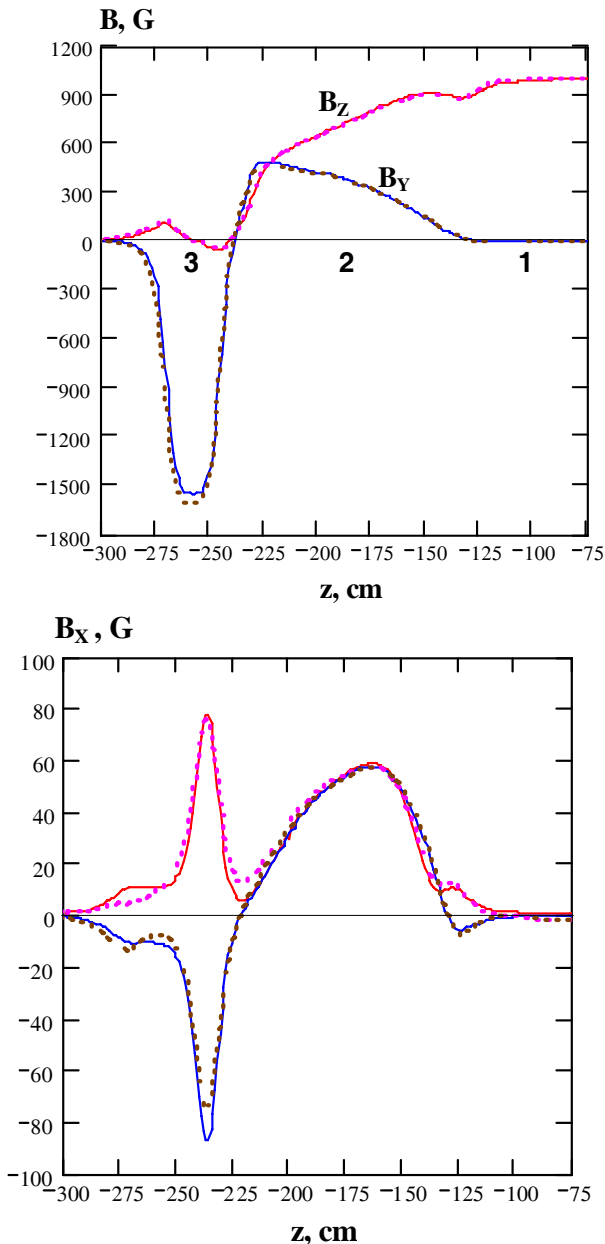


Figure 4: Longitudinal  $B_z$  and vertical  $B_y$  magnetic field components (upper plot) and horizontal  $B_x$  component along two lines with  $x = \pm 2$  cm,  $y = 0$  (lower plot) versus cooling solenoid axis  $z$ . Dots represent measured curves, solid lines- computed curves (MAG3D). The origin is determined in the centre of the cooling solenoid ( $z = -75$  cm). 1-cooling solenoid, 2-toroid, 3-dipole corrector.

Dipole magnets are installed along the proton orbit for compensation of the vertical field action on protons by the toroids. For better compensation of transverse components of magnetic field generated by current leads, two types of coils with opposite direction of winding are used. Magnetic field measurement along the electron beam orbit from gun to collector was performed by a set of calibrated Hall probes, which were located on a carriage. Representative parts of the magnetic system were selected for measurements. Longitudinal, normal and binormal magnetic field components are measured. Each component is measured at four different points that gives information about dipole and gradients of these field components. In Fig. 4 the magnetic field components along the path of the ion beam (cooling section, toroid, correction dipole) as example of measurements are shown.

### High Voltage Terminal

The high voltage terminal is supported by a column consisting of 33 identical high voltage sections. The whole assembly is placed inside a vessel filled with  $SF_6$  under pressure up to 10 bar. Each HV section contains two coils providing guiding magnetic field for acceleration and deceleration tubes and the high voltage power supply generating up to 60 kV. Each section is powered by a separate winding of the cascade transformer. Total power consumption of one section is about 300 W. The high voltage vessel is produced in Germany. In case of high pressure of 12 bar  $SF_6$  there is a deformation in the bottom flange of some mm, which is taken into account by the mechanical design (see Fig. 5) [12].

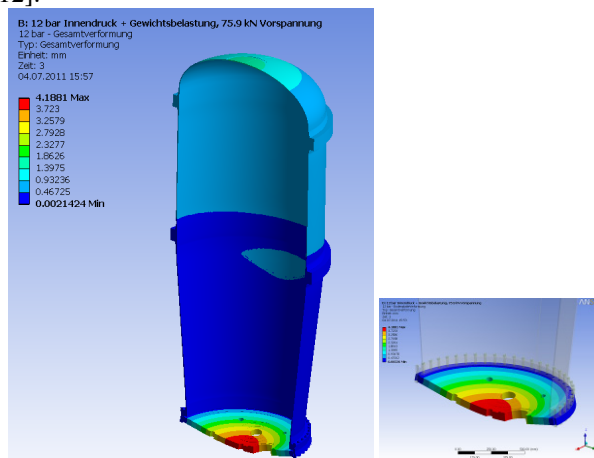


Figure 5: Mechanical stresses and deformations of the high voltage vessel.

### Cascade Transformer

The power supply of the regular high voltage sections, high voltage terminal and collector is based on the concept of a high frequency cascaded resonant transformer. The system consists of 33 transformers with cascaded connection. At time of first testing high level of heating of stainless steel rings enclosing the cascade transformer was observed. Initial testing showed a 1.2 kW

loss at each transformer. After coating the stainless steel with copper (by galvanic process) the power losses decreased to 464 W according to the difference of cooling oil temperature

### *Beam Diagnostics*

For measurement of the electron beam position 10 pickups (5 in the beam line from gun to the cooling section and 5 from cooling section to collector) are foreseen. 2 pickups are installed in the cooling section for measuring the proton as well as the electron beam positions. The last two ones have a special design due to the fact that the in-situ magnetic field measurement system needs space for the magnetic sensor which is mounted on the cart moving along the solenoid axis. Each pickup consists of 4 sectors. To study the dynamics of electron cooling in a synchrotron only non-destructive instrumentation can be used. Beam diagnostics based on recombination is usually used to optimize electron cooling of protons ( $H^0$ -diagnostics). In some cases insertion devices may prevent the  $H^0$  particles from reaching the detector (e.g. ANKE detector at non-zero position in the COSY ring). In the future HESR ring, for example, this technique is not applicable due to antiprotons being accelerated. An Ionisation Profile Monitor delivers real time data in both transverse planes allowing detailed analysis of beam profile evolution in COSY. Attempts to use scintillation of residual gas to measure beam profiles were very promising. So ionisation and possibly scintillation profile monitors become vital for optimization of electron cooling of antiprotons. The IPM was designed at GSI keeping the requirements for the future FAIR machines in mind [13]. The ionisation products are guided to a position sensitive detector by transverse electric field. An arrangement consisting of an MCP stack ( $100 \times 48 \text{ mm}^2$ ), a luminescent screen, and a  $656 \times 494$  pixel CCD camera is used to detect ions in high resolution mode. The IPM actually contains two identical units to provide simultaneous measurements in both, horizontal and vertical, planes. The IPM is installed in COSY in the arc downstream of the cooler telescope. The data acquisition software was developed at FZJ with an emphasis on real-time display of beam profiles. The software also performs fitting and plots beam width and position vs. time. The beam current measured by the beam current transformer (BCT) is also displayed. A Scintillation Profile Monitor (SPM) is being developed at COSY as a robust and inexpensive alternative to the IPM. The disadvantage of much lower event rate compared to the IPM and thus the necessity to locally add nitrogen to the residual gas is compensated by the much simpler mechanical design of the SPM. The light emitted by the gas in the vacuum chamber is focused by a lens onto a multichannel photomultiplier (PMT) array (Hamamatsu 7260-type, 32 channels,  $0.8 \cdot 7 \text{ mm}^2$  photocathode, 1 mm pitch). The readout is performed using a multichannel current digitizer, developed at iThemba LABS [14]. The problem of low rate of scintillation events detected by a multichannel photomultiplier is coped with by injecting

small amounts of pure nitrogen into the SPM vacuum chamber. This leads to a temporary local pressure bump of no more than an order of magnitude. A commercially available piezo-electric dosing valve allows good control over the amplitude and duration of the pressure bump. Since the average pressure in the machine is hardly changed, the method is fully compatible with experiment operation [15.] A method using Thomson scattering is proposed to measure the electron beam profile in the cooling section [16].

### SUMMARY

The main components of the 2 MeV electron cooler are manufactured and the whole system is now being assembled at BINP Novosibirsk. The commissioning with electron beam starts end of summer 2011. The installation at COSY is expected in winter 2011. Since the straightness of magnetic field in the cooling section needs to be better than  $10^{-5}$  an in-situ magnetic field measurement system was installed. Diagnostic tools for optimisation of the electron cooling system were developed and tested. Modifications to the COSY ring and its infrastructure were done.

### ACKNOWLEDGEMENTS

The authors would like to thank the members of the project teams at BINP and at COSY for their cooperation and support.

### REFERENCES

- [1] L.R. Prost et al., Electron Cooling Status and Characterization at Fermilab's Recycler, COOL07.
- [2] Conceptual Design Report, BINP, Novosibirsk 2009.
- [3] X.D. Yang et al., Commissioning of Electron Cooling in CSRm, Proceeding of COOL07, Bad Kreuznach, Germany p.59-61.
- [4] G. Tranquille, Cooling results from LEIR, Proceeding of COOL07, Bad Kreuznach, Germany p.55-58.
- [5] E.I. Antokhin et al., Conceptual Project of an Electron Cooling System at an Energy of Electrons of 350 keV, ECOOL'99, NIM A 441 (2000) 87-91.
- [6] V. Reva et al., this conference.
- [7] V.M. Panasyuk et al., this conference.
- [8] A. Bublely et al., this conference.
- [9] M. Bryzgunov et al., this conference.
- [10] J. Dietrich et al., Status of the 2 MeV Electron Cooler for COSY-Juelich/ HESR, PAC11, 2011.
- [11] L. Mao et al., this conference.
- [12] J. Wolters, ZAT, FZ Jülich, 2011.
- [13] T. Giacomini et al., Development of Residual Gas Profile Monitors at GSI, Proceedings BIW04.
- [14] C. Böhme et al., Gas Scintillation Beam Profile Monitor at COSY Jülich, Proceedings BIW10.
- [15] J. Dietrich et al., Performance of the Scintillation Profile Monitor in the COSY Synchrotron, Proceedings IPAC 2011.
- [16] T. Weilbach et al., this conference.

## RECENT STATUS OF BEAM COOLING AT S-LSR\*

A. Noda, M. Nakao, H. Souda, H. Tongu, ICR, Kyoto U., Kyoto, Japan,  
 K. Jimbo, IAE, Kyoto U., Kyoto, Japan, T. Fujimoto, S. Iwata, S. Shibuya, AEC, Chiba, Japan,  
 K. Noda, T. Shirai, NIRS, Chiba, Japan, H. Okamoto, Hiroshima U., Higashi-Hiroshima, Japan,  
 I. N. Meshkov, A. V. Smirnov, E. Syresin, JINR, Dubna, Moscow Region, Russia,  
 M. Grieser, MPI-K, Heidelberg, Germany

### Abstract

At S-LSR in ICR, Kyoto University, electron cooling of 7 MeV protons has been applied. A relative velocity sweep scheme reduced the cooling time from 30.4 s to 1.7 s for the initial momentum spread of 1 %. One dimensional ordering by electron cooling was also realized at a proton number of approximately 2000, resulting in 2K and 11 K in the longitudinal and the horizontal directions, respectively. With the combination of electron cooling and phase rotation techniques a very short bunch length of ~3 ns was realized, which should be used for bio-medical irradiation. For multi-dimensional laser cooling of  $^{24}\text{Mg}^+$  ions, synchro-betatron coupling has been applied for a bunched ion beam. The realized beam temperatures are 24K and ~200 K for the longitudinal and horizontal directions, respectively at resonance, while the corresponding values are 15K and ~600 K, respectively at the off resonance condition.

### INTRODUCTION

A small laser equipped storage ring (S-LSR) was constructed at ICR, Kyoto University, in order to investigate acceleration of hot laser-produced ion beams. The ion beams produced by laser plasma interaction has a large energy spread. The capability of efficient electron cooling of these hot proton beams by a relative velocity sweep was investigated at S-LSR. S-LSR is also oriented for the beam cooling research to realize ultra low beam temperature. For this purpose, the S-LSR lattice was

designed with a rather large super symmetry of 6 to satisfy the so called maintenance condition [1]. With deflection elements composed of magnetic and electric fields, a dispersion less lattice can be realized [2]. In Fig.1 the S-LSR is shown together with other accelerators in our accelerator building. The main parameters of S-LSR are listed up in table 1 and the layout of S-LSR with its injectors is shown in Fig. 2.



Figure 2. Photograph of S-LSR and its injector.

Up to now, we have applied electron cooling to a 7 MeV proton beam to realize one dimensional ordering [3]. “Synchrotron-betatron coupling” [4], was applied for the laser cooling experiments using 40 keV  $^{24}\text{Mg}^+$  ions, where the beams, however, still have a rather hot transverse temperatures.

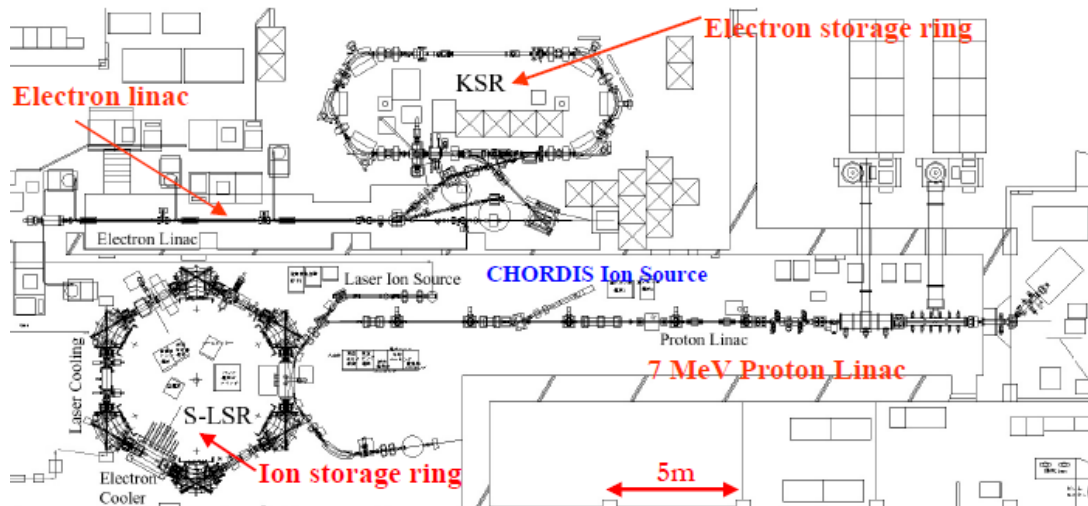


Figure 1. Layout of S-LSR located in the accelerator building together with other accelerators.

\*project by MEXT of Japanese government. It is also supported by GCOE project at Kyoto University, “The next generation of Physics-Spun from Universality and Emergency.”  
 #noda@kyticr.kuicr.kyoto-u.ac.jp

Table 1: Main parameters of S-LSR

Ion, Kinetic Energy	proton, 7 MeV $^{24}\text{Mg}^+$ , 40 keV
Circumference of the ring	22.557 m
Average radius of the ring	3.59 m
Length of long straight section	1.86 m
Radius of curvature	1.05 m
Betatron tune	(1.645, 1.206) :proton (2.068, 1.105) : $^{24}\text{Mg}^+$
Momentum Compaction	0.502
Average Vacuum Pressure	$\sim 10^{-8}$ Pa
<b>Electron Cooling</b>	
Electron Energy	3.8 keV
Electron Density	$2.2 \times 10^6 /\text{cm}^3$
Effective Cooler Length	0.44 m
Expansion Factor	3
Temperature at transition to ordered state	$T_{\parallel}=2$ K, $T_{\perp}=11$ K
<b>Laser Cooling</b>	
Synchrotron tune	0.0376~0.1299
Laser frequency	1074110.3 GHz $\pm$ 0.05GHz
Laser detuning	$\leq -0.2\text{GHz} \pm 0.05\text{GHz}$
Laser power at exit window	11~20 mW

## CHARACTERISTICS OF S-LSR

### Ring Lattice Symmetry

In order to suppress the shear heating effect [1], the S-LSR has a symmetry of 6 with the operating point of  $(v_H, v_V)=(1.645, 1.206)$  (for electron beam cooling of protons) and  $(2.068, 1.105)$  (for laser cooling of  $^{24}\text{Mg}^+$  ion beams) [4], satisfying the so called maintenance conditions given by the following relations [1],

$$\gamma < \gamma_t \quad (1)$$

$$N_s > 2\sqrt{v_H^2 + v_V^2} \quad , \quad (2)$$

where  $\gamma_t$  and  $N_s$  are Lorentz  $\gamma$  at the transition energy and

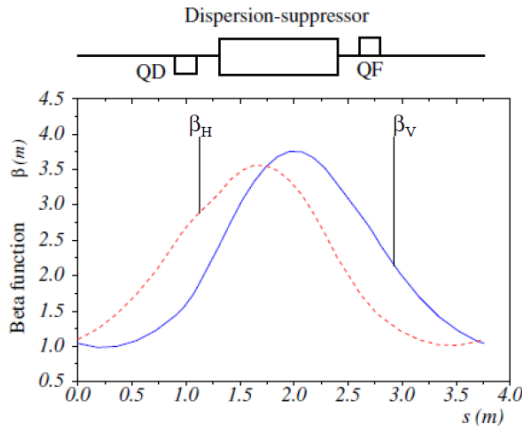


Figure 3. Beta-functions in the dispersion free operation mode of S-LSR. The operating point is  $(v_H, v_V) = (2.07, 2.07)$

Laser cooling

20

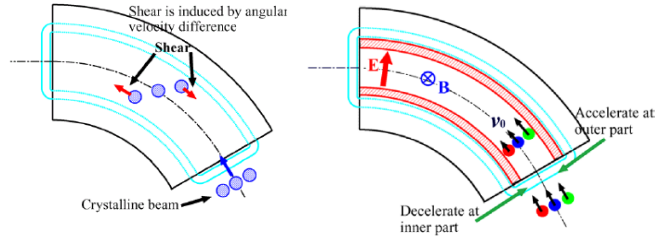


Figure 4. Basic concept of dispersion suppressor. (taken from ref.[2])

the super periodicity of the ring, respectively. At S-LSR, its super periodicity was chosen to be 6 to fulfil the Eq. (2). At this S-LSR settings, formation of one dimensional ordering has been realized for a proton beam.

### Dispersion Suppressed Lattice

The deflection elements at S-LSR with a deflection angle of 60 degrees have another unique capability as the realization of dispersion free straight sections as shown in Fig. 3 by applying additional electrostatic field  $\vec{E}$  satisfying the following relation:

$$(1 + \frac{1}{\gamma^2})\vec{E} = -v_0 \times \vec{B} \quad , \quad (3)$$

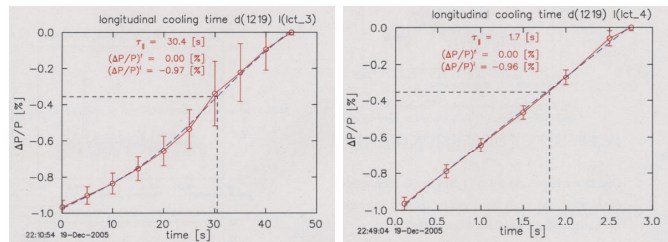
where  $\vec{B}$  is the magnetic field in the deflection elements [2]. As shown in Fig. 4, the ions cooled to a certain energy in the straight section get the different energy change due to their radial positions in the electrostatic field,  $\vec{E}$  and thus they have the same angular velocity, which suppresses the shear heating.

## ELECTRON COOLING OF PROTON BEAM

The motive force to construct S-LSR was the demonstration of post acceleration of laser-produced ion beams to realize a compact cancer therapy ion accelerator, guided by the Advanced Compact Accelerator development project by MEXT of the Japanese government.

### Efficient Electron Cooling of Hot Ion Beam by Relative Velocity Sweep

A laser-produced ion beam, usually has a relatively large energy spread, where most of the ions cannot interact



(a)

(b)

Figure 5. Electron cooling of a 7 MeV hot proton beam without (a) and with (b) a relative velocity sweep.

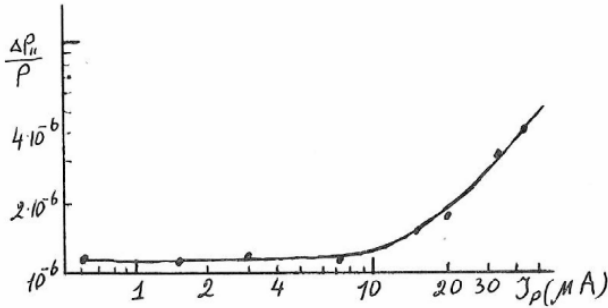


Figure 6. The first data claiming one dimensional ordering by application of an electron cooling..(borrowed from Ref. [7])

effectively with the electron beam due to the very small cooling force in the large relative velocity ( $v_i$ ) range, where the electron cooling force ( $F$ ), scales as

$$F \propto 1/v_i^2. \quad (4)$$

The measured cooling time of a 7 MeV ion beam for different momentum spreads are shown in Fig. 5(a). However, a fast cooling can be achieved if we apply an external force to assist the electron cooling force in the large relative velocity range. We utilize an induction accelerator to rapidly push the ions toward the stable point of the cooling force. An alternative method to reduce the cooling time is a change of the electron velocity by sweeping the cathode potential. With this scheme of the relative velocity sweep, the cooling time was reduced from 30.4 s to 1.7 s (Fig.5(b)). This scheme has previously been tested at TSR of MPI-K in Heidelberg for  $^{12}\text{C}^{6+}$  ion beams [6].

### One Dimensional Ordering of Proton Beam

Stimulated by the data shown in Fig. 6, reported at ECOOL84 from NAP-M at Novosibirsk, many efforts have been made world wide to attain an ordered state. At ESR and SIS in GSI, Darmstadt and CRYRING in Stockholm, a clear sudden jump in the momentum spread and/or transverse beam size has been reported at a certain beam particle number for heavy ions [8, 9] and even for  $^{12}\text{C}^{6+}$  ions [10]. For proton beam, however, due to its

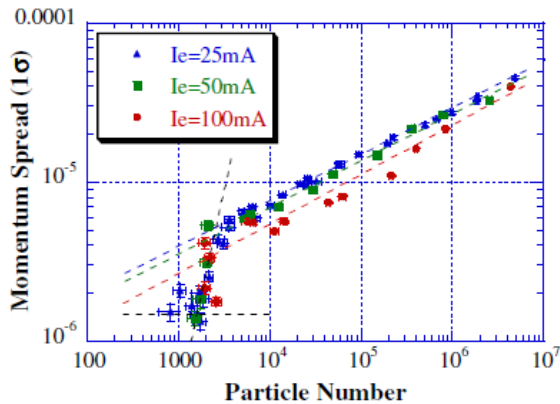


Figure 7. Clearly observed sudden jump of the momentum spread of a 7 MeV proton beam at S-LSR, which is considered as one dimensional ordering [3].

Laser cooling

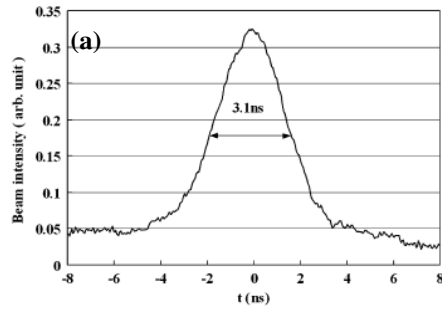
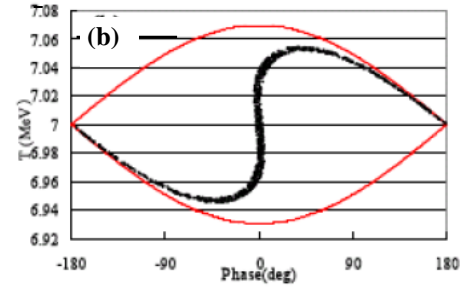


Figure 8. (a) Realized shortest proton bunch (3.1 ns at  $2\sigma$ ) by application of phase rotation as illustrated in (b).



(b) Illustration of the phase rotation scheme after electron cooling to create a short bunch beam after electron beam cooling.

single charge, the electron cooling force is very weak compared with other ions and a clear jump in the momentum spread or beam size had not been observed so far. Owing to the high S-LSR symmetry of 6 suited for stable beam dynamics, we can observe a sudden jump in the momentum spread as indicated in Fig. 7 after various improvement of power supplies of the ring magnets and high voltages for electron cooler in collaboration among

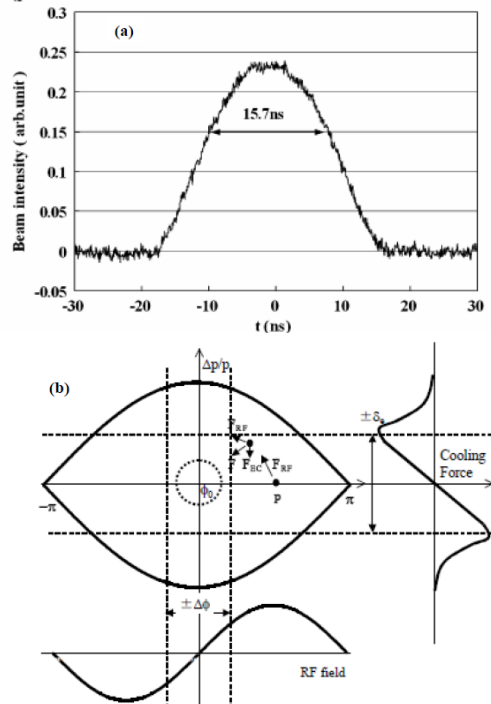


Figure 9. Short bunch formation by bunched beam cooling.

JINR, Dubna Moscow, MPI-K, Heidelberg and ICR, Kyoto [3]. The attained beam temperatures at the transition to the ordered state are  $\sim 2$  K and  $\sim 11$  K for the longitudinal and vertical directions, respectively.

### Short Bunch Formation and Its Fast Extraction

Recently DNA double strand break with the use of laser-produced proton beam was reported [11], which is considered to be due to the very high peak intensity of the laser-produced proton beam. In order to provide a much higher proton beam peak intensity, mainly for bio-medical irradiation with much more flexibility and controllability, we have combined electron cooling with phase rotation techniques.

#### Phase Rotation of Electron Cooled Beams.

With electron cooling (RF off) the coasting proton beams are cooled to a very small momentum spread. Then an RF electric field was applied in a quarter period of the synchrotron oscillation as indicated in Fig.8(b), the beam becomes a very short length as shown in Fig. 8(a) [12]. With this scheme, a very short bunch of  $\sim 3$  ns can be realized for an initial beam intensity of  $1.4 \times 10^8$  protons (7 MeV). The extraction efficiency of about 20%, however, is not so high, because of the formation of a hallow tail as indicated in Fig.8 (b).

#### Electron Cooling of RF Bunched Beam

In order to reach higher extraction efficiencies, a scheme to apply electron cooling after ion capturing into the separatrix was also studied. This method, illustrated in Fig. 9 (b), can create a beam bunch of 15.7 ns as is shown in Fig. 9(a). The resonator voltage in this measurement was 800 V with a harmonic number 2, which was the same as the case of phase rotation case above mentioned. With this scheme, the bunch length measured at a proton number of  $1.4 \times 10^8$  is about 5 times longer compared with the other scheme. The extraction efficiency, however, is almost 100 % and the peak intensity is almost the same order of  $\sim 10^{16}$  particles/s, which is to be irradiated into the transverse beam radius of 2 mm (FWHM).

#### Bio-medical Irradiation System with Vertical Beam

Our both beam cooling and extraction schemes above mentioned have the beam size of 2 mm in FWHM

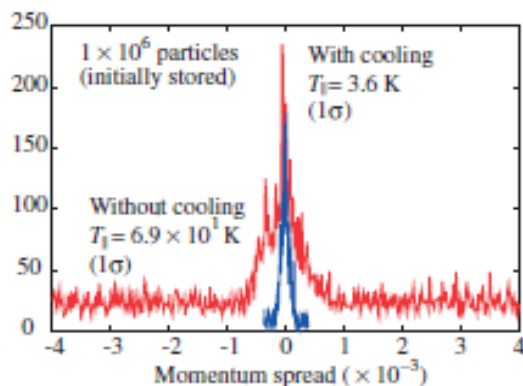


Figure 10. Momentum distributions of  $^{24}\text{Mg}^+$  ion beam without (a) and with (b) the laser cooling.

resulted in the estimated proton flux of  $\sim 2 \times 10^6 \text{ mm}^{-2} \text{ ns}^{-1}$ , which well surpasses the one in Ref. [11] with  $\sim 10^3 \text{ mm}^{-2} \text{ ns}^{-1}$ . In consideration of the fact that our scheme is operated below 1 Hz of Ref. [11] due to needed cooling time, it surpasses this scheme because of the available flux range, flexibility and easiness to control by using accelerator based beams. We are now trying to develop a beam course mainly oriented for bio-cell irradiation, which can irradiate cells kept in a breeding liquid by a vertically bent up beam in collaboration with NIRS.

## LASER COOLING OF MG IONS

### Laser Cooling of Coasting Beam in the Longitudinal Direction

From the point of view of attaining the lowest possible beam temperature, it is required to apply laser cooling because of its strong longitudinal cooling force. In the first step, we have applied laser cooling for 40 keV  $^{24}\text{Mg}^+$  ion beams with an intensity of  $10^6$  ions. In Fig. 10 a typical result of longitudinal laser cooling of a coasting beam is shown. The reached longitudinal equilibrium temperature is limited to 3.6 K due to the heat flow from transverse directions to the longitudinal one by intra-beam scattering (IBS).

### Transverse Laser Cooling by Synchro-Betatron Coupling

The transverse beam temperature has been decreased by laser cooling with the use of intrabeam scattering [13] and dispersive cooling [14], which have been found to be insufficient to reach such low beam temperature to realize a crystalline structure. To realize a much stronger cooling rate in the transverse direction, the above mentioned ‘‘Synchro-Betatron Coupling’’ has been proposed [4]. We have tested this scheme experimentally.

### Observation of Horizontal Beam Size

In order to evaluate the horizontal beam temperature, measurements of the horizontal beam size are necessary. We have observed spontaneously emitted photons from the laser-excited Mg ions [15]. In Fig. 11, the observation system to detect the horizontal beam size is shown. To measure the size of the ion beam, excited by a laser beam

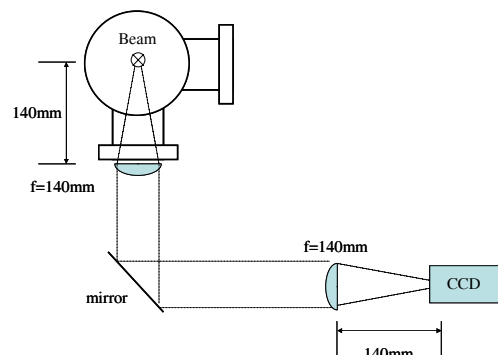


Figure 11. Observation scheme of the horizontal beam size of  $^{24}\text{Mg}^+$  ion beam.

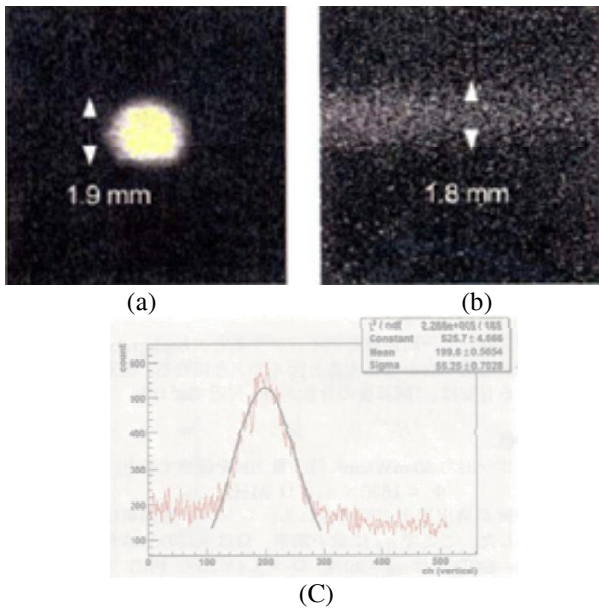


Figure 12. (a) Transverse laser profile (FWHM 1.9 mm) used to measure the spontaneous emission from the excited  $^{24}\text{Mg}^+$  ions, (b) Observed spontaneous emitted photons and (c) Fitted results of the observed photon intensity resulting in a horizontal beam size of 1.8 mm (FWHM).

with a size of 1.9 mm (FWHM) (Fig.12 (a)), the spontaneously emitted photons from the  $^{24}\text{Mg}^+$  ions are observed by a cooled CCD camera (Hamamatsu Photonics C7190-11W; -20 °C) as shown in Fig.12 (b). The intensity profile of the spontaneous emitted photons is fitted, as shown in Fig.12 (c), resulting in a horizontal ion beam size of 1.8 mm (FWHM).

The above results are evaluated in connection with the synchro-betatron resonance together with the equilibrium momentum spread after laser cooling, measured by a voltage sweep applied to a PAT (Post Acceleration Tube) [15]. The present experimental measurements have been performed at the operation point of  $(\nu_H, \nu_V)=(2.068, 1.105)$ . The measured horizontal beam size has a local minimum at a synchrotron tune of about 0.068 (upper) while the momentum spread has a local maximum at the

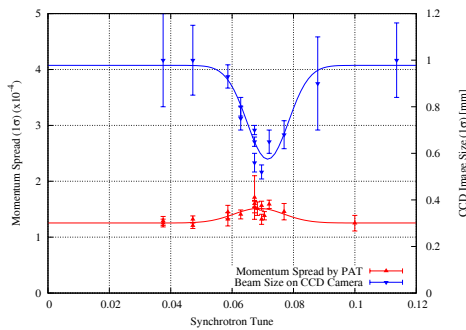


Figure 13. Experimental demonstration of synchro-betatron resonance coupling. Longitudinal momentum spread after laser cooling has a local maximum at  $\nu_s \sim 0.068$  (lower), while the horizontal beam size has a local minimum at the same position (upper).

Laser cooling

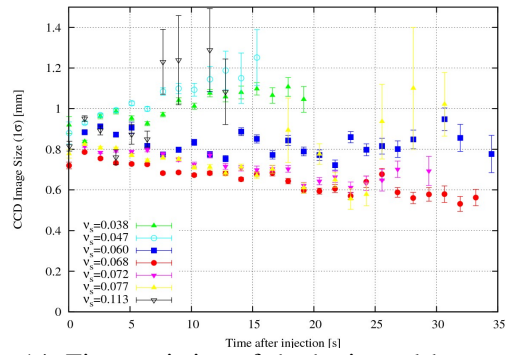


Figure 14. Time variation of the horizontal beam size for various synchrotron tunes.

same synchrotron tune (lower) as shown in Fig. 13, which is an experimental demonstration of “Synchro-Betatron Resonance Coupling”.

At the peak of this resonance, the beam temperatures are evaluated to be 24 K and  $\sim 200$  K ( $1\sigma$ ) for the longitudinal and horizontal directions, respectively. At the off resonance condition, the longitudinal and horizontal temperatures are  $\sim 15$  K and  $\sim 600$  K, respectively.

In Fig.14, the developments of the horizontal beam width as a function of time for different synchrotron tunes are shown. According to the data shown in Fig.14, the transverse laser cooling rates by our present system seems to be comparable with the IBS rate, which is insufficient to realize crystalline ion beams.

### Evaluation of Results and Further Perspectives

In our laser cooling system of bunched beam, above mentioned, a fixed laser detuning after optimization is utilized, as shown in Fig. 15. Recent reinvestigation of the results, shown in Fig.14, pointed out that the  $^{24}\text{Mg}^+$  ion beam includes two components plasma with different life times as shown in Fig. 16. The time domain beam signals observed by an oscilloscope at the time of 10 s, 60 s and 150 s after injection (when laser cooling starts) are shown in Fig.16 (a), (b) and (c), respectively. These data demonstrate that the  $^{24}\text{Mg}^+$  ion beam has two components with different beam life times. By fitting these data, the life times of these two components are determined to be  $\sim 26$  s and  $\sim 42$  s for un-cooled and cooled beams,

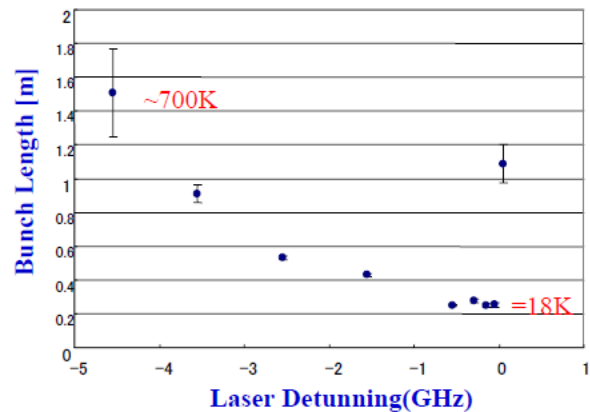


Figure 15. Optimization of laser detuning for bunched beam laser cooling.

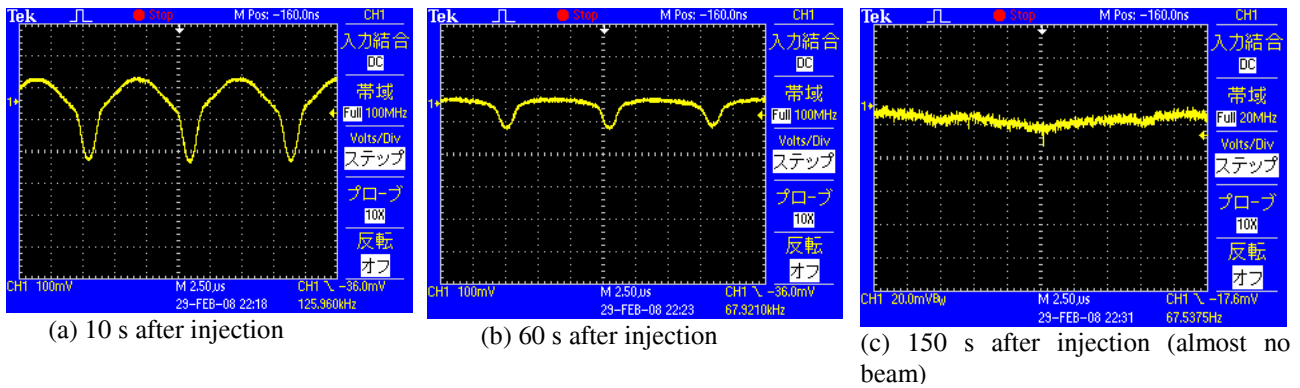


Fig. 16. Time domain beam signals observed after 10 s. (a), 60 s (b) and 150 s after injection. The laser cooling start at the injection time and these times also represent the time after the start of the cooling. Judging from the data of (c), almost no significant noises are included in these beam signals.

respectively as shown in Fig. 17 [16].

Up to now, the beam cooling time in the longitudinal direction has been evaluated by a spectrum analyzer using Schottky signals in the frequency domain, which however, seems to include both two components, laser cooled and un-cooled ions, which might be the reason why our laser cooling time is rather long and realized temperature is rather high compared with the theoretical prediction.

Our recent investigation on transverse laser cooling with the use of “Synchro-Betatron Coupling” has to be improved by sweeping the laser detuning or equivalently sweeping the RF frequency for bunching.

Another possible approach to much lower beam temperature is the application of pre-electron cooling for 40 keV  $^{24}\text{Mg}^+$  ion beams. As the corresponding electron energy of 0.9 eV for the 40 keV  $^{24}\text{Mg}^+$  ion beam seems to be too low to attain enough current for electron cooling, a scheme to use a higher voltage of  $\sim 12.5$  V for the extraction from the cathode and a ensuing deceleration to the ion velocity before reaching to the cooling section is under investigation.

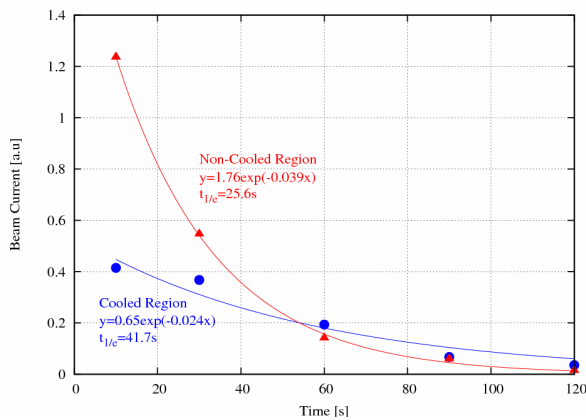


Fig.17. Fitted life times of the two components in the  $^{24}\text{Mg}^+$  ion beam during laser cooling..

## REFERENCES

- [1] J. Wei, X.P. Li and A.M. Sessler, Phys. Rev. Lett. **73** (1994) 3089.
- [2] A. Noda, M. Ikegami and T. Shirai, New Journal of Physics, **8** (2006) 288. The idea of dispersion free mode was originally proposed by W. Henneberg (Ann.Phys.,Lpz.( 1934) 19335) and recently mentioned by R. E. Pollock Z. Phys. A: Hadrons and Nuclei (1991) 34195). Our deflectors are first really fabricated one.
- [3] T. Shirai et al., Phys. Rev. Lett. **98** (2007) 204801.
- [4] H. Okamoto, A.M. Sessler and D. Möhl, Phys. Rev. Lett. **72** (1994) 3977
- [5] A. Noda, Nucl. Instr. Meth. Phys. Res. **532** (2004) pp150-156.
- [6] H. Fadil et al., Nucl. Instr. Meth. Phys. Res. **A517** (2004) pp1-8.
- [7] V.V. Parkhomchuk, Proc. of ECOOL84 , Karlsruhe
- [8] M. Steck et al., Phys. Rev. Lett. **77** (1996), 3803.
- [9] H. Danared et al., Phys. Rev. Lett. **88**. (2002) 174801.
- [10] M. Steck et al., Nucl. Instrum. Methods Phys. Res., **A532** (2004) , 357.
- [11] A. Yogo et al., Appl. Phys. Lett. **94** (2009),181502.
- [12] T. Fujimoto et al., Nucl. Instr. Meth. Phys. Res. **588** (2008) pp330-335.
- [13] H.J. Miesner et al., Phys. Rev. Lett. **77** (1996) 623 (coasting beam), . H.J. Miesner et al., Nucl. Instr. Meth. in Phys. Res. **A383**(1996) 634-636 (bunched beam).
- [14] I. Lauer et al., Phys. Rev. Lett. **81** (1998) 2052.
- [15] M. Nakao, Master Thesis (in Japanese).
- [16] H. Souda et al., under preparation for publishing.

# APPLICATION OF COOLING METHODS TO NICA PROJECT

S.Kostromin, I.Meshkov, A.Sidorin, A.Smirnov, G.Trubnikov\*, JINR, Russia

## Abstract

The Nuclotron-based Ion Collider fAcility (NICA) is a new accelerator complex being constructed at JINR aimed to provide experiments with colliding heavy ions up to Au for experimental study of hot and dense strongly interacting baryonic matter and search for possible signs of the mixed phase and critical endpoint in the centre-of-mass energy range  $\sqrt{s_{NN}} = 4-11$  GeV. Beam cooling systems are proposed for elements of the NICA project. The Booster synchrotron will be equipped with an electron cooling system. Two beam cooling systems – stochastic and electron will be used in the collider rings. Parameters of cooling systems, proposed scenario of operation and peculiarities of their design intended to achieve required average luminosity of the order of  $10^{27} \text{cm}^{-2}\text{s}^{-1}$  at high energies are presented in this report.

## INTRODUCTION

The goal of the NICA project [1] is construction at JINR of the new accelerator facility that consists of:

- cryogenic ESIS ion source “KRION” with 6T solenoid;
- source of polarized protons and deuterons;
- the existing linac LU-20 (energy up to 5 MeV/u);
- a new heavy ion linear accelerator (3 MeV/u);
- a new 600 MeV/u Booster-synchrotron;
- modernized heavy ion synchrotron Nuclotron (4,5 GeV/u maximal kinetic energy for ions with  $Z/A = 1/3$ );
- two new superconducting rings of the collider;

The facility will have to provide ion-ion ( $1 \div 4.5$  GeV/u), ion-proton collisions and collisions of polarized pp ( $5 \div 12.6$  GeV) and dd ( $2 \div 5.8$  GeV/u) beams. The Booster will be equipped with a slow extraction system to provide medicine, biological and other applied researches.

The collider will have two interaction points. The Multi Purpose Detector (MPD) in the first IP, and the second IP is used for the Spin Physics Detector (SPD).

Collider will be operated at fixed energy without acceleration of injected beam. Correspondingly the maximum energy of the experiment is determined by the Nuclotron magnetic rigidity that is equal to about 45 T·m. Main goal of the NICA facility is to provide collider experiment with heavy ions like Au, Pb, or U at average luminosity above  $1 \cdot 10^{27} \text{cm}^{-2}\text{s}^{-1}$  in the maximal wide energy range up to 4,5 GeV/u. Therefore in this report it is discussed heavy ion mode of the facility operation only, and  $^{197}\text{Au}^{79+}$  are chosen as the reference particles.

To reach the required parameters a beam cooling is proposed both in the Booster and in the collider rings.

## ELECTRON COOLING SYSTEM FOR BOOSTER. OPERATION MODES.

The maximum design ion energy of 4.5 GeV/u can be achieved at Nuclotron with fully stripped ions only. To provide high efficiency of the ion stripping one has to accelerate them up to the energy of a few hundreds of MeV/u. For this purpose a new synchrotron ring – the Booster is planned to be used (Table 1). The Booster has maximum magnetic rigidity of 25 T·m that corresponds to about 600 MeV/u of the ion energy, and the stripping efficiency is not less than 80%.

The Booster is equipped with room-temperature electron cooling system that allows to provide efficient cooling of the ions in the energy range from injection energy up to 100 MeV/u (Fig.1). Electron cooling at injection energy 3 MeV/u is required to accumulate intense beam especially if multiple injection is used. Such mode will be required also for storing highly charged ion states (for example  $\text{Au}^{65+}$  ions) or polarized ions (for example  $\uparrow\text{H}$  atoms) with high intensity. Beam cooling at higher energies (up to 100 MeV/u) could be useful to achieve special beam parameters required by fixed target experiments on the extracted beam from Booster.

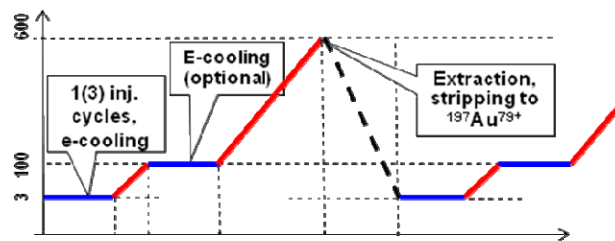


Figure 1: Booster cycle diagram (Y-axis: energy, MeV/u)

The magnetic system of the Booster is superconducting. Its design is based on the experience of construction of the Nuclotron SC magnetic system [3]. Parameters of the Booster cooler are typical for conventional electron cooling systems. Design of the cooler had been performed by JINR and its construction is planned to be done in collaboration with Budker INP.

Main goal of the cooling of heavy ion beam at 100 MeV/u energy could be decreasing its longitudinal emittance to the value required for effective injection and acceleration in the Nuclotron before injection into the collider. Transverse beam emittance has to be stabilized at relatively large value to avoid space charge limitations in the Nuclotron and collider rings. Simulations of such a regime of the cooler operation performed with Betacool code showed that during 1 second of the cooling one can decrease the longitudinal beam emittance by about 3 times at practically constant transverse emittance.

\*E-mail: trubnikov@jinr.ru



maximum tune shift. The dominated effect is the Lasslet tune shift which can be estimated as

$$\Delta Q = -\frac{Z^2 r_p}{A} \frac{N_b}{4\pi\beta^2 \gamma^3 \varepsilon} F_{sc} F_b, \quad F_b = \frac{C_{Ring}}{\sqrt{2\pi}\sigma_s} \quad (3)$$

where  $Z$ ,  $A$  and  $r_p$  are the charge, mass numbers and classical radius of the ion correspondingly,  $F_{sc}$  – image force correction factor (usually  $F_{sc} \sim 1$ ),  $F_b$  is the bunching factor. Expressing the luminosity via the tune shift we have the following estimation:

$$L = 8\pi^2 \beta^5 \gamma^6 \Delta Q^2 \frac{A^2}{Z^4} \cdot \frac{\varepsilon c}{r_p^2 \beta^* l_{bb}} \cdot \left( \frac{\sigma_s}{C_{Ring}} \right)^2 \cdot f_{HG} \quad (4)$$

That shows that in the IBS dominated regime the luminosity scales with the beam energy approximately as  $\beta^5 \gamma^6$  (Table 1).

Table 1. Collider beam parameters and luminosity

Ring circumference, m	503,04		
Number of bunches	23		
Rms bunch length, m	0.6		
$\beta$ -function in the IP, m	0.35		
FF lenses acceptance	40 $\pi$ mm mrad		
Long. acceptance, $\Delta p/p$	$\pm 0.010$		
Gamma-transition, $\gamma_{tr}$	7.091		
Ion energy, GeV/u	1.0	3.0	4.5
Ion number per bunch	2.75 $\cdot 10^8$	2.4 $\cdot 10^9$	2.2 $\cdot 10^9$
Rms momentum spread, $10^{-3}$	0.62	1.25	1.65
Rms beam emittance, h/v, (unnorm), $\pi$ -mm-mrad	1.1/ 1.01	1.1/ 0.89	1.1/ 0.76
Luminosity, $10^{27} \text{ cm}^{-2} \text{ s}^{-1}$	1.1e25	1e27	1e27
IBS growth time, sec	186	702	2540

The beam accumulation in the collider is planned to be realized in longitudinal phase space with application of RF barrier bucket (BB) technique. This provides independent optimization of the bunch intensity, bunch number as well as controlling of the beam emittance and momentum spread during the bunch formation.

The Keil-Schnell criteria for longitudinal microwave instability is satisfied for the bunch intensity in whole energy range.

## REQUIRED COOLING TIMES. THE COOLING STRATEGY

The beam cooling application in the collider rings has two goals:

- beam accumulation using cooling-stacking procedure;
- luminosity preservation during experiment.

The first goal can be achieved with stochastic cooling system of reasonable technical parameters, because in this case the beam has rather low linear particle density. The second goal is more important. Dedicated scenario of using stochastic and electron beam cooling systems to cover whole energy range with maximal achievable

luminosity at low energies and to have luminosity of the order of  $1 \cdot 10^{27} \text{ cm}^{-2} \text{ s}^{-1}$  at maximal energies is discussed below.

In equilibrium between IBS and the cooling the luminosity life-time is limited mainly by the ion interaction with the residual gas atoms. The vacuum conditions in the collider rings are chosen to provide the beam life time of a few hours. The beam preparation time is designed to be between 2 and 3 minutes. Therefore, the mean luminosity value is closed to the peak one.

To realize this regime the cooling times have to be equal to the expected IBS heating times (Fig. 3) for all degrees of freedom.

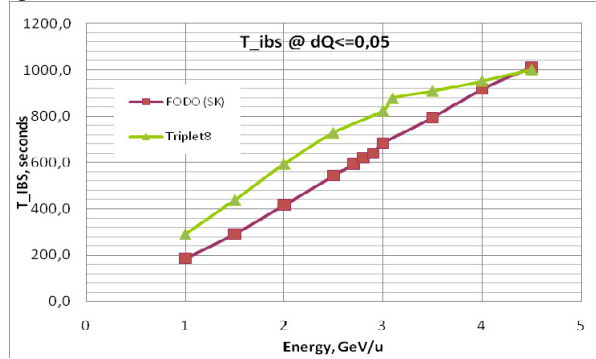


Fig. 3: Expected IBS heating times at maximum luminosity for different arc optics.

The way to increase the luminosity at low energy is to provide powerful cooling at cooling times sufficiently shorter than the IBS ones. In such a regime (so called space charge dominated regime) the bunch emittance is limited by achievable tune shift value but the momentum spread and the bunch length are determined by synchrotron tune suppression. In this case the bunch parameters and beta-function in the collision point can be re-optimized depending on the experiment energy.

For instance, at the energy of 1 GeV/u the beam emittance can be increased up to dynamic aperture limitation (about  $3 \pi$ -mm-mrad) with the corresponding increase of the particle number. If the bunch length and tune shift are kept constant, the luminosity scales linearly with the emittance. However, to avoid the aperture limitation we need to increase the beta-function in the collision point. The geometry acceptance is equal to

$$A \approx \frac{a^2}{\beta_{max}}, \quad (5)$$

where  $a$  – the lens aperture  $\beta_{max}$  is the beta function in the final focus triplet, that depends on the  $\beta^*$  approximately as

$$\beta_{max} \approx \beta^* + \frac{l_{tr}^2}{\beta^*}, \quad (6)$$

$l_{tr}$  is the distance from the triplet to the collision point. To have the geometry acceptance equal to the dynamic one the  $\beta^*$  has to be increased up to about 1 m. The luminosity in this case is proportional to

$$L \sim \frac{\varepsilon}{\beta^*} \cdot f_{HG} \left( \frac{\sigma_s}{\beta^*} \right) \sim \frac{a^2}{\left( \beta^* + \frac{l_{tr}^2}{\beta^*} \right) \beta^*} f_{HG} \quad (7)$$

This dependence plotted in the Fig. 4 shows that increase of the beam emittance and  $\beta^*$  can give about 60% increase of the luminosity. Further increase of the luminosity is related to design of final focus lenses with large aperture.

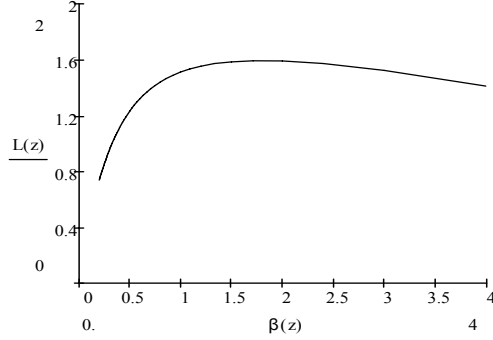


Fig. 4. Luminosity (normalized by its value at  $\beta^* = 35$  cm) versus  $\beta^*$  in meters.

Thus, at the energy range from 3 to 4.5 GeV/u a cooling system has to provide the cooling times of about 500 s (that will be achieved by stochastic cooling system at bandwidth of 3 GHz) and at 1 GeV/u of the order of ten seconds (that will be provided by electron cooling system).

## STOCHASTIC COOLING

The stochastic cooling (SC) is assumed to be used in the collider to preserve the required luminosity at higher energies. For this goal the SC has to provide equilibrium with the expected IBS heating.

For cooling of the longitudinal degree of freedom more preferable is to use Palmer method because of wider dynamical range on momentum deviation in comparison with other methods. At the optimum gain and neglecting the amplifier noise the stochastic cooling rate can be estimated for all degrees of freedom by the following formula [5]:

$$\frac{1}{\tau} = \frac{W}{N_{eq}} \frac{(1 - 1/M_{pk}^2)^2}{M_{kp}} \quad (8)$$

$W = f_{max} - f_{min}$  is the system bandwidth. For the bunched beam the equivalent particle number  $N_{eq}$  is calculated in accordance with the bunching factor (formula 5) as:

$$N_{eq} = N \frac{C}{\sqrt{2\pi}\sigma_s} \quad (9)$$

The “unwanted” mixing factor from pickup to kicker:

$$M_{pk} = \frac{1}{2(f_{max} + f_{min})\eta_{pk}T_{pk} \frac{\Delta p}{p}} \quad (10)$$

imposes a limit on the upper frequency  $f_{max}$  of the system band, that can be estimated as

$$f_{max} \leq \frac{1}{2\eta_{pk}T_{pk} \frac{\Delta p}{p}} \quad (11)$$

The “wanted” mixing from kicker to pickup is given by

$$M_{kp} = \frac{1}{2(f_{max} - f_{min})\eta_{kp}T_{kp} \frac{\Delta p}{p}} \quad (12)$$

and in ideal case it has to be close to unity. Here  $\eta_{pk}$ ,  $\eta_{kp}$ ,  $T_{pk}$ ,  $T_{kp}$  – are the partial slip-factor and time of flight from pickup to kicker and from kicker to pickup correspondingly. Usually for the cooling rate estimation the momentum spread is substituted as  $\Delta p/p \sim 2\sigma_p$ , where  $\sigma_p$  is its r.m.s. value.

The chosen lattice of the collider permits to optimize the pickup and kicker positions to provide small partial slip factor from the pickup to kicker (to avoid unwanted mixing) in the total required energy range. For the Palmer method (longitudinal cooling) the pickup is located at the entrance into arc section near maximum of the dispersion function. The kicker is located in the long straight section at 132 m downstream from the pickup (Fig. 5).

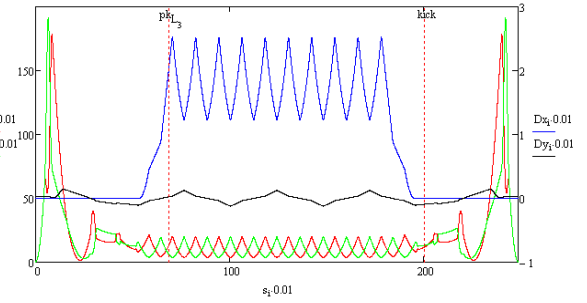


Fig. 5. Lattice functions at the half of the collider circumference with positions of pick up and kicker for longitudinal cooling.

The kicker position is chosen to have negative  $\eta_{pk}$  at maximum energy and positive at minimum energy (Fig. 6). In this case we exclude practically the unwanted mixing in the all energy range and sufficiently increase the wanted one.

At such position of the kicker the condition (11) gives for the acceptable upper frequency of the band the value of about 20 GHz (at the momentum spread equal to the ring dynamic aperture  $\pm 0.01$ ).

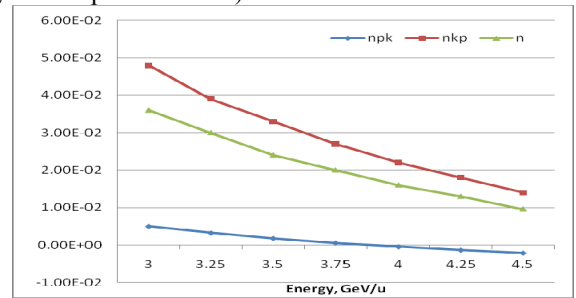


Fig. 6. Total and partial slip-factors of the ring as the function of ion energy.

It means that the system bandwidth is limited mainly by technical reasons. The luminosity of  $1 \cdot 10^{27} \text{ cm}^{-2} \text{ s}^{-1}$  corresponds to about  $2.3 \cdot 10^9$  ions per bunch, the effective ion number is about  $8 \cdot 10^{11}$ .

To provide the cooling time two-three times shorter than the IBS ones (to have a technical reserve) the cooling bandwidth can be chosen from 3 to 6 GHz (Fig. 7).

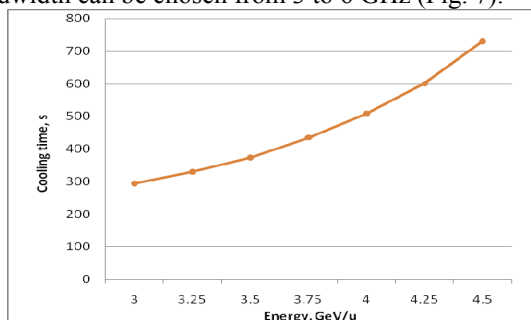


Fig. 7. Stochastic cooling time as the function of the ion energy at system bandwidth from 3 to 6 GHz.

The same pickup can be used for cooling of longitudinal and vertical degrees of freedom. The kicker for vertical degree of freedom is located in the long straight section in the position providing required phase advance.

Pickup for horizontal degree of freedom is located in the straight section upstream the arc in the zero dispersion point, the kicker in the straight section downstream the arc in the position providing required phase advance.

### ELECTRON COOLING

The electron cooling is aimed to completely suppress IBS heating at low energy and provide the collider operation in the space charge dominated regime. In this case at small momentum spread the transverse emittance can be sufficiently larger, than determined by equipartitioning condition. Therefore the luminosity at small energy can be sufficiently increased in comparison with IBS dominated regime.

For the cooling section at reasonable technical parameters (Table 2) the cooling times were estimated in accordance to Parkhomchuk formula [6] for the total ion energy range (Fig. 8). In the energy range from 3 to 4.5 GeV/u the cooling times are slightly shorter than expected IBS heating times and are comparable to stochastic cooling times. However at small energies the cooling times are about 20 times shorter than IBS heating times and the electron cooling is strong enough to provide space charge dominated regime of the collider operation.

Table 2. Main parameters of the collider electron cooler

Maximum electron energy, MeV	1.5
Cooling section length, m	6.0
Electron beam current, A	0.5
Electron beam radius, cm	0.8
Magnetic field in cooling section, T	1.0
Magnetic field imperfection	$2 \times 10^{-5}$
Beta functions in cooling section, m	20
Longitudinal electron temperature meV	5.0

Cooled beam dynamics

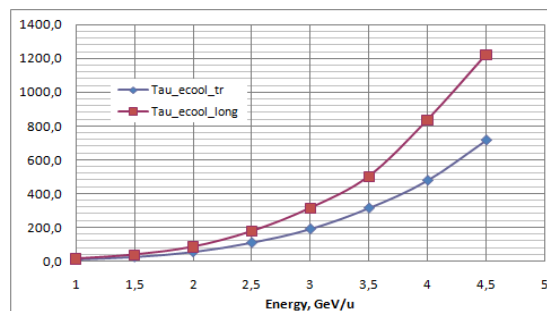


Fig. 8. Dependence of the electron cooling (transverse and longitudinal) times on the ion beam energy.

General problem which has to be solved for effective application of the electron cooling is the ion recombination with the cooling electrons. At typical temperature of electron transverse degree of freedom below 1eV the beam life-time due to recombination is about a few hundreds of seconds. There are two ways to increase the life-time: either to increase artificially the electron transverse temperature or to introduce energy shift between electrons and ions.

The magnetic field in the cooler of 1T is required mainly to provide adiabatic transport of the electron beam from HV source to the cooling section. Additionally such a large value resulted in strong magnetization of electrons and permits to provide effective cooling at large transverse electron temperature. The cooling rate is determined mainly by longitudinal electron temperature (that is dominated by HV generator stability) and logarithmically depends on the transverse one. In the Fig.9 transverse electron temperature required for obtaining of the beam life-time of 10 hours is plotted versus ion energy.

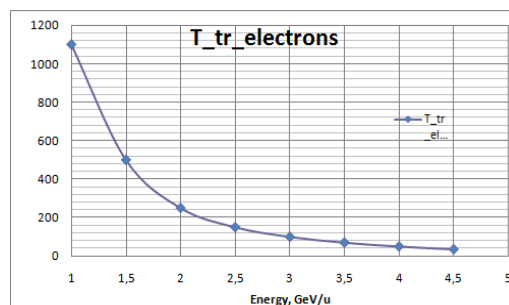


Fig. 9. Electron transverse temperature in eV required to have the ion life-time of 10 hours.

More effective way of the recombination suppression – shift of the electron energy – is discussed in [7].

### R&D FOR COLLIDER COOLING SYSTEMS

Design of the collider electron cooling system is performed in co-operation with All-Russian Electrotechnical Institute (VEI, Moscow) on the basis of dynamitron-type high voltage generator.

For the stochastic cooling development we plan to perform the cooling experiment with ion beam circulating in the Nuclotron. The existing Nuclotron RF system can not provide the same large bunching factor for heavy ion beam as required for the collider operation. But the cooling system can be tested at the same linear particle density of a bunched deuteron or carbon beam, which has intensity by two orders of magnitude larger than expected one for the heavy ions. The first step in realization of stochastic cooling experiment is longitudinal cooling of the coasting beam. Scheme with a notch filter and octave bandwidth 2-4 GHz was chosen for the system. The pick-up and kicker electrodes of the stochastic cooling system prototype will be elaborated in cooperation with COSY and will be similar to that one designed for the HESR of the FAIR project [8].

Simulations of the stochastic cooling process have been performed for different types of particles: protons and carbon ions C(6+). The results are presented in [9]. The results of the simulation give the following requirements for the system: in case of proton coasting beam, the power required for performing this experiment lays in 30-40W margins and gain is approximately 140dB. If the C(+6) beam will be used, the power requirements significantly decreases to 10W and 130dB gain correspondingly.

It is also proposed to study experimentally at Nuclotron the band overlapping process (if such occurs) in the energy range  $E = 2.5 - 4 \text{ GeV/u}$  which is extremely important for collider. Here it is possible carefully study of stochastic cooling time dependence for the bunched beam when increasing RF amplitude one has to measure beam momentum spread ( $dP/P$ ) which gives direct estimation of the efficient mixing factor.

## CONCLUSION

Application of the cooling methods is a key feature of the NICA project being developed at JINR. The project realization requires elaboration of novel cooling systems that can be done using both numerical simulations and experimental work with prototypes.

Booster synchrotron will be equipped with standard electron cooling system operating at electron beam energy from 1.5 to 50 keV

Stochastic and electron cooling technique at the collider are proposed to be used to have required luminosity with possibility of energy scan. Stochastic cooling application looks very attractive because it does not lead to additional particle loss and keeps the shape of ion distribution close to Gaussian one. However it cannot provide short cooling time at low energy.

Proposed cooling scenario for NICA collider is the following (Fig.10): in the ion energy range from 1 to 3 GeV/u the electron cooling can provide rather short cooling times to realize space charge dominated regime and increase luminosity in comparison with IBS dominated one. HV electron cooling system with energy up to 1.5 MeV looks realistic and realizable. In the energy range from 3 to 4.5 GeV/u the usage of the stochastic

cooling system is more preferable. Here the luminosity is equal to  $1 \cdot 10^{27} \text{ cm}^{-2} \text{ s}^{-1}$  and the collider can operate in IBS dominated regime. If one optimizes the ring lattice and Pick-up (PU) and Kicker (KK) positioning to have partial slippage factor (from PU to KK) close to zero the upper frequency of the system band is limited only by a technical reasons. The system at reasonable bandwidth of 3-6 GHz provides sufficient technical reserve (the cooling times by about three times less than IBS growth times). Final choice of the system bandwidth will be done after experimental test at the Nuclotron.

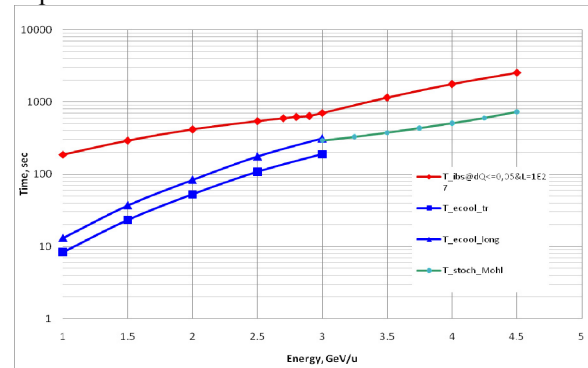


Fig. 10. IBS growth times in the IBS dominated regime, electron cooling times (below 3 GeV/u) and stochastic cooling time (above 3 GeV/u).

Numerical simulations of the beam dynamics in the collider under stochastic and electron cooling are in progress. The electron cooling system of the collider will be designed and constructed in collaboration with BINP, FZJ and VEI. Elaboration of the stochastic cooling system is performed in collaboration with FZJ, FNAL, CERN and BNL. The prototype of the stochastic cooling will be tested at the Nuclotron in the end of 2011.

## REFERENCES

- [1] G. Trubnikov, et.al., Proceedings of EPAC08, Genoa, Italy, p.2581
- [2] Khodzhbagiyani, H.G., and Smirnov, A.A., Proc. of the 12<sup>th</sup> Int. Cryogen. Eng. Conf., 1988, pp. 841–844.
- [3] NICA Conceptual Design Report, [http://nucloserv.jinr.ru/nica\\_webpage/Nica\\_files/reports/CDR\\_07/](http://nucloserv.jinr.ru/nica_webpage/Nica_files/reports/CDR_07/), editors I.Meshkov and A.Sidorin, JINR, Dubna, 2008
- [4] S. Nagaitsev, Intrabeam scattering formulas for fast numerical evaluation, Physical Review Special Topics – Accelerators and Beams, 8, 064403 (2005)..
- [5] D.Moehl, Stochastic cooling.
- [6] V.V.Parkhomchuk, New insights in the electron cooling, NIM A 441 (2000) 9-17, p.9
- [7] A.Philippov, these proceedings
- [8] R. Stassen, et al, Recent developments of the HESR stochastic cooling system, Proceedings of COOL07, Bad Kreuznach, Germany, 2007.
- [9] N.Shurkhno, G.Trubnikov et al, Stochastic cooling system prototype for Nuclotron, Proceedings of RuPAC10, Protvino, p.74

# ULTIMATE PERFORMANCE OF RELATIVISTIC ELECTRON COOLING AT FERMILAB\*

A. Shemyakin<sup>#</sup> and L. R. Prost, FNAL, Batavia, IL 60510, U.S.A.

## Abstract

Fermilab's Recycler ring employs a 4.3 MeV, 0.1A DC electron beam to cool antiprotons for accumulation and preparation of bunches for the Tevatron collider. The most important features that distinguish the Recycler cooler from other existing electron coolers are its relativistic energy, a low longitudinal magnetic field in the cooling section, ~100 G, and lumped focusing in the electron beam lines. The paper summarizes the experience of designing, commissioning, and optimizing the performance of this unique machine.

## INTRODUCTION

An electron cooler was envisioned as an important part of the Recycler ring [1]. The main cooler parameters (Table 1) were chosen to satisfy the Recycler goals: store antiprotons coming from the Accumulator, prepare bunches for Tevatron shots, and "recycle" particles left over from Tevatron stores. Because of the longitudinal injection scheme of the Recycler, the main emphasis was made on longitudinal cooling. Note that later changes, most notably the decision not to "recycle" antiprotons from the Tevatron and the lower than predicted emittances of the bunches coming from the Accumulator, relaxed the operational requirements for the cooler.

Table 1: Parameters of the cooler

Parameter	Unit	Design	Operation
Electron energy	MeV	4.33	4.33
Beam current, DC	A	0.5	0.1
Magnetic field in the cooling section	G	100-200	105
Beam radius in the cooling section	mm	~5	~2
Pressure	nTorr	1	0.3
Total length of the beam line	m	90	90

As soon as the electron beam could be reliably sustained in 2005, relativistic electron cooling was demonstrated [2] and within days was put into operation. Since then, electron cooling significantly contributed to a several-fold increase of the Tevatron luminosity until the end of operation in October 2011.

In this paper, we discuss the choice of the cooler's scheme and its implementation, describe the setup and cooling measurement procedures, and present the ultimate results .

## CHOICE OF THE SCHEME

The scenario of using the Recycler electron cooler [3] assumed typical cooling times of tens of minutes.

Estimations showed that at a reasonable electron current (~0.5A) it could be achieved without using the benefits of a strong magnetic field in the cooling section. Such "non-magnetized" approach was a clear deviation from the tested way of building coolers, creating serious questions about the stability of the electron beam transport and ability to provide low transverse electron velocities in the cooling section. On the other hand, estimations of the budget available and time needed to develop an "all-magnetized" version of the cooler and contribute to Fermilab's Run II showed that it was not realistic.

Nevertheless, simply leaving a lumped focusing in the cooling section to counteract the electron beam's space charge looked dangerous because of beam interactions with the residual ions background and with the vacuum chamber walls [4]. However, it was realized that it is theoretically possible to transport an electron beam from one solenoid to another through a lumped-focusing section without excitation of additional angles with the appropriate choice of optics for this section [5]. As a result, a novel scheme was chosen where the electron gun and the cooling section are both immersed in a longitudinal magnetic field but the beam focusing in between is provided by separate solenoidal lenses.

Applicability of such scheme is critically dependent on the magnetic flux in the cooling section. When a beam with no transverse velocities inside a solenoid exits into a free space, conservation of the canonical angular momentum results in a coherent angular rotation of the beam. In the paraxial ray equation, it is equivalent to the addition of an effective normalized emittance [5]

$$\varepsilon_{B,eff} = \frac{e\Phi}{2\pi m_e c^2}, \quad (1)$$

where  $\Phi = B_{CS} R_{CS}^2$  is the magnetic flux through the beam cross section in the solenoid,  $e$  and  $m_e$  are the electron charge and mass, and  $c$  is the speed of light. As in the case with a real emittance, the beam transport with lumped focusing is possible only if this emittance is low enough. For example, a transport channel for  $\gamma = 10$  with a typical beam radius of ~1 cm and the beta-function of ~1 m to bring the beam into a cooling section at the radius of  $R_{CS} \sim 1$  cm limits the solenoid magnetic field to ~300G. To use lumped focusing during acceleration (i.e. at lower  $\gamma$ ), the magnetic flux had to be decreased in comparison with this example by limiting both the beam size and the magnetic field strength in the cooling section down to  $R_{CS} = 2 - 4$  mm and  $B_{CS} = 100 - 200$  G.

Because of the large (reactive) beam power required in the cooling section, ~1 MW, using the energy recovery

scheme, standard for electron coolers, is even more important for the Recycler cooler.

## SETUP

Elevation views of the electron cooler are shown in Figure 1.

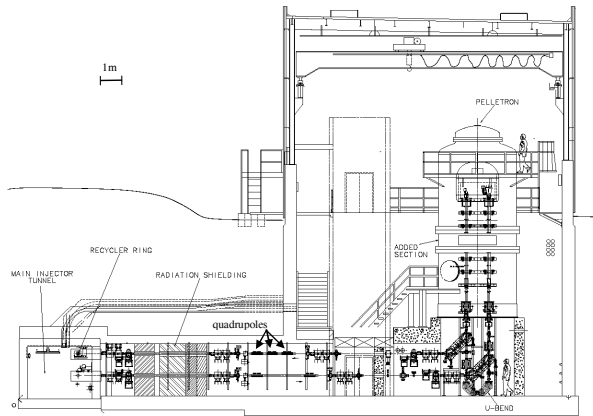


Figure 1a: Elevation view showing the Pelletron, the transfer lines passing through the connecting enclosure to the Recycler ring, and the cross-section of the Main Injector (MI) tunnel which houses the Recycler ring.

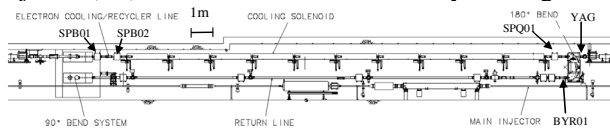


Figure 1b: Elevation view of the MI tunnel showing the 90°-bend system which injects the electron beam from the transfer line into the Recycler ring, the cooling section of Recycler, the 180°-bend system which extracts the electron beam from the Recycler, and the return line.

Electrons are emitted by a thermionic cathode, accelerated inside an electrostatic accelerator, Pelletron [6], and transported through a beam “supply” line to the cooling section where they interact with antiprotons circulating in the Recycler. After separation of the beams by a 180 degree bend, electrons move through the “return” beam line out of the tunnel, and then through a “transfer” line back to the Pelletron. Inside the Pelletron, the electron beam is decelerated in the second (“deceleration”) tube and is absorbed in a collector at the kinetic energy of 3.2 keV. The main ideas for a low-halo gun are described in [7], and performance of the collector is presented in [8].

The vacuum chamber is pumped down by ion and titanium sublimation pumps. The diameter of the vacuum pipe is 47 mm in the cooling section and 75 mm in the beam lines, where the aperture is limited by the BPM's inner diameter also of 47 mm. The typical pressure is 0.3 nTorr (mainly hydrogen).

When both main bending magnets under the Pelletron are turned off, the beam can be passed through a short beam line, denoted as U-bend in Fig.1a. This so-called U-bend mode was used for commissioning purposes.

## BEAM RECIRCULATION

Insufficient stability of the electron beam recirculation was the main obstacle at the R&D and commissioning stages. Frequently, the terminal voltage was dropping by tens or hundreds of kV, and the protection system was turning the beam off (“a beam trip”). Sometimes, the terminal voltage would go down to nearly zero, with the vacuum pressure in the tubes increasing by several orders of magnitude and with electromagnetic waves often damaging the equipment (“a full discharge”).

Most of these events result from a charge accumulation on the tube ceramic, coming from lost electrons, and following partial discharges in the acceleration gaps. These discharges occur all the time, with frequency dependent on the tube voltage gradient and amount of beam loss. By itself, a discharge of a single gap cannot significantly change the overall voltage distribution. The structure of the Pelletron column contains large aluminium discs, called separation boxes, which are connected every ~60 cm (2') to both tubes resistive dividers as well as to a column resistive divider. When only one of 42 gaps contained between neighbouring separation boxes is discharged, the effect on the voltage outside this portion of the tube is negligible. However, with some probability a plasma plume from such discharges can also shorten one or several neighbouring gaps. If the unaffected portion of the tube is capable of holding the entire voltage, the gaps are charged up again, and the beam does not trip. If the envelope modification resulting from the altered voltage distribution is large but induces a beam loss only somewhere outside of the Pelletron, the protection system interrupts the beam and normal operation can be restored in a matter of seconds. Otherwise, the entire tube shortens, causing a full discharge.

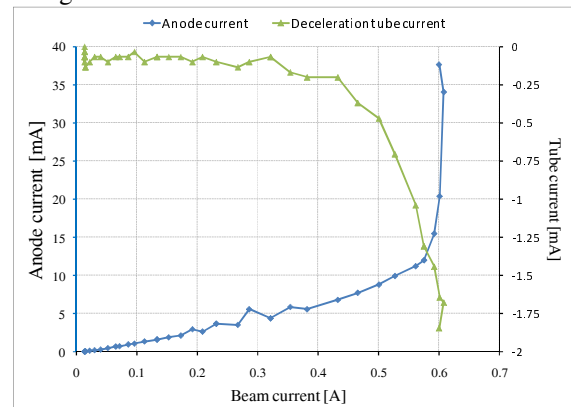


Figure 2. Anode current and changes in the deceleration tube current as functions of the beam current. Full line; ion clearing mode (December 31, 2011.).

Several steps allowed making the cooler an operational system.

- Development of an effective gun and collector with parameters well above operational requirements. The maximum current achieved and the typical relative beam loss were, correspondingly, 2.6 A and  $2 \cdot 10^{-6}$  on

a low-energy test bench, 1.8 A and  $1.2 \cdot 10^{-5}$  in the U-bend mode at 4.3MeV, and 0.6 A and  $1.8 \cdot 10^{-5}$  in the full line (Fig.2). The higher beam loss in longer systems is attributed to electron scattering on the residual gas and Intra Beam Scattering (IBS) [9].

- Decreasing the beam loss to the tubes, primarily by tuning the beam envelope in the deceleration tube to transport out of the Pelletron all electrons escaping from the collector. It was found that if the current of resistive dividers of either tube changes by more than  $\sim 1\mu\text{A}$ , the frequency of beam trips increases in accordance with the discharge model explained above.
- Increasing the total length of the accelerating tubes by 1/5 improved dramatically the recirculation stability at 4.3MV (operation voltage), in accordance with the logic of the previous paragraph. Note that in a test recently performed at much lower energy, 1.6 MeV, no single beam trip or full discharge have been observed [10].
- Adjusting the beam envelope in the acceleration tube to keep the beam core far from the tube electrodes in the time of the beam trips. It made a difference in preventing full discharges originating in the acceleration tube.
- Protection of the deceleration tube from irradiation in the time of beam trips by using optics with high dispersion in the return line.
- Fast protection circuitry, turning the beam off in  $1\mu\text{s}$  after detecting a Pelletron voltage drop of more than 5 kV or other abnormal conditions.

The implementation of these measures allowed operating typically with only several beam trips per day and full discharges as rare as once a year.

### ELECTRON COOLING IN OPERATION

Since 2005, the Recycler Electron cooler is used in operation around the clock to accumulate antiprotons in the Recycler and prepare them for shots to the Tevatron. A typical stacking cycle is shown in Fig.3. Every 40-50 minutes,  $\sim 25 \cdot 10^{10}$  antiprotons are transferred from the Accumulator into a free longitudinal space in the Recycler ring and then are merged with the main stack. The stack length stays constant all the time to minimize the longitudinal emittance dilution. After reaching the target stack size, antiprotons are aggressively cooled and transferred into the Main Injector for acceleration and injection into the Tevatron.

The manipulation of the electron beam is different for these two stages. During accumulation, the emphasis is on preserving a good life time while maintaining reasonable antiproton emittances. For that purpose, the electron beam is kept at 0.1 A and at a constant 2mm offset (propagating in the cooling section parallel to the axis of the antiproton beam). Recently, adding a small-amplitude helical motion of the electron beam was found to be beneficial as well.

During the stage of final preparation of bunches and their transfer out of the Recycler, the strength of cooling

is increased to the level where the antiproton phase density comes close to an instability threshold. The helix is removed; the electron beam is brought “on axis” (i.e. position concentric with the antiproton beam); during the summer of 2011, in addition the beam current was increased to 0.2A in the ion clearing mode (see below).

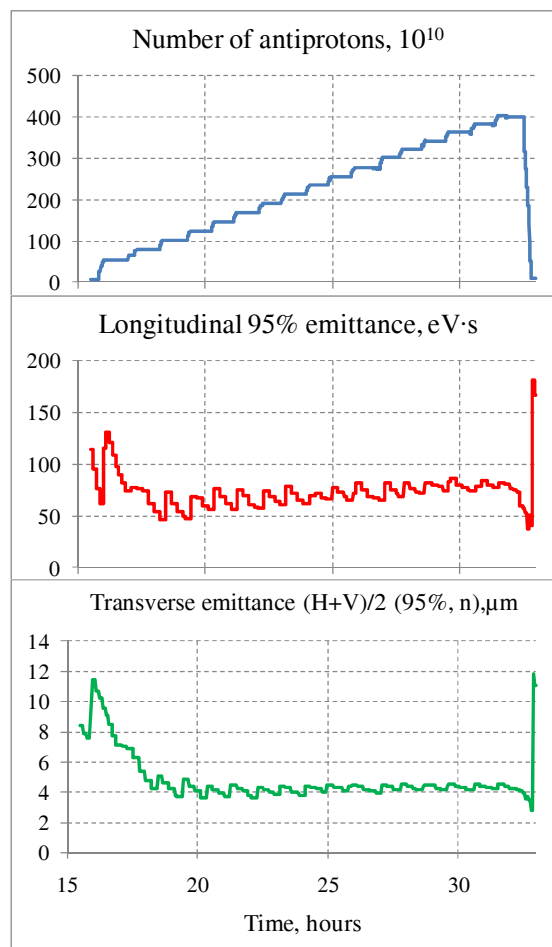


Figure 3. Typical cycle of accumulation of antiprotons in the Recycler ring and following extraction. June 17-18, 2011. Electron beam was kept at 0.1A, shifted by 2 mm from the axis except until right before extraction, when it was switched to 0.2A in ion clearing mode and moved on axis. The average life time was 256 hours, and initial luminosity in the Tevatron was  $408 \cdot 10^{30} \text{ cm}^{-2} \text{ s}^{-1}$ .

This procedure allows limiting the antiproton loss related to the final life time in the Recycler to 3-6% while increasing the beam brightness to the threshold determined by the capability of the Recycler transverse dampers. A significant progress to the accumulation rate and the life time resulted, in part, from enhancing electron cooling.

### OPTIMIZATION OF COOLING

Details about the quality of the electron beam and strength of cooling are obtained from ‘drag rate’ measurements by a voltage jump method [11] similar to the one used at the early age of electron cooling [12]: a

“pencil” coasting antiproton beam is cooled to an equilibrium, the electron energy is changed by a jump, and the rate of change of the mean value of the antiproton momentum is recorded while the antiprotons are dragged toward the new equilibrium. If the momentum spread remains small in comparison with the difference between the two equilibriums, this ‘drag rate’ is equal to the longitudinal cooling force.

The results can be compared with the classical cooling model [13] ignoring the contribution of the magnetic field. In the simplified case of a constant Coulomb logarithm  $L_c$ , the formula can be expressed as [14]

$$F_{Lz}(\Delta p_p) = F_0 \int_0^{p_1} \frac{e^{-u^2} u^2}{u^2 + \left(\frac{\Delta p_p}{p_2}\right)^2} du \quad (2)$$

which parameters are related to the lab-frame electron beam properties as follows:

$$p_1 = \delta W_e \cdot \sqrt{2} \frac{M_p}{\beta m_e c}; \quad p_2 = \vartheta_t \cdot \sqrt{2} \gamma^2 \beta c M_p;$$

$$F_0 = \frac{n_{el}}{\vartheta_t^2} \cdot \frac{2}{\sqrt{\pi}} \cdot \frac{4\pi \cdot e^4 \eta_{CS} \cdot L_c}{m_e c^2 \gamma^3 \beta^2}$$

where  $\theta_t$  is the 1D r.m.s. electron angle in the cooling section,  $\delta W_e$  the r.m.s. energy spread of the electron beam,  $n_{el}$  the electron density in the lab frame,  $M_p$  the proton mass,  $\eta_{CS}$  the portion of the ring occupied by the cooling section, and  $p_e = \gamma \beta m_e c$  the electron beam momentum. Graphically Eq.(2) is presented in Fig.4. If the cooling force is measured near its maximum, it depends on the transverse electron angles approximately as  $\theta_t^{-2}$  and can be used to estimate changes in the angle.

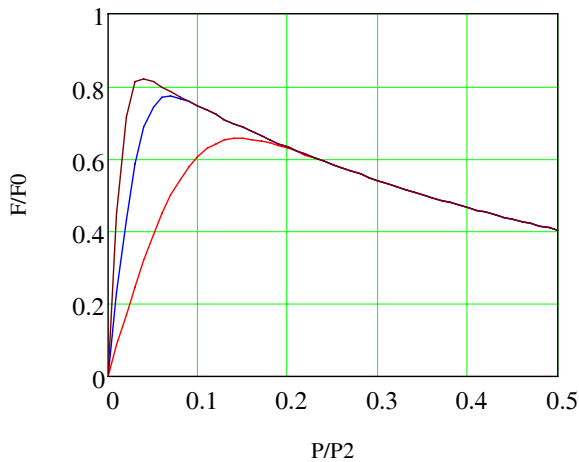


Figure 4. Normalized cooling force calculated with Eq.(2) as a function of  $\Delta p_p/p_2$  for three ratios of  $p_2/p_1$ : 10 (red), 25 (blue), and 50 (brown).

Results of the ‘drag rate’ measurements performed at different currents throughout the cooler history are shown in Fig. 5.

Electron cooling

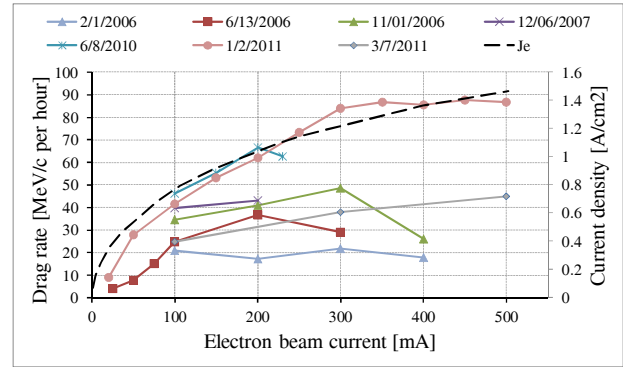


Figure 5. Cooling force as a function of the beam current measured on axis at various dates with a 2 kV voltage jump. The current density calculated at the beam center (dashed curve) is shown for comparison.

The significant enhancement of the cooling force presented in Fig.5 came mainly from three improvements that decreased the electron angles in the cooling section.

First, focusing was optimized by adjusting the corrector quadrupoles based on drag rate measurements at the electron beam periphery [15].

Second, a beam-based procedure for aligning the magnetic field in the cooling section was developed. The cooling section consists of 10 two-meter long solenoid modules, which are rigid but move with respect to one another when the tunnel deforms or the temperature changes. Compensation of the resulting transverse fields was made by adjusting 10 pairs of dipole correctors in each module. For this, a special electron trajectory was created that passed on axis for the module being optimized and with a large offset through the other parts of the cooling section. The cooling force measured in such configuration is determined mainly by the module with the beam on axis, and the transverse fields were adjusted module-by-module to maximize the force. For optimum performance, such optimization needs to be performed a couple times a year.

Finally, the electron angles were found to be affected by ions created by the electron beam and captured by its space charge. With no ion clearing mechanisms, the ion density would increase until reaching the electron one. At the neutralization factor of  $\eta \sim 1$ , the focusing effect from ions is a factor of  $\gamma^2 \sim 100$  higher than defocusing from the beam space charge, thus an effective ion clearing is required.

All capacitive pickups monitoring the beam position in the cooler (BPMs) have a negative DC offset on one of their plates, while the other plate is DC grounded. The resulting electric field removes ions in the vicinity of each BPM. The neutralization time (17 sec for 0.3 nTorr of hydrogen) is much longer than the time for a thermal – velocity  $H_2^+$  ion to fly  $\sim 5$  m between two neighbouring BPMs,  $\sim 3$  ms, and, therefore, clearing with the electric field in BPMs should be effective. However, significant size variations of both the electron beam and the vacuum pipe along the beam line create local potential minimums that prevent ions from travelling to the clearing field in

the BPMs. Also, solenoidal lenses providing focusing in the beam line create additional barriers for ions.

While this danger was realized at the design stage, the hope was that the focusing effect of the ion background would be mainly linear and, therefore, could be compensated by adjusting the lens settings. Indeed, the cooling properties of the electron beam were found good enough for what is the standard operation mode, at  $I_e = 0.1$  A. However, cooling efficiency peaked at 0.1 – 0.2 A and decreased at higher currents while it is supposed to be monotonically increasing with  $I_e$ . Transverse scans of drag rates (Fig.6a) revealed that at  $I_e = 0.3$ A only three narrow areas provide significant drag rates. This profile corresponds to high-order focusing perturbations that cannot be corrected by adjusting solenoidal lenses and quadrupoles.

The remedy to decrease the average ion concentration was found to be periodic interruptions of the electron beam. In the potential well created by electrons, ions gain the kinetic energy of up to 10 eV (at  $I_e = 0.3$  A).

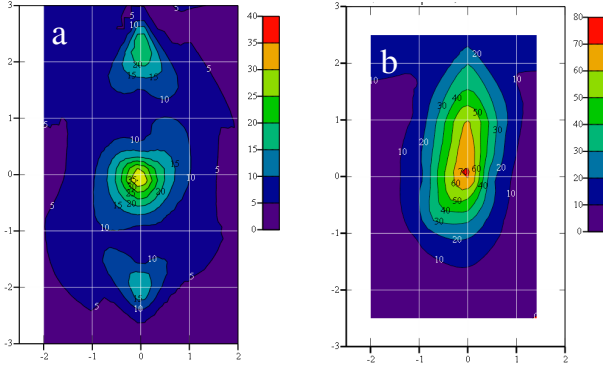


Figure 6. Contour plot of drag rates without (a) and with (b) ion clearing by beam interruptions. Voltage jump of 2 kV,  $I_e=0.3$ A. In the mode with ion clearing, the interruption frequency was 100 Hz. Contour levels are in MeV/c/hr. Note the difference in scales.

Thus, if the electron beam is abruptly turned off, an  $H_2^+$  ion reaches the vacuum pipe in 1-2  $\mu$ s. The capability of interrupting the electron current for 1 – 30  $\mu$ s with a frequency up to  $f_{int} = 100$  Hz was implemented in the electron gun modulator in 2009 [16].

Dependence of the cooling force measured at 1mm offset on the interruption frequency is shown in Fig. 6. The results can be compared with the following greatly simplified model.

a. The beam space charge outside of the Pelletron tubes is relatively small, so that the envelope electron angle in the cooling section changes linearly with variation of the beam current and the offset  $r$ ,  $\Delta\alpha = k_{sc} \cdot r \cdot \Delta I_e$ . According to OptiM [17] simulations, the coefficient  $k_{sc} \approx 1$  rad/A/m.

b. The effect of accumulated ions is similar,

$$\Delta\alpha_i = k_{sc} \cdot r \cdot \Delta I_e \cdot \delta \cdot \eta \cdot \gamma^2 \quad (3)$$

where  $\delta < 1$  is a fitting coefficient representing that ions can be accumulated only in a portion of the

Electron cooling

beam line, far from clearing fields of BPMs.

c. Neutralization drops to zero at the interruption, increases linearly with time until reaching an equilibrium at some value  $\eta_0$ , and then stays constant:

$$\eta(t) = \begin{cases} t / \tau_c, & t \leq \tau_0 \\ \eta_0, & t > \tau_0 \end{cases} \quad \tau_c = \frac{1}{n_a \sigma_i \beta c}; \quad \tau_0 = \eta_0 \tau_c \quad (4)$$

where  $n_a$  is the atom density and  $\sigma_i$  is the ionization cross section of hydrogen.

d. The cooling force  $F_c$  changes with the additional envelope angle introduced by neutralization as

$$F_c = \frac{F_0}{1 + (\Delta\alpha_i / \alpha_0)^2}, \quad (5)$$

where  $\alpha_0$  and  $F_0$  are the rms angle and drag force at optimum focusing.

e. The measured drag rate  $F_d$  is the cooling force averaged over the period between interruptions (assuming that the pencil antiproton beam is sensitive mainly to the electron angles in the location of its center)

$$F_d = f_{int}^{-1} \int_0^{1/f_{int}} F_c(t) dt \quad (6)$$

Calculation with Eq. (3) - (6) for  $\delta = 0.5$ ,  $\eta_0 = 0.02$ , and  $F_0 = 73$  MeV/c/hr, shown as a dashed line in Fig. 7, follows well the experimental data.

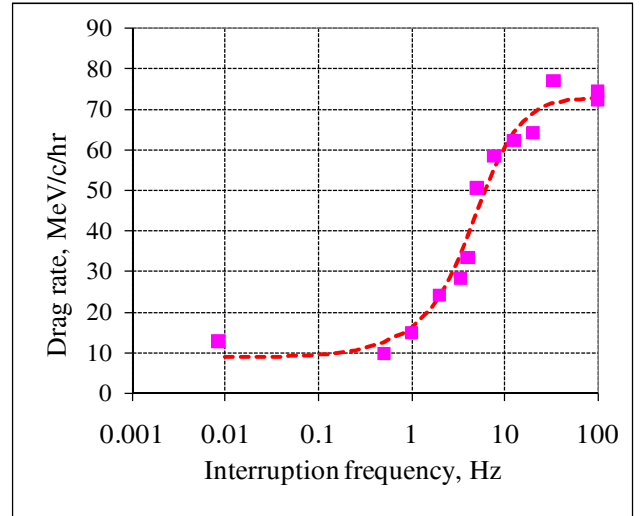


Figure 7. Drag rate as a function of the interruption frequency  $f_{int}$  for  $I_e = 0.3$ A and separation between beams of 1 mm. January 2, 2011. The interruption pulse was 2  $\mu$ s. Focusing was optimized on axis at 20 Hz. The squares represent the data, and the line is the model.

Clearing ions by beam current interruptions significantly increased the area of the electron beam cross section with good cooling (Fig. 6b) as well as improved the drag rate measured on axis at higher electron currents

(Fig. 5). The latter result is probably related to the finite transverse size of the “pencil” antiproton beam in the measurements.

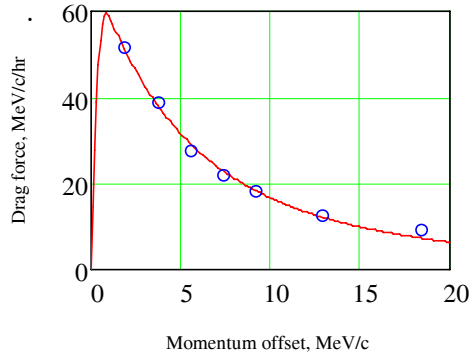


Figure 8. Drag rate as a function of momentum offset.  $I_e=0.1A$ , focusing is optimized for ion clearing, 100 Hz. The circles are data, and the solid line is a calculation with Eq.(2) at  $\theta_e=80\mu\text{rad}$ ,  $\delta W_e=200\text{eV}$ ,  $L_c=9$ . January 4, 2011.

The cooling force measured at different momentum offsets with ion clearing is presented in Fig. 8 for  $I_e=0.1A$ . Note that attempts to measure the force at momentum offsets lower than shown there (3.8 MeV/c) were unsuccessful because the longitudinal distribution moved too quickly toward the new equilibrium in order to reliably extract the value of the force. As a result, this set of measurements cannot give a reasonable estimation of the electron energy spread.

It is interesting to compare the angle in the cooling section from the fit to the data of Fig.8 with independent estimations of various components (Table 2). Each component is shown averaged over the electron beam size of 2 mm (radius), cooling section length, and time. The total, showing the components summed in quadrature, is close to that estimated from the drag rate measurements.

Table 2. Contributions to the total electron angle in the cooling section. Shown values are 1D, rms.

Effect	Angle, $\mu\text{rad}$	Method of evaluation
Thermal velocities	57	Calculated from the cathode temperature
Envelope mismatch	~50	Comparing resolution of tuning and simulations
Dipole motion (above 0.1 Hz)	~35	Spectra of BPMs in the cooling section
Dipole motion (field imperfections)	~50	Magnetic field measurements
Non-linearity in lenses	~20	Trajectory response to dipole kicks
Ion background	< 10	Cooling measurements
<b>Total</b>	<b>~100</b>	<b>Summed in quadrature</b>

## CONCLUSION

Electron cooling was an effective tool for increasing the luminosity of the Tevatron complex. The maximum strength of cooling was noticeably increased in the course of Run II, with the main improvements being tuning the beam envelope with quadrupoles, aligning the magnetic field in the cooling section, and removing ions captured by the beam.

## ACKNOWLEDGEMENTS

The success of electron cooling at Fermilab came as a result of efforts of many people, whose list would not fit into this paper. Authors are thankful to all of them for their dedicated work and for the joy working as a great team.

## REFERENCES

- [1] Fermilab Recycler Ring Technical Design Report, FERMILAB-TM-1991, 1996
- [2] S. Nagaitsev et al., Phys. Rev. Lett. 96, 044801 (2006)
- [3] FERMILAB-TM-2061, Oct 1998. 91pp., edited by J.A. MacLachlan.
- [4] N. Dikansky et al., Electron beam focusing system, in FERMILAB-TM-1998 (1996)
- [5] A.Burov et al., PRST – AB, 094002 (2000)
- [6] Pelletrons are manufactured by the National Electrostatics Corporation, www.pelletron.com
- [7] A. Sharapa et al., NIM-A 417 (1998) 177
- [8] L.R. Prost and A. Shemyakin, Proc. of PAC'05, Knoxville, USA (2005) p.2387
- [9] A. Burov et al., Proc. of COOL'05, Galena, USA (2005), p. 159, also available as FERMILAB-CONF-05-462-AD
- [10] L. R. Prost et al., Proc. of PAC'11, New York, USA (2011), WEP113
- [11] L. Prost et al., Proc. of HB2006, Tsukuba, Japan, May 29-June 2, 2006, WEAY02
- [12] G.I.Budker et al., Preprint IYaf 76-32 (1976), <http://cdsweb.cern.ch/record/118046/files/CM-P00100706.pdf>
- [13] Ya.S. Derbenev and A.N. Skrinsky, Particle Accelerators, 8, p.1 (1977)
- [14] A. Shemyakin and L.R. Prost, Proc. of APAC'07, Indore, India (2007), TUPMA094
- [15] A. Shemyakin et al., Proc. of PAC'09, Vancouver, Canada (2009), TU6PFP076
- [16] A. Shemyakin et al., Proc. of IPAC'10, Kyoto, Japan (2010), MOPD075
- [17] V. Lebedev, “OptiM”, at <http://www-bdnew.fnal.gov/pbar/organizationalchart/lebedev/OptiM/optim.htmA>.

## THE FIRST COMMISSION RESULTS OF THE HIGH VOLTAGE MAGNETIZED COOLER FOR COSY

V.B. Reva, N. Alinovsky, A.M. Batrakov, T.V. Bedareva, E.A. Bekhtenev, O.V. Belikov, V. N. Bocharov, V.V. Borodich, M.I. Bryzgunov, A.V. Bublely, V.A. Chekavinskiy, V.G. Cheskidov, B.A. Dovzhenko, A.I. Erokhin, G. A. Fatkin, M.G. Fedotov, A.D. Goncharov, K.M. Gorchakov, V. K. Gosteev, I.A. Gusev, A.V. Ivanov, G.V. Karpov, Yu.I. Koisin, M.N. Kondaurov, A.M. Kryuchkov, AD. Lisitsyn, I.A. Lopatkin, V.R. Mamkin, A.S. Medvedko, V.M. Panasyuk, V.V. Parkhomchuk, I.V. Poletaev, V.A. Polukhin, AYu. Protopopov, D.N. Pureskin, A.A. Putmakov, E.P. Semenov, D.V. Senkov, D.N. Skorobogatov, N.P. Zapiatkin BINP SB RAS, Novosibirsk, Russia

### Abstract

The electron cooler of a 2 MEV for COSY storage ring FZJ is assembling in BINP. The cooling section is designed on the classic scheme of low energy coolers like cooler CSRm, CSRe, LEIR that was produced in BINP before. The electron beam is transported inside the longitudinal magnetic field along whole trajectory from an electron gun to a collector. This optic scheme is stimulated by the wide range of the working energies 0.1(0.025)-2 MeV. The electrostatic accelerator consists of 34 individual unifi section. Each section contains two HV power supply (plus/minus 30 kV) and power supply of the magnetic coils. The electrical power to each section is provided by the cascade transformer. The cascade transformer is the set of the transformer connected in series with isolating winding. This paper describes the status of the electron cooling assembling processing;

### INTRODUCTION

New generation of the accelerators for study nuclear physics at range of relativistic physics 1-8 GeV/u requires very powerful cooling to obtain high luminosity. For example the experiments with 15 GeV antiproton for investigation of meson resonances on PANDA detector require an internal hydrogen target with effective thickness  $4 \times 10^{15}$  hydrogen atoms per  $\text{cm}^2$  and  $10^{10} - 10^{11}$  antiprotons circulating in HESR. In this case the peak luminosities ranging from  $2 \times 10^{31}$  to  $2 \times 10^{32} \text{ cm}^{-2} \text{ s}^{-1}$  are achievable. These experiments provide to observe meson resonances in proton-antiproton annihilations. Resolution of the experiments is limited only by momentum spread in antiproton beam, which must be better than  $10^{-4}$ .

The average momentum losses on such target (for antiprotons with energy 4 GeV) will be about  $(dp/dt)/p = 4 \cdot 10^{-6} \text{ s}^{-1}$  and heating rate of momentum spread by fluctuation of ionization losses will be near  $(dp^2/dt)/p^2 = 2 \cdot 10^{-9} \text{ s}^{-1}$ . Easy to see that to obtain momentum spread  $10^{-5} - 10^{-4}$  we need cooling time at range

$$\tau_{cool} = 2(dp/p)^2 / (dp^2/dt/p^2) = 0.1 \div 10 \text{ s.}$$

The electron cooler with energy 4.34 MeV at RECYCLER (FNAL) [1] has cooling time near 1 hour. New cooler for COSY should have few order magnitude

more powerful cooling that required new technical solutions. The basic idea of this cooler is to use high magnetic field along all orbit of the electron beam from the electron gun to the electron collector. At this case we have chance to have high enough the electron beam density at cooling section with low effective temperature. For example the electron beam density  $2 \cdot 10^8 \text{ cm}^{-3}$  (beam diameter 6 mm and current 1.5 A) magnetized with longitudinal magnetic field 2 kG will have at beam reference system drift velocity  $2.7 \cdot 10^6 \text{ cm/sec}$ . This velocity lets (at principle) to have cooling time near 0.1 sec for the beam with low angular spread  $\Delta p_{\perp} / p = 10^{-5}$ .

The basic idea of the design 2 MeV electron cooler for COSY ring is to test main features of the 4-8 MeV electron cooler for HESR GSI. The step at the energy of electron beam from 200-300 keV today to 8 MeV for HESR looks too large. The new technical solution should be tested at smaller step for example 2 MeV cooler for COSY. The design of the electron cooler for existing synchrotron COSY give additional limitation by existing building (upper points for lifting crane hook 7 m) and existing free space for cooler 6390 mm.

The structure of the 2 MeV cooler for COSY is shown in Fig. 1.

### MAGNETIC SYSTEM

The optics of 8 MeV cooler for COSY is designed close to the classical low-energy coolers. The motion of the electron beam is magnetized (or close to magnetized conditions) along whole trajectory from a gun to a collector. This decision is stimulated by requirement to operate in the wide energy range from 25 keV to 2 MeV. So, the longitudinal field has maximum value with compare to the transverse component of the magnetic fields.

The magnetic system of the cooler consists of the coils of gun and collector, accelerating/decelerating tubes, transport channels from high-voltage tank to the cooling section, cooling section and transport channel of the return way. The transport channels contains the six 90 degree bend toroidal magnets, two matching sections between high-voltage tank and transport channel, two matching section between transport channel and cooling section and six straight section for technological purpose.

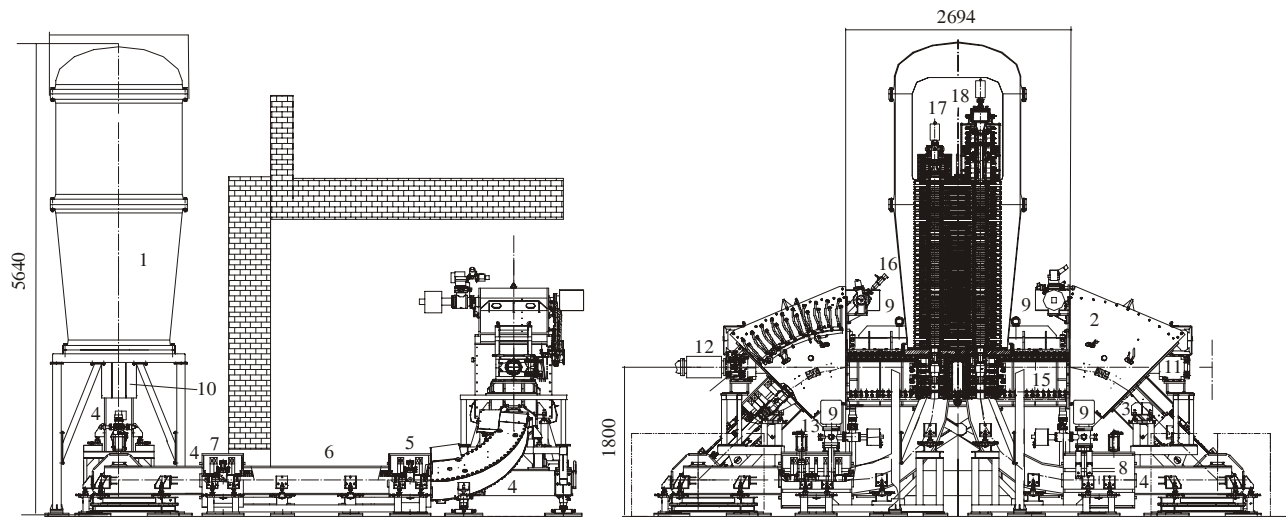


Figure 1 Sketch of the 2 MeV Cooler COSY. High voltage tank is 1, 45° toroid is 2, magnetic system of the transition section from 45° toroid to the transport channel is 3, magnetic system of the 90° bend is 4, magnetic systems of the straight line 0.5 m are 5 and 7, the straight section 1.7 m is 6, the straight section 1m is 8, the pump is 9, the transition section accelerating tube – transport is 10, the dipole correction of the ion beam is 11, the fast ramping kicker is 12, the vacuum gate is 13, the quadrupole lens of COSY ring is 14, the cooling section is 15, the rotary motion feedthrough to the vacuum for the magnetic compass probe is 16, the electron gun is 17, the electron collector is 18.

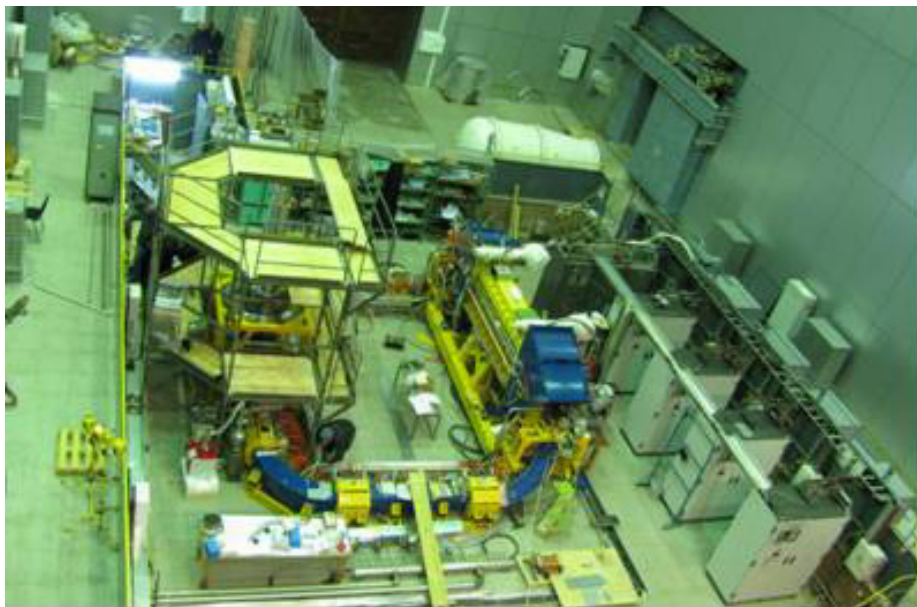


Figure 2: Photo of the electron cooler 2 MeV in assembling.

The magnetic field in the accelerating tube is taken 500 G and this value is related to the maximum power that can be transfer to a high voltage potential with help of the cascade transformer. The value in the transport channel is located in the range 0.5 kG – 1 kG. The energy 2 MeV is high enough in order to don't have the complete adiabatic motion of the electrons because the magnetic field of the bend elements is chosen to provide the length of bend equal to integer number of Larmor lengths. In such a case the kick on entry to bend is compensated by kick on leaving and the excitation of the transverse motion of the electron is small. The magnetic field in the cooling section is taken 2 kG in order to have the maximum Larmor

oscillation ( $\sim 10$ ) of the electron during its interaction with ion in order to have the magnetized Coulomb collisions even the highest electron energy 2 MeV. The transition from accelerating tubes to transport channel is made with 7 coils with independent power supplies [2]. The transition from the transport channel to the cooling section is made with 5 coils with small regulation of the longitudinal current with regulated electrical shunt. In this region the magnetic field is strong and the electron motion is close to adiabatic so the matching can be realized by the proper location of these coils in order to minimize the amplitude of the transverse motion.

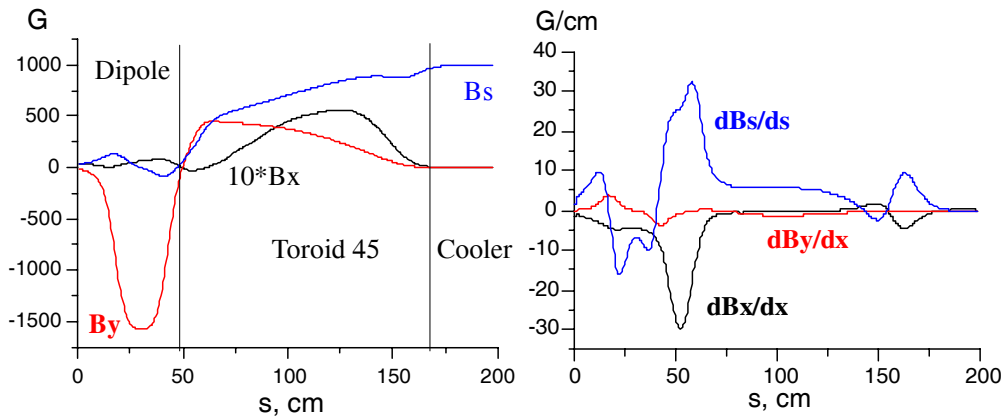


Figure 3: Magnetic field along ion channel. The currents are 175A in the cooling section, 500A in the toroid section, 200A in the dipole correction of the ion beam and 200A in the bending coils of the toroid.

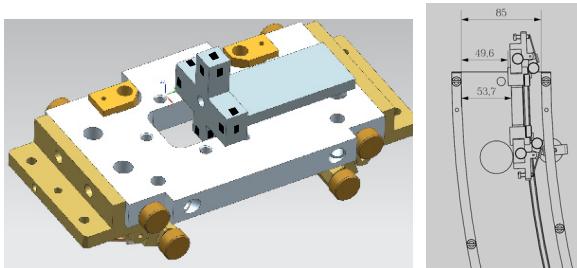


Figure 4: System of Hall probes measurements.

The tuning of the electron optics demands to knowledge of the maps of the magnetic fields for all optics elements. The special magnetic system measurement system was done for this purpose (see Fig. 4). The carriage with 12 Hall sensors is moved along the electron and ion trajectory. The sensor displacement allows measuring 3 component of the magnetic field in the 4 space point. So, the main component of the magnetic field and first derivative can be measured.

The Fig. 3 shows the primary dates of the measurement along ion orbit (dipole, toroid and entrance to the cooling section). The currents are 175A in the cooling section, 500A in the toroid section, 200A in the dipole correction of the ion beam and 200 A in the bending coils of the toroid. It is possible to see the features in the function related to the transition cooler/toroid and ion dipole corrector. The vertical field is determined by 45 degree toroid and dipole corrector. The integral of the vertical field should be compensated in normal cooler operation. The horizontal field in toroid is related to the bend magnetic field for the electron beam in the place of the ion and electron orbit interference. The Fig. 5 shows the primary data along electron orbit on the entrance to the cooler section. One can see the component of the horizontal bend magnetic field that has influence to the ion orbit.

The details of the magnetic field measurements is described in [3].

### DIAGNOSTIC SYSTEM

The mapping of the magnetic field gives only the preliminary information about optics of the electron beam. The calculation of the orbit on the base of this data should be supplement with a diagnostic of the electron beam. The special electron gun with 4-sectors control electrode was designed and manufactured for this purpose. The design of the gun is shown in Fig. 6. The modulation signal can be supplied to each sector of the control electrode. So, the position of one quadrant sector of the electron beam can be measured by pick-up system. Comparing the positions of each sectors from pick-up to pick-up or the sector positions in the single pick-up between the different values of the corrector coils it is possible to analyze the optics of the electron beam in the transport channel (see Fig. 6). The coordinates of the centres of the modulation regions are marked 1,2,3 and 4. The coordinates of the centres on another pick-up are mark by prime. The distance between these coordinates indicates changing of the beam shape.

The operation of the electron gun with sector electrodes was investigated on the special test-bench gun-collector [4-5]. The perveance characteristics of the electron beam are shown in Fig. 7 for the different number sectors in the operation.

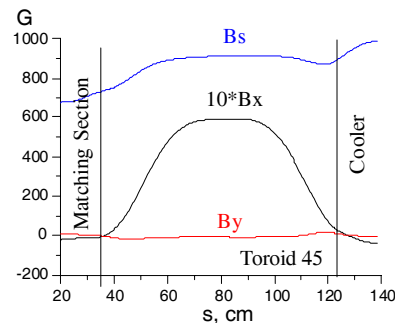


Figure 5: Magnetic fields along electron trajectory in the entrance to the cooling section.

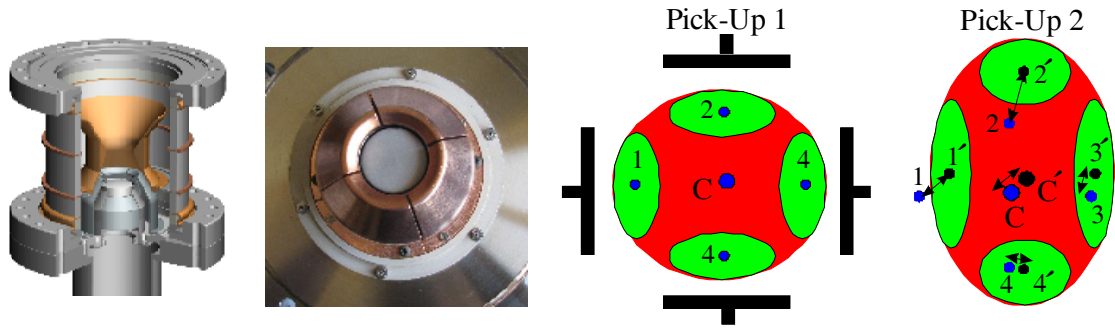


Figure 6: From left to right: sketch of the electron gun, the photo of the sectors of the control electrode, the sketch of the measurements of the shape of the electron beam with pick-up system.

Unfortunately the test-bench wasn't equipped by the full-fledged pick-up system because the electrode of the Wien filter was used for the qualitative analyze. The figure shows the experimental results and comparing it with calculation codes. There is an agreement in the trend of the beam size changing estimated by the experimental and simulation methods but the additional improvement of the 3D calculation methods is desirable. The electron motion in the beam isn't strongly magnetized and the complete 3D simulation with space-charge effects should be done. The Fig. 8 shows that the perveance characteristic is changed at the magnetic fields that may be interpreted as not strong magnetizing dynamic of electrons in the gun.

The situation with beam profile can be cleared on the cooler with profile beam monitor consisting from many Farady cells. The electron gun has possibility to work in pulsing regime (~10 mks). During this time the control electrode is positive and the electron beam is registered by the Faraday cells in the rest time the electron beam is turned off by the negative voltage on the control electrode [6]

### COLLECTOR

The main goal of the collector is minimized the number of the reflected electron from the collector. The efficiency of the collector may be improved due to installing the special filter of the velocity [4]. The

region with crossed electrical and magnetic fields transmits the electron moving in one direction and strongly deflects the electrons moving in opposite direction ( $E \times B$  Wien velocity filter).

The sketch of the collector is shown in Fig. 9. The collector keeps the secondary electrons with help of the magnetic and electrostatic barriers. The magnetic barriers is formed by the collector coil (see Fig. 9) connected in the opposite direction to the other coils of the collector. The electrostatic barrier is formed by combination voltage applied to collector, suppressor and pre-collector electrodes. The suppressor electrode is powered by the independent power supplies (+5 /- 3kV). The pre-collector electrode has the potential collector or one/half of the collector voltage.

The electron that leaves the collector is deflected by the Wien Filter and is absorbed by high-voltage terminal ground (Jleak2). The electrons leaving the system Wien Filter plus collector is analyzed by the special analyzing electrode (Jleak2).

It was discovered usefulness to apply to pre-collector electrode the negative voltage about  $0.5 \cdot U_{coll}$  respect to the collector. Due to large length the radial uniform electrostatic barrier is formed and it good reflects the essential part of the secondary electrons leaving collector.

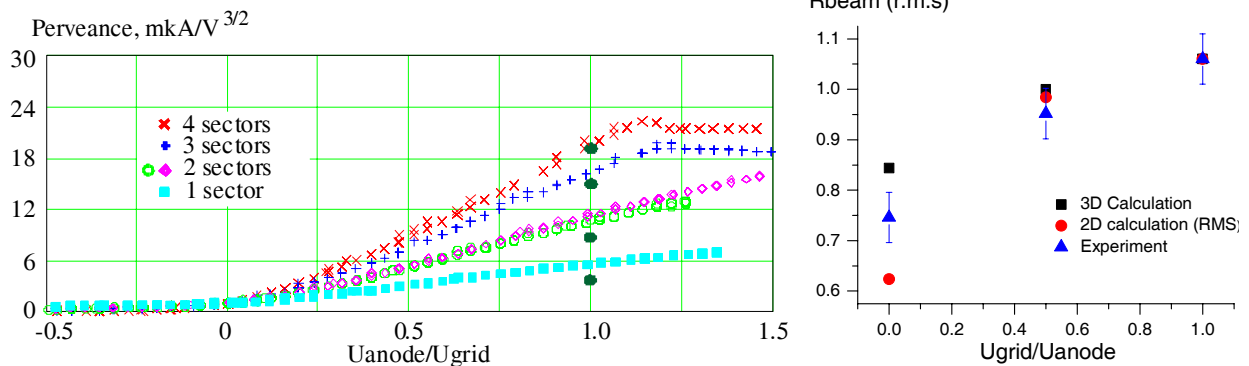


Figure 7: Perveance characteristics of the electron gun at the different number of the sectors in the operation (left picture). The comparison of the experimental observed radii of the electron beam with the computer simulations.

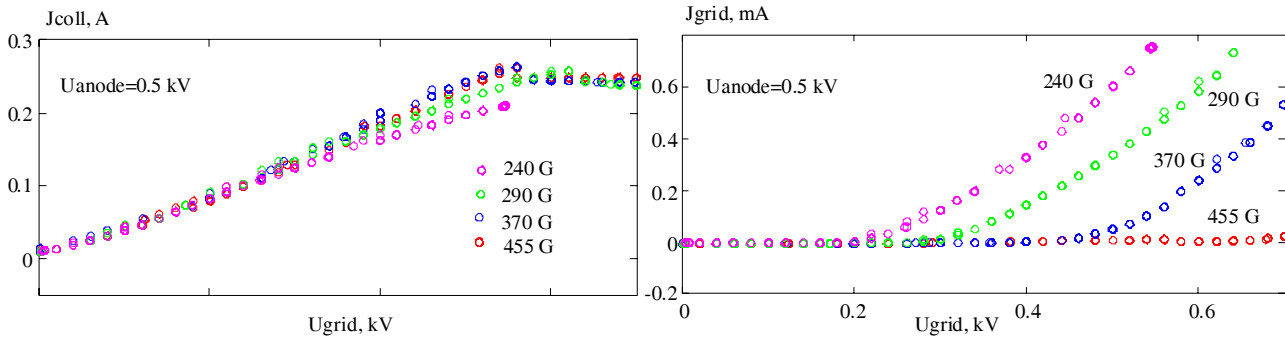


Figure 8: Electron current versus the grid voltage at the different values of the magnetic fields (left picture) and the leakage current to the grid voltage (right picture).

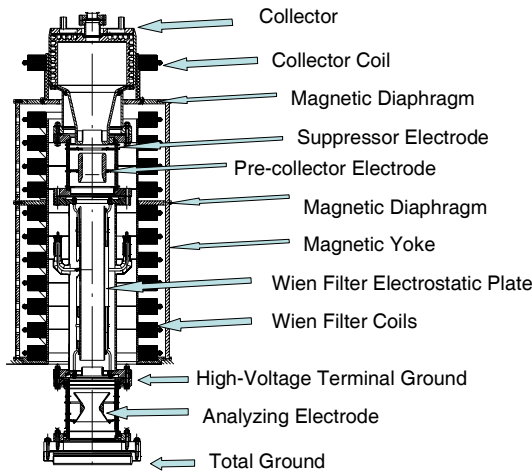


Figure 9: Collector design.

The typical curves the leakage currents from the current in the collector coil are shown in Fig. 10. The parameters of the electron gun and collector are  $J_{coll} = 220$  mA,  $U_{sup} = -0.2$  kV,  $U_{an} = 1.0$  kV,  $U_{grid} = 0.35$  kV,  $U_{precoll} = 0.5 \cdot U_{coll}$ . The effectiveness of the collector is  $6 \cdot 10^{-4}$ . The effectiveness of the system collector plus Wien filter is  $5 \cdot 10^{-6}$  in this regime.

The effectiveness of the collector can be improved by the adding bend of the magnetic field in the collector. The magnetic diaphragm of the collector is circle made from two half. One half can be removed and the magnetic field is strongly turned to the other part of the diaphragm (see Fig. 11). The result of the

measurements of the leakage current in the new system is shown in Fig. 12. One can see that the collector efficiency of the collector and filter is about  $5 \cdot 10^{-6}$  in the axial symmetric case. But the efficiency of the system with the magnetic bend is better than  $10^{-6}$ . The efficiency of the collector only isn't changed. This regime of the collector operation is closed to be proposed in [7].

The details of the experiments with collector system are described in [4].

### CASCADE TRANSFORMER

The key problem of the accelerating/decelerating column is transfer energy to 33 sections, gun and collectors are located at high voltage potential. The base idea of the power supply is based on idea of a high frequency cascaded resonant transformer. The system consists of 33 transformers with cascaded connection. The electrical energy is transmitted from section to section from the ground to high-voltage terminal. Along this way the energy is consumed by the regular high-voltage section. The main problem of such decision is leakage inductance of the transformers. They are connected in series and the voltage from power supply is divided between inductance leakage and a useful load. In order to solve this problem the special compensative capacitance is used. The impedance of leakage inductance is decreased significantly on the resonance frequency.

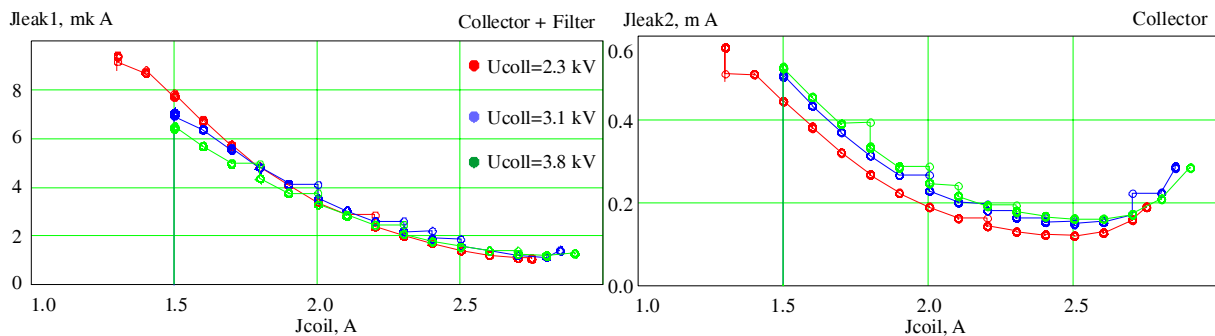


Figure 10: Leakage current from the system collector plus Wien filter (left picture) and the leakage current from the collector only versus the current in the collector coil.

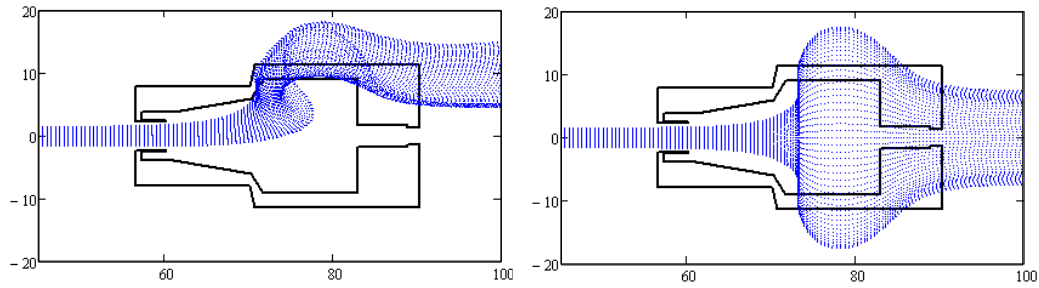


Figure 11: Distribution of the magnetic field in the collector configuration with bending field (left picture) and the collector configuration in the symmetrical case. The points are force lines of the magnetic field.

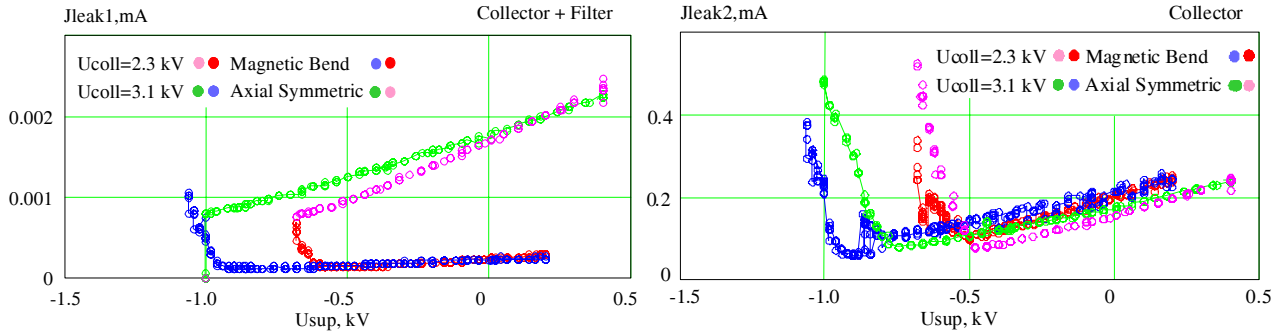


Figure 12: Leakage currents in the symmetrical configuration of the collector and with bend component of the magnetic field.

The figure shows the coefficient of the transfer of power as function of the generator frequency. The experiments is made on the complete transformer column containing 33 section. At the r.m.s. voltage 700 V from power supply of the cascade transformer the output power will be 20 kWt.

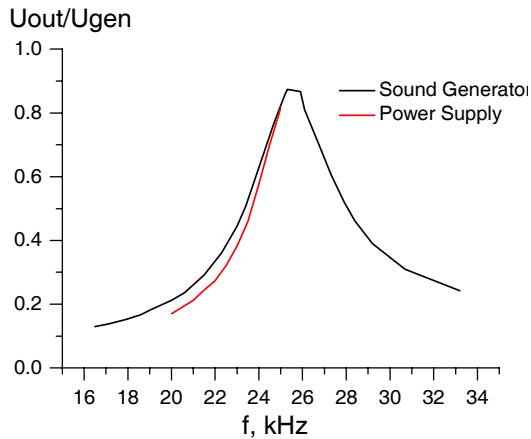


Figure 13: Coefficient of the energy transfer .of 33 sections of the cascade transformer. The load is 20 Ohm.

### CONCLUSION

The key problems of the electron cooler 2 MeV is experimentally verified in the different test-benches [3-5,8]. The strong surprises aren't observed and the elements of cooler are ready to continue assembly and commissioning.

### REFERENCES

- [1] L.R. Prosr et al, "Status of antiproton accumulation and cooling at FermiLab recycler", COOL'09, Lanzhou, China, Semptember 2009, MOM1MCIO01, p. 1; <http://www.JACoW.org>.
- [2] M.I. Bryzgunov et al, "Calculation of electron beam motion in electron cooling system for COSY", COOL'09, Lanzhou, China, Semptember 2009, THPMCP004, p. 134.
- [3] M. Bryzgunov, "Magnetic system of electron cooler for COSY", COOL'11, TUPS10, Alushta, Ukraine, September 2011, <http://www.JACoW.org>.
- [4] M.I. Bryzgunov et al, "Electron collector for 2 MeV electron coller for COSY", COOL'11, TUPS07, Alushta, Ukraine, September 2011.
- [5] M.I. Bryzgunov et al, "Electron gun with variable beam profile for COSY cooler", COOL'11, TUPS06, Alushta, Ukraine, September 2011.
- [6] V.B. Reva et al, "Conceptual Design Report Electron Cooler COSY 2 MEV", Novosibirsk 2009.
- [7] L.R. Prost, A. Shemyakin "Efficiency of the Fermilab electron cooler's collector", Proceedings of 2005 Particle Accelerator Conference, Knoxville, Tennessee, p.2387-2389.
- [8] V.N. Bocharov et al, "System of Measurement of magnetic field line straightness in solenoid of electron cooler for COSY", COOL'11, TUPS08, Alushta, Ukraine, September 2011.

# THE ADVANCE TECHNOLOGY EXTRACTION FOR THERAPY IONS BEAM FROM CARBON STORAGE RING WITH ELECTRON COOLING

V.V. Parkhomchuk, V.B. Reva, BINP, Novosibirsk 630090, Russia.

## Abstract

The electron cooling because of increasing the 6D phase space density of ion beams is the path for development compact accelerator ions beam therapy. The aperture magnets for the main synchrotron, the transport lines and the moveable ion gantry can be decreased very fundamentally. The systems for the extraction ions will operate with the smaller aperture and the low fields that improves reliability of dose control. The first experiments made at Landzow Institute of Modern Physics with cooling carbon beam on the energy 200 and 400 MeV/u increased enthusiasm of authors this report at these sort therapy systems.

## INTRODUCTION

At Institute Modern Physics the electron cooling systems was install at the main ring CSRm and at experimental ring CSRe. In the treatment phase the stripping injection of carbon beam with few repeated cycles accumulation by e-cooling (7 MeV/u) to insure the current and stability of slow-extracted carbon beam with energy range 150 to 250 MeV/u [1]. But using the electron cooling directly at the energy treatment will open high perspective for shrinking the ion beam diameters. The reasons connected with the space charge limitation of the intensive ion beam. The transverse beam emittance limited so called the tune shift at the range of values  $\delta\nu \leq 0.1 - 0.2$  as follow from equation:

$$\epsilon_{\perp} = \frac{r_i N_i g}{2\pi\delta\nu\beta^2\gamma^3}, \quad (1)$$

with the classical ion radius  $r_i = (Z_i e)^2 / M_i c^2$ , the relativistic quantities  $\beta, \gamma, g$  is the bunch factor or the ratio the peak current of the ion beam to average current. As was showed at many experiments the electron cooling [2,3] effectively cooled the ions beam up to this limits and increasing energy will inverse proportional decrease the ion beam emittance. The carbon beam on energy 7 MeV/u at the storage ring with betafunctor 20m and intensity  $N_i = 10^{10}$  have the ion beam diameter (for  $\delta\nu = 0.1$ ) 2 cm but on 400 MeV/u only 2 mm..

## ELECTRON COOLING RESULTS OF THE CARBON BEAM IN CSRE

For illustration we can used results the first electron cooling experiments with 400 MeV/u the carbon ion beam in CSRe. After injection from CSRm ring the ion beam cooled as show fig. 1 at the momentum spread.

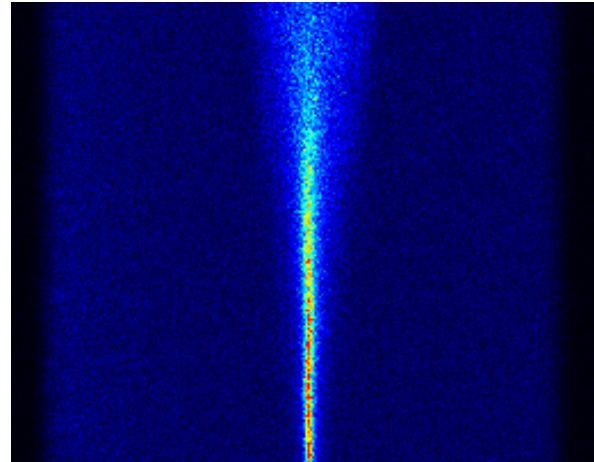


Fig. 1. The signal of Schottky signal after new injection.

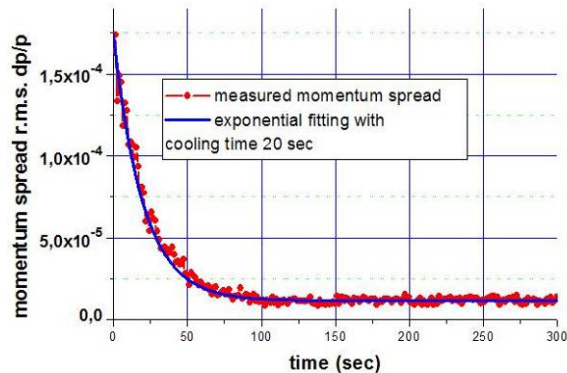


Fig. 2. The momentum spread at process electron cooling versus time.

The experiments with cooling the bunch beam (with RF on) demonstrated that the cooling was continued up to the compensations the RF field the own space charge field. At this case the longitudinal shape of the ion beam bunch are close to parabolic but the longitudinal potential well becomes very flat. There is correspond low synchrotron frequency for individual ions and the momentum spread demonstrated its self as the small tails near edges of the ion bunch. This phenomena was the subject of PD these dissertation S.Negaitsev many years ago. At this regime the momentum spread at many times less estimation from the bunch length according single particle oscillation at RF field. This phenomena's interesting for using at ion-ion colliders but increased problems for stochastic cooling the bunches beam.

The same shrinking the transverse the ion beam size was measured with scanning the ion beam aperture with moveable collimator.

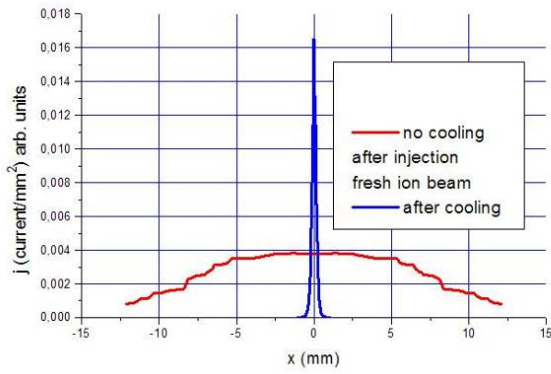


Fig. 3. The transverse profile of the carbon ion beam ( $700 \mu\text{A}$  ( $N_i = 0.44 \cdot 10^9$ )) measured at CSRe.

Before cooling r.m.s. radius ion beam is  $\sigma=8$  mm, after cooling  $\sigma=0.15$  mm, according equation 1 for this conditions tune shift is equal to  $\delta\nu = 0.08$ .

This experiments was made with electron beam current 0.75 A. Carefully extraction so cooled ion beam will help to have very precise irradiation dose control and the low aperture transport lines.

### 3-ORDER RESONANCE EXTRACTION WITH COOLING

The common use of slow resonant extraction from a synchrotron extends the beam spill time sufficiently to perform on-line dosimetry at the patient and to switch the ion beam on and off according to the dose required. Usually used the slow extraction ion beam system based on the third-integer resonance [2]. The present at the storage ring the local sextuple divided betatron phase space on the stable region with almost linear betatron oscillation, separatrice and zone with the spirals increasing amplitude zone as show fig. 4.

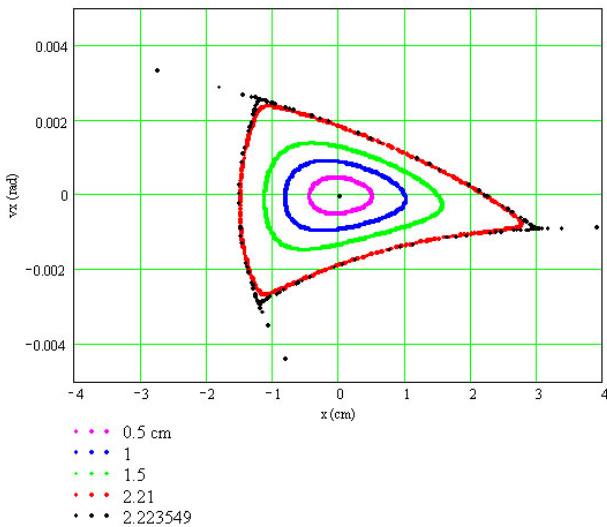


Fig. 4. The computer simulation the horizontal phase plane motion of ions for different initial amplitude with: tune  $\nu_x = 0.36$ , the sextupole value  $\delta = 2 \cdot 10^{-4} \text{ cm}^{-2}$  that introduce nonlinear additional focusing proportional  $1/F = \delta \cdot x$ .

Electron cooling

When the horizontal tune are moved slowly to 1/3 the separatice are go to the 0 amplitude and all the ions of the beam kick out the position electrostatic septum knife as demonstrated at figure 5.

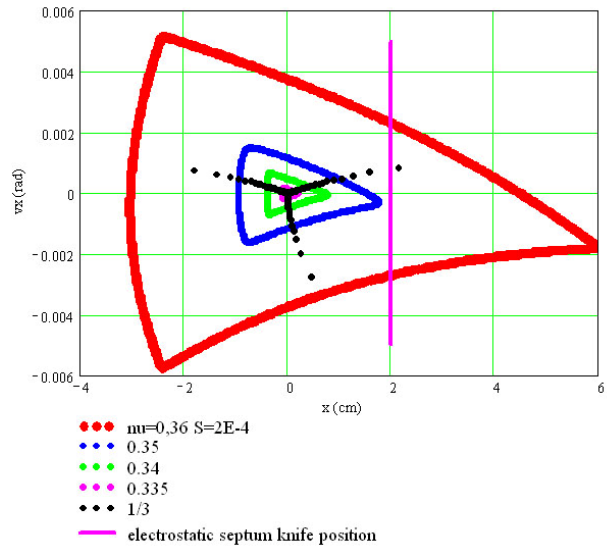


Fig. 5. The profile of separatrice for different horizontal tune.

The electron cooling shrink the ion beam at center of separatrice and for extraction we should have extremely small separatrice that decreased emittance extracted ion.

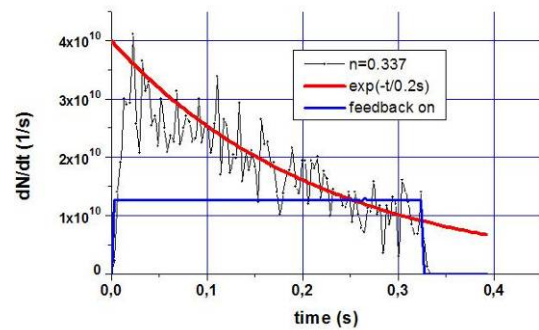


Fig. 6. The computer simulation the electron cooled carbon beam with constant tune and with the feedback for constant extract ion current by modulation the tune storage ion beam..

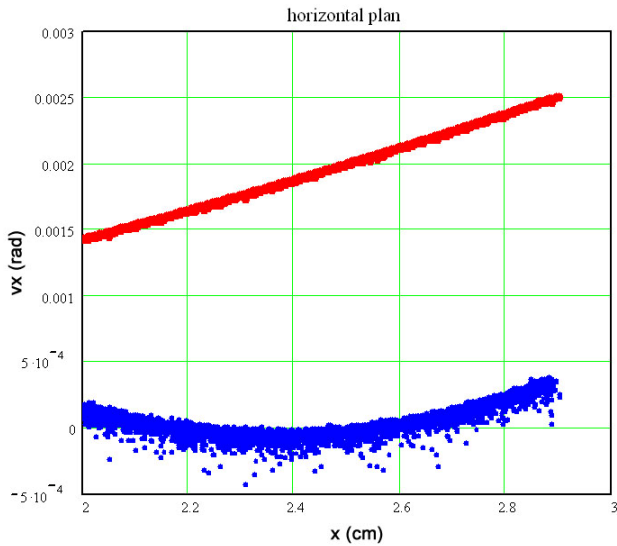


Fig. 7. The horizontal phase plane extracted ion beam. The blue points after pass the focusing lengths at extraction line (vertical scale increased at 10 times).

The emittance of extracted beam are:

$$\epsilon_x := \sqrt{x^2 \cdot vx^2 - vx^2 x^2} \quad \epsilon_x = 2.498 \times 10^{-6} \text{ cm}$$

$$\epsilon_y := \sqrt{y^2 \cdot vy^2 - vy^2 y^2} \quad \epsilon_y = 5.722 \times 10^{-6} \text{ cm}$$

So low ion beam emittance help to made low aperture line for ion beam. For example: interlock switcher for ion beam can have collimator slot with size 1 mm on distance 10 m and the electrostatic kicker with storage energy only  $10^{-6}$  J for 100% modulation intensity.

### SPLITTING THE ION BEAM AT MOMENTUM SPACE

The electron cooling effectively concentrated the ion beam at point of momentum space where the ion beam and electron beam have the same velocity.

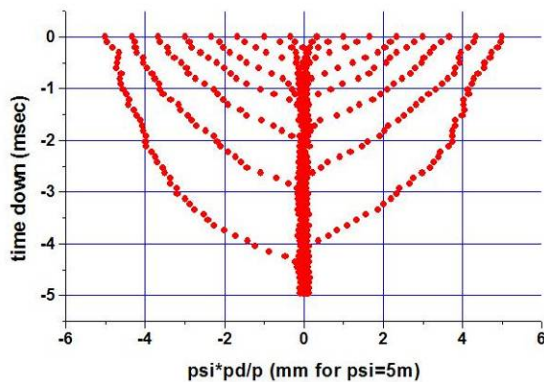


Fig. 8. The computer simulation of initially injected beam cooling (momentum): electron current 0.5 A, electron energy 16 kV, time range arrow is shown from up to down in milliseconds.

The presence of electron cooling in the synchrotron provides a small size and energy spread of the cooled beam thus enabling the realization of the original beam extraction scheme by small precisely dosed portions, the so-called pellet extraction. Electron cooling allows concentrating a portion of the ion beam in a given place of the phase space and then getting the ion beam low density in the neighboring regions for decreasing the “tails” of the distribution and losses at the extraction septum. The operation scheme is the following. Upon the ion beam acceleration up to the required energy, RF voltage is off and the beam is de-bunched. In the period of 50-200 ms (depending on the extraction energy) the beam is cooled down to the relevant equilibrium state. Then the beam is prepared for its extraction, for example, by scanning the electron beam energy with respect to the mean energy of the ion beam we produce the flat distribution of ions with  $\Delta p/p = \pm 2 \div 2.5 \cdot 10^{-3}$ . Then it is necessary to separate a portion of particles with energy deviation from the main beam. The portion intensity should be controlled in the range of  $N = 10^6 \div 10^7$  particles. The neighbouring ions are concentrated under the friction force action. The intensity of obtained portion is controlled by the time of storage and de-tuning of the electron beam energy from the distribution edge. By placing the kicker at the azimuth of the ion orbit where the dispersion is sufficient to separate the main beam from the portion the single turn extraction of the portion is realized. It is clear that ions concentrate in a portion but close to the storage portion region there are many ions nearing the ion cooling region, which will be bombarded the septum knife. In order to improve the extraction efficiency, it is necessary to clean the septum knife region. One of simplest solutions is to use the betatron core for accelerating the ion beam and “separating” the main beam from the region where the beam is prepared for its extraction. The magnet field in the core slowly increases so that the energy of the ion beam also increases on every turn moving the beam aside the septum. In this case, the maximum electron cooling force should be sufficient for the confinement and cooling the ions in the extraction region (Fig.9). It is seen that the main beam is moving away from the storage region and the left side portion is concentrated in the extraction area. Such an ion energy swiping accelerates noticeably the beam preparation for its extraction and cleans the “knife” region from the lost particles.

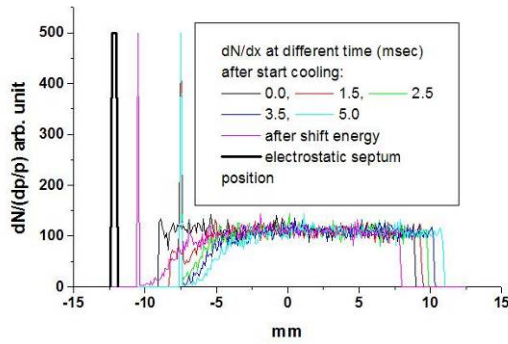


Fig. 9. The 5 msec cycle of carbon ions extraction with electron cooling.

Upon completion of the extracted portion storage and cooling, the betatron core exchanges polarity rapidly enough and the stored portion is rapidly moving to the kicker and the main beam distribution tail returns again in the cooling region for storing a new portion. In the scheme of using swiping, the extraction efficiency is much higher for the system repetition frequency up to 500 Hz. In the region of 1-2 kHz, the losses are still high 20-30 % for the septum knife with thickness 0.5 mm.

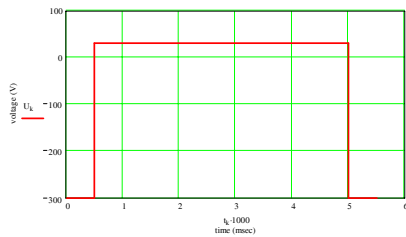


Fig. 10. The voltage on betatron core versus time at cycle.

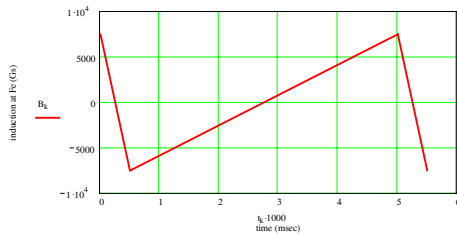


Fig. 11. The voltage on betatron core versus time at cycle.

For the beam extraction the fast kicker, electrostatic septum and permanent septum of the Lambertson type are used. Since the dispersion function at the kicker azimuth and electrostatic septum has the maximum value of 4.3 m, the main beam orbit and portions are separated by  $\Delta X \approx 10$  mm. After kick, the portion reaches the electrostatic septum aperture and acquiring an additional deflection along radius reaching the aperture of the Lambertson-type septum magnet, by which it is extracted vertically at the angle  $\varphi_s = 13.5^\circ$  with respect to the equilibrium orbit. The beam deflection angle corresponds to the  $\Delta X = 10$  mm beam drop to the electrostatic septum aperture and,

correspondingly, the electrostatic septum drops the beam into the septum magnet at the value of  $\Delta X = 14$  mm. The kicker kicks the beam by purely electric field and has the pulse duration of 80 ns with the fronts about 10 ns by order of magnitude. The presence of the cut in the inner plate causes the stray field and field non-uniformity inside the kicker aperture. With the separation of orbits by 10 mm, the main beam perturbation is  $\Delta\varphi \leq 5 \cdot 10^{-6}$ .

Fig. 12 shows the 10 cycles of extraction when main beam during each 200 Hz cycles linearly moved to right and just before extraction jumped to the left (the time of the magnetic field polarity exchange). Slow moving to the left is connected with action of the cooling force which shifts the main beam to extraction zone.

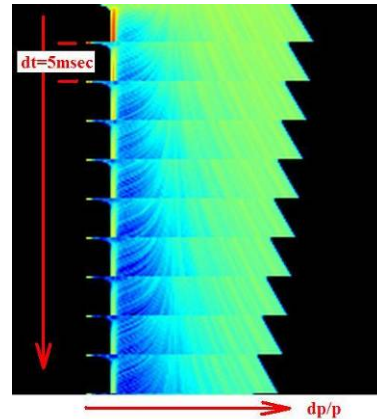


Fig. 12. The computer simulation of 10 cycles of extraction with period 5 msec (full time 50 msec.), initial momentum spread  $\Delta p/p = \pm 0.001$ .

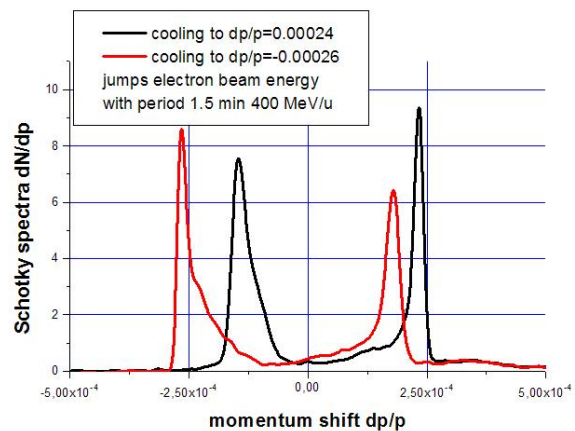


Fig. 13. CSRe momentum spectra of 400 MeV/u carbon beam after procedure of cyclic jump the electron beam energy.

The experiments with splitting the ion beam at CSRe ring was made at 2009 for prove the idea of this sort extraction by manipulation of the electron beam energy (fig.13). Practically its correspond existing the two electron beam with different energy, and the ion beam can be distributed

to the each momentums by changing duty factor for each energy of electron beam.

## SLOW EXTRACTION BY RECOMBINATION

The project of the storage ring for the cancer therapy proposed by BINP team proposes using recombination reaction  $C^{+6}+e^{-}\rightarrow C^{+5}$  for the extraction of the ion beam. The charge states  $C^{+6}$  and  $C^{+5}$  have difference 20% in momentum, so it is possible to organize the strong shift between primary and extracted beam by the proper choice of the dispersion with very low ion density in the gap between these two orbits. So, the flow of the particles on the septum elements can be low according the extraction scheme. It leads to small leakage of the particles during extraction and liberalizes the requirement to the power supply of the storage ring because the ripple of the magnetic field doesn't produce the interference of the primary and extraction beam in the space. The ion beam after cooling on high energy 100-400 MeV/u have very small diameter (see Fig.6) and after recombination diameter extracted beam will be small. For example, fig. 14 show photo of nuclear emulsion after exposition at hydrogen beam on distance 10 m from the electron cooler NAP-M.



Fig. 14. The first photo of hydrogen atoms beam after recombination at NAP-M cooler [6], distance between mark points 1 mm.

The recombination coefficient is proportional to electron density. This enables to operate by the dose of the extraction beam. The electron gun as an electron tube can modulate the electron current in the megahertz frequency range. This frequency is certainly enough for any regime of the tumor scanning. The presence of the diagnostic of the extraction dose enables to have a feedback for the stabilization dose in the tumor. Moreover the recombination extraction is more safety because it is very difficult to have breakdown extraction of all stored ion beam during very short time. Protection system can quickly switch off the electron current and stop the

extraction. The main disadvantage of the recombination extraction is relatively small rate of the extraction namely  $10^7$  /s at the number of the ions in the storage ring  $10^{10}$  and the electron density  $10^8$  1/cm<sup>3</sup> in the cooling section. But this value is enough for the treatment of the small cancer tumor. For example, the tumor with diameter 30 mm should be irradiated ions those have the rest kinetic energy near 50 MeV/u. For accumulation doze of 5 Gy with ion flux  $10^7$  /s required exposition time is near 1 min.

## CONCLUSION

The carbon ion beam system is based on a few approved key innovations historically came from BINP (Novosibirsk) such as: electron cooling, using negative ions for stripping injection, storage rings. Electron cooling helps to make operation of the system easier by decreasing the beam emittance which results in stable ions energy and easy extraction. Example of CSRm operation shows that electron cooler can stable operates many months without switching off.

## ACKNOWLEDGMENTS

This report is only small part of BINP team work for development of the carbon ion treatment accelerator system. Authors are gratefully acknowledged IMP accelerator team in the person X.D. Yang for possibility made experiments at CSRe storage ring.

## REFERENCES

- [1] The clinical facility in Heidelberg [http://www.gsi.de/portrait/Broschueren/Therapie/Klinikanlage\\_e.html](http://www.gsi.de/portrait/Broschueren/Therapie/Klinikanlage_e.html)
- [2] K. Noda, S. Shibuya, ... NIM and Methods in Physics Research A 532 (2004) 129-136. COOL-03.
- [3] J.Beebe-Wang, F.A Dilmanian, S.Peggs, D.J. Schlyer, P. Vaska, "Feasibility of Positron Emission Tomography of Dose Distribution in Proton Beam Cabcer Therapy". Proceeding of EPAC 2002, p. 2721-2723 (2002).
- [4] J.Beebe-Wang, S. Peggs, L. Smith, "Dependence of the Production Yields of Positron Emitters in Proton Therapy on the Cross Section Data Variations", preprint C-A/AP/#109, Sep. 2003, BNL.
- [5] Radiation therapy facility based on carbon ion cooler synchrotron. V. Kiselev, V. Vostrikov, S. Konstantinov, G. Kurkin, E. Levichev, V. Parkhomchuk , Yu. Pupkov, V. Reva, R. Salimov, A. Semenov, S. Sinyatkin, A. Skrinsky, Proceeding RuPAC08 <http://cern.ch/AccelConf/r08/papers/THBAU01.pdf>
- [6] G.I. Budker, A.N.Skrinsky Electron cooling and new perspective at physic of particles, UFN, 1978, 124, #4, p.561

# RADIATIVE RECOMBINATION OF HEAVY BARE NUCLEI AND IONS IN ELECTRON COOLING SYSTEM

A.V. Philippov<sup>#</sup>, A.B. Kuznetsov, I.N. Meshkov  
Joint Institute for Nuclear Research, Dubna, Russia

## Abstract

An overview of experimental data of radiative recombination (RR) rate of nuclei (from helium to uranium) and various intermediate charge states of ions in electron coolers is presented at the report.

The fit of RR rates energy dependence the electron energy shift is found (formula (1) below). This dependence is significantly different from that one presented in theoretical works of H. Kramers and R. Schuch. It was found also the dependence of bare nuclei RR rates on transverse temperature as  $T_{\perp}^{-0.95}$  that differs with theoretical result obtained by M. Bell and J. Bell.

Analysis of the experimental data for cooled heavy ions in intermediate charge state shows a RR critical dependence on the ion charge state (electron configuration of ion shells). Particularly, for some charge states RR rate increases essentially having a resonant character.

The estimations of RR rate losses of the  $\text{Au}^{32+}$ ,  $\text{Au}^{33+}$ ,  $\text{Au}^{50+}$ ,  $\text{Au}^{51+}$  ion beams in the electron cooler of the Booster is presented. The limitation of  $\text{Au}^{79+}$  ions lifetime by RR process in the electron cooler of the Collider NICA is analyzed and measures of its increasing are considered.

## INTRODUCTION

Application of the electron cooling of heavy ions to the Booster and the Collider of the NICA accelerator facility is necessary to obtain the project luminosity [1]. However, according to the theoretical models [2]-[4] RR can significantly affect the beam losses in the Booster and the Collider NICA. Therefore an experimental verification of theoretical formulae validity is of a great importance. Such a verification has been performed on the basis of the experimental works results [5]-[16].

## THE BARE NUCLEI EXPERIMENTAL DATA ANALYSIS

The experimental data of RR rate dependence on the electron energy shift  $\Delta E$  (relatively to optimal electron energy value) in different electron coolers for different nuclei  $\text{U}^{92+}$  [5],  $\text{Bi}^{83+}$  [6],  $\text{Ar}^{18+}$  [7],  $\text{Cl}^{17+}$  [8],  $\text{Si}^{14+}$  [9],  $\text{Ne}^{10+}$  [10],  $\text{N}^{7+}$  [9],  $\text{C}^{6+}$  [11] and  $\text{He}^{2+}$  [9] can be fitted (Fig. 1 a, b) with the following formula:

$$\nu_{Z \rightarrow Z-1}^{\text{Fitted}}(\Delta E) = a_1 \cdot Z^2 \cdot \left( \frac{\Delta E + b_1}{\text{Ry}} \right)^{-3/8}. \quad (1)$$

Here  $\nu_{Z \rightarrow Z-1}^{\text{Fitted}}(\Delta E)$  is RR rate fit in  $\text{cm}^3/\text{s}$ ;  $\Delta E$  is electron energy shift from its optimal value in the particle rest frame (PRF);  $a_1 = 2.8 \cdot 10^{-13} \text{ cm}^3/\text{s}$  and  $b_1 = 2 \cdot 10^{-4} \text{ eV}$  are the fit parameters;  $\text{Ry} = 13.6 \text{ eV}$  is the Rydberg constant. In all figures below the fit is shown with black dot line.

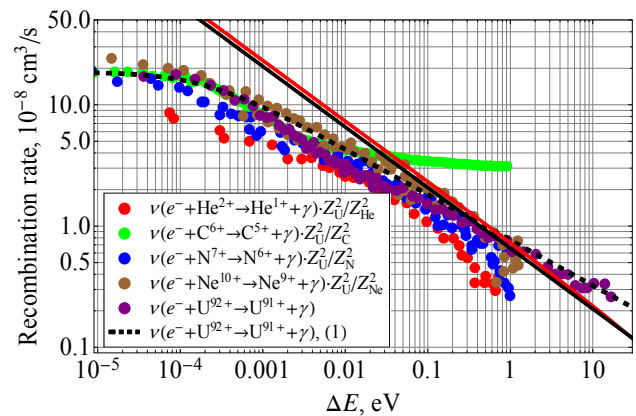


Figure 1 a. Experimental values of RR rates in  $10^{-8} \text{ cm}^3/\text{s}$  for bare nuclei:  $\text{U}^{92+}$  [5],  $\text{Ne}^{10+}$  [10],  $\text{N}^{7+}$  [9],  $\text{C}^{6+}$  [11] and  $\text{He}^{2+}$  [9] (in dots) and theoretical dependences by Kramers [2] (red line) and Schuch [3] (black line); the black dot line is the fit with formula (1).

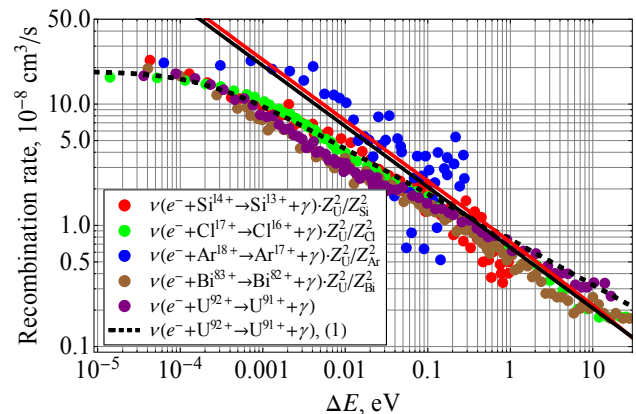


Figure 1 b. Experimental RR rates in  $10^{-8} \text{ cm}^3/\text{s}$  of bare nuclei  $\text{U}^{92+}$  [5],  $\text{Bi}^{83+}$  [6],  $\text{Ar}^{18+}$  [7],  $\text{Cl}^{17+}$  [8] and  $\text{Si}^{14+}$  [9] (in dots) and theoretical dependences by Kramers [2] (red line) and Schuch [3] (black line); the black dot line is the fit with formula (1).

<sup>#</sup> [philippov@jinr.ru](mailto:philippov@jinr.ru)

Note that in Ref. [5]-[11], the RR rates are given for energy shift in the Laboratory RF:  $\Delta E_{\text{lab}} = \gamma_Z \Delta E$ , where  $\gamma_Z$  is the Lorentz factor.

The experimental results shown in Fig. 1 were recalculated to common scales: ordinate values by multiplying with ratio of  $Z_{\text{nuc}}^2 / Z_U^2$ , abscissa as  $\Delta E = \Delta E_{\text{lab}} / \gamma_Z$ . As the data in Fig. 1 a, b show, the normalized experimental results for most of the nuclei in the whole  $\Delta E$  range are well described by the approximating formula (1) (taking into account the coefficient  $Z_{\text{nuc}}^2 / Z_U^2$ ).

The  $C^{6+}$  nucleus RR rate (Fig. 1 a, green dots) is also well described by formula (1) at  $\Delta E < 0.01$  eV, but differs significantly at  $\Delta E > 0.01$  eV. Similar deviation takes place for  $Ar^{18+}$ . However, both experimental results have been obtained with rather poor accuracy.

In Fig. 1 a, b the calculations based on the Kramers [2] and Schuch [3] formulae for  $n_{\text{max}} = Z_U$  are shown also. One can see their significant disagreement experimental data.

Consequently, we can assume that the dependence (1) applicable to other heavy nuclei.

In Ref. [5], [6] the dependence of the RR rate of the  $U^{92+}$  and  $Bi^{83+}$  nuclei on the longitudinal magnetic field value in the cooling system is presented (Fig. 2). As can be seen from this figure, the magnitude of this dependence is mostly manifested at  $\Delta E < 0.1$  eV.

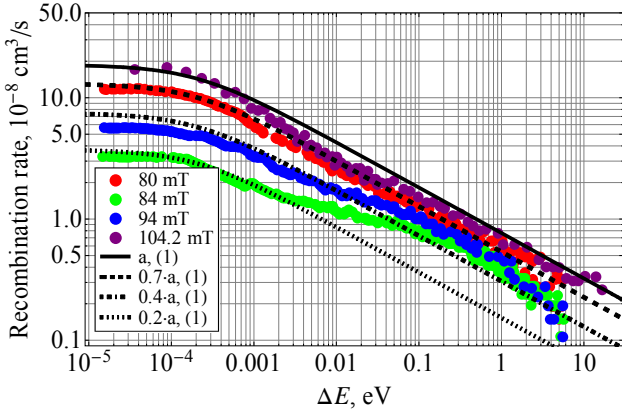


Figure 2: RR rates in  $10^{-8} \text{ cm}^3/\text{s}$  of  $U^{92+}$  depending of  $DE$  measured at four different magnetic guiding field values [5].

Most probably this effect is related to the electron beam quality that varies with fine tuning of the magnetic field (“the resonant optics effect”).

## ANALYSIS OF THE EXPERIMENTAL DATA FOR IONS IN INTERMEDIATE CHARGE STATE

The RR rate vs. electron energy shift  $\Delta E$  measured for ion  $U^{28+}$  ( $[Xe]6s^2 4f^7 5d^1$ ) [12] and the fit with formula (1) are presented see Fig. 3. One can see a perfect agreement the experimental data and the fit. One should note this ion has “solitary” electron in the shell  $5d$ .

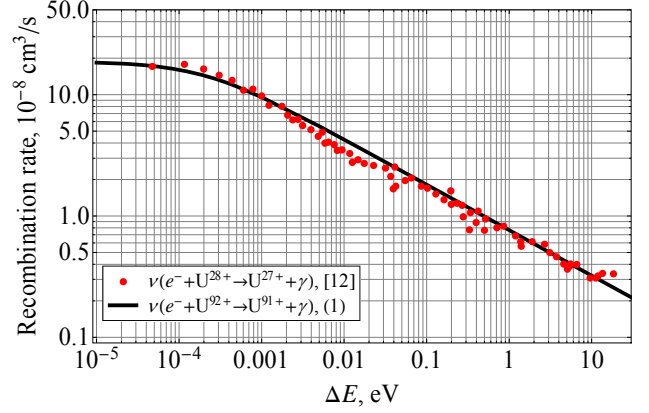


Figure 3: Experimental RR rate in  $10^{-8} \text{ cm}^3/\text{s}$  of  $U^{28+}$  ions (dots) [12] and fit with formula (1) (solid line).

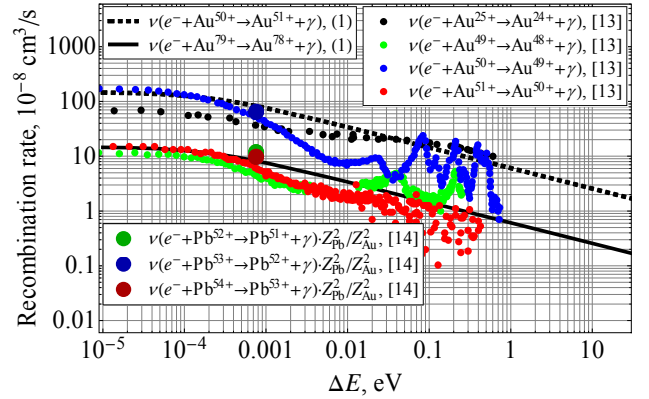


Figure 4: Dependence of experimental RR rates of intermediate charge state of  $Au^{25+}$ ,  $Au^{49+}$ ,  $Au^{50+}$ ,  $Au^{51+}$  ions [13],  $Pb^{51+}$ ,  $Pb^{52+}$  and  $Pb^{53+}$  ions [14] on electron energy shift (colored points) fitted with formula (1) for  $Au^{79+}$  nuclei black dots and solid curves).

Moreover in Fig. 4, one can see there two pronounced levels of RR rates which differ by one order of magnitude practically. The higher level to the ions having one missing electron in outer shell.

Note that the configuration of the electron shells are similar for pairs of ions:  $Au^{51+}$  and  $Pb^{54+}$  are  $[Ar]4s^2 3d^8$ ,  $Au^{50+}$  and  $Pb^{53+}$  are  $[Ar]4s^1 3d^{10}$ ,  $Au^{49+}$  and  $Pb^{52+}$  are  $[Ar]4s^2 3d^{10}$ ,  $Au^{48+}$  and  $Pb^{51+}$  are  $[Ar]4s^2 3d^{10} 4p^1$ . The RR rates for these ion pairs have close values (Fig. 4). As we understand these data in Fig. 5 were taken at optimal cooling conditions when  $\Delta E \sim 1$  meV.

The same peculiarity can be seen in the experimental dependence of the RR rates of different ions on the number of electrons in the ion shells (Fig. 5).

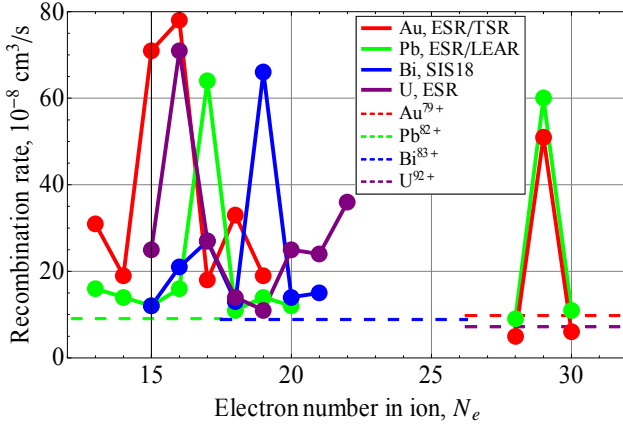


Figure 5: Experimental RR rates in  $10^{-8} \text{ cm}^3/\text{s}$  of intermediate charge state of gold [13], [15], lead [14], bismuth [15] and uranium ions [15]. The horizontal dashed lines correspond to the bare nuclei RR rates of the same ions (not scaled by  $Z_{\text{nucl}}^2/Z_U^2$ ).

As one can see, the majority of ions RR rates are close to those ones of the corresponding bare nuclei. However, for some ions the RR rates are larger by almost one order of magnitude higher than the RR rate of the corresponding nuclei. That looks like a resonance capture for ions which have one missing electron in outer shell see  $\text{Au}^{50+}$  ( $N_e=29$ ),  $\text{Pb}^{53+}$  ( $N_e=29$ ). The same situation we have for  $\text{Bi}^{64+}$  ( $N_e=19$ ) and  $\text{Pb}^{65+}$  ( $N_e=17$ ). However there are exceptions of such a simple model:  $N_e=19$  for  $\text{Au}^{60+}$ ,  $\text{Pb}^{63+}$ ,  $\text{U}^{73+}$  and  $N_e=17$  for  $\text{Au}^{62+}$ ,  $\text{U}^{75+}$ ,  $\text{Bi}^{66+}$ .

### RADIATIVE RECOMBINATION RATE DEPENDENCES ON TRANSVERSE TEMPERATURE (ESR EXPERIMENT)

The RR rate dependence on electron transverse temperature has been studied in the ESR experiment [16] for  $\text{U}^{92+}$  nuclei at energy of 400 MeV/u. The electron transverse velocity was varied with application of transverse electric field. The experimental data analysis show that initial electron gun cathode temperature was less than 0.1 eV. Approximation dependence of experimental data (Fig. 6) on electron transverse temperature  $T_{\perp}$  (average kinetic energy of electrons in crossed fields) can be fitted with the following formula:

$$\tau_{\text{ESR}}^{\text{Fitted}} = a_2 \left( \frac{T_{\perp}}{\text{Ry}} \right)^{b_2}, \quad (2)$$

$$\tau_{\text{NICA}}^{\text{RR}} = \left( \frac{\gamma_{\text{NICA}} Z_{\text{Au}}}{\gamma_{\text{ESR}} Z_{\text{U}}} \right)^2 \frac{\eta_{\text{ESR}} n_{e,\text{ESR}}}{\eta_{\text{NICA}} n_{e,\text{NICA}}} \tau_{\text{ESR}}^{\text{Fitted}}.$$

Here fit parameters are  $a_2=3 \cdot 10^4 \text{ s}$ ,  $b_2=0.95$ ;  $\gamma_{\text{ESR}}=1.43$  is Lorentz factor of uranium nuclei at 400 MeV/u;  $\tau_{\text{NICA}}^{\text{RR}}$  and  $\tau_{\text{ESR}}^{\text{Fitted}}$  are RR time in seconds. The second formula in (2) has to be applied for lifetime estimation in a cooler ring (e.g.  $\text{Au}^{79+}$  in Collider NICA).

Electron cooling

50

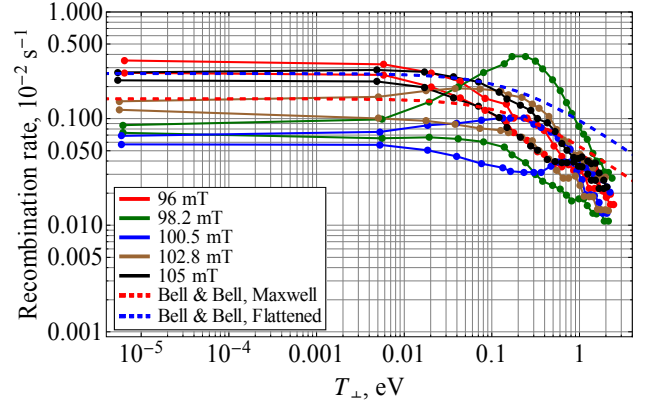


Figure 6: RR rates of  $\text{U}^{92+}$  nucleus vs. transverse electron temperature  $T_{\perp}$  ESR experiment [16].

### ESTIMATION OF IONS LOSSES IN BOOSTER AND NUCLEI LIFETIME IN COLLIDER NICA

The definition of the RR time  $\tau_{q \rightarrow q-1}^{\text{RR}}$  is as follows:

$$\tau_{q \rightarrow q-1}^{\text{RR}} = \frac{\gamma^2}{v_{q \rightarrow q-1}^{\text{RR}} n_e \eta_c}. \quad (3)$$

Here  $\eta_c$  is ratio of the cooling section length to the ring circumference;  $n_e$  is electron beam density in LRF;  $\gamma$  is Lorentz factor; the  $v_{q \rightarrow q-1}^{\text{RR}}$  values are defined by formula (1).

Table 1: Parameters of electron cooling systems of the Booster and the Collider NICA.

	Booster	Collider NICA
Ion energy, GeV/u	0.1	1÷4.5
Electron beam radius, cm	2.5	1
Electron beam current, A	≤1.0	≤0.5
$\eta_c$	0.014	0.012

Two options of ions accelerated in the Booster are considered presently:  $\text{Au}^{33+}$  and  $\text{Au}^{51+}$ . The electron cooling is designed to be applied at the ion energy of 100 MeV/u during acceleration up to energy of 600 MeV/u on a plateau of 1 s duration. Electron cooling of nuclei  $\text{Au}^{79+}$  in the Collider NICA will be used in ion energy range of 1÷4.5 GeV/u (Table 1).

According Fig. 4 and formulae (3), (1) the estimation of RR losses in Booster for gold ions  $\text{Au}^{33+}$  and  $\text{Au}^{51+}$  less than 2% in all  $\Delta E$  range. For  $\text{Au}^{32+}$  and  $\text{Au}^{50+}$  we have the same losses but for  $\Delta E > 0.1 \text{ eV}$ .

The estimation of beam lifetime of  $\text{Au}^{79+}$  nuclei in Collider NICA based on analysis results (formulae (3) and (2)) have been produced (Fig. 7, 8).

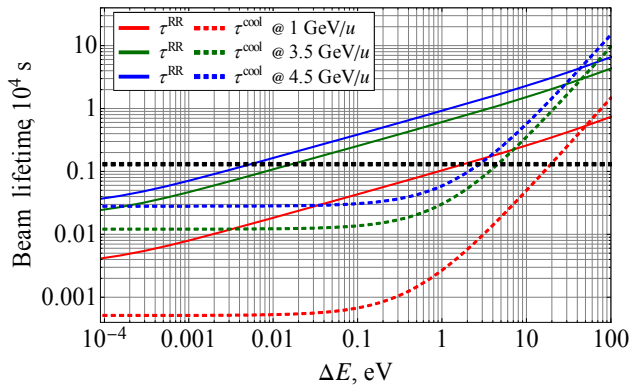


Figure 7: Beam lifetime of Au<sup>79+</sup> nuclei in Collider NICA vs. electron energy shift  $\Delta E$  for different cooling energy. Dashed black line represents to the intrabeam scattering (IBS) time  $\tau_{IBS}=1300$  s.

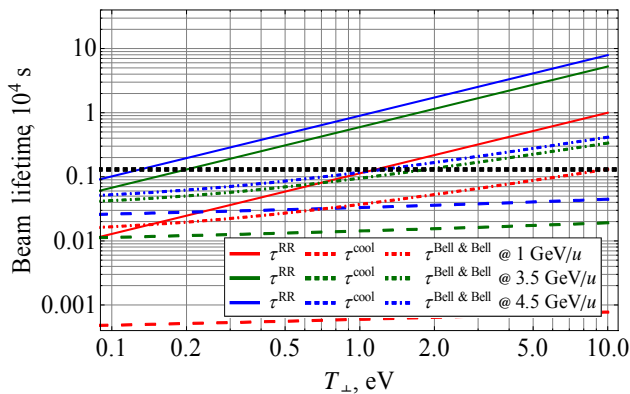


Figure 8: Beam lifetime of Au<sup>79+</sup> nuclei in Collider NICA vs. transverse temperature  $T_{\perp}$  for different values of ion energy. Dashed black line represents to the intrabeam scattering (IBS) time  $\tau_{IBS}=1300$  s.

In Fig. 7, 8 the corresponding cooling time  $\tau^{cool}$  was calculated using "Parkhomchuk formula" [17]. The gold bare nucleus lifetime values according to the M. Bell and J. Bell [4] formula is also shown in Fig. 8 differ significantly with experimental fit.

### CONCLUSION

Energy dependence of the RR rate of bare nuclei is scaled as  $\Delta E^{-3/8}$  (1). At  $\Delta E=0$  the RR rate dependence on transverse temperature scaled as  $T_{\perp}^{-0.95}$  (see inverse formula (2)) that differs with theoretical result obtained by M. Bell and J. Bell.

The RR rates for some ions in an intermediate charge state have resonance character. In order to avoid a large RR rates of such ions one has to choose ions with completed electron shell configuration either having even number of electron in outer shell.

The beam lifetime of gold bare nuclei in cooling system can be increased by two methods: with introduction of optimal electron energy shift  $\Delta E$ , and either with artificial

Electron cooling

increase of the electron transverse temperature  $T_{\perp}$ . The second method is more preferable because its influence is more significant.

### ACKNOWLEDGMENT

The authors thank A.O. Sidorenko for his interest and valuable remarks.

### REFERENCES

- [1] I.N. Meshkov et al. Status of NICA Project These Proceedings. MOIO02.
- [2] H.A. Kramers. Phil. Mag. V. 46. 1923. P. 836.
- [3] M. Pajek and R. Schuch. Phys. Rev. A. V. 45. N. 11. 1992. P. 7894-7905.
- [4] M. Bell and J.S. Bell. Particle Accelerators. 1982. V. 12. P. 49-52. (and references therein for table).
- [5] W. Shi et al. Euro. Phys. J. D. 15. 2001. P. 145-154.
- [6] A. Hoffknecht et al. Phys. Rev. A. 2000. V. 63. 012702.
- [7] O. Uwira et al. Hyperfine Interaction. 1997. V. 108. P. 167-175.
- [8] A. Hoffknecht et al. Phys. Scr. 2001. V. T92. P. 402-405.
- [9] W. Spies et al. Hyperfine Interactions. 1998. V. 114. P. 237-243.
- [10] R. Schuch et al. Acta Physica Polonica B. 1996. V. 27. N. 1-2. P. 307-322.
- [11] L. Andersen et al. Phys. Rev. Lett. 1990. V. 64. P. 729-732.
- [12] A. Müller et al. Phys. Scr. 1991. V. T37. P. 62-65.
- [13] A. Wolf et al. NIMA. 2000. V. 441. P. 183-190. / A. Hoffknecht et al. HYINT. 1998. V. 114. P. 257-261.
- [14] S. Baird et al. Phys. Lett. B. V. 361. Iss. 1-4. 1995. P. 184-186.
- [15] I. Meshkov. Ion Recombination in Electron Coolers. Working meeting. 14 March 2011. CERN. Geneva. Private communication.
- [16] P. Beller et al. NIM A. 2004. V. 532. P. 427-432.
- [17] V.V. Parkhomchuk, A.N. Skriskii. Phys. Usp. 2000. V. 43. Num. 5. P. 433-452.

# NUMERICAL INVESTIGATION OF STOCHASTIC COOLING AT NICA COLLIDER

T. Katayama, GSI, Darmstadt, Germany  
I. Meshkov and G. Trubnikov, JINR, Dubna, Russia.

## Abstract

At the heavy ion collider NICA promoted at the Dubna, JINR, the stochastic cooling will play the crucial roles to manipulate the beam. The primary goal is to prevent the IBS diffusion effects to keep the high luminosity during the experimental cycle. The other purpose is to accumulate the beam intensity up to several times  $1e10$  from the injector Nuclotron with use of barrier bucket method. With this method, the short bunch formation is not necessary in the Nuclotron, and is transferred to the collider as a long bunch condition. After the BB accumulation the coasting beam is adiabatically bunched with the help of RF field and the stochastic cooling. In the present paper the detailed simulation results are presented for the above three process mainly longitudinal freedom.

## INTRODUCTION

The low energy heavy ion collider is proposed at the JINR which aims to achieve the 1-4.5 GeV/u (kinetic energy) gold beam head-on collision with the luminosity  $1e27/cm^2/sec$ . [1] The number of bunches in the collider is  $\sim 24$  and each bunch should contain the ion number of  $\sim 5e9/bunch$ , depending upon the operation energy. Thus totally around  $1e11$  ions should be accumulated in the collider ring. The injector for the collider is planned to use the existing superconducting heavy ion synchrotron, Nuclotron which provides the beam 1-4.5 GeV/u with the intensity of  $1e8-1e9/cycle$ , the cycle time of 10 sec. The bunch length of the beam from the Nuclotron is around  $1/3$  of the circumference, 300 nsec. [2]

The main task of the beam cooling is to realize the beam parameters required for the experiment, beam accumulation and the short bunch formation and keep their qualities during the experimental cycle.

In the present scenario, the beam is transferred to the collider without the manipulation of short bunch formation in the Nuclotron which allows us much easier operation of the Nuclotron. The long bunch beam is transferred in the longitudinal injection area which is provided by the barrier voltages, and is accumulated with the assistance of stochastic cooling, for low energy operation, say below 2 GeV/u, the electron cooling will be used.

Thus accumulated high intensity heavy ion beam in the collider is the coasting beam condition, and then the large voltage RF field is applied adiabatically as well as the stochastic cooling. The beam is gradually bunched to the required rms bunch length for the collision experiment, 2ns (rms). The bunch length is the equilibrium condition of the RF field, stochastic cooling force and the Intra Beam Scattering (IBS) force.

In the present simulation work, the RF field (barrier or normal RF), IBS heating effects and the cooling force are taken into account. The space charge repulsion force is not included which might be significant effects at the low energy, high intensity and short bunch condition. This subject will be treated in the future work.

Table 1 Basic parameters of NICA collider

Ion species	197Au79+	Transverse Emittance	1.0 Pi mm.mrad
Operation energy	1-4.5 GeV/u	Momentum spread	1.0-1.5e-3
Circumference	503.04 m	Beat function at colliding point	0.35 m
Number of ions/bunch	$3e8-5e9$	Expected luminosity	$3e27/cm^2/sec$
Number of bunch/ring	24	Bunch length (rms)	0.6 m
Injector	Nuclotron	Injected intensity	$1e9/cycle$
Emittance	0.5 Pi mm.mrad	Momentum spread (rms)	$3e-4$
Bunch length	300 nsec		

## LATTICE AND IBS GROWTH RATE

The Intra Beam Scattering (IBS) effects are critical diffusion factor for the low energy high charge state ion collider. The growth rate is numerically calculated with use of the formula by Martini including the lattice function in Fig. 1. The lattice structure is the race-track shape with two long straight sections for the colliding experiments and the arc section, basically being composed of the FODO structure. The IBS growth rate can be analytically obtained for the high energy, much higher than the transition energy, and for the lattice structure with only normal lattice. The present lattice is a complicated structure and the IBS growth rate has to be numerically analyzed.

The bunched beam IBS growth rates of the energy 4.5 GeV/u with  $6e9/bunch$  and 1 GeV/u with  $3e8/bunch$  are given in Fig. 2. The typical growth rates for 4.5 GeV/u are  $3.65e-3$  (momentum spread),  $4.86e-4$  (horizontal beam size) and  $-6.1e-5$  for the vertical beam size. For 1.0 GeV/u, they are  $-7.95e-5$ ,  $3.86e-3$  and  $6.03e-3$ , respectively.

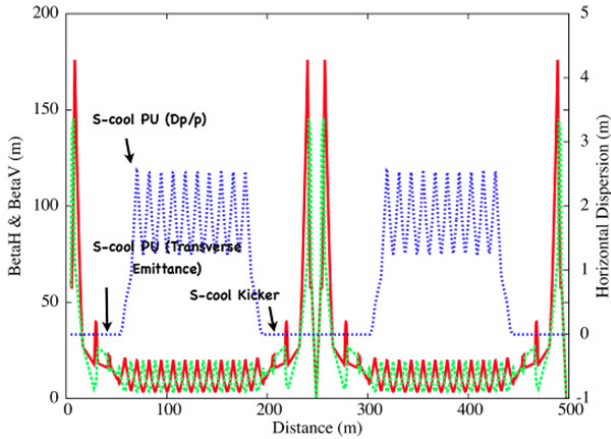


Fig. 1 The lattice function of Collider. The red line shows the horizontal beta function, the green line the vertical beta function and the blue the horizontal dispersion. The transition energy is 7.09.

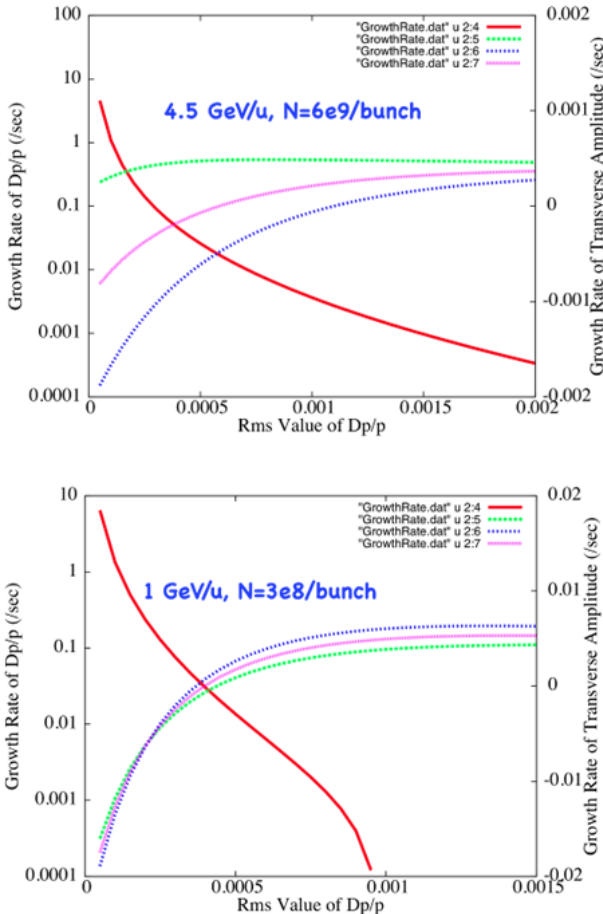


Fig. 2 The IBS growth rate calculated with Martini formula. The top is for the 4.5 GeV/u and the bottom the 1 GeV/u.

The negative IBS growth rate means the shrinkage of beam size or momentum spread so as to exchange the energy to become the isotropic temperature condition in the particle rest frame.

### SLIPPING FACTOR & BAND WIDTH

The operation energy of the collider is from 1 GeV/u to 4.5 GeV/u where the relativistic factor, gamma is largely varied and hence the ring slipping factor is also drastically changed. In Table 2 the ring slipping factor (transition gamma is fixed as 7.09) and the local slipping factor from the stochastic cooling PU to Kicker is tabulated. The distance from PU to kicker is assumed as 170 m as is illustrated in Fig. 1. The bunching factor is defined as

$$Bunching\ Factor = \frac{Circumference}{2\sqrt{\pi}\sigma_s N_b}$$

where  $\sigma_s$  is the rms bunch length and  $N_b$  the bunch number in the ring. The coasting equivalent particle number is given as the product of bunch number/ring, number of ions /bunch and the bunching factor. Thus obtained coasting equivalent particle number is corresponding to the condition that the peak intensity of the bunched beam are populated as the coasting beam in the ring.

Table 2 Beam Parameters for Various Energies  
Transition gamma is fixed as 7.09.

Energy (GeV/u)	1.5	2.5	3.0	4.5
Ring slipping factor	0.1268	0.0537	0.0350	0.00949
Local slipping factor	0.1173	0.0442	0.02546	-5.4e-5
Particle number/bunch	3.0e8	1.50e9	2.50e9	6.0e9
Coasting equivalent particle number	7.26e10	3.63e11	6.05e11	1.45e12

The band width of the stochastic cooling system is preferably as wide as possible because the cooling is inversely proportional to the band width. On the other hand the momentum acceptance of the cooling system is, in general, becomes narrower for the wider band width. Also the momentum acceptance is closely related with the ring slipping factor as well as the local slipping factor.

In Fig. 3 the evolution of momentum spread are analyzed with use of the Fokker-Planck solver for various energies with two band widths, 3-6 GHz and 2-4 GHz. The IBS effects are not included in this analysis, just to compare the momentum acceptance of two bands. For the 4.5 GeV/u, the ring slipping factor is well small and the momentum acceptance is wide enough for both band widths while for 2.5 GeV/u the slipping factor (ring and local) are 0.04~0.05 and then the momentum acceptance becomes critical for the band 3-6 GHz. Presently we are discussing the possibility of two band systems.

Typical example of momentum cooling including IBS effects are given in Fig. 4. Beam parameters are as follows. Energy=4.5 GeV/u, particle number=1.44e12 coasting equivalent beam intensity, Initial momentum spread=1.5e-3 (rms), band width=3-6 GHz, gain=47 dB.

The ring slipping factor=0.00927, and the local slipping factor=-0.0018.

The IBS effects are included from the calculated results as a function of momentum spread as in Fig. 2. Transverse emittance are assumed as constant as 1.1 Pi (horizontal) and 0.9 Pi mm.mrad, respectively. This assumption will be realized with the application of horizontal and vertical stochastic cooling to keep the transverse emittance as constant.

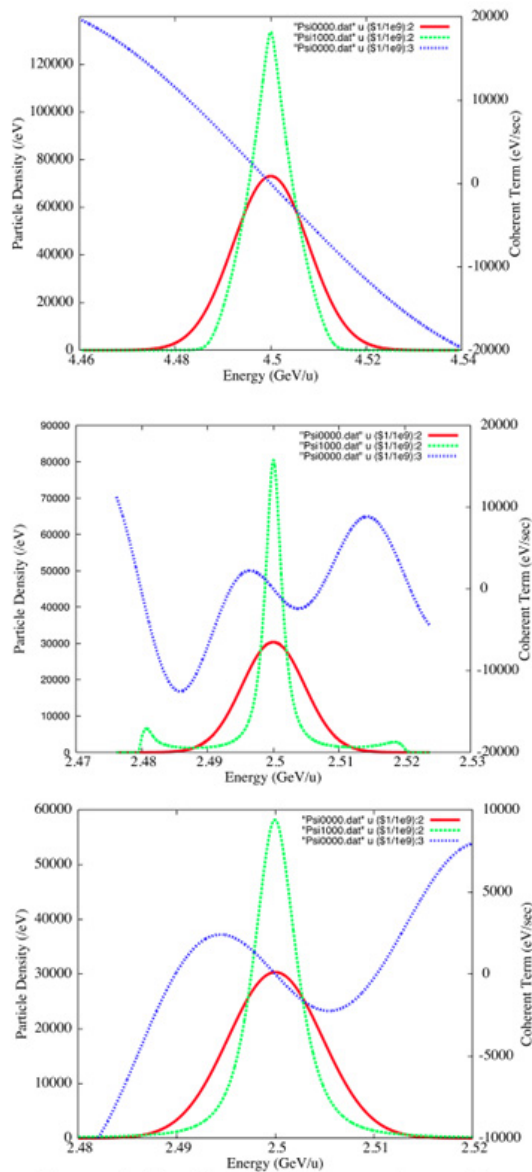


Fig. 3 The analysis of momentum cooling with Fokker-Planck code without IBS effects. Red: initial particle distribution corresponding to  $Dp/p=1.5e-3$  (rms). Green: particle distribution after 1000 sec cooling. Blue: the cooling term. The system gain is set as 50 dB. (Top) 4.5 GeV/u, 3-6 GHz, (Middle) 2.5 GeV/u 3-6 GHz, (Bottom) 2.5 GeV/u 2-4 GHz.

It is found that the momentum spread is gradually increased due to the IBS heating effects and after 1000 sec later, it reaches to the equilibrium value  $2.1e-3$ . Required microwave power is around 2 Watt as the gain

Stochastic cooling

is as small as 47 dB to suppress the Schottky diffusion noise.

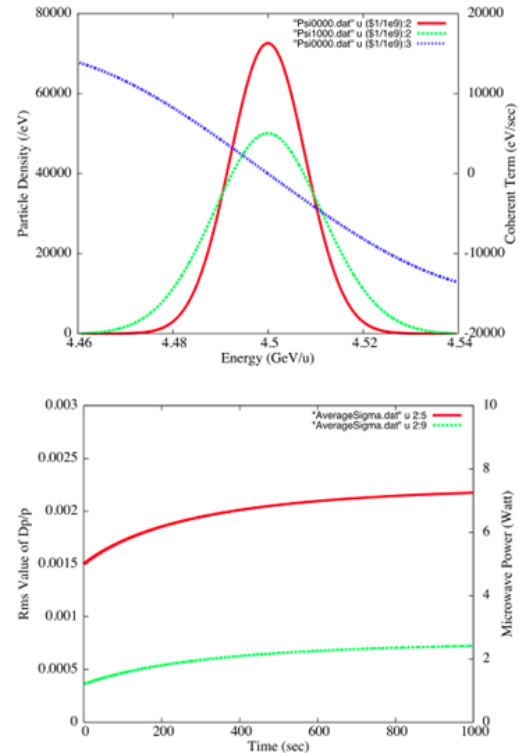


Fig. 4 Typical example of momentum cooling with IBS diffusion effects. Beam energy is 4.5 GeV/u, particle number is  $1.44e12$  coasting equivalent, initial momentum spread= $1.5e-3$  (rms) and the cooling gain=47 dB.

### BARRIER BUCKET ACCUMULATION

The beam accumulation in the collider is designed to use the barrier bucket accumulation method which was experimentally verified at the POP (Proof Of Principle) experiment at the ESR GSI. [3, 4] The parameters of stochastic cooling system and the barrier voltage for the BB accumulation are tabulated in Table 3.

Table 3 Parameters of Stochastic Cooling & Barrier Voltage

Particle	197Au79+, 4.5 GeV/u
Ring circumference	503.04 m
Number of injected particle	$1e9$ /cycle
Injected momentum spread	$3e-4$ (rms)
Injected bunch length	300 nsec (uniform)
Ring slipping factor	0.00845
Dispersion at PU & Kicker	5.0 m & 0.0 m
Band width	2 – 4 GHz
Number of PU & Kicker	128
PU Impedance	50 Ohm
Gain	120 dB
Atmospheric temperature	300 K
Nose temperature	40 K
Barrier voltage	2 kV
Barrier Frequency	2.5 MHz (T=400 nsec)
Injection kicker pulse width	500 nsec
Transverse emittance	0.3 Pi mm.mrad

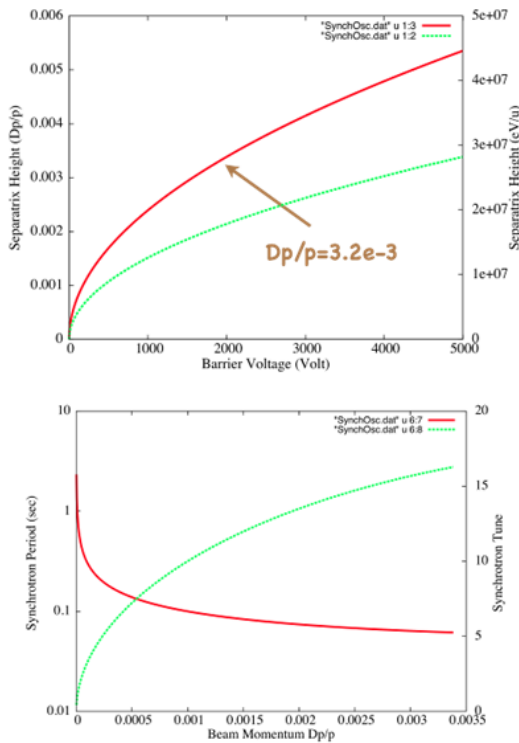


Fig. 5. The separatrix height (top) is given as a function of barrier voltage. Red: Separatrix height of  $Dp/p$  (left scale) and  $\Delta E$  (right scale). The synchrotron period (bottom red line; left scale) and the synchrotron tune (Green, right scale).

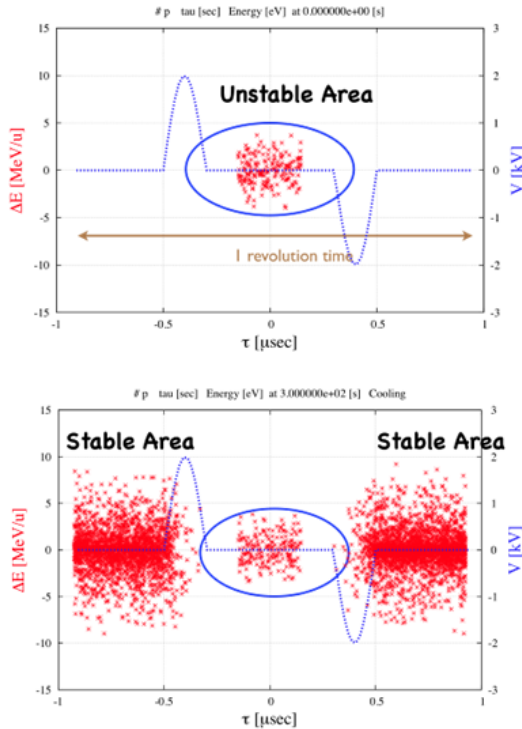


Fig. 6 Phase space mapping of the particles at the 1<sup>st</sup> injection (top) and after 30 stacking (bottom). The particles are represented with red points and the barrier voltage is blue line. The injected beam is located in the central part.

The separatrix height and the synchrotron tune are calculated as a function of barrier voltage as is given in Fig. 5. The separatrix height is  $3.2 \times 10^{-3}$  ( $Dp/p$ ) when the BB voltage is 2 kV. The synchrotron period is around 0.1 sec at the edge of separatrix. The particles are injected in the unstable area between two barrier pulses and they are flowed into the lower potential region, stable area within the cycle time of 10 sec. The particle distribution after 30 pulse stacking is represented in Fig. 6. Details of beam simulation code are given in the reference paper [5]. The increase of the accumulated particle number is given as a function of time in Fig. 7 where also the accumulation efficiency is given. The accumulation efficiency is defined as the ratio of accumulated particle number to the total injected particle number. It is gradually decreased to 90 % after 50 pulse injection. The cooling system gain should be reduced against the increase of particle number so as to suppress the Schottky noise as given in Fig. 8. The required microwave power is 800 Watt at the beginning of the gain 115 dB.

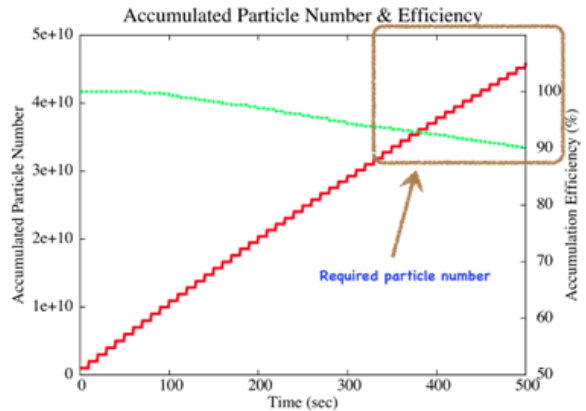


Fig. 7 Increase of accumulated particle number as a function of time. red line: Accumulated particle number. green line: Accumulation efficiency.

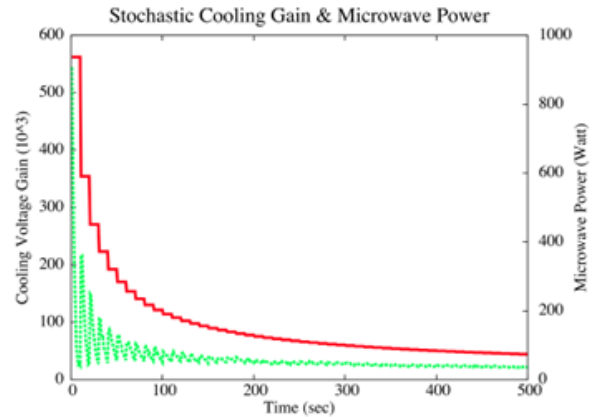


Fig. 8 Variation of cooling gain during the accumulation process (red line, left scale) and the required microwave power (green line, right scale)

### SHORT BUNCH FORMATION

The accumulated beam with the barrier bucket method is a coasting beam condition. We have to make the required short bunches from this coasting beam. The one method is to use the phase jump technique of which the simulated process is illustrated in Fig. 9. First the RF voltage of harmonic number being equal to the required bunch number ( $h=26$ ) is adiabatically applied to the coasting beam. (a) and (b) in Fig. 9. The maximal RF voltage is 200 kV. After the adiabatic bunching is completed, the phase of RF is changed by 180 degrees (c). After stretching the bunch length (d), the phase is changed back to the original position (e), and the bunch is rotated 1/4 synchrotron oscillation (f). Then apply the higher harmonic number RF voltage ( $h=130$ ) of 500 kV to maintain the short bunches.

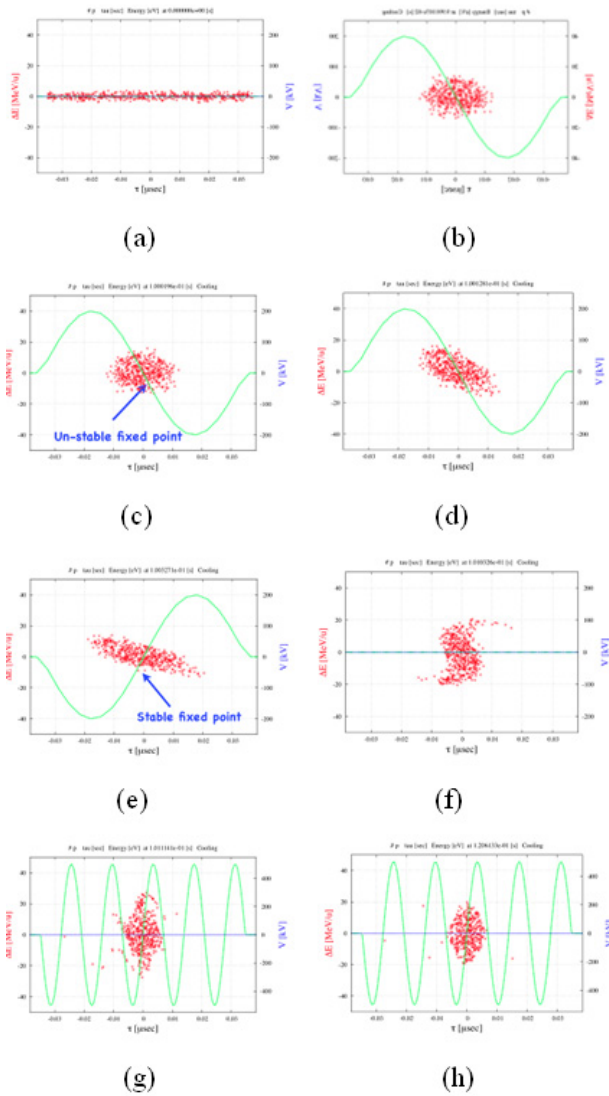


Fig. 9 Phase jump method to make the short bunch. From the top left to right and bottom is a sequence of bunching process. (a)  $t=0$  sec, (b)  $t=0.1$  sec,  $V_{rf}=200$  kV, (c)  $t=0.100019$  sec, (d)  $t=0.10012$  sec, (e)  $t=0.10032$  sec, (f)  $t=0.101$  sec, (g)  $t=0.1011$  sec,  $V_{rf}=500$  kV, (h)  $t=0.1206$  sec.

Stochastic cooling

The other way of making the short bunch is to use the stochastic cooling with RF field. The process can be separated two steps as similar to the phase jump method. In the first step the RF voltage of harmonic number equal to the required bunch number ( $h=26$ ), is adiabatically applied. In parallel the stochastic cooling system is applied of which the gain is gradually decreased as is given in Fig. 10.

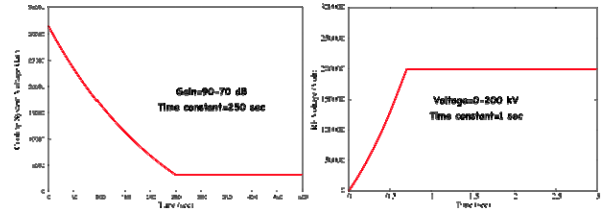


Fig. 10 Adiabatic gain reduction and the RF voltage increase for the short bunch formation. Harmonic number is 26.

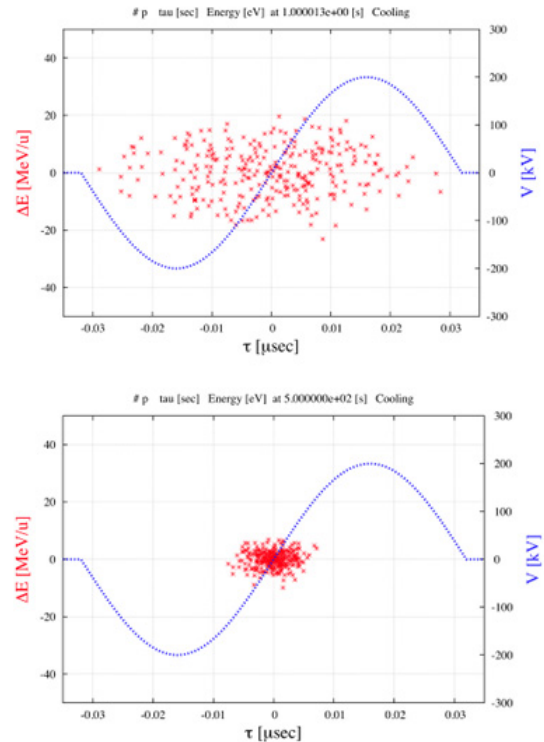


Fig. 11 The phase space mapping at the time= 1 sec (top) and 500 sec (bottom). red: particles, blue: RF voltage.

Thus formed pre-bunched beam is re-captured by the higher harmonic RF voltage. The pre-bunched beam has the bunch length of 3 ns (rms) and  $Dp/p$  of  $6e-4$  (rms). (Gaussian distribution in both dimensions). This bunch is re-captured by the RF field of harmonic=130. Again the RF voltage is increased from 0 to 500 kV with the time constant of 1 sec for the adiabatic capturing. The gain of stochastic cooling system is kept constant as 80 dB and wait further cooling and bunching.

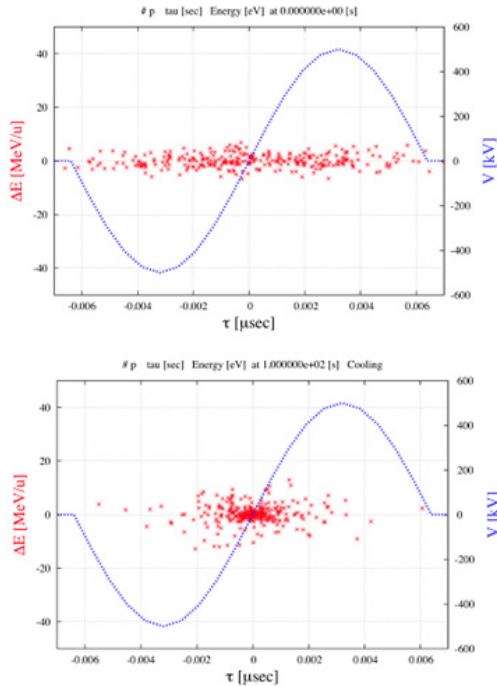


Fig. 12 The final bunching process with higher harmonic number=130 which is 5 times larger than the harmonic number for the pre-bunching. From the top to bottom, time=0 sec and 100 sec.

The evolution of bunch length and the relative momentum spread during the final bunching process are given in Fig. 13. When the stochastic cooling is applied, the equilibrium values of bunch length is attained at 1.2 nsec and  $Dp/p$  (rms) is  $8e-4$  while they are increased gradually due to the IBS heating effects without cooling.

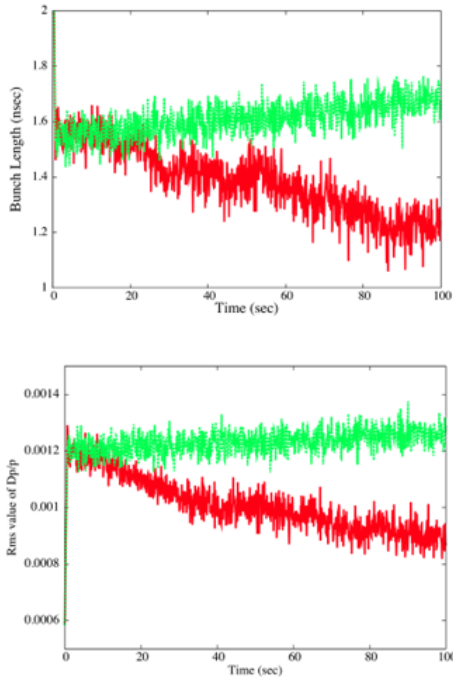


Fig. 13 The evolution of rms bunch length (top) and the  $Dp/p$  (bottom) are illustrated as a function of time. red: with stochastic cooling, green: without stochastic cooling.

Stochastic cooling

## ELECTRON COOLING

In the preceding sections we have investigated the BB accumulation and the short bunch formation with stochastic cooling with RF field. However for the lower energy than 2.5 GeV/u the stochastic cooling could not work as the ring slipping factor becomes so large (see Table 2). For such low energy operation, obviously the electron cooling is effective. The designed electron cooler parameters are given in Table 3.

Table 3 Parameters of Electron Cooler for NICA

Particle	197Au79+, 2.0 GeV/u
Ring circumference	503.04 m
Cooler length	6 m
Electron current	1 A
Electron diameter	2 cm
Effective electron temperature	1 meV
Transverse electron temperature	1 eV
Longitudinal magnetic field	0.1 T
Beta function at cooler section	16 m

Typical cooling process is illustrated in Fig. 14 where the beam energy is 2 GeV/u and the particle number is  $3e11$  as a coasting beam equivalent. The equilibrium values are attained at 25 sec cooling as the emittance ( $h$ )= 0.12, emittance ( $v$ )=0.09 mm.mrad and  $Dp/p=3.7e-4$ , respectively. The IBS effects are included.

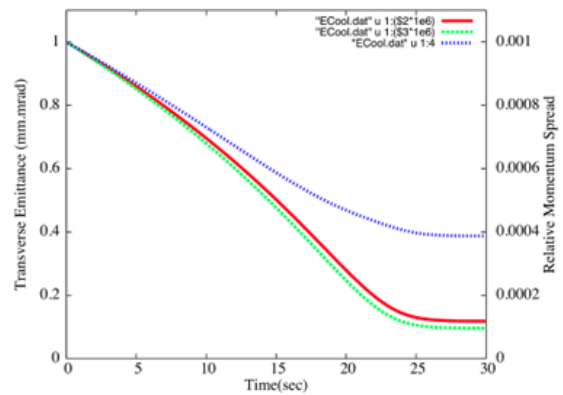


Fig. 14 Evolution of emittance (red: horizontal, green: vertical) and  $Dp/p$  (blue) of 2 GeV/u beam with electron cooling.

## REFERENCES

- [1] I. Meshkov, "NICA Project at JINR" in this Proceedings
- [2] G. Trubnikov et al., "Application of Cooling Method at NICA Project" in this Proceedings.
- [3] M. Steck et al., "Demonstration of Longitudinal Stacking in the ESR with Barrier Bucket and Stochastic Cooling", in this Proceedings
- [4] T. Katayama et al., "Simulation Study of Barrier Bucket Accumulation with Stochastic Cooling at GSI ESR" in this Proceedings.
- [5] T. Katayama et al., Proc. of IPAC10, Kyoto, May, 2010.

# SIMULATIONS OF STOCHASTIC COOLING OF ANTIPROTONS IN THE COLLECTOR RING CR

C. Dimopoulou, A. Dolinskii, T. Katayama, F. Nolden, C. Peschke, M. Steck,  
GSI, Darmstadt, Germany

D. Möhl, L. Thorndahl, CERN, Geneva, Switzerland

## Abstract

The Collector Ring at FAIR will be equipped with pertinent stochastic cooling systems in order to achieve fast cooling of the hot secondary beams, antiprotons and rare isotopes, thus profiting from the repetition rate of the SIS100 synchrotron. Detailed simulations of the system performance are needed for optimization as well as input for the users of the CR pre-cooled beams, e.g. HESR. We presently focus on the antiproton cooling in the band 1-2 GHz. After a comprehensive overview, results from Fokker-Planck simulations with the CERN code of the momentum cooling of antiprotons will be presented. The performance of the betatron cooling of antiprotons, which has to proceed simultaneously with the momentum cooling, was calculated separately by means of an analytical model. First results and their implications will be discussed, including an outlook to future simulation work.

## INTRODUCTION

The main purpose of the Collector Ring (CR) within the FAIR project [1] is the fast reduction of the phase space occupied by the hot secondary beams. The latter are antiprotons at 3 GeV and rare isotope beams (RIBs) at 740 MeV/u, coming from the production targets in a very short ( $\approx 50$  ns) bunch. At injection into the CR, they have the largest momentum spread and fill the transverse aperture. After bunch rotation and adiabatic debunching their momentum spread is reduced, whereas the transverse emittances remain unchanged. The reduced  $\delta p/p$  is a prerequisite for stochastic cooling. Otherwise, the effect of undesired mixing (see below) would exclude particles at the tails of the momentum distribution from being cooled. In order to meet the requirements of maximum production rate the CR stochastic cooling system has to strongly reduce all 3 phase subspaces, within 9 s for the antiprotons (with the option of 5 s after future upgrade) and 1 s for the highly charged RIBs (Table 1). The recent scenario according to which, in the first phase of the FAIR project, the pre-cooled antiprotons from the CR will be accumulated in the HESR instead of the RESR calls for 20% lower (if possible) final emittances and momentum spread than those in Table 1 in order to match the very small acceptances of the HESR [2].

The CR lattice is governed by the demands from stochastic cooling: (i) flexibility in setting different transition energy values for antiprotons and RIBs to reach an optimal compromise for the mixing parameters of the stochastic cooling, as explained below, (ii) accommodation of pickups and kickers in regions of appropriate dispersion, (iii) control of the horizontal and vertical betatron phase advance

Stochastic cooling

Table 1: Requirements for the CR stochastic cooling  
Antiprotons, 3 GeV,  $10^8$  ions

	$\delta p/p$ (rms)	$\epsilon_{h,v}$ (rms) $\pi$ mm mrad
Before cooling	0.35 %	45
After cooling	0.05 %	1.25
Phase space reduction	$9 \times 10^3$	
Cooling down time	$\leq 9$ s	
Cycle time	10 s	
	$\delta p/p$ (rms)	$\epsilon_{h,v}$ (rms) $\pi$ mm mrad
Rare isotopes, 740 MeV/u, $10^9$ ions		
Before cooling	0.2 %	45
After cooling	0.025 %	0.125
Phase space reduction	$1 \times 10^6$	
Cooling down time	$\leq 1$ s	
Cycle time	1.5 s	

between pickups and kickers of the transverse stochastic cooling systems, (iv) reducing chromaticity over the whole momentum range.

## OVERVIEW OF THE CR STOCHASTIC COOLING SYSTEM

### Design criteria

In a simplified model, one can write the stochastic cooling rate, e.g. for transverse emittance, as

$$\frac{1}{\tau_{\perp}} = \frac{2W}{N} \left[ 2gB |\sin(\mu_{pk})| - g^2(M + U) \right], \quad (1)$$

where  $W$  is the system bandwidth,  $N$  is the number of particles in the beam,  $g$  is the system gain,  $U$  is the ratio of power densities of the system thermal noise to the Schottky signal. For transverse cooling the CR lattice satisfies the condition of proper betatron phase advance  $\sin(\mu_{pk}) \approx \pm 1$  between pickup and kicker. The undesired mixing parameter  $B$  (mixing between pickup and kicker) can be written in the form  $B = \cos(m_c \phi_u)$ , where  $m_c$  is the central harmonic in the band and  $\phi_u = -2\pi \chi_{pk} \eta_{pk} \delta p/p$ . At the beginning of cooling i.e. for the maximum total ( $2\sigma$ ) momentum spread  $m_c \phi_u \leq \pi/2$ , otherwise the cooling force changes sign i.e. heats up the beam. Here,  $\chi_{pk} = (s_k - s_p)/C$  is the ratio of the path from pickup to kicker to the closed orbit circumference  $C$ ,  $\eta_{pk}$  is the lo-

cal frequency slip factor between pickup and kicker. The desired mixing parameter  $M$  (mixing between kicker and pickup) can be approximated as  $M = (m_c \eta |\delta p/p|)^{-1}$ , for the total ( $2\sigma$ ) momentum spread, with the frequency slip factor of the ring  $\eta = \gamma^{-2} - \gamma_t^{-2}$ . This holds if the Schottky bands do not overlap. If they do,  $M=1$ .

For momentum cooling, the mixing aspects are similar. The Palmer-Hereward technique [3] is a special case of horizontal cooling. It uses a pickup at high dispersion and appropriately located kickers to correct the horizontal orbit displacement due both to betatron oscillation and momentum deviation, the latter correction corresponds to longitudinal cooling. The notch filter method [4] uses the dependence of the particle revolution frequency on its momentum deviation. The transfer function of an ideal filter (with infinitely deep notches), plus a  $90^\circ$  phase-shifter, is

$$H_{nf} = \frac{i}{2} (1 - e^{-i2\pi m \eta \delta p/p}) = -e^{-i\pi f/f_0} \sin(\pi f/f_0).$$

It has no effect at the exact harmonics  $m f_0$  of the revolution frequency (notches) and accelerates/decelerates particles with wrong revolution frequency to the nearest harmonic of the correct revolution frequency. Prerequisite for filter cooling are not overlapping Schottky bands ( $M > 1$ ), so that the particles are driven into the notches. For filter cooling the undesired mixing phase becomes [5]  $\phi_{u,nf} = -\pi(2\chi_{pk}\eta_{pk} + \eta)\delta p/p$  i.e. the momentum acceptance of the system is further reduced. This dictates very small values of  $\eta$  (and  $\eta_{pk}$ ).

Antiproton beams and RIBs set different requirements. Antiproton cooling is limited by the poor ratio of Schottky signal to thermal noise, due to the low charge state. To cope with that it is foreseen in the CR: (i) to keep the pickup electrodes and the pickup signal preamplifiers at cryogenic temperatures (in the present scenario, 20-30 K and 80 K, respectively, yielding an effective temperature of 73 K at the preamplifier input), (ii) to strive for the largest possible electrode sensitivity during cooling by moving (plunging) the pickup electrodes, following the shrinking beam size, (iii) to choose the notch filter technique for momentum cooling, which uses the higher sum signals from the pickups (compared to the low difference signals of the Palmer method) and advantageously filters out the thermal noise at all harmonics of the revolution frequency in the band. In order to have sufficient momentum acceptance (and well-separated Schottky bands) for the notch filter cooling the optimum choice is to operate the CR slightly above transition at  $\eta=-0.011$  ( $\gamma_t=3.85$ ). The drawback is that the transverse cooling suffers from the resulting high value of  $M \approx 11$ . (Eq. 1).

For RIBs, the undesired mixing limits the momentum acceptance of the system. The phase  $m_c \phi_u$  must be kept small by minimizing (i)  $\eta_{pk}$  by increasing the dispersion in the dipoles and (ii)  $\chi_{pk}$  by placing pickup and kicker as close as possible. For the chosen lattice  $\eta=0.186$ . Even so, initially the Schottky bands overlap, so that only the Palmer method can be applied in the beginning of cooling.

Stochastic cooling

## System parameters

Along the above lines, the following concept has been developed (Fig. 1). The CR stochastic cooling system will operate in the frequency band 1-2 GHz. It consists of 2 pickup (PH, PV) and 2 kicker tanks (KH, KV), all in straight sections with zero dispersion, and one Palmer pickup tank (PP) at high dispersion. Antiproton cooling makes use of PH, PV, KH, KV. Longitudinally the notch filter technique is implemented and to improve the signal to noise ratio, signals from both PH and PV are taken in sum mode. For RIBs only the Palmer pickup PP is useful in the first stage. It serves to detect signals in all 3 phase space planes. After the rms  $\delta p/p$  has decreased below 0.1%, it is possible to switch off the signals from the PP and turn to cooling from PH and PV combined with the notch filter down to the final emittances and momentum spread.

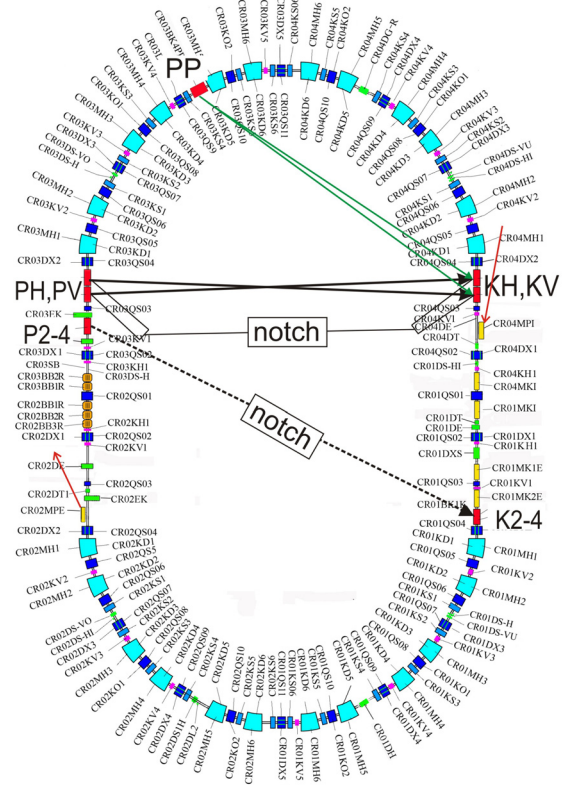


Figure 1: CR layout with stochastic cooling paths, incoming and extracted beams. Solid black line: 1-2 GHz, pbar 3D cooling, RIB 3D cooling final stage; Solid green line: 1-2 GHz, RIB 3D cooling first stage; Dashed black line: 2-4 GHz, pbar longitudinal cooling (future option).

As a future option, for the antiprotons, an additional momentum cooling system in the band 2-4 GHz by means of a notch filter is foreseen. It consists of a pickup tank (probably with plunging electrodes) and a kicker tank, both in dispersion-free straight sections. The design  $\eta=-0.011$  guarantees optimum momentum acceptance for both bands. The handshake between the 1-2 and 2-4 GHz mo-

mentum cooling systems will have to be investigated by simulations.

Each pickup and kicker tank (PH, PV, KH, KV) consists of two plates (up/down for vertical, left/right for horizontal). Each plate consists of 8 arrays (modules) of 8 identical slotline electrodes, i.e. 64 electrodes. The pickup modules are plungeable. These structures [6] as well as an optical notch filter [1] are being developed at GSI.

In the circuit convention, the longitudinal impedance of the electrodes acting as pickup or kicker is defined in terms of the rms beam current, the rms voltage applied to the beam, time-average pickup signal power and applied power to kicker:  $Z_p \equiv P_p/I_{b,rms}^2$ ,  $Z_k \equiv U_{b,rms}^2/P_k$ . Due to reciprocity  $Z_k = 4Z_p$ . According to HFSS [7] simulations with the present electrode geometry, the longitudinal impedance at midband frequency  $f_c=1.5$  GHz, of one electrode pair acting as pickup is  $11.25 \Omega$  and  $37.75 \Omega$ , for electrode aperture  $\pm 60$  mm (unplunged case) and  $\pm 10$  mm (fully plunged), respectively. These values are obtained for a beam centered in the pickup without considering its transverse dimensions i.e. they are conservative because in reality particles with high amplitudes "see" a higher sensitivity. Relative measurements on the GSI prototype pickup module [8], indicate that  $\sqrt{Z_{p,k}(f,y)} \approx \sqrt{Z_{p,k}(f_c)}S1(y)S2(f)$ , where  $y$  stands for horizontal or vertical beam coordinate, and yield the functions  $S1(y)$  and  $S2(f)$ . For simplicity,  $S1(y)$  is approximated to increase linearly i.e.  $\partial\sqrt{Z}/\partial y=\text{slope}=\text{const}$ . The sensitivity  $S2(f)$  is about 1 between 1-1.5 GHz and drops down to 0.65 between 1.5-2 GHz, as is characteristic for such slotlines.

The foreseen installed output power at the kickers of the 1-2 GHz system is 4.8 kW, it has to cover both momentum and betatron cooling. It is limited by funding, but could be increased in a future upgrade.

Table 2: Parameters for the stochastic cooling of  $E_0=3$  GeV antiprotons with the 1-2 GHz system in the CR.

Circumference $C$	221.45 m
Revolution frequency $f_0$	1.315 Tm
Slip factor ring $\eta$ , PU-K $\eta_{pk}$	-0.011, -0.033
Distance PU-K/C $\chi_{pk}$	0.378
Beam intensity $N$	$10^8$
Initial rms emittance $\epsilon_{h,v}$	$45 \pi$ mm mrad
Initial rms momentum spread (Gaussian/parabolic distribution)	$3.5 \times 10^{-3}$
System bandwidth $W$	1-2 GHz
PU, K midband impedance $Z_{p,k}(f_c)$	$11.25 \Omega$ , $45 \Omega$
unplunged electrodes at $\pm 60$ mm	
PU/K sensitivity $S1(y)=1+\text{slope}\cdot y$	$\text{slope}=24.5\text{m}^{-1}$
PU/K sensitivity $S2(f)$	
Number of PU $n_p$ , of K $n_k$ (longitudinal)	128, 128
Number of PU $n_p$ , of K $n_k$ (transverse)	64, 64
Effective temperature (preamp.) $T_{eff}$	73 K
Total installed power at kickers	4.8 kW

Stochastic cooling

60

Table 2 summarizes the parameters, which are used as input in the following simulations. Plunging of the pickup electrodes i.e. time variation of  $Z_p$  is not considered yet. It can be included after complete treatment of the betatron cooling, which provides information on how the beam emittance shrinks with time.

## MOMENTUM COOLING

Momentum cooling is described in terms of the Fokker-Planck (FP) equation for the energy distribution of the particles  $\Psi(E, t) \equiv \partial N / \partial E$ :

$$\frac{\partial \Psi}{\partial t} = \frac{\partial}{\partial E} \left[ -F\Psi + \left( D_s\Psi + D_n \right) \frac{\partial \Psi}{\partial E} \right]. \quad (2)$$

The basic formalism is explained in detail in [9]. In short, the coherent effect  $F$  and the incoherent effects (diffusion) due to thermal noise and Schottky noise are:

$$\begin{aligned} F(E, t) &= 2ef_0^2 \sqrt{n_p n_k} \sum_{m \in W} \sqrt{Z_p(m)Z_k(m)} \cdot \\ &\quad \cdot \text{Re} \left\{ \frac{G(m, E)}{1 - S(m, E, t)} \right\}, \\ D_n(E, t) &= \frac{1}{2} f_0^2 k_B T_{eff} n_k \sum_{m \in W} Z_k(m) \left| \frac{G(m, E)}{1 - S(m, E, t)} \right|^2, \\ D_s(E, t) &= e^2 f_0^3 \frac{1}{|\eta|} \frac{\gamma + 1}{\gamma} E_0 n_p n_k \cdot \\ &\quad \cdot \sum_{m \in W} Z_p(m) Z_k(m) \frac{1}{m} \left| \frac{G(m, E)}{1 - S(m, E, t)} \right|^2, \end{aligned} \quad (3)$$

where  $m$  are the harmonics of the revolution frequency in the band  $W$ ,  $E_0=3$  GeV and  $\sqrt{Z_{p,k}(m)} = \sqrt{Z_{p,k}(m_c)}S2(m)$ .

The system gain  $G(m, E) = G_{||}H_{nf}(m, E)e^{im\phi_u(E)}$  includes the notch filter response and undesired mixing. The electronic gain  $G_{||}$ , real and constant within the bandwidth, is the variable parameter. The effect of feedback by the beam enters into the open loop gain  $S(m, E, t) = \sqrt{n_p n_k Z_p(m)Z_k(m)}G(m, E)BTF(m, E, t)$  via the beam transfer function

$$\begin{aligned} BTF(m, E, t) &= -\frac{ef_0^2}{m} \left[ \frac{\pi}{|\kappa|} \frac{d\Psi}{dE} + \right. \\ &\quad \left. + \frac{i}{\kappa} \cdot PV \left( \int_{-\infty}^{+\infty} \frac{d\Psi/dE^*}{E^* - E} dE^* \right) \right], \\ \frac{1}{\kappa} &\equiv \frac{1}{2\pi f_0 \eta} \frac{\gamma + 1}{\gamma} E_0. \end{aligned}$$

The CERN program solves numerically the FP equation and computes the particle density  $\Psi(E, t)$ . An example is given in Fig. 2. The coefficients  $F$  and  $D$  are updated in time through their dependence on  $d\Psi/dE$  entering into the beam transfer function. Fig. 3 shows the calculated cooling

force. Fig. 4 shows that in our case the Schottky noise is higher than the thermal noise before cooling. During notch filter cooling, the Schottky noise dominates over the thermal noise within the limits of the beam distribution. Therefore, one can anticipate that the longitudinal cooling time will be roughly proportional to the beam intensity. As expected, the feedback by the beam suppresses the Schottky noise in the middle of the distribution and deforms accordingly the cooling force  $F$ , especially at high gain (see also Eq. 3). The cooling loop was stable since in the Nyquist plot in Fig. 5 the curve lies far on the left from the point  $S=1$ .

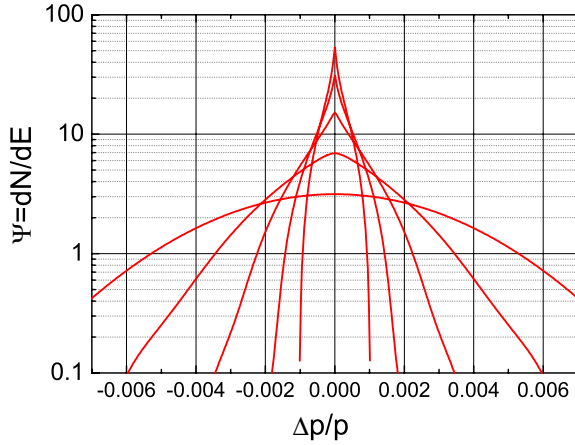


Figure 2: Evolution of the particle density  $\Psi$  during cooling with gain=150 dB. Plots at  $t=0, 2.5$  s, 5 s, 7.5 s and 10 s.

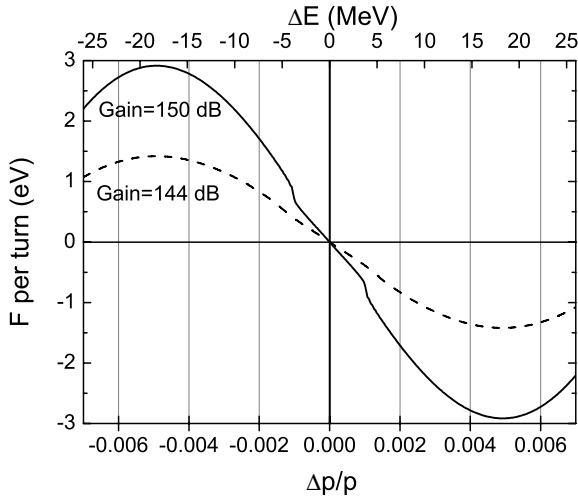


Figure 3: Coherent effect  $F$  per revolution at the end of the cooling process ( $t=10$  s for 150 dB gain,  $t=15$  s for 144 dB gain) plotted against the relative momentum spread  $\Delta p/p$  and the deviation  $\Delta E$  of the beam particles from the nominal kinetic energy of 3 GeV.

Stochastic cooling

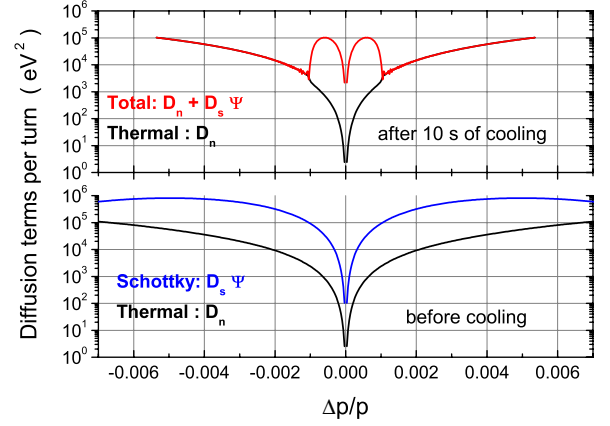


Figure 4: Incoherent effects due to Schottky particle noise  $D_s \cdot \Psi$  and (filtered) thermal noise  $D_n$  at the beginning and at the end of the cooling process. Gain=150 dB, total cooling time  $t=10$  s.

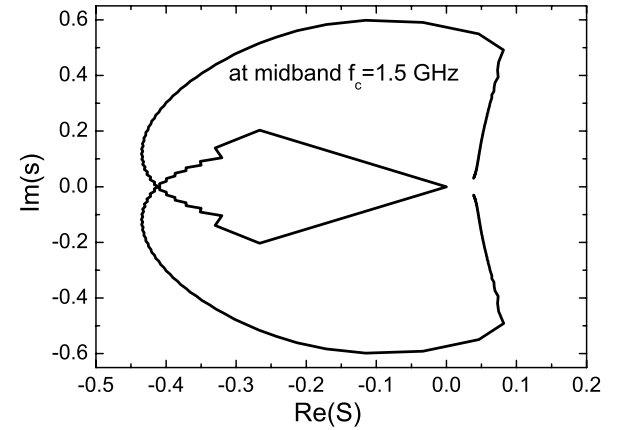


Figure 5: Nyquist plot of the open loop gain  $S$  at midband, at the end  $t=10$  s of the cooling process. Gain=150 dB.

The rms energy (momentum) spread is calculated as the second moment of  $\Psi(E, t)$ . The simulations yield the maximum total cw power in the bandwidth at the kicker. It is the sum of the initial maximum Schottky power and of the constant filtered amplifier power:

$$P_s = 2(e f_0)^2 n_p \sum_{m \in W} \sum_E Z_p(m) \left| \frac{G(m, E)}{1 - S(m, E, t)} \right|^2 \Psi(E, t)$$

$$P_n \approx \frac{1}{4} k_B T_{eff} W G_{||}^2.$$

The required installed power is taken by rule of thumb to be 4 times higher than the total cw power, in order to account for statistical fluctuations of the signals. The results are summarized in Fig. 6. The gain of 158 dB was found to be optimum, for higher gain cooling was slower, but the required power is not realistic. As expected [9], for this gain

$\min[Re(S)]$  is close to -1, i.e. it maximizes the particle flux  $\Phi = F\Psi - (D_s\Psi + D_n)\frac{\partial\Psi}{\partial E}$ .

To conclude, the requirements of Table 1 can be met with the notch filter cooling at  $G_{||}=150$  dB even with the conservative assumption of no plunging at the pickups. However, there seems to be no safety margin.

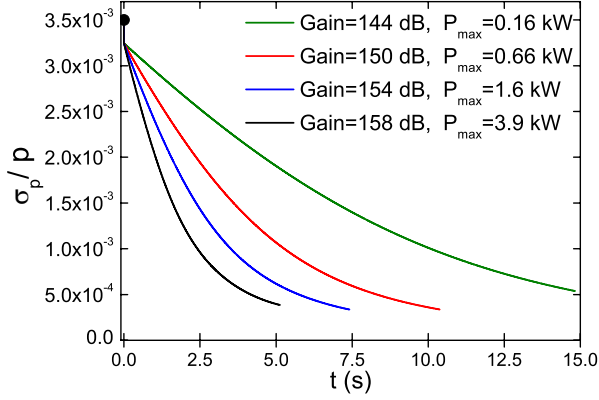


Figure 6: Evolution of the rms momentum spread of the beam during cooling for different gains and corresponding maximum required cw power (up to 20% Schottky, 80% thermal noise).

## BETATRON COOLING

The betatron cooling is studied with an analytical model based on the standard "rms" theory [3, 10, 11] leading to Eq. 1. The instantaneous rate of change of the horizontal or vertical rms emittance is  $-(1/\epsilon(t))(d\epsilon(t)/dt) = 1/\tau_{\perp}(t)$ ,

$$\frac{1}{\tau_{\perp}(t)} = \frac{2W}{N} \left[ 2gB(t)|\sin(\mu_{pk})| - g^2(M(t) + U(t)) \right]. \quad (1)$$

Simultaneous momentum cooling takes place for 10 s. The Ansatz for the variation of the momentum spread with time is an exponential fit of the form  $\sigma_p(t)/p = 0.0035 e^{-t/\tau_1}$ ,  $t \leq 10$  s to the results of the FP simulations for gain  $G_{||}=150$  dB (see Fig. 6). The parameters entering into Eq. 1 are given by:

$$B(t) \approx \cos[m_c \phi_u(t)], \quad \phi_u(t) = -2\pi \chi_{pk} \eta_{pk} \Delta p(t)/p;$$

for an exact expression, the cooling rate term

$(2W/N)2gB(t)|\sin(\mu_{pk})|$  in Eq. 1 is replaced by

$$\frac{2f_0}{N} g \sum_{\substack{m=-\infty \\ m \in W}}^{m=+\infty} Re \left\{ e^{i(m\phi_u(t) + \mu_{pk} - \pi/2)} \right\},$$

$$M(t) \approx \frac{1}{m_c |\eta| \Delta p(t)/p},$$

$$U(t) = \frac{k_B T_{eff}}{N e^2 f_0 \beta_p \text{slope}^2 n_p} \left( \frac{f_0}{2W} \sum_{\substack{m=-\infty \\ m \in W}}^{m=+\infty} \frac{1}{Z_p(m)} \right) \frac{1}{\epsilon(t)},$$

Stochastic cooling

where  $\Delta p(t)/p$  is taken as the  $2\sigma$  value,  $\beta_p, \beta_k$  are the beta functions at the pickup and kicker, respectively.

The system gain  $g(t)$ , assumed to be constant within the bandwidth, is the variable function in the calculations. It is connected via

$$G_{\perp}(m) = g \frac{m}{\sqrt{n_p n_k Z_p(m) Z_k(m)}} \frac{4\pi p}{N e^2 \text{slope}^2 \sqrt{\beta_p \beta_k}}$$

with the electronic gain  $G_{\perp}(m)$ , which ideally should follow the above frequency dependence in the band and also vary in time with shrinking betatron amplitudes.

The gain  $g_{opt}(t) = B(t)|\sin(\mu_{pk})|/[M(t) + U(t)]$  maximizes at each  $t$  the rate  $\tau_{\perp}^{-1}(t)$ , the optimum rate is  $\tau_{\perp, opt}^{-1}(t) = (2W/N) B^2(t) \sin^2(\mu_{pk})/[M(t) + U(t)]$ . During cooling, the heating terms from  $M(t)$  and  $U(t)$  continuously grow, so that to keep on cooling  $g$  should decrease with time, ideally as  $g_{opt}(t)$ .

Since  $G_{\perp}(m) \sim m$  (a consequence of the Panofsky-Wenzel relation), the power scales with the square of the working frequency in the band. The total cw power in the bandwidth at the kicker is the sum of the initial maximum Schottky power and the constant amplifier power:

$$P_s \sim N \epsilon(t) g^2(t) \sum_{m \in W} \frac{m^2}{S 2^2(m)},$$

$$P_n \sim k_B T_{eff} g^2(t) \sum_{m \in W} \frac{m^2}{S 2^4(m)}.$$

Depending on how the PU-K pairs in Fig. 1 are assigned to horizontal and vertical cooling, respectively, there are two cases to investigate and choose the best one in terms of cooling performance:

Case 1

horizontal	$\beta_p=20.5$ m	$\beta_k=5.2$ m	$\sin(\mu_{pk})=-0.92$
vertical	$\beta_p=8.3$ m	$\beta_k=8.3$ m	$\sin(\mu_{pk})=-1.00$

Case 2

horizontal	$\beta_p=11.0$ m	$\beta_k=11.0$ m	$\sin(\mu_{pk})=-1.00$
vertical	$\beta_p=5.5$ m	$\beta_k=13.6$ m	$\sin(\mu_{pk})=-0.96$

In Figs. 7 and 8 we summarize preliminary results for case 1 and for horizontal cooling only. Similar results are expected for vertical cooling. Also, in this first approach the feedback by the beam is not taken into account. For a proper quantitative treatment it must be included, in particular since in our case with  $N = 10^8$  ions the Schottky noise dominates over the thermal one. Nevertheless, these results already allow us to identify the main challenges for the antiproton cooling in the CR. Initially,  $M=11$  and  $U=1.2$ , so that  $M$  dominates the heating rate at all times i.e.  $M(t) \sim 10 U(t)$  (Fig.7). The emittance  $\epsilon = 4 \pi$  mm mrad is reached (Fig. 8), with a maximum required cw power of 950 W (40% Schottky, 60% thermal noise). This goes far beyond the power limitation foreseen for the system (Table 2). In order to reach the required 3 times lower emittance (Table 1), the transverse cooling must proceed at lower gain and take longer than 10 s.

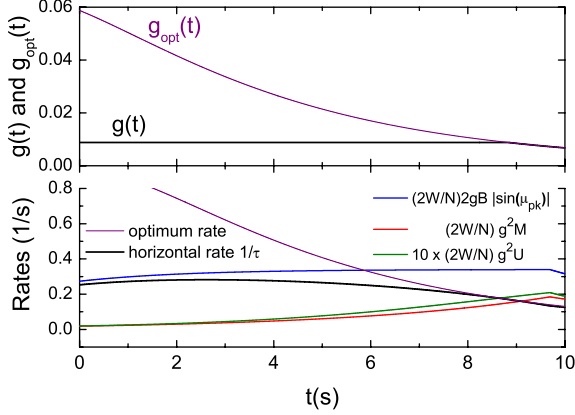


Figure 7: Upper part: Assumed system gain  $g(t)$  compared to the optimum gain. The initial  $g$  corresponds to an electronic gain  $G_{\perp}(m_c)=141$  dB at midband. Lower part: The instantaneous rate  $\tau_{\perp}^{-1}(t)$  (black line) and its partial rates according to Eq. 1: cooling rate (blue line), heating rate due to mixing  $M$  (red line) and heating rate due to noise/signal ratio  $U$  multiplied by the factor 10 (green line). The optimum rate  $\tau_{\perp, opt}^{-1}(t)$  is also shown (purple line).

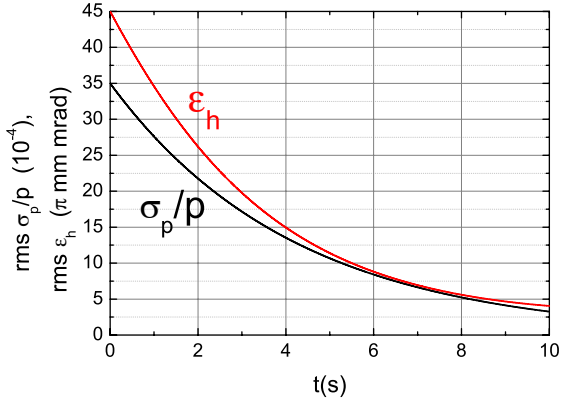


Figure 8: Evolution of the horizontal rms emittance within 10 s of cooling for  $g(t)$  as shown in Fig.7. Evolution of the rms momentum spread for simultaneous longitudinal notch filter cooling with  $G_{||}=150$  dB.

## CONCLUSIONS AND OUTLOOK

We have seen that, whereas the momentum cooling proceeds optimally, the betatron cooling must proceed very slowly, unless we could somehow restrict  $M(t)$ . This essentially means to reduce the performance of the momentum cooling at the profit of the betatron cooling until a reasonable compromise is found. A straightforward way is to have in a first stage low-gain notch filter momentum cooling (i.e. slower decrease of  $\delta p/p$ ) with high-gain betatron cooling and inverse the situation at a later stage. An alternative would be to apply momentum cooling in two Stochastic cooling

stages: first with the time-of-flight (TOF) method [12] and then with the notch filter method. The TOF method is not only slower but it also has a larger momentum acceptance through its undesired mixing phase  $\phi_u$  (instead of  $\phi_{u, nf}$  of filter cooling). Thus, it can be envisaged to increase slightly the  $\eta$  (e.g.  $\eta \approx -0.02$ ) before the TOF cooling, thus reducing the initial value of  $M$ , and bring it down to the required  $\eta = -0.011$  when notch filter cooling takes over.

In any case, the interplay between momentum and betatron cooling will have to be investigated in detail. The aim is a simultaneous optimization of both processes, by distributing the available installed power accordingly, so as to fulfill as much as possible the very challenging requirements of the CR. As a next step, plunging of pickup electrodes can be included to study the ultimate performance of the cooling system. It is expected that the plunging will dramatically reduce the diffusion by factors like 4 to 9, especially in the transverse planes.

Cooling of  $N = 10^8$  antiprotons is of course the most demanding case, but during the commissioning of the CR intensities  $N = 10^6 - 10^7$  are expected. In this case, the filter momentum cooling becomes more relaxed, whereas in the betatron cooling the relative weights of the incoherent effects change ( $U$  comparable or greater than  $M$ ), calling for a dedicated optimization procedure.

Concerning the cooling of RIBs, the Palmer pickup has still to be designed. Then, the cooling performance in all 3 planes for the two foreseen stages and in particular the handshake between Palmer and notch filter cooling [5] have to be investigated in extensive simulations.

## ACKNOWLEDGEMENT

We thank H. Stockhorst for fruitful discussions.

## REFERENCES

- [1] M. Steck et al., these proceedings, MOIO03 (2011).
- [2] R. Maier et al., PAC'11, New York, USA, THOCN2 (2011).
- [3] H. G. Hereward, in: Proc. Int. School of Particle Accelerators, Erice, 1976, CERN 77-13 p.281 (1977); R. B. Palmer, BNL, private communication (1975).
- [4] G. Carron, L. Thorndahl, CERN-ISR-RF/78-12 (1978).
- [5] F. Nolden et al., NIM A 564, p.87 (2006).
- [6] C. Peschke et al., NIM A 532, p.459 (2004) and COOL'05, AIP Conference Proceedings 821, p.221 (2005).
- [7] [www.ansoft.com/hfss/](http://www.ansoft.com/hfss/).
- [8] C. Peschke et al., COOL'09, Lanzhou, China, THPMCP003 (2009).
- [9] D. Möhl, G. Petrucci, L. Thorndahl, S. van der Meer, Physics Reports 58, p.73 (1980).
- [10] F. Sacherer, CERN-ISR-TH/78-11 (1978).
- [11] S. van der Meer, CERN/PS/84-33 (AA) (1984).
- [12] W. Kells, in: Proc. of 11th Int. Conf. on High Energy Accelerators, Geneva, p.777 (1980).

# STOCHASTIC COOLING PROJECT AT THE EXPERIMENTAL STORAGE RING, CSRE AT IMP \*

J.X. Wu#, Y.Zhang, M.Li, Y.Liu, X.J.Hu, J.X. Xia, J.C.Yang, IMP, China  
 Fritz Caspers, CERN, Geneva, Switzerland  
 T. Katayama and F.Nolden, GSI, Germany.

## Abstract

Stochastic cooling at the experimental Cooler Storage Ring, CSRe [1] at the Institute of Modern Physics (IMP) in China, will be used mainly for the experiments with radioactive fragment beams. RI beams arrive from the fragment separator with emittance of 20-50  $\pi$  mm. mrad and momentum spread  $\delta p/p$  of  $\pm 0.5\sim 1.0\%$ . The electron cooler, which is running now at the CSRe, is not able to cool down this hot beam rapidly enough. Stochastic cooling is effective for these RI beams to reduce the emittance to less than 5  $\pi$  mm.mrad and of  $\delta p/p = 5e-4$  within 2-20 sec. After stochastic pre-cooling, electron cooling will further cool down the emittance and momentum spread within several seconds. The paper gives the design of the stochastic cooling system and the simulation results. A recently developed forward traveling wave structure is presented as well as the measured results of a test model.

## INTRODUCTION

CSRe ring has the circumference of 128.801 m with the layout in Fig.1. A combination of stochastic precooling and subsequent electron cooling is needed to get overall cooling times of the order of 10 seconds for injected secondary heavy ion beams and beams cooled by electron cooling to equilibrium phase space density. The development of a stochastic cooling system is very useful for performing competitive experiments with secondary rare isotope beams. Example of the setup of the stochastic cooling system is illustrated in the figure. It is planned to cool RI beam energies between 300 MeV/u and 400 MeV/u. As no straight section is available for the installation of pickups and kickers for the stochastic cooling and they have to be installed in the C type bending magnet chambers. The aperture of the bending vacuum tube is 236 mm \*74 mm thus the useful aperture is 220 mm \* 70 mm. The space at two sides in vertical direction can be increased to 4-5 mm if the electrodes are not placed in the middle. So the space is very limited inside it, especially in vertical direction, and the feedthrough is an issue. Thus the size and the number of pickups/kickers are severely limited.

For present operation mode which stochastic cooling will be used, internal-target mode with  $\gamma_{tr} = 2.457$  and normal mode with  $\gamma_{tr} = 2.629$ , the frequency will be very low with large momentum dispersion of  $\pm 0.5\sim 1.0\%$  which causes the slow cooling. A new optical mode at  $\gamma_t = 1.86$  is developed which allows for an upper limit of the

usable stochastic cooling bandwidth at about 1 GHz (of course the high frequency requires the microwave propagation attenuation in CSRe). At this optical mode the stochastic cooling system can be arranged in figure 1, sharing one pickup tank for the whole cooling system. The twiss parameters and the phase advance are shown in table 1. As this optical mode is never operated, the systematic simulation and experimental studies, such as optical optimization and beam acceptance measurement, will be performed in future.

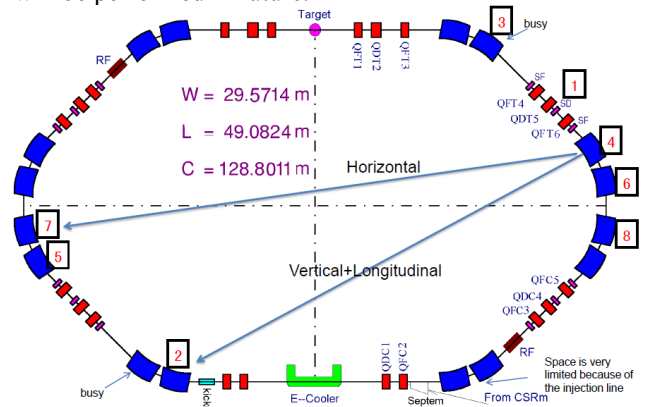


Figure 1 Typical layout of stochastic cooling pickup and kicker system

Table 1 Twiss parameters at pick-up/kicker position

	Horizontal		Vertical+Momentum	
	Pickup	Kicker	Pickup	Kicker
$\beta_x$ (m)	19.9-14.3	6.6-7.6	19.9-14.3	16.8-11.9
$\beta_y$ (m)	12.9-13.7	6.7-9.4	12.9-13.7	10.6-9.6
$D_x$ (m)	9.3-7.5	6.0-6.1	9.3-7.5	0-0.4
$\theta$	76°		78°	
L(m)	67		49	

## PICK-UP/KICKER STRUCTURE

A novel type of perforated travelling wave pick-up/kicker structure is developed which was originally proposed by F.Caspers at CERN in 1998 [2], shown in Fig.2. The unit cell length is 12 mm and the thickness of the electrode metal foil amounts to 0.4 mm. The electrode which is following the bending vacuum chamber inside the dipole magnet is 87 mm wide and 1 m long. The distance between the electrode and the ground is 3 mm. The characteristic impedance is 17 ohm and it can be raised if the distance between the electrode to ground is increased, but in our case it is limited. A large number

\*Work supported by NSFC (10705039), HIRFL-CSR

#wujx@impcas.ac.cn

of small slots (5 slots in a row and 80 cells along the beam path) in this electrode provides distributed inductive loading, slowing down the phase velocity of the travelling wave structure. The reduction in phase velocity is a function of slot length, slot width, electrode thickness, and the spacing between the electrodes to ground. In contrast to other similar looking electrodes (Faltin type pick-up [3], McGinnis type slotted waveguide structure [4] for  $\beta=1$ ) this device is very broadband and operating from low frequencies onwards as a forward coupler. Also

advantages of the proposed structure are the simple and cheap construction as well as low mechanical height. This low height permits installation in a bending magnet where in our case vertical aperture is a big issue. This kind of inductive loading, using a large number of rather small slots is applicable for a  $\beta$  range from about 0.5 to 0.95. Due to the small size of the slots the frequency dependency of the inductance of these slots is very low and thus leading to a small dispersion over a large frequency range.

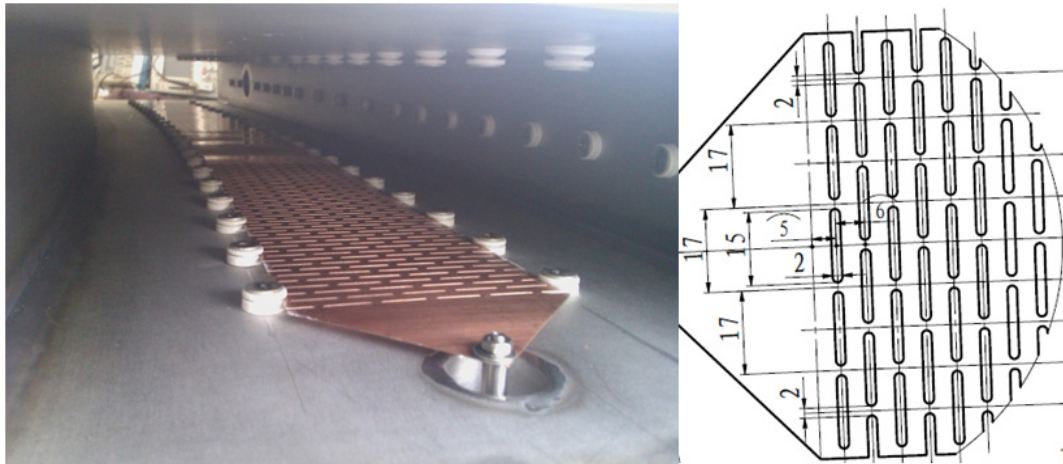


Figure 2: The slotted structure of travelling wave mode, number of cells = 80 and the length L is about 1 meter.

The measured transmission of the electrode is shown in Fig.3. Below 3 GHz the amplitude of the transmission is nearly flat. The phase difference from the linear phase (subtracted=delay term) is not more than 45 degree at 1.5 GHz for the nearly 1 m long electrode. Thus in a frequency range from a few MHz to 1.5 GHz this structure has a phase dispersion acceptable for CSRe stochastic cooling. As this structure has a good phase response, the length of the structure can further be increased, for example 2 m long and then one whole electrode inside the bending vacuum tube will overcome the problems of the signal feedthrough. Also the beam coupling impedance scales with the square of the electrode length.

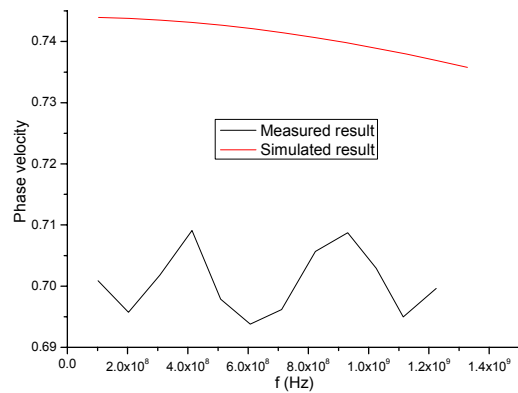


Figure 4: Phase velocity of 87 mm wide electrode

The measurement (resonant method [5]) and simulation results of the phase velocity are shown in Fig.4. The measurement result is roughly about 0.7 which is correspond to the beam energy of 380 MeV/u. The simulation result is a little bit larger than the measurement because in the simulation the attenuation of the electrode cannot be considered very well. For resonant method, of course the resonance frequencies can be very well defined but defining the correct effective length of the electrode is not straightforward. The geometrical length between the ends amounts to 106 cm, including triangular transition sections. Distributing the capacitance of these transition regions from a triangle to a strip with the full width of the electrode returns an effective length of 103 cm. The

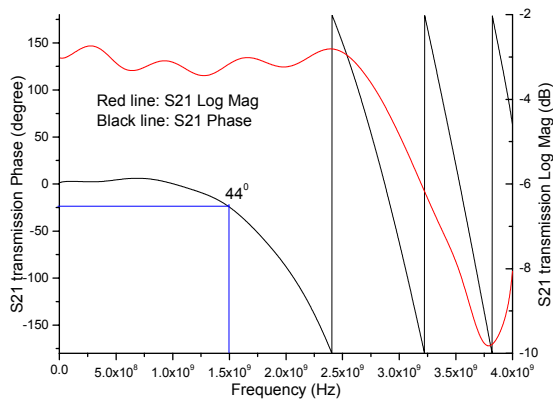


Figure 3: S<sub>21</sub> transmission for 80 cells

relatively strong variations for the indicated phase velocity vs frequency are raw data and have not a physical meaning. The variations from the resonator method are very likely due to the fact that the electrode is not completely parallel to ground (slight mechanical undulations that we can see from Fig.2).

The attenuation of the electrode is shown in Fig.5. It will be better if the stainless steel of the vacuum chamber and copper electrode is coated with 10 micron silver and a flash of gold which will be done in the following manufacturing. But for stainless steel this process requires a thin nickel layer on it and there is interaction with bending magnetic field. The analysis will be done further.

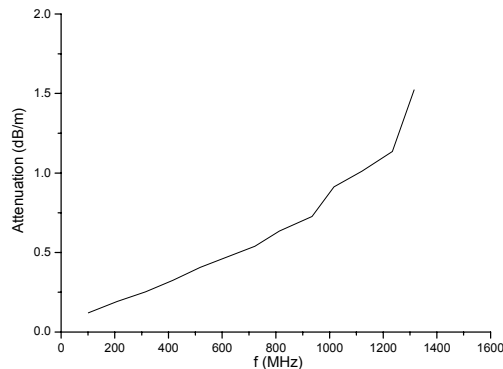


Figure 5: Attenuation values of the electrode

About the pick-up/kicker structure the detailed measurement, simulation and the analysis will be found in this committee presented by Y.Zhang [6].

## COOLING SIMULATIONS

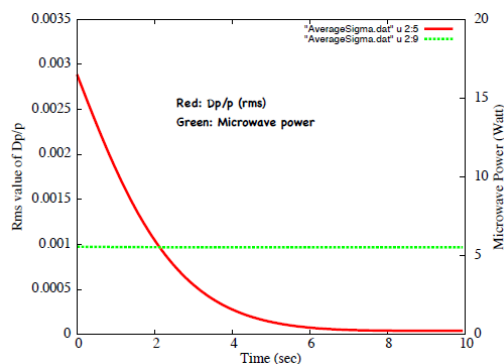


Figure 6: Evolution of rms  $\Delta p/p$  & RF power

The upstream end of the pick-up will be connected to the input of a low noise pre-amplifier to get low noise temperature around  $70^0$  [7]. Then for the above pick-up/kicker structure if the bandwidth is 0.5-1 GHz, noise temperature is 80 K and gain is 130 dB, for beam  $^{132}\text{Sn}^{50+}$  with particle number of  $5e3$  and beam energy of 380 MeV/u, the simulated result for the longitudinal cooling and the needed RF power is shown in Fig.6. We can get

that in 3 s the rms momentum width can be reduced from  $3e-3$  to  $5e-4$ . Since the pick-up/kicker structure has broad bandwidth more than one octaves we can even increase the bandwidth and get even faster cooling. Also the low RF power means less money to build the system.

## CONCLUSION

The perforated travelling wave structure seems to fit best the requirement of the CSRe stochastic cooling system. It features a sufficiently broad bandwidth (amplitude flatness and phase linearity inside the required cooling band), good beam coupling impedance which scales with the square of the length of the device, low losses (low effective noise temperature at ambient physical temperature when operated as a pick-up) and a comparatively easy mechanical construction and installation into the CSRe dipole chamber. As a kicker structure the same design would lead to uncritical thermal cooling requirements in vacuum.

The low gamma transition lattice is preferable to get the effective cooling so as to extend the band width up to 0.5 GHz or more. From the simulation, as a pre-cooling of RI beams stochastic cooling is very effective and useful. Also the RF power is much small. Hopefully next step we can get the IMP support to precede the investigation and build the whole stochastic cooling.

The authors express their sincere thanks to Lars Thohndahl (CERN) for his analysis and advice of the perforated travelling wave structure.

## REFERENCES

- [1] XIA JW et al., Nucl. Instrum. Methods, 2002, A488:11.
- [2] F.Caspers, A novel type of forward coupler slotted strip-line pickup electrode for non-relativistic particle beams, AT/Note/2011/075(TECH), 2011-09-09.
- [3] L.Faltin, Slot-type pick-up and kicker for stochastic cooling, NIM 148, 1987.
- [4] D. McGinnis, Slotted waveguide slow-wave stochastic cooling arrays; proc. PAC99.
- [5] T. Kroyer, F. Caspers, E. Gaxiola, Longitudinal and transverse wire measurement for the evaluation of impedance reduction measures on the MKE extraction kickers, AB-Note-2007-028.
- [6] Y.Zhang et al., An improved forward travelling wave structure design for stochastic cooling at Experimental Cooler Storage Ring (CSRe), at the Institute of Modern Physics (IMP) in China, COOL 11.
- [7] F. Nolden et al., A Resonant Schottky Pick-up for the Experimental Storage Ring ESR at GSI, submitted to Nul.Inst.Meth.A.

## HELICAL COOLING CHANNEL DEVELOPMENTS\*

R. P. Johnson<sup>#</sup>, C. Yoshikawa, Muons, Inc., Batavia, IL, U.S.A.  
 Y. S. Derbenev, V. S. Morozov, JLab, Newport News, VA, USA

### Abstract

Several beam phase space manipulation and cooling stages are required to provide the extraordinary reduction of emittances required for an energy-frontier muon collider. From the pion production target, the pions and their decay muons must be collected into RF bunches, rotated in phase space to reduce momentum spread, cooled in 6 dimensions by 6 orders of magnitude, cooled in each transverse plane by another order of magnitude, and accelerated and matched to the RF system used to accelerate the muons to the final collider energy. Many of these stages have Helical Cooling Channel (HCC) [1] solutions based on superimposed solenoid, helical dipole, and helical quadrupole magnetic fields. The HCC was invented to achieve efficient ionization cooling with continuous emittance exchange. We first describe the essential HCC equations and describe how they can be applied for longitudinal and transverse emittance matching. We then describe simulations of HCC segments with a continuous gaseous hydrogen energy absorber suitable for basic 6d cooling as well as new results of related pressurized RF cavity beam tests. We then describe a new and creative application of the theory and use of the HCC that has been developed for Parametric-resonance Ionization Cooling (PIC), and the phase space matching needed for transitions between various cooling channel subsystems

### INTRODUCTION

Considerable progress has been made in developing promising subsystems for muon beam cooling channels to provide the extraordinary reduction of emittances required for an energy-frontier muon collider. A high-performance front end from the target to the cooling systems has been designed and simulated [2], and many advances in theory, simulation codes, and hardware development have been achieved, especially regarding the 6d HCC described below. However, the HCC theory is not necessarily restricted to channels having solenoid fields. For example, the Twin Helix [3], which is also described below, does not possess a solenoid field component. The HCC theory and its extensions can describe a wide variety of beam dynamics and is thus well suited to provide the platform from which matching sections can be designed. We now review the theory of the HCC and examine how it can be used for emittance matching between cooling segments that have been independently developed.

#### Basic Helical Cooling Channel

In the HCC, a solenoid field is augmented with a transverse helical field that provides a constant dispersion

\*Work supported in part by DOE HEP STTR Grant DE-SC00005589.  
<sup>#</sup>rol@muonsinc.com

along the channel as necessary for the emittance exchange that allows longitudinal cooling. The Hamiltonian that describes motion in this magnetic configuration is easily solved by a transform into the frame of the rotating helical magnet, where it is seen that the addition of a helical quadrupole field provides beam stability over a very large acceptance.

The helical dipole magnet creates an outward radial force due to the longitudinal momentum of the particle while the solenoid magnet creates an inward radial force due to the transverse momentum of the particle:

$$F_{h-dipole} \approx p_z \times b; \quad b \equiv B_{\perp}; \quad F_{solenoid} \approx -p_{\perp} \times B; \quad B \equiv B_z,$$

where  $B$  is the field of the solenoid, the axis of which defines the  $z$  axis and  $b$  is the field of the transverse helical dipole. By moving to the rotating frame of the helical fields, a time- and  $z$ -independent Hamiltonian can be formed to derive the beam stability and cooling behaviour [1]. The motion of particles around the equilibrium orbit is shown schematically in Figure 1.

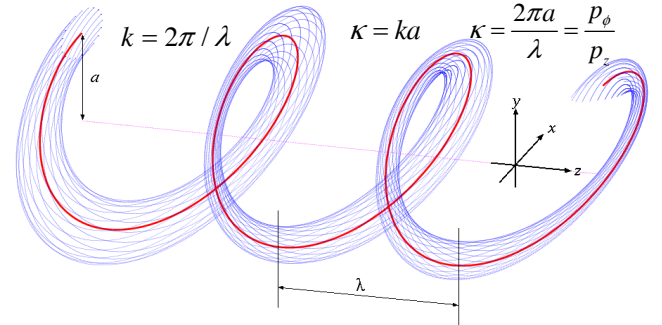


Figure 1: Schematic of beam motion in a HCC.

The equilibrium orbit shown in red follows the equation that is the Hamiltonian solution:

$$p(a) = \frac{\sqrt{1+\kappa^2}}{k} \left[ B - \frac{1+\kappa^2}{\kappa} b \right] \quad (1)$$

The dispersion factor  $\hat{D}$  can be expressed in terms of the field components  $B$ ,  $b$ , and the transverse magnetic field radial gradient  $\partial b / \partial a$  on the particle's orbit:

$$\hat{D} = \frac{p}{a} \frac{da}{dp} = \left( \frac{a}{p} \frac{dp}{da} \right)^{-1}; \quad \hat{D}^{-1} = \frac{\kappa^2 + (1-\kappa^2)q}{1+\kappa^2} + g; \quad g \equiv \frac{-(1+\kappa^2)^{3/2}}{pk^2} \frac{\partial b}{\partial a},$$

where  $g$  is the effective field index at the periodic orbit.

The magnetic field ratio on the equilibrium trajectory satisfies the condition

$$\frac{b}{B} = \frac{\kappa}{1+\kappa^2} \left( 1 - \frac{k}{k_c} \right) = \frac{\kappa}{1+\kappa^2} \left( \frac{q}{q+1} \right), \quad \text{where } q \equiv \frac{k_c}{k} - 1.$$

For stability, the following condition has to be satisfied

$$0 < G \equiv (q-g)\hat{D}^{-1} < R^2 \equiv \frac{1}{4} \left( 1 + \frac{q^2}{1+\kappa^2} \right)^2. \quad (2)$$

Use of a continuous homogeneous absorber takes advantage of a positive dispersion along the entire cooling

path, a condition that has been shown to exist for an appropriately designed helical dipole channel. We have also shown that this condition is compatible with stable periodic orbits.

## HCC LONGITUDINAL TRANSITIONS

Longitudinal emittance matching in transition sections can be facilitated, subject to simultaneously satisfying stability criterion (2), by continuously varying the RF bucket area to match RF parameters from one cooling section to the next. The RF bucket area is given by:

$$A_{bucket} \cong \frac{16}{w_{rf}} \sqrt{\frac{eV'_{max} \lambda_{RF} m_{\mu} c^2}{2\pi |\eta_H|}} \left[ \frac{1 - \sin(\phi_s)}{1 + \sin(\phi_s)} \right] \quad (3)$$

Where the term in brackets is an approximation for the moving-bucket factor,  $w_{rf}$  is the RF frequency in radians/second,  $V'_{max}$  is the maximum E-field voltage gradient,  $\lambda_{RF}$  is the RF wavelength,  $m_{\mu}$  is the mass of the muon,  $\phi_s$  is the synchronous particle RF phase, and  $\eta_H$  is the translational mobility or slip factor, derived in [1] for the HCC as:

$$\eta_H = \frac{\sqrt{1 + \kappa^2}}{\gamma \beta^3} \left( \frac{\kappa^2}{1 + \kappa^2} \hat{D} - \frac{1}{\gamma^2} \right) \quad (4)$$

where  $1/\gamma_T^2 = (\kappa^2 / (1 + \kappa^2)) \hat{D}$  and the dispersion factor  $\hat{D}$  relates to apparatus quantities and design momentum via:

$$\hat{D}^{-1} = \frac{a}{p} \frac{dp}{da} = \frac{\kappa^2 + (1 - \kappa^2) [B \sqrt{1 + \kappa^2} / pk - 1]}{1 + \kappa^2} - \frac{(1 + \kappa^2)^{3/2}}{pk^2} \frac{\partial b}{\partial a} \quad (5)$$

where  $p$  is the reference momentum;  $a$  reference radius,  $\kappa = p/p_z = \text{helix pitch}$ ,  $B$  the solenoid  $B_z$ ,  $k = 2\pi/\lambda$ ;  $\lambda$  is the helix period, and  $\partial b/\partial a$  the quadrupole component.

Thus, in matching between sections with different longitudinal dynamics, the RF bucket area can be continually manipulated by varying any of the following: the gradient of the dipole field ( $\partial b/\partial a$ ), the reference momentum ( $p$ ), the accelerating phase ( $\phi_s$ ), the transition energy  $\gamma$ , or the maximum gradient ( $V'_{max}$ ).

## HCC TRANSVERSE TRANSITIONS

In the case of transverse matching, equation (1) would be used to compute the evolution of the solenoid  $B$  and helical dipole  $b$  fields between cooling segments, where  $\partial b/\partial a$  is subject to constraint (2).

### G4beamline HCC 6d Cooling Simulations

The analytic relationships above have been used to guide GEANT [4] simulations using G4beamline [5] and ICOOL [6]. Simulation results [7] show a 190,000-fold 6d emittance reduction for a series of eight 250 MeV/c HCC segments, where the reference orbit radii are decreased and fields are increased as the beam cools. Longitudinal and transverse emittances at the end of each HCC segment are shown in Table 1 and are also plotted as red dots in Figure 2. The peak RF field is 27 MV/m and 60  $\mu\text{m}$  Be windows make the cavities true pillboxes. The

hydrogen gas pressure is 160 atm at 300 K. Forty per cent of the beam is lost in the 303 m long channel. About 22% of the beam is lost due to muon decay while the rest of the loss is due to emittance mismatches, which can be improved. A new Helical Solenoid (HS) magnet design [8] that uses simple offset coils to generate the required solenoid, dipole and quadrupole field components, was invented and superconducting prototypes are being tested.

Table 1: The parameters of the 8 HCC cooling channel segments used by Yonehara [7].

#	Z	b	b'	b <sub>z</sub>	$\lambda$	$\nu$	$\epsilon_T$	$\epsilon_L$	$\epsilon_{6D}$	$\epsilon$
	m	T	T/m	T	m	GHz	$\mu\text{m}$	mm	$\text{mm}^3$	
1	0	1.3	-0.5	-4.2	1.0	0.325	20.4	42.8	12900	1.0
2	40	1.3	-0.5	-4.2	1.0	0.325	5.97	19.7	415.9	0.92
3	49	1.4	-0.6	-4.8	0.9	0.325	4.01	15.0	10.8	0.86
4	129	1.7	-0.8	-5.2	0.8	0.325	1.02	4.8	2.0	0.73
5	219	2.6	-2.0	-8.5	0.5	0.65	0.58	2.1	3.2	0.66
6	243	3.2	-3.1	-9.8	0.4	0.65	0.42	1.3	0.14	0.64
7	273	4.3	-5.6	-14.1	0.3	0.65	0.32	1.0	0.08	0.62
8	303	4.3	-5.6	-14.1	0.3	1.3	0.32	1.0	0.07	0.60

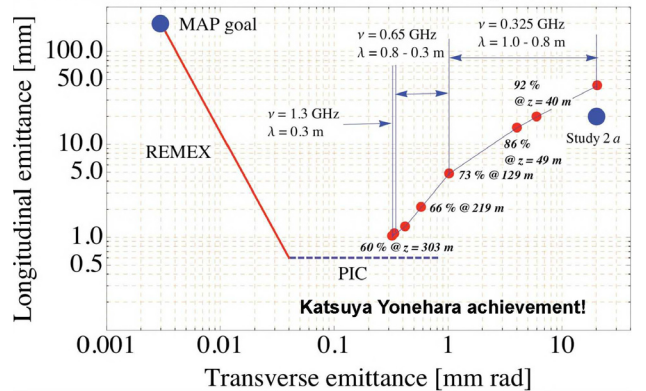


Figure 2: Fernow-Neuffer plot of the G4beamline simulated emittance evolution shown in Table 1.

## RF BEAM TESTS

The simple idea that emittance exchange can occur in a practical homogeneous absorber without shaped edges followed from the observation that RF cavities pressurized with a low Z gas are possible [9]. Recent experiments with the proton beam at the Fermilab MuCool Test Area have verified that such cavities will not suffer RF breakdown in a beam. Other parameters have been measured that verify many features of models of the cavities as well. The recombination rate of the ionized electrons produced by the beam is fast enough that the RF amplitude is likely to be adequate for the muon beam that will be less than 100 ns long. Figure 3 shows the first tests of a pressurized RF cavity being hit by a charged particle beam. The voltage drops due to the absorption of energy by the ionized electrons and to the change in impedance of the cavity due to the plasma causing the power from the klystron to be reflected.

The use of a 1 part in 10,000 SF<sub>6</sub> dopant has been shown to largely mitigate the drop in RF voltage caused by the motion of ionized electrons in the RF field that

heat the gas. Namely, the electrons attach to the SF<sub>6</sub> and the large mass of the resulting ion inhibits its motion in the RF field and its energy transfer to the hydrogen gas. Figure 3 shows the influence of a proton beam in a high pressure gas filled cavity without the aid of SF<sub>6</sub> to inhibit the effect of electrons, while Figure 4 illustrates the improvement by addition of the SF<sub>6</sub> dopant. Preliminary models indicate that for short bunch trains (< 100 ns), the doped RF cavity stability allows HCC use as in Figure 2.

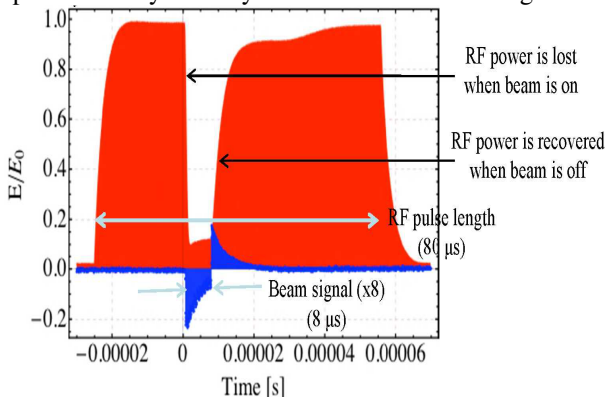


Figure 3: Beam influence on 950 psi hydrogen-filled RF test cell. Red is the 802 MHz RF envelope which rises to E<sub>0</sub>~20 MV/m. Blue is the toroid signal from the beam from the 400 MeV H- Linac to the MTA.

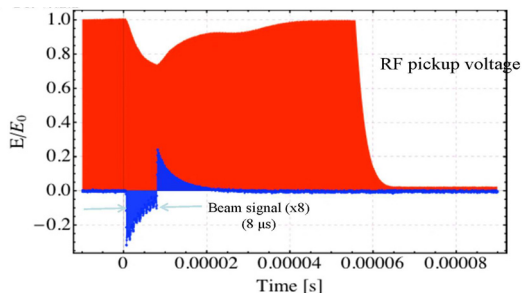


Figure 4: Beam influence on 950 psi hydrogen-filled RF test cell with a 0.01% dopant addition of SF<sub>6</sub>. The gradient drops by about 30% during the 8 μs beam pulse, where some of that is due to the impedance mismatch caused by the plasma that in turn causes most of the klystron power to be reflected.

### OTHER HCC SEGMENT EXAMPLES

In all cases we can imagine, the pions are produced in a strong solenoid that becomes weaker along the channel so that transverse momenta are folded forward. The decay muon phase space must be matched to the acceptance of the HCC for 6d cooling, a matching that goes from solenoid with no helical dipole to an HCC.

At the end of a 6d HCC segment as shown in Figure 2, you could either match into a strong field solenoid channel for extreme cooling or to a PIC channel. While the former is an example of HCC to solenoid transition, the PIC channel being discussed is even more of a challenge in that it is made up of two helical magnets with no solenoid field component.

### PIC and the Twin-Helix Example

Parametric-resonance Ionization Cooling (PIC) requires a half integer resonance to be induced in a ring or beam-line such that the normal elliptical motion of particles in  $x-x'$  phase space becomes hyperbolic, with particles moving to smaller  $x$  and larger  $x'$  as they pass down the beamline. (This is almost identical to the technique used for half integer extraction from a synchrotron where the hyperbolic trajectories go to small  $x'$  and larger  $x$  to pass the wires of an extraction septum.) Thin absorbers placed at the focal points of the channel then cool the angular divergence of the beam by the usual ionization cooling mechanism, where each absorber is followed by RF cavities. Thus, in PIC the phase space area is reduced in  $x$  due to the dynamics of the parametric resonance and  $x'$  is reduced or constrained by ionization cooling.

The main constraint in parametric-resonance ionization cooling channel design is the requirement to combine low dispersion at the wedge absorber plates (for emittance exchange to compensate energy straggling) with large dispersion in the space between plates (where sextupoles can be placed to compensate for chromatic aberration). The desired large angular divergence of + 200 mr at the absorber plates also implies significant corrections for spherical aberrations and the next step in the development of this channel is to compensate for aberrations. The horizontal and vertical optics also have to be correlated such that there must be places where each plane has a focus at the absorber plates.

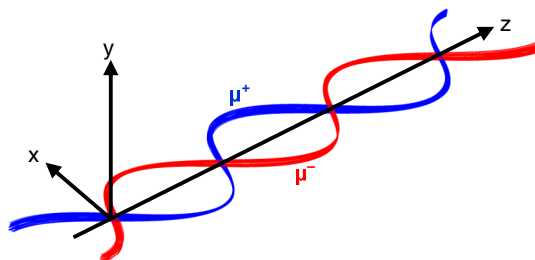


Figure 5: G4beamline display of planar trajectories of muons of both signs in the Twin Helix magnet system.

Perhaps one of the more interesting recent cooling channel developments follows from the realization that two helical dipole magnetic fields of opposite helicity can be superimposed to create a purely vertical magnetic field that varies sinusoidally in amplitude along the magnet axis. This magnet system, called the Twin-Helix [10], produces muon orbits as shown in Figure 5, with a possible coil configuration shown in Figure 6. Here the horizontal and vertical betatron wavelengths differ by a factor of two so energy loss wedge absorbers are placed at every focal point in one plane where the same position corresponds to every other focal point in the other plane. The dispersion is also correlated in that it is small but not zero at the focal points and RF cavities, but large between absorbers where aberration correction magnets can be located.

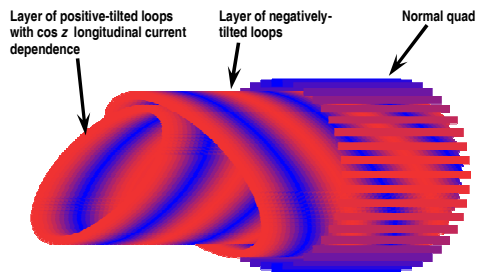


Figure 6: Possible coil configuration for the Twin Helix magnet system.

### Space Charge

At some points in the muon cooling channel, the bunching could be extreme, where some estimates are as high as  $10^{13}$  muons in an RF bucket, and the energy low enough to anticipate that space charge effects can be problematic. Through a project supported by the SBIR-STTR program, space charge calculation capability has been added to G4beamline. The transitions between cooling channel segments will incorporate the appropriate criteria to manage any space charge tune shifts.

### Gas, Vacuum, and Liquid transitions

Transitions between cooling channel segments may also involve windows or pressure barriers to separate vacuum, pressurized gas, or liquid hydrogen regions. It is quite likely that the beam sizes or beta functions at the window locations will have to be included in the constraints for the matching regions in order to reduce emittance growth from multiple scattering or to help solve engineering problems.

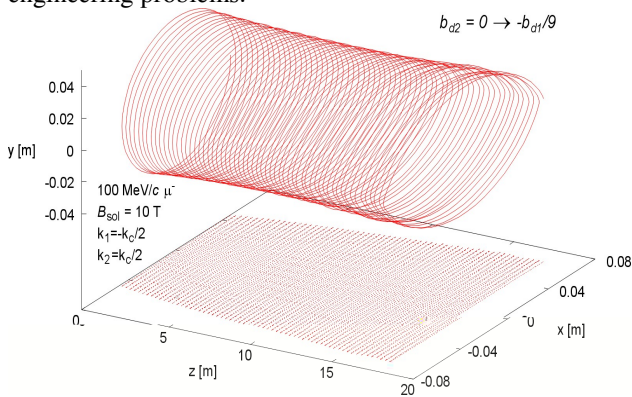


Figure 7: Adiabatic turn-on of the secondary helical dipole. The cyclotron wave number is  $k_c = qB/cp_z$ . The wave numbers  $k_1$  and  $k_2$  refer to the primary and secondary dipole fields, respectively.

As for creating the matching sections, one approach is an adiabatic turn-on of various components of an HCC. A demonstration of this is shown in Figure 7, where a particle is initially in an HCC that consists of a single helical dipole component. The desire here is to match into another HCC that consists of two helical dipoles, the second of which has a magnetic strength of  $-1/9$  of the primary dipole, and what is shown is an adiabatic turn on

of that second helical dipole component. Note how the initially circular orbit transforms into an elliptical trajectory.

Since a solenoid may be thought of as a special case of an HCC with the dipole component turned off, this adiabatic approach seems promising to match between a solenoid and any type of helical channel. Furthermore, the HCC theory may be extended to segments without solenoid field components such as the Twin-Helix.

## CONCLUSIONS

The HCC theory and its extensions can be used to solve a wide variety of emittance manipulation and beam cooling problems that are needed to create intense muon beams suitable for a collider. A new use under development is to provide the emittance matching sections between cooling section segments which have very different parameters. Helical solenoid engineering solutions for HCC fields and recent proof of principle hydrogen pressurized RF cavity experiments with intense beams give confidence that practical, complete muon cooling designs will enable an energy frontier collider.

## REFERENCES

- [1] Y. S. Derbenev and R. P. Johnson, Phys. Rev. ST – Accelerators and Beams 8 (2005) 041002
- [2] D. Neuffer, C. Ankenbrandt, R. P. Johnson, C. Yoshikawa, “Muon Capture, Phase Rotation, and Precooling in Pressurized RF Cavities,” PAC09, WEGPFP089
- [3] V. S. Morozov, Y. S. Derbenev, A. Afanasev, R. P. Johnson, “Epicyclic Twin-Helix Ionization Cooling Simulations.” IPAC11, WEPZ009
- [4] <http://wwwasd.web.cern.ch/wwwasd/geant4/geant4>
- [5] T. J. Roberts et al., "G4BL Simulation Program for Matter-dominated Beamlines", Proc. PAC07, Albuquerque, NM, pp. 3468-3470 (2007)
- [6] R. Fernow, ICOOL, <http://pubweb.bnl.gov/users/fernaw/www/icool/readme.html>
- [7] K. Yonehara, R. P. Johnson, M. Neubauer, Y. S. Derbenev, “A helical cooling channel system for muon colliders” , IPAC10, MOPD076 <http://epaper.kek.jp/IPAC10/papers/mopd076.pdf>
- [8] V. Kashikhin et al., “Design Studies of Magnet Systems for Muon Helical Cooling Channels”, Proc. EPAC 08, Genoa, Italy, 23-27 Jun 2008, pp. 2437-2439.
- [9] R. P. Johnson et al., “High Pressure, High Gradient RF Cavities for Muon Beam Cooling”, Proc. LINAC 2004, Lubeck, Germany, p.266 (2004)
- [10] V. S. Morozov, Y. S. Derbenev, A. Afanasev, R. P. Johnson, B. Erdelyi, J. A. Maloney, PAC11 WEPZ009

# MICE STEP I: FIRST MEASUREMENT OF EMITTANCE WITH PARTICLE PHYSICS DETECTORS

R. Asfandiyarov\*, DPNC, University of Geneva, Switzerland  
On Behalf of the MICE Collaboration

## Abstract

The muon ionization cooling experiment (MICE) is a strategic R&D project intending to demonstrate the only practical solution to prepare high brilliance beams necessary for a neutrino factory or muon colliders. MICE is under development at the Rutherford Appleton Laboratory (UK). It comprises a dedicated beam line to generate a range of input emittance and momentum, with time-of-flight and Cherenkov detectors to ensure a pure muon beam. The emittance of the incoming beam is measured in the upstream magnetic spectrometer with a scintillating fiber tracker. A cooling cell will then follow, alternating energy loss in liquid hydrogen absorbers and RF acceleration. A second spectrometer identical to the first and a second muon identification system measure the outgoing emittance. In the 2010 run the beam and most detectors have been fully commissioned and a first measurement of the emittance of a beam with particle physics (time-of-flight) detectors has been performed. The analysis of these data is presented here. The next steps of more precise measurements, of emittance and emittance reduction (cooling), that will follow in 2011 and later, are also outlined.

## INTRODUCTION

The Muon Ionization Cooling Experiment (MICE) collaboration is building a lattice cell of the cooling channel [1] of Neutrino Factory of Neutrino Factory Feasibility Study-II [2] at a muon beam line at the ISIS proton accelerator at the Rutherford Appleton Laboratory in the UK. In order to demonstrate cooling over a range of emittances and momenta, the beam line must generate several matched beams with different optical parameters at TOF1.

The normalized root mean square (RMS) emittance in 6 dimensions is defined as

$$\epsilon_{rms} = \frac{1}{m_\mu} \sqrt{|V|},$$

$|V|$  is the determinant of the  $6 \times 6$  covariance matrix of the phase space vector  $\vec{U} = (\vec{x}, \vec{p})$ , where  $\vec{x} = (x, y, t)$  and  $\vec{p} = (p_x, p_y, E)$ . All these 6 variables will be measured in spectrometers before and after cooling cell on a particle-by-particle basis and then bunched to up to  $10^6$  particles for emittance calculation. The beam before colling channel can be measured by timing detectors. Data from TOF0 and TOF1 were used already to analyze the performance of the existing MICE muon beam line.

\* ruslan.asfandiyarov@unige.ch

## Technique

Data from timing detectors TOF0 and TOF1 are used to analyze the performance of the MICE muon beam line (Figure 1). Both detectors are composed of two orthogonally oriented planes of scintillator slabs read out at each end by photomultiplier tubes, and measure time with resolution  $\sigma_t = 50$  ps [3]. Particle species is determined by measuring the time of flight between TOF0 and TOF1. Longitudinal momentum may then be reconstructed using an iterative method.

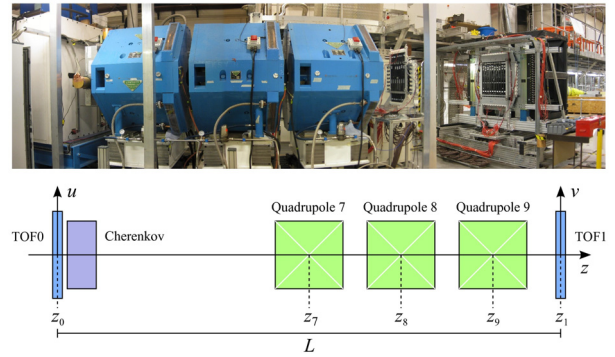


Figure 1: The MICE time of flight system.

The average momentum between the TOFs is given by

$$p(s, t) = \frac{m_0 s/t}{\sqrt{1 - s^2/(ct)^2}},$$

where the path length  $s = L + \delta$  is reconstructed by tracking (Figure 2) the particle's trace-space vectors  $(x, dx/dz)$  and  $(y, dy/dz)$  through the beam line, and integrating the path length through each section. The initial trace space vector at TOF0 can be transported to TOF1 by a transfer matrix  $(x_1, x'_1) = M(x_0, x'_0)$  defined by quadrupole parameters. Since the TOFs provide a measurement of  $(x_0, x_1)$  and that  $\det M = 1$  for linear transformation, it is possible to find the angles  $x' = dx/dz$  and  $y' = dy/dz$  needed for path length calculation:

$$\begin{pmatrix} x'_0 \\ x'_1 \end{pmatrix} = \frac{1}{M_{12}} \begin{pmatrix} -M_{11} & 1 \\ -1 & M_{22} \end{pmatrix} \begin{pmatrix} x_0 \\ x_1 \end{pmatrix}$$

A set of beam line optics configurations have been generated and corresponding beam parameter measured by TOF system. All variables measured in data have been compared with simulation.

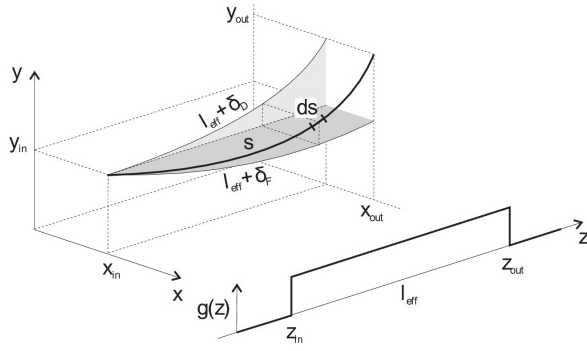


Figure 2: Particle reconstruction technique.

## MEASURED OPTICAL BEAM PARAMETERS

A sample time of flight spectrum for a base line  $\mu^-$  beam is shown in Figure 3. An electron peak is clearly distinguishable at 25.7 ns. As the electrons have  $E \sim m$ , this is used to calibrate the time of flight of the muons. The broad peak at 28.3 ns is mainly made up of muons. This is borne out by the Monte Carlo simulation results plotted on the same graph, which indicate a pion contamination  $\approx 1\%$ . The simulated beams were generated by G4Beamline, a beam line simulation program which models particle interactions in matter in detail [4].

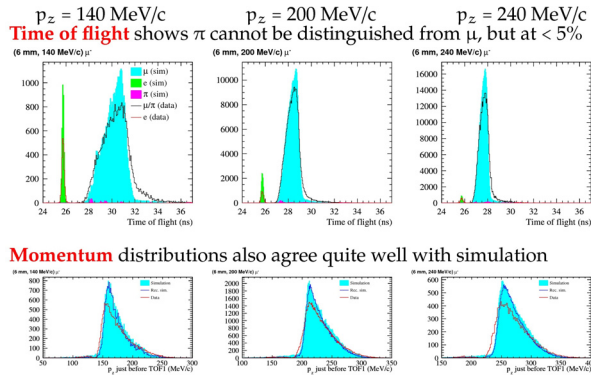


Figure 3: A comparison of the simulation and data.(top) The time of flight between TOF0 and TOF1. (bottom) The longitudinal momentum at TOF1.

The discrepancy between data and reconstructed simulation at the low- $p_z$  edge is ascribed to model sensitivity to the size of the magnet apertures given the significant horizontal dispersion, and the fast variation in  $M(p_z)$  at low momenta. This anomaly is not a concern for MICE as this portion of the momentum spectrum is not optimized for transmission in the subsequent cooling channel.

The distribution of the baseline beam in trace space thereby deduced is shown in Figure 4. The transverse trace space distribution of the base line beam is reconstructed with resolution  $\sim 10$  mrad arising from the position resolution and the effects of multiple scattering in equal part. The Muon cooling

orientation of the trace ellipse varies as a function of  $p_z$ , resulting in the visible skew. The reconstruction procedure is shown to skew the true distribution predominantly in the fringes of the distribution, where nonlinear effects are not negligible.

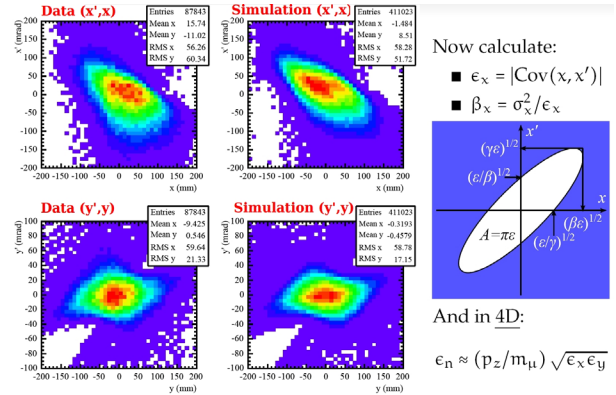


Figure 4: The reconstructed transverse trace space of the baseline beam at TOF1.

As the beam size in a plane is uniquely determined by the emittance and betatron function, contours of constant beam size are drawn in Figure 5. In both horizontal and vertical phase space, we note that all beams have RMS beam sizes between 5 and 7 cm. This illustrates further that this beam line is dominated by scraping in the quadrupoles, as demonstrated in simulations, where  $\sim 60\%$  of muons are scraped in quadrupole 7. As a result of the constancy of  $\sigma_x$  and  $\sigma_y$ , the betatron function is determined by the emittance to first order. Trends may also be observed in polarity and momentum. In both planes,  $\mu^+$  beams tend to have a higher emittance than  $\mu^-$  beams. This is a result of the inclusion of a proton absorber in the  $\mu^+$  beams which heats the beams slightly. We also observe that low- $p_z$  beams have a higher emittance. This is because the focusing strength of a quadrupole is proportional to  $1/p_z$ . As the 140 MeV/c beams are focused more powerfully by the magnets, they have a higher amplitude acceptance, and therefore a higher emittance.

Beams designed to have every combination of  $\epsilon_n = (3, 6, 10)$  mm upstream of the first liquid hydrogen absorber, and  $p_z = (140, 200, 240)$  MeV/c in the center of each absorber. Muon beams of both polarities were generated and key optics parameter measured at TOF1. The transverse normalized emittance is related to the measured values of  $\epsilon_x$  and  $\epsilon_y$  as  $\epsilon_n \approx (p_z/m) \sqrt{\epsilon_x \epsilon_y}$ . The emittance of the incoming beam, measured by TOF0, TOF1 is much smaller than that of the beam that will go through the cooling channel. In order to generate the desired large emittance the beam goes through a high Z diffuser of adjustable thickness situated inside the first solenoid (Figure 6).

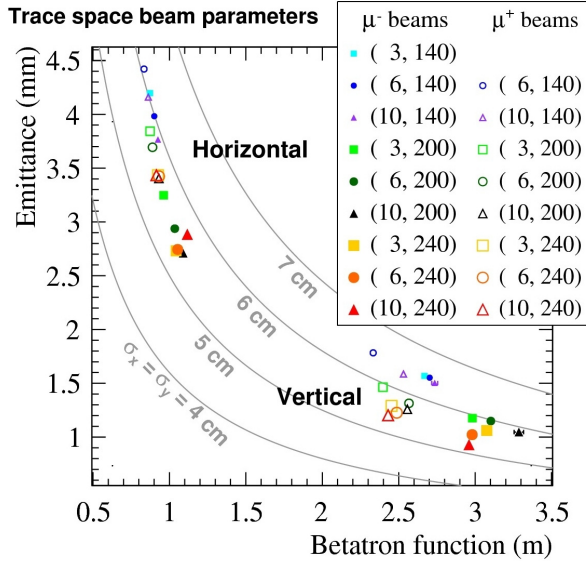


Figure 5: The betatron function and RMS trace emittance for all of the matched beams in both the horizontal and vertical planes, as measured just before the TOF1 detector.

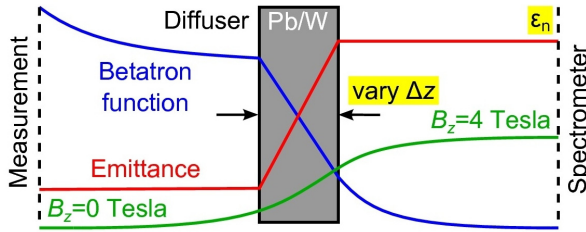


Figure 6: Diffuser matching.

## SIMULATION OF THE MEASURED BEAM

A beam, starting at TOF1, with the transverse distributions characteristic of the measured beam was simulated in full MICE cooling channel. The simulated beam was generated according to the measured covariance matrix of the four transverse phase space coordinates and therefore had the emittance and optical parameters of the real beam (Figure 7). Dashed line is the reference particle traveling along the axis.

The evolution of the transverse beta function along the MICE cooling channel of the real beam has been also simulated (Figure 8). The optics of the beam are seen to be similar to the ideal optics (red line) derived from a numerical solution to betatron equation:

$$2\beta_{\perp}\beta'_{\perp} - (\beta'_{\perp})^2 + 4\beta_{\perp}^2\kappa^2 - 4 = 0$$

where  $\kappa$  is the focusing strength.

Figure 9 shows the evolution of the emittance of the simulated real beam. The emittance of the simulated real beam Muon cooling

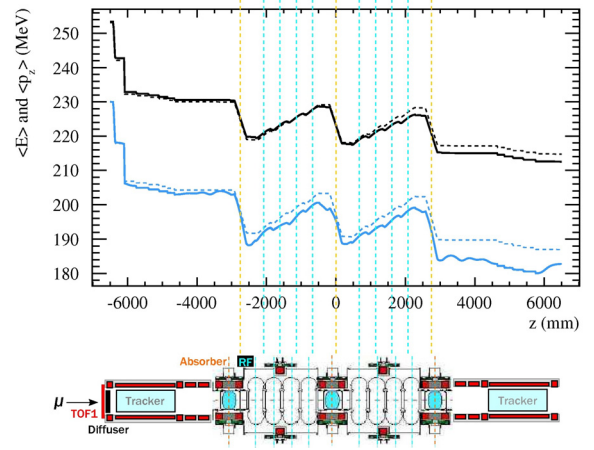


Figure 7: Measured beam simulation.

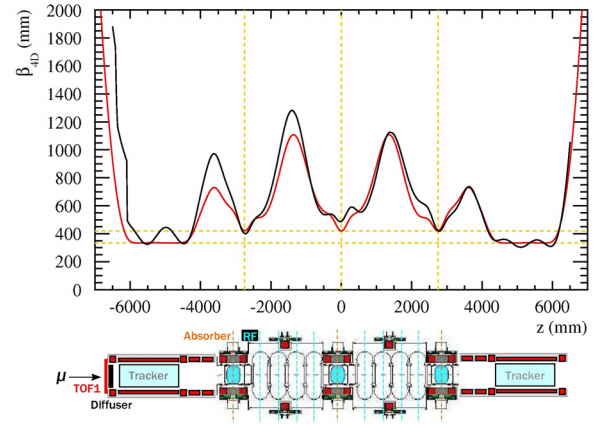


Figure 8: Beam envelope.

is slightly higher than the nominal 6 mm but decreases as expected at the absorbers. The initial overinflation of the emittance to 8 instead of 6 mm may be corrected by the use of a thinner lead diffuser disc. Despite no transverse selection or re-weighting having taken place, the optics of the beam behave tolerably well and the simulated real beam is seen to be cooled. It is anticipated that only a small re-weighting of the measured beam will be required.

## CONCLUSIONS

The MICE collaboration intends to use beams with central momenta ranging from 140 MeV/c to 240 MeV/c, and normalized emittances between 3 and 10 mm. Several beams designed to have appropriate optical parameters were generated in a successful data taking campaign in 2010. Timing detectors of  $\sim 50$  ps resolution confirm the generation of beams dominated by muons at the required momenta.

Distributions of the trace space vectors of individual muons have been reconstructed for the various beams, and promising agreement is observed with Geant4 simulations.

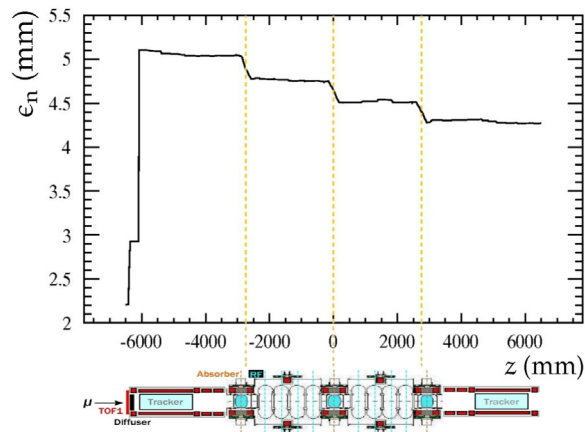


Figure 9: The baseline beam distribution measured in 2010 evolved through the final MICE lattice.

The evolution through MICE of the optical parameters of a measured baseline beam has then been simulated; the beam is relatively well matched, and tuning magnet currents and diffuser thickness should be sufficient to generate a well matched beam.

## REFERENCES

- [1] R.Asfandiyarov, Progress in the Construction of the MICE Cooling Channel, this proceedings.
- [2] S. Ozaki, R. Palmer, M. Zisman, and J. Gallardo (eds.), Feasibility Study-II of a Muon-Based Neutrino Source, Tech. Rept. BNL-52623 (2001). <http://www.cap.bnl.gov/mumu/studyii/FS2-report.html>
- [3] R. Bertoni et al., The Design and Commissioning of the MICE Upstream Time-of-Flight System, Nucl. Instrum. Meth. A, 615 (2010) pp. 1426. <http://arxiv.org/abs/1001.4426v2>
- [4] T. Roberts. A Swiss army knife for Geant4, optimized for simulating beam lines: <http://www.muonsinc.com/tiki-index.php>

# PROGRESS IN THE CONSTRUCTION OF THE MICE COOLING CHANNEL

R. Asfandiyarov\*, DPNC, University of Geneva, Switzerland  
On Behalf of the MICE Collaboration

## Abstract

The international Muon Ionization Cooling Experiment (MICE), sited at Rutherford Appleton Laboratory in the UK, aims to build and test one cell of a realistic ionization cooling channel lattice. This comprises three AbsorberFocus-Coil (AFC) modules and two RF-Coupling-Coil (RFCC) modules; both are technically challenging. The Focus Coils are dual-coil superconducting solenoids, in close proximity, wound on a common mandrel. Each pair of coils is run in series, but can be configured with the coil polarities the same (solenoid mode) or opposite (gradient mode). At the center of each FC there is a 20-L liquid-hydrogen absorber, operating at about 14 K, to serve as the energy loss medium for the ionization cooling process. The longitudinal beam momentum is restored in the RFCC modules, each of which houses four 201.25-MHz RF cavities whose irises are closed with 42-cm diameter thin Be windows. To contain the muon beam, each RFCC module also has a 1.4-m diameter superconducting coupling solenoid surrounding the cavities. Both types of magnet are cooled with multiple 2-stage cryo-coolers, each delivering 1.5 W of cooling at 4 K. Designs for all components are complete and fabrication is under way. Descriptions of the various components, design requirements, and construction status is described.

## INTRODUCTION

Neutrino Factory [1] (Figure 1) based on muon storage ring is the ultimate tool for studies of neutrino physics [2]. It is also a first step towards a muon collider. One of the challenges posed is the control of the large emittances possessed by muons produced from pion decay at the proton driver target. Ionization cooling is a proposed mechanism to reduce this on a suitably short timescale. It has never been demonstrated in practice but has been shown by simulation and design studies to be an important factor both for the performance and for the cost of a Neutrino Factory.

The MICE collaboration has designed an experiment [3] in which a section of cooling channel is exposed to a muon beam, which would demonstrate and explore this technique for the first time in practice. It is proposed to install MICE at the ISIS facility [4], at Rutherford Appleton Laboratory (RAL).

The MICE collaboration started in 2001 and now rallies about 140 people, engineers, accelerator and particle physicists from more than 40 institutes in Europe, USA, China

\*ruslan.asfandiyarov@unige.ch

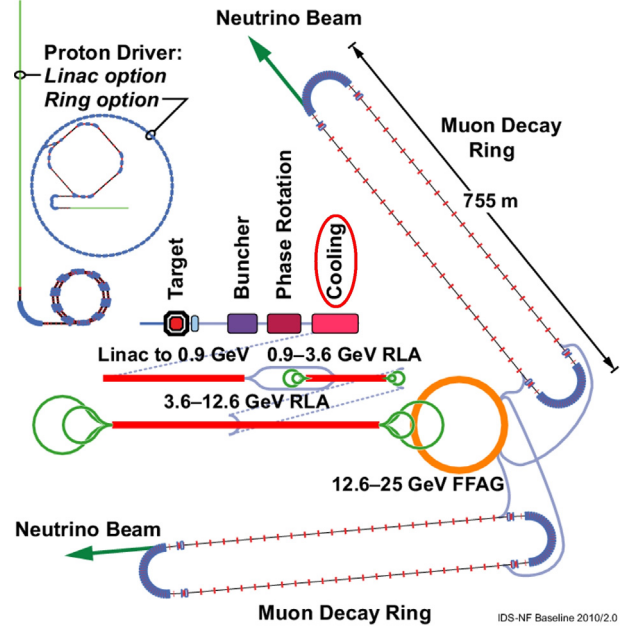


Figure 1: Neutrino Factory baseline scheme.

and Japan. The MICE collaboration is working together with the US MuCool Collaboration with whom it shares several objectives.

## Ionization Cooling

The principle of ionization cooling relies on the cooling rate formula, expressing the emittance variation in a medium with thickness  $X$  ( $g \cdot cm^2$ ) due to ionization (cooling) and multiple scattering (heating):

$$\frac{d\epsilon_n}{dX} = -\frac{\epsilon_n}{\beta^2 E_\mu} \left\langle \frac{dE_\mu}{dX} \right\rangle + \frac{\beta_t (0.014 GeV)^2}{2\beta^3 E_\mu m_\mu X_0} \quad (1)$$

where  $\epsilon_n$  is the normalized 4D emittance of the beam,  $\beta_t$  is the betatron function, and  $\beta$  is the velocity of the particle. The ideal cooling channel should produce the lowest possible emittance:

$$\epsilon_{eq} = \frac{\beta_t (0.014 GeV)^2}{2\beta m_\mu X_0} \left\langle \frac{dE_\mu}{dX} \right\rangle^{-1} \quad (2)$$

Hence, the goal is to minimize the  $\beta_t$  and maximize  $X_0 \left\langle \frac{dE_\mu}{dX} \right\rangle$ . Therefore liquid hydrogen has been chosen for the first realization of the absorber of a cooling channel.

Due to the short muon lifetime ( $2.2 \mu s$ ), ionization cooling must be used. The cooling of the transverse phase-space coordinates of a muon beam can be accomplished

by passing it through a light energy-absorbing material and an accelerating structure as shown in Figure 2, both embedded within a focusing magnetic lattice. Longitudinal and transverse momentum are lost in the absorber while the RF-cavities restore only the longitudinal component.

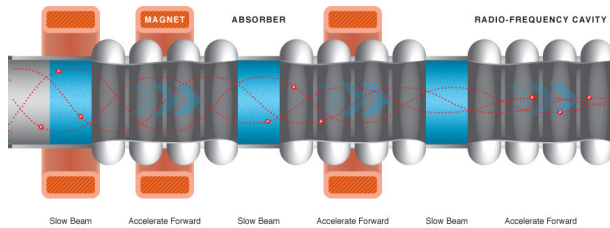


Figure 2: To create a narrow, uniform muon beam, particles are sent through a series of absorbers and cavities.

The MICE aims to construct a cooling cell (Figure 3) with all the equipment necessary to measure the emittance of a muon beam before and after this cell based on single particle measurements and achieve 10% cooling of 200 MeV/c muons. The cooling cell will be sandwiched between two identical trackers inside 4T superconducting solenoids, complemented by upstream and downstream particle detectors.

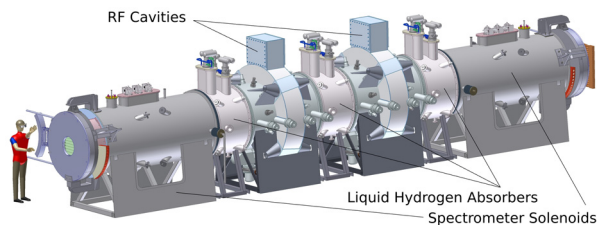


Figure 3: 3D view of the MICE cooling cell.

## BEAM LINE

The ISIS synchrotron accelerates a high intensity proton up to 800 MeV,  $300\mu\text{A}$  at 50 Hz. To provide muons for MICE, an internal target is installed, which provides a source of pions for a pion-muon decay channel, and thereby provide muons for MICE. The muon beamline [5] makes use of existing dipole and quadrupole magnets, together with a superconducting solenoid contributed by PSI in Switzerland. MICE requires muon momenta 140-240 MeV/c, with a  $\pm 10\%$  momentum acceptance. Both muon signs can be obtained by switching magnet polarities.

The beamline splits into three parts: a pion capture and selection section, a pion-muon decay section and a transport line to convey muons to MICE. The last section also hosts a thick lead scatterer, and serves to generate the large emittances and match the beam into the experiment. A schematic of the beamline layout is shown in Figure 4.

The beamline has been already installed: target, Q1, Q2, Q3, D1 inside ISIS synchrotron enclosure; decay solenoid,

Ionization cooling

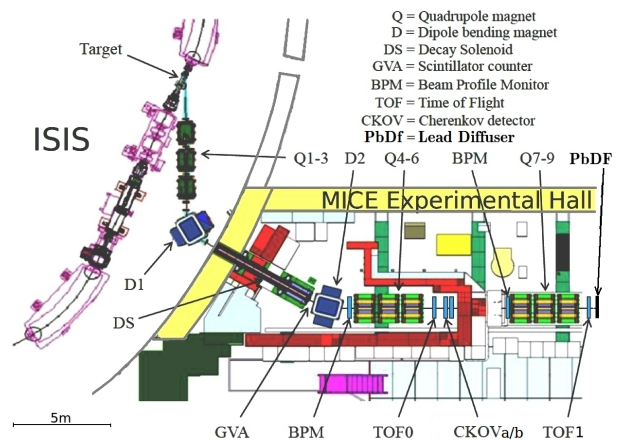


Figure 4: The layout of MICE muon beamline.

Q4, Q5, Q6, TOF0, CKOVa/b inside decay solenoid area and Q7, Q8, Q9, TOF2, KL in the MICE Hall (Figure 5).



Figure 5: Recent photo of the MICE Hall.

A dedicated system has been designed in Sheffield to dip the Ti target into the halo of the beam in the few milliseconds preceding the extraction of the primary proton beam. The main constraint was that the target should be completely out of the way when the injection of the next ISIS bunch starts. The acceleration of  $80g \text{ m/s}^2$  necessary to meet this requirement has been achieved recently with the target attached to a leaded bronze shaft driven by induction coils. The system has been running reliably for more than 12 weeks at a rate of 1 Hz, producing more than 5 millions actuations.

The first section of the beamline is designed to capture as large a pion acceptance as possible from the target, and to momentum select the pions into the decay section. It has been designed to select high momentum pions, such that the muons are derived from backward decay in the pion rest frame. This has advantages in terms of the final muon flux and purity. The decay solenoid then serves to accumulate as large a flux of muons as possible. Muon extraction section consists of a large aperture dipole, to select muons of the desired momentum, and two sets of large aperture quadrupole triplets to transport the muon beam towards the experiment. The half-widths of the pion-muon beam profile are illustrated in Figure 6.

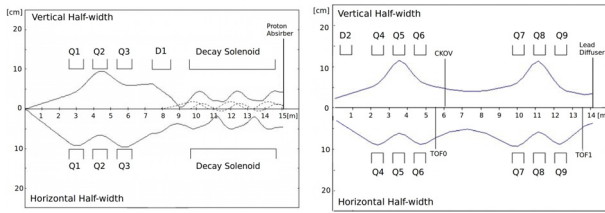


Figure 6: Beam profile for the pion injection, decay and extraction sections.

### COOLING CHANNEL

The Layout of the MICE Cooling Cell is shown in Figure 7. It consists of three, 35 cm, liquid-hydrogen absorbers to achieve a 10% reduction in emittance and eight 201 MHz RF cavities to re-accelerate the muon beam. Trackers within 4 T solenoids make single particle measurements at each end of the cooling channel. Each tracker consists of five scintillating-fibre planes, measuring x, y, px, py, which are transverse coordinates to the beam, and the muon energy. A pair of match coils in each spectrometer tune the magnetic optics to match the muon beam into and out of the cooling lattice.

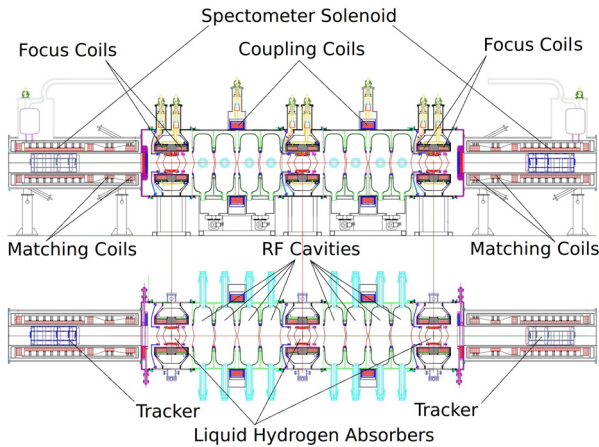


Figure 7: The Layout of the MICE Cooling Cell.

### Liquid Hydrogen Absorber Module

The absorber module is made of two main components - the liquid hydrogen container and distribution system. It represents a considerable safety challenge. The container is 35 cm long for a volume of 20 liters. It is sealed by 0.18 mm, curved aluminum windows. The entire system is double walled for safety reasons. The 3D view of the module is shown in Figure 8. Each muon loses about 12 MeV in the absorber, i.e. 1 W for a beam of  $5 \cdot 10^{11}$  muons per second. The absorbers have been built in KEK, Japan in 2010 and the first one has been already delivered to RAL (Figure 9, left). The set of two focus coils provides small  $\beta_t$  inside the absorber. The winding of the coils is complete Ionization cooling

(Figure 9, right) and installation in the Hall is scheduled for the end of this year.

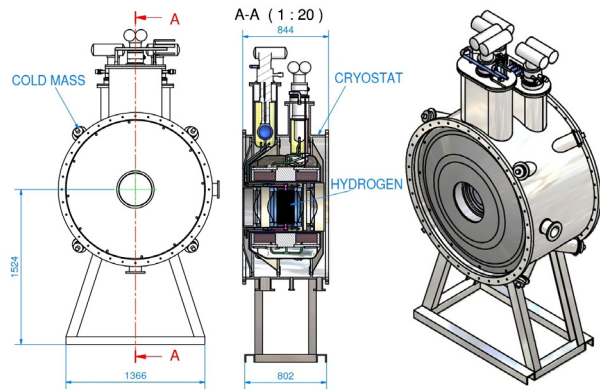


Figure 8: CAD drawings of the liquid hydrogen absorber module.



Figure 9: Progress in construction of the liquid hydrogen absorber module and focusing coils.

### RF and Coupling Coil (RFCC) Module

RFCC module (Figure 10) has four 201 MHz normal-conducting RF cavities and one superconducting coupling coil (solenoid) magnet. Each RF cavity has a pair of curved Be windows and it operates in a few Tesla magnetic field at 8 MV/m.

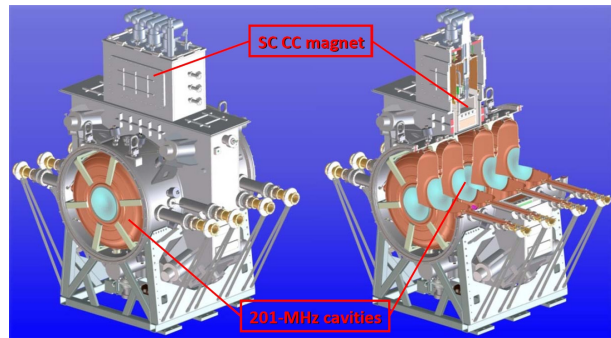


Figure 10: 3D view of the RFCC module.

Ten RF cavities (Figure 11, left) and nine berilium windows (Figure 11, middle) have been manufactured and received at BNL for further tests in 2010. First coupling coil

winding is completed at Qi Huan Company already (Figure 11, right).

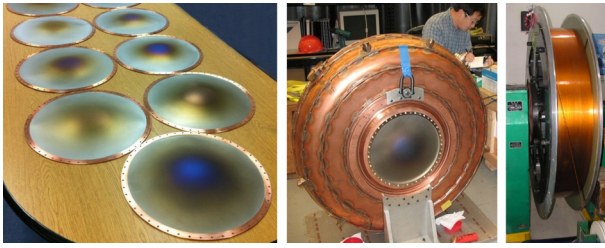


Figure 11: Progress in construction of the RFCC Module.

### Spectrometer Solenoids

The two spectrometers modules (Figure 12) are fully symmetrical. Each is made of a cylindrical tracker immersed into a solenoid field of 4 T. The main solenoid coil is flanked by two correcting coils ensuring field uniformity. Two additional coils on the absorber side provide matching optics with the cooling cell. The three coils are connected in series and are powered by a single 300 amp power supply.

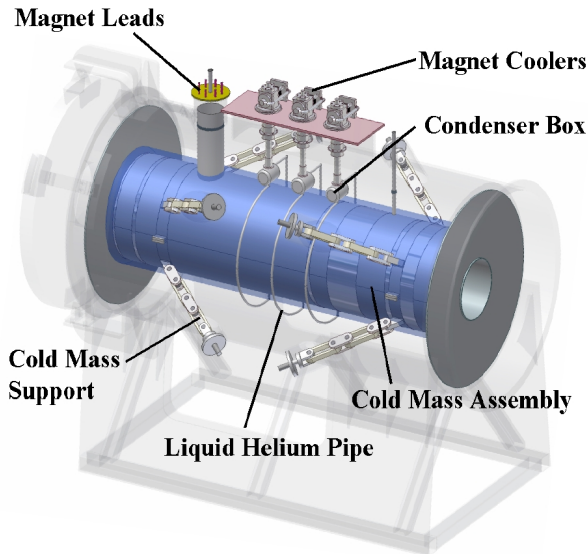


Figure 12: The layout of the spectrometer solenoid module.

The magnets have been produced in US (Figure 14). The first module is to be completed and ready for tests by the end of 2011 and the second one in three months. The modules will be delivered to RAL in 2012.

### Scintillating Fibers Tracker

The tracker (Figure 15) is made of 5 stations of 350 $\mu$ m scintillating fibers perpendicular to the beam axis. The station is made of three planes of fibers rotated by 120. This allows to reconstruct the full helix track and obtain the momentum. The optical connectors on the station mates seven

Ionization cooling

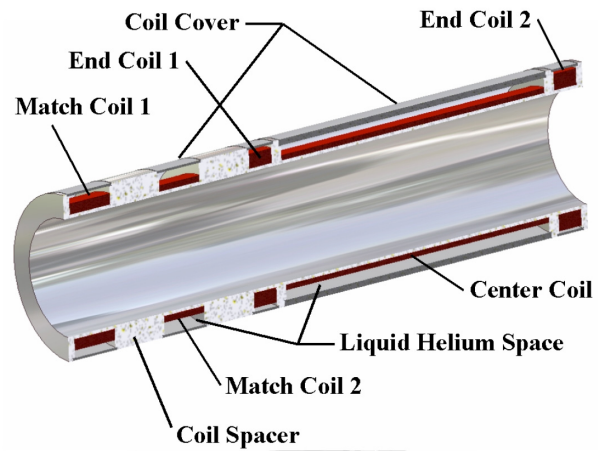


Figure 13: Composition of the spectrometer solenoid module.



Figure 14: Progress in construction of the spectrometer solenoid modules.

scintillating fibers to 1.05 mm clear-fiber light guide which transports the light from the stations to an optical patch panel mounted on the end flange of the magnet cryostat. The scintillation light is detected by Visible Light Photon Counters - low band-gap silicon avalanche detectors operated at  $\sim$ 9K.

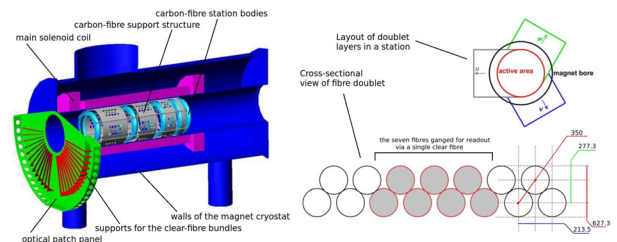


Figure 15: Scintillating fibers tracker layout.

Both of the upstream and downstream trackers have been constructed (Figure 16) and performance has been examined with cosmic-ray runs performed at RAL in 2008-2009: light-yield  $11.23 \pm 0.01$  photo electrons; RMS of the residual distributions  $682 \mu\text{m} \pm 1 \mu\text{m}$ ; channel resolution  $470 \mu\text{m}$ ; space-point efficiencies 99.7% for each station.



Figure 16: Progress in construction of the scintillating fibers tracker.

### PARTICLE IDENTIFICATION (PID) DETECTORS

PID is obtained upstream of the first tracking solenoid by two TOF stations (TOF0/TOF1) [6] and two threshold Cherenkov counters (CKOVa/CKOVb), that will provide muon/pion/electron separation up to 300 MeV/c. Downstream the PID is obtained via a further TOF station (TOF2) and calorimeters (KL and EMR), to separate muons from decay electrons. All TOF detectors are used to determine the time coordinate in the measurement of the emittance.

#### Time of Flight Stations: TOF0, TOF1, TOF2

The TOF stations (Figure 17) are used in establishing a precision particle trigger which can be synchronized to within 70 ps of the RF cavity phase. TOFs are made of two crossed planes of plastic scintillator bars 2.54 cm thick and 4-6 cm wide and cover ~50 cm<sup>2</sup> active area. The signal is readout from both ends of scintillator bars by fast PMTs shielded against stray magnetic field which provide 50-60 ps intrinsic timing resolution. A trigger signal is given by the first dual coincidence of the PMTs connected to the same TOF0 bar.

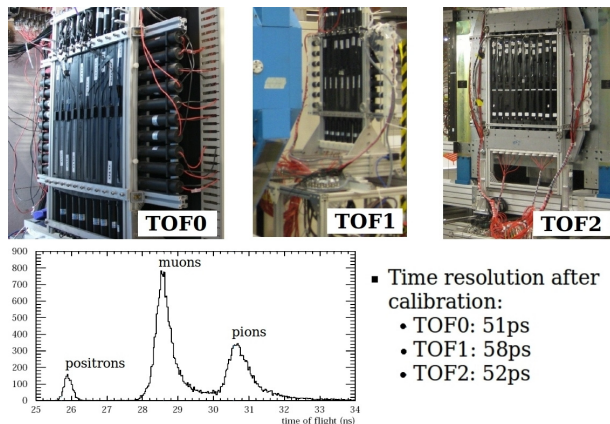


Figure 17: Progress in construction of the time of flight stations.

Ionization cooling

#### Cherenkov Counters: CKOVa, CKOVb

The two Cherenkov counters share the same design (Figure 18). The Cherenkov light produced in a 2.3 cm thick layer of hydrophobic aerogel is collected by four intersecting conical mirrors reflecting it on four 8" PMTs. Refractive indices of 1.07 and 1.12 are used respectively for the two aerogel planes, ensuring a good muon/pion/electron separation at high momentum: electrons trigger both counters, muons - only one and pions - none. At lower momentum, the TOF counters can be used to complete the PID. CKOVs have been installed in the beamline (Figure 19).

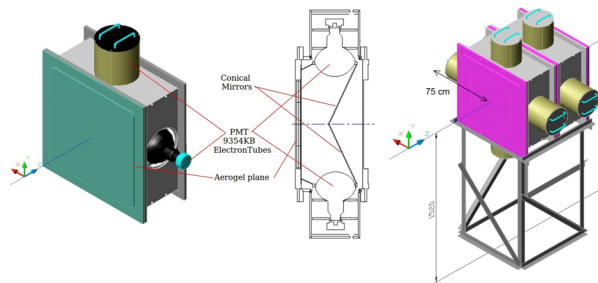


Figure 18: 3D view of the Cherenkov detectors.



Figure 19: Progress in construction of Cherenkov Counters: CKOVa, CKOVb

#### Calorimeter: KL

The calorimeters are dedicated to the separation between the muons and the electrons produced by muon decaying in the cooling channel. A design study has demonstrated that a better particle identification is obtained with a detector made of two parts. The first part (KL) is a 4 cm thick conventional sampling calorimeter made of grooved lead foils interleaved with scintillating fibers. It forces the electrons to shower while most of the muons are going through. The second part is EMR.

The KL electromagnetic calorimeter was installed in the MICE Hall in June 2008 and operates successfully since then. It allows to distinguish between electrons, muons and pions at different energies. Muons/electrons/pions with momentum above 135/160/70 MeV/c at KL entrance will pass through KL.

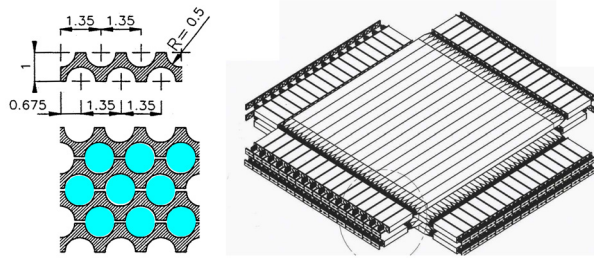


Figure 20: 3D view of KL detector.

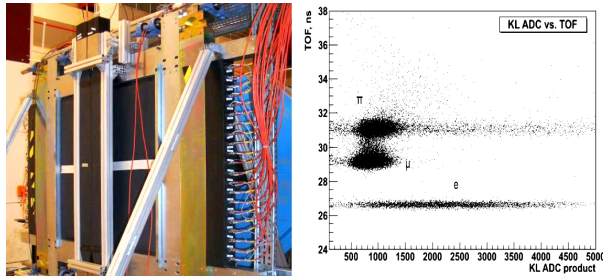


Figure 21: Progress in construction of KL calorimeter.

### Calorimeter: Electron-Muon Ranger (EMR)

A fully active scintillator calorimeter (Figure 22) is located at the very end of the cooling channel. It will stop all muons and electrons and give very distinct signatures for both allowing to measure particle range. It has  $1 \text{ m}^3$  of active volume, 48 planes composed of 59 triangular scintillator bars with glued 1.2 mm wavelength shifting fibers; light is collected by single-anode PMT on one side of a plane and by 64-channel PMTs - on the other: 3120 channels in total; the granularity of the detector allows it to reconstruct individual tracks and measure energy deposition in every bar.

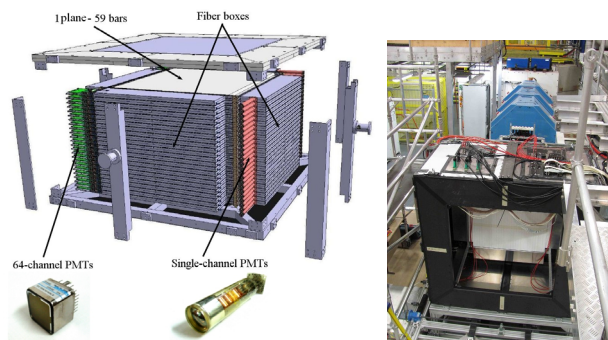


Figure 22: EMR detector design (left) and first tests at RAL (right).

EMR with 3 X-Y modules (6 planes) was installed in the MICE hall on June 16<sup>th</sup> for preliminary tests. Electronics and DAQ have been successfully tested. Construction will be finished next year.

Ionization cooling

## CONCLUSIONS

The installation of the MICE [7] experiment is underway at RAL, UK. The major challenge of the experiment is the operation of large gradient RF cavities in intense magnetic field and in the vicinity of liquid hydrogen cells. The beam line was commissioned in early 2008. Particle identification detectors have been installed in MICE hall and used for the first emittance measurements. Most of the components of the cooling channel have been produced and under commissioning. The first observation of ionization cooling with a partial setup is expected for October 2012, after the delivery of the first absorber. The setup with RF cavity is aimed for April 2014 (Figure 23).

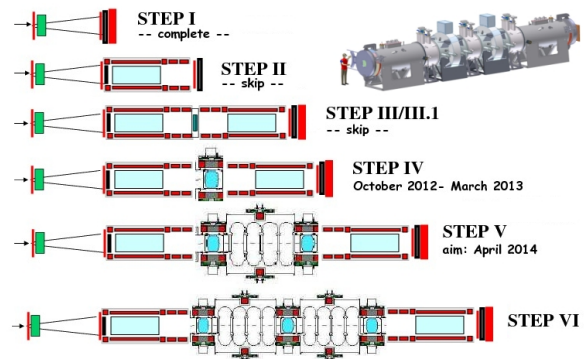


Figure 23: MICE Schedule.

## REFERENCES

- [1] S. Choubey et al., International Design Study for the Neutrino Factory, Interim Design Report, IDS-NF-20, <https://www.ids-nf.org/wiki/FrontPage/Documentation/IDR>
- [2] Albright, C. and Anderson, G. and Barger, V. and Bernstein, R. and Blazey, G. and others, Physics at a neutrino factory, 2000, <http://arxiv.org/abs/hep-ex/0008064v2>
- [3] An International Muon Ionization Cooling Experiment (MICE), Proposal to RAL, The MICE Collaboration, Jan 10th 2003. <http://mice.iit.edu/mnp/MICE0021.pdf>
- [4] ISIS Facility: <http://www.isis.stfc.ac.uk>
- [5] Coney, L. and Dobbs, A., Particle Production in the MICE Beamline, Presented at 2011 Particle Accelerator Conference (PAC'11), New York, NY, 28 Mar - 1 Apr 2011
- [6] R. Bertoni et al., The design and commissioning of the MICE upstream time-of-flight system, Nucl. Instr. Meth. A615, 14, 2010.
- [7] <http://mice.iit.edu>

# METHODS FOR OPTIMIZATION OF THE DYNAMICS OF THE STORAGE OF POSITRONS IN THE SURKO TRAP\*

A. G. Kobets, I.N. Meshkov, A.Y. Rudakov, S.L.Yakovenko, JINR, Dubna, Russia  
 M.K. Eseev<sup>#</sup>, Northern (Arctic) Federal University, Arkhangelsk, Russia

## Abstract

Surko traps are used successfully, example, for the accumulation of positrons and antiprotons in the experiments on the generation of antihydrogen atoms the ALPHA/CERN. The report presents methods for optimizing the dynamics of the storage of positrons in the Surko trap based on experimental studies on the trap the facility LEPTA/JINR and theoretical estimates of the accumulation and dynamics of particles with technique "Rotating Wall".

## INTRODUCTION

Open Penning-Malmberg trap successfully used in the generation of antihydrogen experiments ALPHA [1]. For the accumulation and compression of charged plasma of positrons and antiprotons before injection into the central part of the trap with magnetic mirrors, restraint produced atoms of antimatter, the method of rotating electric field (RW-«rotating wall») [2]. Stabilizing and compressive action of RW-field was first discovered in experiments on the accumulation of ions Mg+ [3]. Then the method used in the experiments with electron [4] and positron bunches [5]. In our experiments on the LEPTA [6,7], whose ultimate goal is to generate a directed flow of atoms of orthopositronium, we investigated the accumulation of positrons before introducing them into the storage ring. It was found that an increase in the lifetime and the number of accumulated particles of the bunch requires highly monochromatic flux of positrons from the sources. A study of instabilities of a non-neutral plasma in the trap, limiting the lifetime and the number of particles accumulated a bunch of positrons [8].

## EXPERIMENTS

We represent the results of our experiments on the accumulation of electron and positron plasma in the trap Surko.

### Experiments setup

Our facility is the trap open Penning-Malmberg type in the form of the hollow cylinder. Confinement of non-neutral plasma in the transverse direction with respect to the axis of the trap is carried out by the longitudinal of magnetic field magnetic field produced by solenoids. In the longitudinal direction of the storage plasma electrostatic potential for blocking electrodes. One-third of the storage region by the accumulation of the split RW-electrodes, giving the opportunity to include in the accumulation of rotating in the transverse direction the RW electric field.

Typical values for our the trap are shown in Table 1:

Table 1: The typical parameters of the our the trap

Parameters	Value	Comments
$E_{\omega}$ , V/cm	0.05	RW electric field
$f_{RW}$ , kHz	600	Frequency RW-field
$n_e$ , cm <sup>-3</sup>	$10^7 \div 10^8$	Density of storage particle
$\omega_p$ , c <sup>-1</sup>	$3.5 \cdot 10^7 \div 2 \cdot 10^8$	Plasma frequency
B, Gauss	1200	Longitudinal of magnetic field
$\omega_B$ , c <sup>-1</sup>	$2 \cdot 10^{10}$	Cyclotron frequency
$P_{N_2}$ , Torr	$2 \cdot 10^{-6}$	Buffer gas pressure (in storage region)
$R_T$ , cm	10	Radius of transverse plan electrode in the trap (in storage region)
$L_T$ , cm	48	Length of the electrodes in the trap (in storage region)
R, cm	$\sim 1 \div 2$	Radius of transverse plan the storage bunch
L, cm	$\sim 40$	Length of the storage bunch

Inside the trap creates a vacuum base. To capture the particles in the trap from a buffer gas (nitrogen) is used. The role of the buffer gas will be discussed further on. To trap a series of experiments were conducted with both electrons and positrons with. Here we can distinguish experiments:

- by measuring the collector current for damp the bunch collector,
- on photographing the dump discharge in the bunch to bunch phosphor screen,
- to measure the signal from the photomultiplier tube at the positron annihilation bunch.

### Storage of the electrons. Results of experiments with the collector

Measurements of the collector current can determine the number of storage particles. Performing these measurements at fixed times, we define the dependence of the accumulated particles from the accumulation time. To clarify the role of the rotating field, we carried out experiments on and off the field during accumulation. The results are shown in Fig. 1. Accumulation occurred at found us the optimal parameters: buffer gas pressure, the

\*Work supported by grant RFBR №09-02-00084, 11-02-08399.

<sup>#</sup>m\_eseev@mail.ru

magnitude magnetic field, amplitude, frequency and the direction of rotation of the RW-field.

Obviously, the strong influence of the rotating field in the process of storage. Proper use of this field allows you several times to increase the number of storage particles.

*Results of experiments with the CCD camera.  
Compress the bunch rotating field*

Next, we directly measured changes in the transverse dimensions of the bunch during the accumulation of the CCD camera, courtesy of colleagues of Budker INP.

The experiments presented in Figure 2. carried out as follows. Century 30 seconds went accumulation of electrons in the trap. Then turned off injection of particles into the trap and deduct the confinement particles. Switched on while holding the rotating field. From the experimental data shows that with increasing time of this field is compressed in the transverse bunch sizes. On brightness can be concluded that in the centre of the bunch increased concentration of particles. When you turn off the rotating field is the reverse process, i.e. expansion of the bunch.

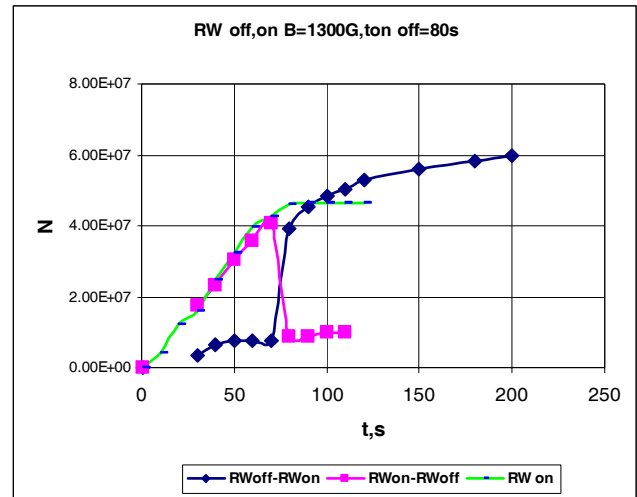


Figure 1: The dynamic storage electron bunch. Curve RWoff-on is dependence of the number of storage particles from the accumulation time, the RW-field is on after 80 sec. Curve RWon-off – the RW-field is off after 80 sec. Curve RWon – the RW-field is on all time of storage.

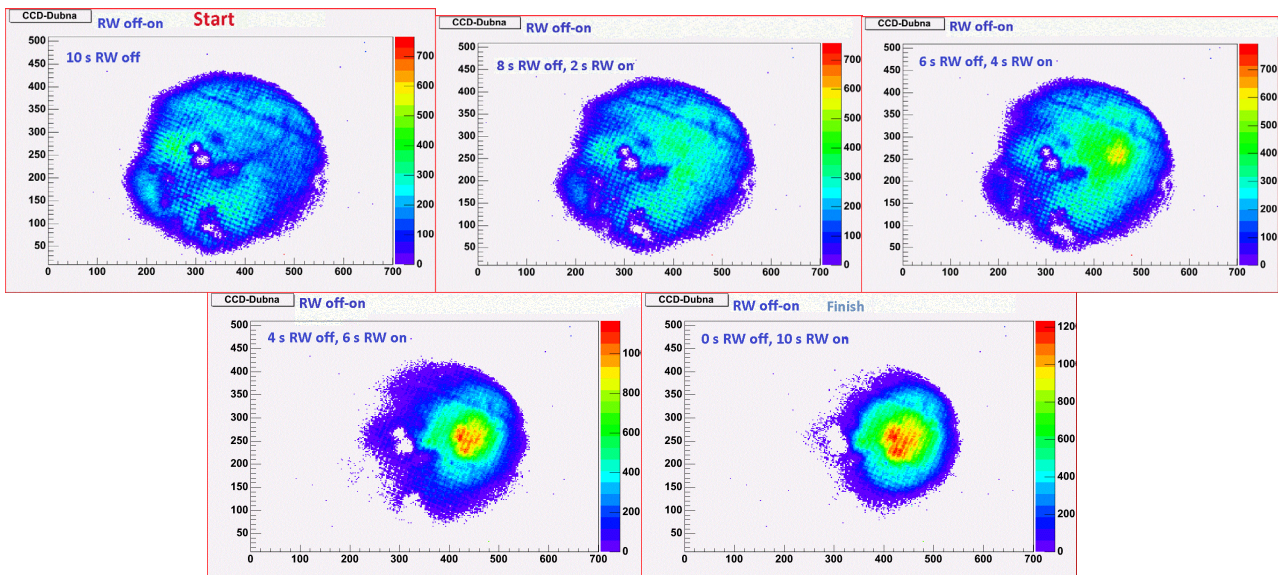


Figure 2: The photo (CCD) transverse plane of the storage electron bunch independent on time RW-field work. The effect is the bunch transverse compression RW-field.

*First experiments with positron storage*

The experiments on slow positron accumulation into the positron trap were started. The first results of the experiments are presented in the Figure 3. The experimental curve of the trapped positrons versus accumulation time (Upt – the signal from photoelectron tube proportional to the number of the accumulated positrons). These experiments show that the rotating field increases the number of accumulated particles, the lifetime of the bunch and compresses the bunch in the transverse size.

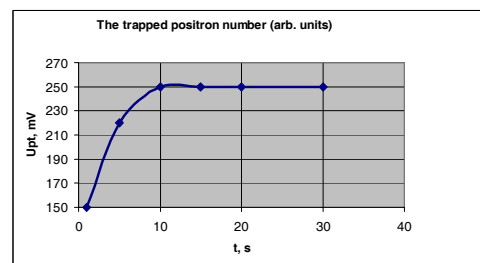


Figure 3: PMT signal (proportional to the trapped positrons number) vs accumulation time.

Storage and cooling of particles in antiproton and heavy ion traps

## TIMING OF THE TRANSVERSE AND LONGITUDINAL MOTION OF THE BUNCH IN THE TRAP

In the theoretical analysis of the accumulation of particular interest to the role of the rotating field. It should be noted that the frequency of the rotating field is significantly different from the characteristic frequencies for a fiery bunch in a magnetic field (see Table 1.). Previously, it was determined that the frequency and direction of this RW-field should coincide with the drift of the particle bunch in the crossed fields of space charge and longitudinal magnetic field [9]:

$$f_{RW} \gg f_E = \frac{cE_R}{2prB} = \frac{cne}{B}. \quad (1)$$

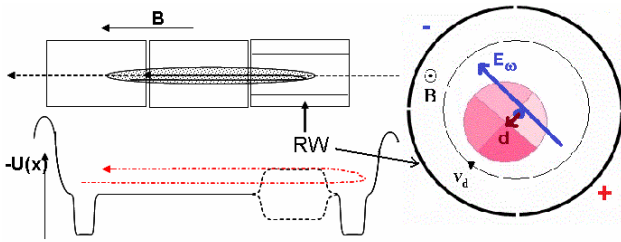


Figure 4: Simulation of transverse and longitudinal motion of the bunch in the trap.

In the accumulation of a small number of positrons [10] has been observed that this frequency is in good agreement with the frequency of the bounce motion of particles trapped. Also stated that the storage region occupied by the RW-electrodes should not take more than half of the region storage of particles.

On the basis of solving the equations of motion of particles and simulation confinement the bunch in the trap, we can offer the following explanation of the influence of the RW-field (see Fig. 4.). Continuing the particles at entry into the trap of quickly thermalized (to the velocity of thermal motion  $v_{term}$ ) by collisions with buffer gas molecules. The frequency (or period) of longitudinal oscillations (or period) of the particles on the order of frequency drift motion (1):

$$T_{long} \approx 2L/v_{term} \approx T_E \approx 1-3 \mu s, f_{RW} \approx T_{long}^{-1} \approx f_E.$$

This synchronization (auto synchronization) and provides a grouping of particles and subsequent compression of the bunch. Rotating field shifts the center of the bunch with respect to the trap axis, creating a non-zero dipole moment  $\mathbf{d}$ . And while confinement the bunch particles must from time to time to leave the area of a rotating field, in order to whip in those moments when the field has a maximum torque of forces in the bunch:

$$M_{\theta}^{RW} = \frac{dP_{\theta}}{dt} = \mathbf{d} \times \mathbf{E}_{\omega}.$$

Until the particles come out of a bunch of RW-electrodes in the RW-field of the electrodes should rotating so as to provide maximum torque the bunch about the trap axis.

Because of the magnetic field inhomogeneity and scattering on residual gas bunch slows its rotation. This leads to an increase in the drift of particles to the walls of the trap. Synchronization of the longitudinal and transverse motion of particles trapped in the RW-field provides the greatest "spinning" the bunch, and compensates for the slowing rotation. This increases the stability and lifetime of the bunch. However, the mechanism of compression of the bunch due to the RW-field remains uncertain.

## METHODS OF POSITRON LIFETIME INCREASE AND BUNCH COMPRESSION. THE MAIN RESULTS

1. Optimal parameters of the Surko trap at LEPTA have been found:

- magnetic field value  $B > 1000$  G,
- base vacuum  $\sim 10^{-9}$  Torr,
- buffer gas pressure in storage region  $\sim 10^{-6}$  Torr,
- RW amplitude = 0.5 V and frequency  $\sim 600$  kHz,
- RW rotation direction along the particle drift;

2. Compression and stabilization of the stored bunch by RW-field application:

- achievable bunch life time  $> 100$  sec,
- achievable stored particle number  $> 10^9$  (electrons),  $10^7$  (positrons),
- achievable bunch transverse size  $< 1$  cm;

3. Bunch intensity increase by the controlled storage regime:

- dynamic magnification of frequency of the RW field and depth of the potential well with growth of number of the storage up particles.

## RESULTS AND DISCUSSION

- "The Rotating Wall" method was studied experimentally at LEPTA injector and a high efficiency of particle storage with RW application has been obtained.
- Optimal Surko trap parameters have been found.
- It was found that the RW mechanisms were discussed at the LEPTA Trap parameters.
- Methods of optimization of the particle storage and bunch compression in the Surko trap has been obtained.
- First experimental results of positron storage in the LEPTA trap have been presented.

**REFERENCES**

- [1] G.B. Andresen, M.D. Ashkezari, M. Baquero-Ruiz et al. *Nature*, 468 (2010), 673.
- [2] G.B. Andresen, W. Bertsche, P.D. Bowe et al. *Phys. Rev. Lett.*, 100 (2008), 203401.
- [3] X.-P. Huang, F. Anderegg, E.M. Hollmann, C.F. Driscoll, and T.M. O'Neil. *Phys. Rev. Lett.*, 78 (1997), 875.
- [4] Anderegg, E.M. Hollmann, and C.F. Driscoll, *Phys. Rev. Lett.*, 81, 4875 (1998).
- [5] R.G. Greaves and C.M. Surko, *Phys. Rev. Lett.*, 85, 1883 (2000).
- [6] I. Meshkov, I. Seleznev, A. Sidorin, A. Smirnov, G. Trubnikov, S. Yakovenko, *NIM B*, **214**, (2004) 186.
- [7] E. Akhmanova, V. Bykovskii, M. Eseev, A. Kobets et al. *Physics of Particles and Nuclei Letters*, 7 (2010), 7, 502.
- [8] E. Akhmanova, V. Bykowski, M. Eseev et al. *Book of abstracts XXXVIII International Conference on Plasma Physics and Controlled Fusion (Zvenigorod, 14-18 February 2011)- M: "PLASMAIOFAN" (2011)*, 329.
- [9] J. R. Danielson and C.M. Surko, *Phys. Plasmas*, 13, 055706 (2006).
- [10] R.G. Greaves and J.M. Moxom *Phys. Plasmas*, 15, 072304 (2008).

# ENHANCING TRAPPABLE ANTIPROTON POPULATIONS THROUGH AN INDUCTION UNIT FOLLOWED BY FRICTIONAL COOLING

M.S. Zolotarev<sup>\*</sup>, J.S. Wurtele<sup>†</sup>, A.M. Sessler, G. Penn,  
Lawrence Berkeley National Laboratory, Berkeley, CA, USA;  
A.E. Charman, University of California, Berkeley, Berkeley, CA, USA

## Abstract

The antiproton decelerator (AD) at CERN currently delivers antiprotons for antimatter trapping experiments. The AD slows the antiprotons down to  $\sim 5$  MeV. This energy is currently too high for direct trapping, and foils are used to slow down the antiprotons to energies which can then be trapped. This is an inefficient process. CERN is developing a new machine (ELENA) for further deceleration to  $\sim 100$  keV using a decelerating ring with electron cooling. We describe a frictional cooling scheme that can serve to provide significantly improved trapping efficiency, either directly from the AD or using a standard deceleration mechanism (induction linac or RFQ), in a short time scale and at reasonable cost which could serve in the interim until ELENA is ready for operation. Simulations provide a preliminary assessment of the concept's strengths and limitations, and highlight important areas for experimental studies. We show that the frictional cooling scheme can provide a similar energy spectrum to that of ELENA, but with higher transverse angles.

## INTRODUCTION

Sources of low-energy antiprotons are in increasing demand for various experimental initiatives, including direct measurements of charge-to-mass ratios and production and trapping of antihydrogen, and eventually may lead to measurements of trapped neutral antimatter that test the Weak Equivalence Principle and CPT invariance [1, 2, 3].

The primary source of low-energy antiprotons remains the Antiproton Decelerator (AD) at CERN. Experiments typically suffer from low capture efficiency, because the antiprotons exit the AD at energies around 5.3 MeV, far above achievable electrostatic trap depths. To trap the antiprotons, the beam is first sent through a degrading foil which slows the particles on average but leads to large particle losses and energy spread due to straggling effects, so only a small fraction of the antiproton source are trapped.

To improve trapping efficiencies, the Extra Low ENergy Antiproton (ELENA) upgrade [4, 5, 6] to the AD has been proposed, which would use a post-decelerator and ring-based electron cooling to provide a source of 100 keV antiprotons while maintaining high phase space density. Other laboratories are also proposing low-energy antiproton deceleration and cooling rings, such as the Facility for Antiproton and Ion Research (FLAIR) [7] at GSI.

<sup>\*</sup> max\_zolotarev@lbl.gov

<sup>†</sup> also at University of California, Berkeley, Berkeley, CA, USA

Here we propose a simple scheme for longitudinal slowing and cooling of the antiproton beam delivered by the AD, utilizing an optional deceleration section which could be an induction linac or RF quadrupole (RFQ), followed by a degrading foil and finally frictional cooling. The frictional cooling stage consists of a series of thin carbon foils separated by re-accelerating electrostatic gradients. Such a scheme is not as effective as ELENA will be, but is an adequate and available option for antiproton experiments. Longitudinal losses should be comparable to that of ELENA, but there may be significant transverse losses even with large solenoidal fields for focusing the beam.

After providing a brief overview of our cooling concept, we present preliminary results from Monte Carlo simulations, suggesting that frictional cooling can enhance the population of trapped antiprotons by a factor of 10 or more. Potentially, a factor of 100 gain can be achieved if the frictional cooling is augmented by using an RFQ. We conclude with a discussion of advantages and limitations of the scheme, and of future directions for study.

## OVERVIEW OF FRICTIONAL COOLING FOR ANTIPROTONS

Frictional cooling has been proposed and studied theoretically and experimentally in the context of muons [8, 9, 10]. For antiprotons, frictional cooling might be used to compensate for the large mismatch between the average kinetic energy of the antiproton beam exiting the AD and the kinetic energy of particles that can be trapped — several MeV versus several keV. To compress its energy spread, each antiproton bunch is passed through a series of thin foils separated by electrostatic potential differences that reaccelerate the beam, as shown schematically in Figure 1. For antiprotons with kinetic energy below  $\sim 90$  keV, higher energy particles lose more energy in each foil, so this design causes particles to converge to an equilibrium energy; this is analogous to “terminal velocity” for falling objects in air. Transverse angles reach an equilibrium of order of a fraction of a radian, and solenoidal fields are used to minimize growth in transverse spot size.

Because the stopping power starts to decrease for kinetic energies above  $\sim 90$  keV, the maximum energy acceptance of the frictional cooling section is limited to the energy, typically around 400 keV, where the stopping power drops back down to match that of the equilibrium energy. Thus a degrading foil [11] must still be used, whose thickness is comparable to the range of the incident antiprotons. If the incident antiprotons have an energy of  $\sim 5$  MeV, straggling

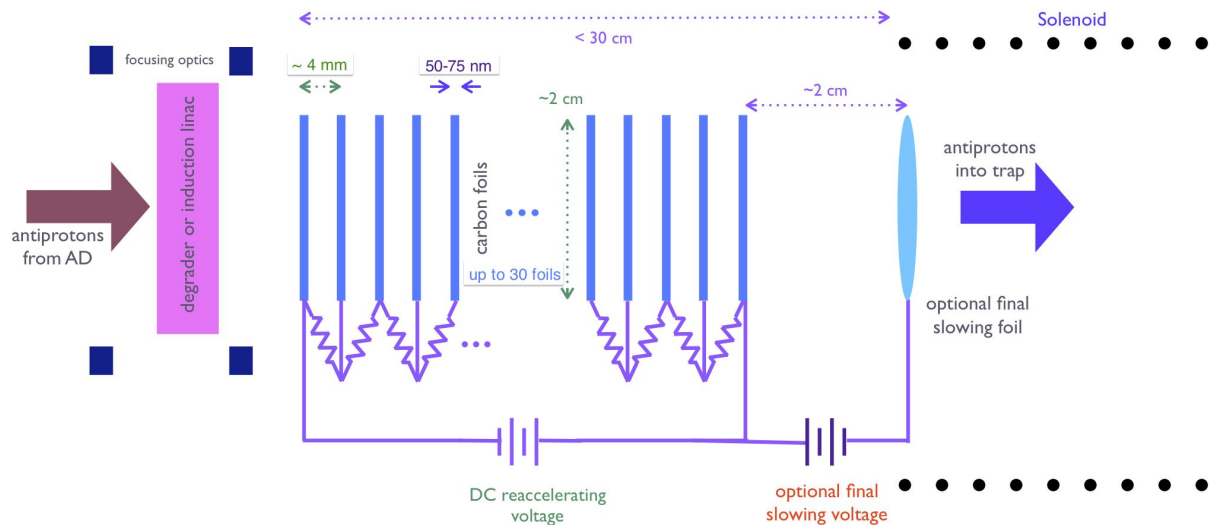


Figure 1: Schematic of the proposed frictional cooling system. The diagram is *not* drawn to scale, but is intended to illustrate the major components. Because the antiproton current is small and therefore the power requirements modest, a resistor chain can be used to divide a single high voltage source.

will lead to a broad initial energy distribution with a small fraction in the acceptance range for trapping. Decelerating the antiprotons to  $\sim 100$  keV before the foil leads to straggling effects only of order 1 keV.

Performance is limited by particle losses, straggling, and multiple scattering. The impact of multiple scattering grows worse at lower energies. To control the effects of multiple scattering in the foils, we choose to use carbon foils as a convenient low-Z option, and the equilibrium energy of the beam is set to be higher than the typical acceptance of traps. To compensate for this, the very last foil will be thicker than the others in order to optimize the trapping efficiency. The number of foils, their thickness, and the potential differences between them are chosen to effect the desired cooling using currently available thin foil technologies while keeping the overall length of the device and the total voltage drop within reasonable bounds.

## DECELERATION SCHEMES

Following the AD, we consider four ideas for deceleration including the ELENA proposal, an induction linac, an RFQ, or a simple foil. Every scheme, including ELENA, will require some degrading foil to further reduce energy. Note that the optimal choice for a degrading foil going directly into a trap may be different from that of a foil going into a frictional cooling section. The deceleration options are quite conventional and well studied. Degrading foils are modeled using the same physics as for frictional cooling.

The AD [12] delivers about  $2 \times 10^7$  antiprotons per bunch of about  $0.3 \mu\text{s}$  duration at a mean kinetic energy of 5.3 MeV every 1.8 minutes. The horizontal and vertical (87%) emittances are about  $1 \pi$  mm mrad and  $2 \pi$  mm mrad, respectively, and the momentum spread after cooling and

re-bunching is about 0.1%, corresponding to an RMS kinetic energy spread of about 10.6 keV. Through electron cooling, ELENA can decelerate this beam to 100 keV with very small energy spread and low divergence. After the degrader, almost all of the beam is in the energy acceptance of a typical trap. An induction linac can achieve a gradient of 1 MeV/m for a long (300 ns) pulse, which can be increased if the pulse duration can be shortened from the nominal AD pulse length. However, that will negatively impact the capture efficiency. The resulting energy spread is expected to be of the order of 25 keV at 50 keV energy. An RFQ can slow the beam to  $\sim 50$  keV with an energy spread of 10 keV. Note that one current experiment at CERN, ACUSA, employs an RF quadrupole system to decelerate bunches from the AD down to about 15 keV. But following a decelerator with active cooling can greatly enhance the number of low-energy antiprotons.

## SIMULATION RESULTS

In Monte Carlo simulations, we use tabulated data for the average energy loss of particles in matter generated by the “txphysics” software package [13], which uses SRIM [14, 15] data. This allows us to use a single methodology for both the degrader and frictional cooling foils, covering a range of kinetic energies from zero up to several MeV where a variety of physical effects come into play. Antiprotons are not included in these tables, and the Barkas effect [16, 17, 18], where antiprotons experience less energy loss than protons at low energies, is estimated as a simple factor of 0.5 for the range of energies considered here. The other major effects, straggling and multiple scatter, are treated according to algebraic expressions based on experimental data [19, 20, 21] and theory [22, 23, 24]. Because

multiple scatter is critical to frictional cooling performance and is not well known for antiprotons, it is parametrized according to a simplified fit of the Molière scattering cross-section to a Gaussian:

$$\frac{d}{ds}\sigma_{\theta}^2 = \left(\frac{13.6 \text{ MeV}}{\beta c p}\right)^2 Z_p^2 \frac{\rho}{x_0} \kappa_{\theta} \approx \kappa_{\theta} \mu_{\theta} E^{-2} \frac{\rho}{\rho_0}, \quad (1)$$

where the second form applies in the limit of low kinetic energy. Here  $x_0$  is the radiation length in units of  $\text{g}/\text{cm}^2$ , or  $43 \text{ g}/\text{cm}^2$  for graphite,  $Z_p$  is the charge of the beam particles,  $\rho$  is the density,  $\rho_0 = 2.21 \text{ g}/\text{cm}^3$  is the nominal density, and  $\mu_{\theta} \approx 2.3 \times 10^5 \text{ rad}^2 \text{eV}^2/\text{nm}$  for protons in carbon. We have incorporated an additional dimensionless factor  $\kappa_{\theta}$  to account for a variety of uncertainties: differences between protons and antiprotons, the scaling at very low velocities, and the distinctive configuration used for frictional cooling. We will consider several values of the parameter  $\kappa_{\theta}$ , but the data suggests it could be as low as 0.05 for antiprotons. Annihilation is neglected, but all stopped, backscattered, or reflected particles are treated as lost.

The frictional cooling consists of multiple foils with a thickness of 50–75 nm, separated by 4 mm gaps with a voltage per gap chosen within the range 4–5 keV. The final foil is typically double this thickness. Straggling turns out to have a very small effect on the frictional cooling section. It is important for the degrader and thus affects the input into the frictional cooler stage.

Results are given in Table 1 for antiproton cooling using various configurations and for  $\kappa_{\theta}$  chosen to be 0.05, 0.1, or 0.25. The RFQ plus frictional cooling configuration can yield similar output to ELENA followed by a degrading foil over a range of values of the scattering rate. At increasing values of  $\kappa_{\theta}$ , more foils and higher voltage per foil are needed, requiring significantly more total voltage. For the RFQ example, the number of foils must be increased from 9 to 10 as  $\kappa$  is increased from 0.05 to 0.1, also requiring the total applied voltage to increase from 40 keV to 52 keV. At even higher levels of scattering, performance begins to degrade more significantly. The kinetic energy spectrum for the RFQ example with and without frictional cooling is shown below, given in units of % of beam per 1 keV. Note that the spectrum is given in terms of total kinetic energy, while the acceptance criterion is based on longitudinal kinetic energy.

## DISCUSSION

Simulations suggest that a simple frictional scheme applied to antiproton bunches delivered by the AD can enhance the numbers of trappable particles by an order of magnitude when compared to the use of a degrading foil alone, and even more if additional upstream deceleration is employed. These simulations include some simplifying assumptions, especially as to the differences between protons and antiprotons.

Frictional cooling can reduce to keV-levels both the mean energy and energy spread of the portion of the beam. Other methods of phase space manipulation

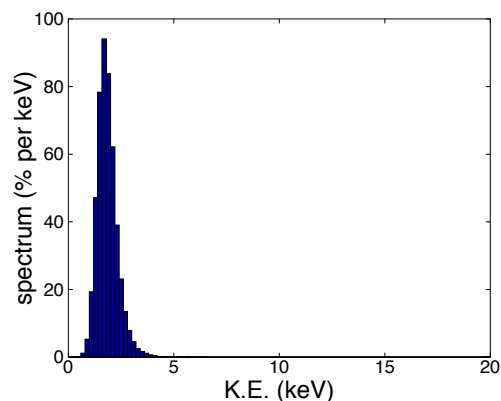


Figure 2: Antiproton spectrum from an RFQ followed by a degrader foil and a frictional cooling section for the case  $\kappa_{\theta} = 0.05$ .

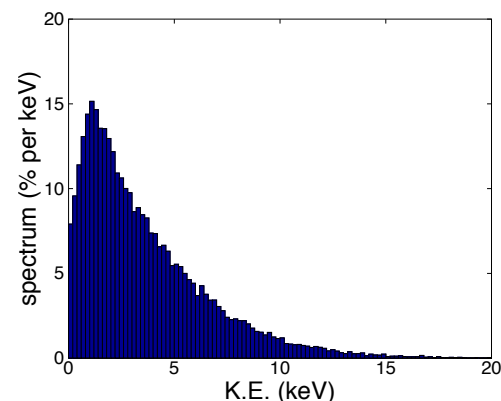


Figure 3: Antiproton spectrum from an RFQ followed by a degrader foil alone for the case  $\kappa_{\theta} = 0.05$ .

that lies below some cutoff energy. Countering this will be particle losses, increases in spot size and bunch length, and a large RMS angular divergence.

The requirements for a frictional cooling section seem technologically feasible:  $< 30$  foils, each about 75 nm thick, and if necessary fitting into a compact space; a total DC voltage source of  $\sim 50$  kV up to possibly 150 kV; and a deceleration mechanism after the AD if a degrading foil by itself does not yield sufficient performance. In addition, because divergence angles become large, a strong solenoidal field may be needed, rising to  $\sim 3$  T, to provide transverse confinement. In many trapping applications the frictional cooling section can piggy-back on the existing solenoidal field.

Within the frictional cooling stage, it is multiple scattering that primarily limits performance. While the results are quite sensitive to the rates of multiple scattering, these are rather poorly known for low-energy antiprotons in carbon or other solid materials. Scattering of antiprotons is likely subject to a Barkas effect, and the observed cross-section

Table 1: Numerical results of antiprotons for different configurations and values for scattering. Only longitudinal acceptance is considered; transverse effects will further reduce the total trapping efficiency.

Type	Init E	Init $\sigma_E$	$\kappa_\theta$	Degraded Thickness	Voltage	# cooling foils	% accepted
AD	5 MeV	10 keV	0.05	185 $\mu\text{m}$	0	0	1.1
			0.05	185 $\mu\text{m}$	114 kV	26	15
			0.10	185 $\mu\text{m}$	135 kV	26	14
Induction Linac	50 keV	25 keV	0.05	450 nm	0	0	16
			0.05	250 nm	40 kV	9	67
RFQ	50 keV	10 keV	0.05	450 nm	0	0	38
			0.05	250 nm	40 kV	9	96
			0.10	250 nm	52 kV	10	94
			0.25	250 nm	72 kV	12	80
ELENA	100 keV	0.1 keV	0.05	770 nm	0	0	94
			0.10	760 nm	0	0	91
			0.25	750 nm	0	0	81

for low-energy protons is already adequate for frictional cooling. Better measurement of these cross-sections would help to define the achievable efficacy of and requirements for frictional cooling. Annihilation effects are expected to be small. Because of the Barkas effect, note that if such a scheme is to be tested using a proton beam, one must either use thinner foils or higher voltages between foils to see equivalent results.

Good understanding of the longitudinal and transverse phase space acceptances of the downstream trap is essential to optimize performance for specific applications. While we have considered for simplicity a repetition of identical foils and gap-voltages, tapering of these quantities might further improve performance. Optimization and improved simulation of the cooling layout, as well as more realistic modeling of the upstream deceleration and downstream trapping dynamics, are goals for future study.

## ACKNOWLEDGEMENTS

The authors thank Joel Fajans and Niels Madsen for useful conversations and communications. This work was supported by the Director, Office of Science, High Energy Physics, of the U.S. Department of Energy under Contract No. DE-AC02-05CH11231, and Grant No. DE-FG02-04ER41289.

## REFERENCES

- [1] J. Fajans, *et al.*, “Discovery Science with Low-Energy Antiproton Sources: the ELENA Upgrade,” report, Symposium on *Accelerators for America’s Future* (2009).
- [2] E. Widmann, *Acta Physica Polonica B* **41** 249–260 (2009).
- [3] N. Madsen, *Philosophical Transactions of the Royal Society A* **368** 3671–3682 (2010).
- [4] W. Oelert, *IJMPA* **26** 390-395 (2007).
- [5] W. Oelert, *et al.*, “ELENA: An Upgrade to the Antiproton Decelerator,” CERN Report CERN-SPSC-2009-026 (2009).
- [6] P. Belochitskii, “Status of the Antiproton Decelerator and of the ELENA Project at CERN,” in R. Hasa, V. Schaa, editors, *Proceedings of COOL 2007*, 6–10. Darmstadt: GSI (2007).
- [7] C. Welsch and J. Ullrich, *Hyperfine Interactions* **172** 71–80 (2006).
- [8] R. Galea, A. Caldwell, and S. Schlenstedt, *Journal of Physics G* **29** 1653 (2003).
- [9] M. Muhlbauer, *et al.*, *Nuclear Physics Proceedings Supplement* **51A** 135–142 (1996).
- [10] R. Galea, *Nuclear Physics B* **149** 295–297 (2005).
- [11] H. Kalinowsky, *Hyperfine Interactions* **7** 73–80 (1993).
- [12] P. Belochitskii, *et al.*, “Commissioning and First Operation of the Antiproton Decelerator (AD),” in P. Lucas and S. Webers, editors, *Proceedings of the 2001 Particle Accelerator Conference*, 580–584 (Piscataway, NJ: IEEE, 2001).
- [13] P.H. Stoltz, S. Veitzer, R.H. Cohen, A.W. Molvik, and J.-L. Vay, *Nucl. Instrum. Methods A* **544** (2005), p. 502-505.
- [14] J.F. Ziegler, J.P. Biersack, and U. Littmark, *The Stopping and Range of Ions in Solids* (New York: Pergamon, 1985). See also [www.srim.org](http://www.srim.org).
- [15] J.F. Ziegler, *Nucl. Instrum. Methods B* **219-220** 1027 (2004).
- [16] R. Medenwaldt, *et al.*, *Physics Letters A* **155** 155-158 (1991).
- [17] A. Adamo, *et al.*, *Physical Review A* **47** 4517–4520 (1993).
- [18] S.P. Möller, *et al.*, *Phys. Rev. Lett.* **88**, 193201 (2002).
- [19] W. Bernstein, A.J. Cole, and R.L. Wax, *Nucl. Instrum. Methods* **90** 325-328 (1970).
- [20] S.P. Möller, *et al.*, *European Physics Journal D* **46**, 89–92 (2008).
- [21] C. Amsler, *et al.*, (Particle Data Group), “2008 Review of Particle Physics,” *Physics Letters B* **667** 1 (2008).
- [22] P. Sigmund and A. Schinner, *European Physics Journal D*, **15** 165–172 (2001).
- [23] P. Sigmund and A. Schinner, *Nucl. Instrum. Methods B* **212** 110–117 (2003).
- [24] G.R. Lynch and O.I. Dahl, *Nucl. Instrum. Methods B* **58** 6 (1991).

Other methods of phase space manipulation

# ION KINETICS IN THE ULTRA-LOW ENERGY ELECTROSTATIC STORAGE RING (USR)

A.V. Smirnov, A.I. Papash, Max Planck Institute for Nuclear Physics, Heidelberg, Germany and  
Joint Institute for Nuclear Research, Dubna, Russia (on leave)

C.P. Welsch, University of Liverpool, UK and The Cockcroft Institute for Accelerator Science  
and Technology, UK

## Abstract

The Ultra-low energy Storage Ring (USR) at the Facility for Low-energy Antiproton and Ion Research (FLAIR) will provide cooled beams of antiprotons in the energy range between 300 keV down to 20 keV and possibly less. A large variety of the envisaged experiments including in-ring collision experiments with a reaction microscope require a comprehensive study of the long term beam dynamics processes in the ring.

Detailed investigations into the ion kinetics under consideration of the effects from electron cooling and multiple scattering of the beam on a supersonic gas jet target have been carried out using the BETACOOOL code.

The life time, equilibrium momentum spread and equilibrium lateral spread during collisions with this internal gas jet target were estimated. The results from simulations were benchmarked against experimental data of beam losses in the ELISA storage ring. In addition, the results from experiments at the TSR ring where a 93 keV/u beam  $CF^+$  ions has been shrunk to extremely small dimensions have been reproduced.

Based on these simulations, conditions for stable ring operation with extremely low emittance beam are presented. Finally, results from studies into the interaction of ions with a gas jet target at very low energies are summarized.

## INTRODUCTION

The next-generation antiproton facility at GSI, the Facility for Antiproton and Ion Research (FAIR), will not only provide future users with antiprotons in the high energy range, but it is also intended to include a dedicated research program for ultra-low energy antiproton research, realized with the FLAIR project [1]. Low-energy antiprotons are the ideal and perhaps the only tool to study in detail correlated quantum dynamics of few-electron systems in the femto- and sub-femtosecond time regime [2]. Within the FLAIR Facility the Ultra-low energy Storage Ring (USR) operates in the variable energy range from 300 keV down to 20 keV and possibly to even lower energies [3,4]. The USR will enable, for the first time, access to kinematically complete antiproton-induced rearrangement and fragmentation measurements. The USR, presently being developed in the QUASAR group [5], is comprised of electrostatic ion optics elements and studies into the long term beam dynamics

and ion kinetics are of crucial importance for the performance of the envisaged experiments.

## BENCHMARKING OF EXPERIMENT

For benchmarking purposes, the ELISA electrostatic ring, successfully in operation since the late 90s and dedicated to atomic physics studies [6], has been chosen. In the original ring design spherical deflectors had been used to provide equal focusing in both the horizontal and vertical plane but were later on substituted by cylinder deflectors [7]. Systematic experimental studies showed strong limitations on the maximum storable beam current and reduced beam life time at higher beam intensities. The nature of these effects was not fully understood [8].

We studied transition processes, i.e. growth rates of beam emittance and momentum spread, as well as equilibrium conditions in ELISA by simulating the rms parameters of the evolution of the ion distribution function with time. For this purpose the BETACOOOL code was applied [9,10]. In this study, the beam parameters summarized in table 1 were used. BETACOOOL allows choosing and switching between different effects and in this particular investigation only heating processes were used: Intra-Beam Scattering (IBS), small angle multiple scattering of the circulating ions on the residual gas atoms, energy straggling and ion losses on the ring acceptance. It was found that beam losses caused by single large angle scattering are negligible at a vacuum level  $2 \cdot 10^{-11}$  Torr, even at such a

Table 1: BETACOOOL beam parameters of ELISA.

Ion	$O^{16}$	$Mg^{24}$
Charge	-1	+1
Ion energy, keV	22	18.4
Initial beam intensities	$5 \cdot 10^5 \div$ $1.6 \cdot 10^7$	$2.7 \cdot 10^7$
Ring circumference, m	7.616	7.616
Initial hor/vert $\varepsilon, \pi$ mm mrad ( $\sigma$ )	1 / 1	0.7/0.35
Initial full $\varepsilon, \pi$ mm mrad ( $3\sigma$ )	6 / 6	4 / 2
Ring acceptance ESD-cyl, $\pi$ mm mrad	10	10
Ring acceptance ESD-sph, $\pi$ mm mrad	6	6
Initial RMS momentum spread, $\Delta p/p$	$10^{-3}$	$10^{-4}$
Equilibrium momentum spread, $\Delta p/p$	$4 \cdot 10^{-3}$	
Electron detachment life time of $O^-$ , sec	26	--
Life time of $O^-$ at 22 keV, sec	$\sim 12$	

low beam energy. The limited life time of  $O^-$  ions due to the electron detachment by collision with the residual gas

\*Work supported by the Helmholtz Association of National Research Centres (HGF) under contract number VH-NG-328 and GSI Helmholtz Centre for Heavy Ion Research GmbH.

as measured by S.P. Møller [8] has been included in the program as an input parameter.

The measured rates of beam intensity decay of a 22 keV O<sup>-</sup> beam were reproduced with good accuracy, see Fig. 1. This gave rise to the conclusion that the main reasons for beam size growth in a keV storage rings are multiple scattering on the residual gas and Coulomb repulsion of the ions from each other at high intensities, i.e. IBS. As a consequence, the beam is then lost on the ring aperture because of a rather small ring acceptance. The rate of beam losses increases at higher intensities because IBS adds to vacuum losses.

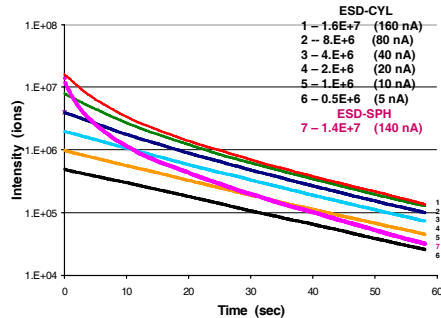


Figure 1: Simulation of beam current decay in ELISA. The intensity of the 22 keV O<sup>-</sup> beam was varied over a wide range, reflecting earlier measurements.

The IBS effect is clearly seen in Fig. 1 as an excessive drop of beam current during the first few seconds when the beam intensity is still high. The long term slope of this loss curve is determined by the ring acceptance and the rate of multiple scattering which is inversely proportional to the vacuum level in the ring. The slope of the decay curve also depends on the life time due to electron detachment for negative ions or electron stripping for positive ions.

An exception is seen in the pink curve, representing the decay of the beam intensity in ELISA with spherical deflectors. In this case, significantly higher loss rates are caused by the significantly reduced ring acceptance. IBS is also much stronger when the beam density is high and thus in particular in regions where the beam is strongly focused. The IBS rates for ELISA with spherical deflectors are significantly higher than with cylindrical electrodes because of the double focusing effect of the first and the resulting small beam size in both planes.

The measured equilibrium profile of an 18.6 keV Mg<sup>+</sup> beam (FWHM=3.43 mm) was compared to BETACOOOL simulations made under the assumption that the transverse beam size is mainly defined by losses on the optical elements of the ring structure, see Fig. 2. The resulting rms width is equal  $\sigma=1.5$  mm and corresponds to a ring acceptance of  $A\approx 8\pi$  mm-mrad.

The ring acceptance was then varied as an input parameter in BETACOOOL. Assuming a ring acceptance of  $\sim 50 \pi$  mm-mrad, an rms beam size of  $\sigma=3$  mm would result, i.e. twice as large as what was measured in the experiment. Also, if the acceptance would be that large the life time of the O<sup>-</sup> beam in ring should be 24 s which

contradicts a measured life time of  $\tau\sim 12$  s. The fast decay in ELISA with spherical deflectors can be explained by a small acceptance of nonlinear nature [11].

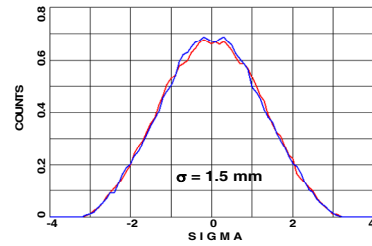


Figure 2: Profile of the Mg<sup>+</sup> beam corresponds to the ELISA ring acceptance of  $A\approx 8\pi$  mm-mrad.

### USR OPERATION WITH TARGET

The BETACOOOL code was used to optimize parameters of the USR electron cooling system during operation with internal gas jet target. The beam parameters summarized in table 2 were used. During deceleration and cooling modes of the USR operation the four fold symmetry ring lattice provides smooth beta-functions in all four achromatic straight sections. At this regime the electron cooling cannot suppress beam heating caused by multiple scattering of low energy antiprotons with high density helium gas jet target. As a consequence the beam life time will be very low. One can operate with low density target at four fold symmetry standard mode but in expense of reduced luminosity of the experiment.

At high target density ( $n_{tgt}\sim 5\times 10^{11}$  cm<sup>-3</sup>) the two fold

Table 2. Beam parameters for USR with internal target

Ring circumference, m	42.598
Antiproton energy, keV	20
Vacuum pressure (hydrogen), Torr	$10^{-11}$
Number of achromatic straight sections	4
Length of achromatic straight sections, m	4
Particle number	$2\times 10^7$
Initial emittance, $\pi$ mm-mrad	5
Acceptance, $\pi$ mm-mrad	40
Initial momentum spread	$10^{-3}$
Helium target density, cm <sup>-3</sup>	$5\times 10^{11}$
Target length, cm	0.1
Beta function at target (hor/ver), m	0.7 / 0.06
Dispersion at target point, m	0
Cross section of He ionization, barn	$5\times 10^7$
Length of electron cooler, m	2
Magnetic field at cooler, G	100
Beta functions at cooler (hor/ver), m	7.3 / 15.6
Dispersion at cooler, m	0
Electron beam radius, cm	2
Electron beam current, mA	0.1
Electron temperature (tran/long), eV	4 / 0.5
Electron energy shift (dp/p units)	$-2\times 10^{-3}$

asymmetric lattice with low beta functions at target location will be more suitable. Request to reduce the

beam size at target to  $\sim 1$  mm will cause the growth of the maximum value of beta-functions in other locations of the ring up to 80 m. So, the USR acceptance will be limited during low beta mode of operation. Another side effect of low beta lattice is an increase of the intra-beam scattering heating rate up to the level comparable to the heating rate from the target itself.

We've found equilibrium conditions when e-cooling suppresses beam heating caused by multiple scattering of ions at high density internal target as well as scattering due to IBS (Fig.3). The beam emittance is reduced in equilibrium to  $\sim 2 \pi$  mm-mrad (Fig.3a). Maximum transferable energy during impact between incident antiprotons and electrons of helium atom will not exceed  $2 \cdot 10^{-3}$  of ion kinetic energy. Thus the maximum energy lost in one ionization event should not exceed the longitudinal acceptance of the USR ring. Also we do not have valuable experimental data of the ratio between ionization and excitation events of He atoms by incident antiproton beam. Due to the lack of the experimental data at ultra-low energy range we assume that each ionization event should lead to the loss of the incident ion i.e. particle number is reduced during USR operation with internal target. We have used experimental cross-sections of He atoms ionization by low energy antiprotons in order to estimate integral of ionization events [12]. Under this assumption the integral of the ionization events (red curve in fig.3b) can not exceed number of beam ions (black curve in fig. 3b). The luminosity will be decreased in proportion with reduced particle number.

The beam transverse distribution in equilibrium is Gaussian. The longitudinal momentum spread (Fig.4.a) is Non-symmetric due to the large influence of the space charge of the electron beam (Fig.4.b). The space charge effect is the main limit of the electron current for coolers in low energy storage rings.

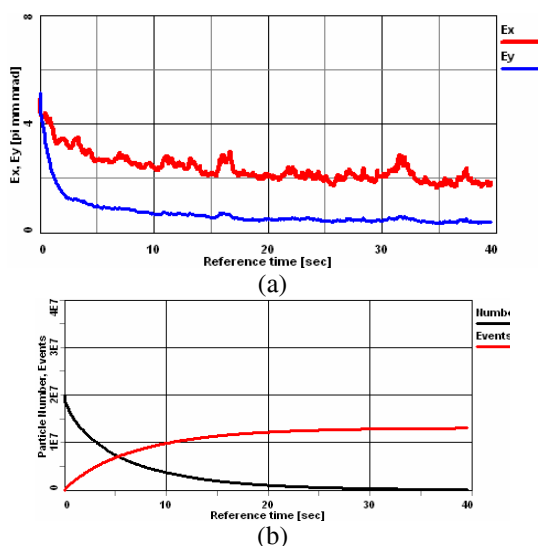


Figure 3. The beam evolution during USR operation with internal target: a) horizontal (red) and vertical (blue) emittances; b) decay of particle number (black) and integral of ionization events (red).

Cooled beam dynamics

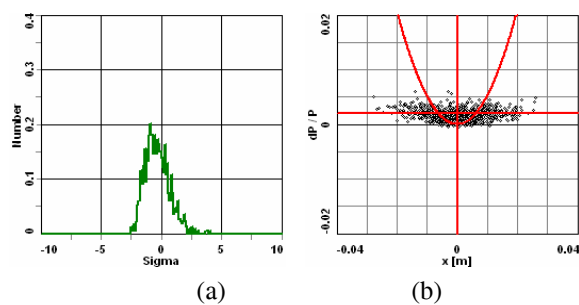


Figure 4. Beam distribution after 40 sec of cooling process. a) longitudinal profile, b) particle distribution at cooler section and space charge parabola of the electron beam.

## SUMMARY

It was shown how the beam behaviour in keV electrostatic storage rings can be described, what processes lead to beam degradation and how the electron cooling will counteract the beam scattering on target. Experimental data from ELISA served as a benchmark and was reproduced with very good agreement in BETACOOOL. The results from these studies were used to estimate the event rates of envisaged future collision studies between low energy antiprotons and gas targets in an Ultra-low energy Storage Ring.

## REFERENCES

- [1] C.P. Welsch, et al., "FLAIR – A Facility for Low-Energy Antiproton and Ion Research at GSI", *Hyperfine Interactions*, **172** (1-3) 71-80 (2007)
- [2] C.P. Welsch, et al., "Exploring Sub-Femtosecond Correlated Dynamics with an Ultra-low Energy Electrostatic Storage Ring", *AIP Conf. Proc.* **796** (2005) p. 266-271
- [3] C.P. Welsch, et al., "An ultra-low-energy storage ring at FLAIR", *NIM A* **546** (2005) 405–417
- [4] A. Papash, C.P. Welsch, "An Update of the USR Lattice: Towards a true multi-user experimental facility", *Proc. Part. Acc. Conf.*, Vancouver (2009)
- [5] <http://www.quasar-group.org>
- [6] S.P. Møller, Design and First Operation of the Electrostatic Storage ring ELISA. *Proc. EPAC* (1998)
- [7] S.P. Møller, "Operational experience with the electrostatic storage ring ELISA". *Proc. PAC* (1999)
- [8] S.P. Møller et al., Intensity Limitations of the Storage Ring ELISA. *Proc. EPAC* (2000)
- [9] A. Sidorin. BETACOOOL program for simulation of beam dynamics in storage rings. *Nucl. Instr. Meth. A* **558** (2006)
- [10] BETACOOOL guide. <http://betacool.jinr.ru>
- [11] A.I. Papash, C.P. Welsch, Simulations of space charge effects in low energy electrostatic storage rings. *Proc. IPAC* (2010)
- [12] H. Knudsen, *private communication* (2009)

## CLOSED ORBIT CORRECTION IN 2 MEV ELECTRON COOLER SECTION AT COSY-JUELICH

J. Dietrich <sup>a</sup>, V. Kamerdzhev <sup>a</sup>, B. Lorentz <sup>a</sup>, L. Mao <sup>a, b, #</sup>, V.V. Parkhomchuk <sup>c</sup>, H.J. Stein <sup>a</sup>

a) Forschungszentrum Juelich GmbH, Juelich 52425, Germany

b) Institute of Modern Physics (CAS), Lanzhou 730000, China

c) Budker Institute of Nuclear Physics, Novosibirsk 630090, Russia

### Abstract

A 2 MeV magnetized electron cooling system will be installed at COSY in order to boost the luminosity for future high density internal target experiments. For an effective electron cooling, the ion beam and electron beam have to overlap coaxially, demanding a perfect orbit correction in the cooler region. Due to the U-shaped arrangement of the toroid magnets the ion beam orbit distortion is anti-symmetric in horizontal plane. With two steerers at each side of cooler the ion beam can be made coaxial in the cooler without disturbing the region outside the cooler. The distortion caused by the bending coils in the toroids is symmetric in the vertical plane. Also here a local correction is suggested for correction. Using the magnetic field data measured at BINP we calculated the orbit distortion of ion beam at injection energy and investigated the schemes for orbit corrections.

### INTRODUCTION

Considering the requests of high luminosity for future COSY internal target experiments, a magnetized electron cooling system up to 2 MeV was suggested to be tested and operated at COSY [1]. This device has been developed together with the Budker Institute in Novosibirsk and will be installed in COSY at the end of 2011. Basically, a strong longitudinal magnetic field is used to guide the electron beam and to magnetize the electrons. The vertical field components in the toroids cause a severe horizontal deflection of the ion beam which has to be corrected by a set of steerers around the cooler. The principles of correction schemes have been described in various articles, e.g. in [2] and [3]. Two horizontal dipole correctors already installed in the toroids and regular steerers around form a fully compensated bump on each side of cooler. A weaker but not negligible orbit distortion in the vertical plane is caused by the bending coils in the toroids which serve to compensate the centrifugal force of the electrons related to the toroid radius. Also here fully compensated bumps are considered.

### MAGNETIC FIELD DISTRIBUTION

The magnetic field map of the 2 MeV cooler produced by the cooling section drift solenoid, the toroids and the bending coils in the toroids have been measured at BINP [4]. The dipole correctors are connected in series with the

toroids using the same power supply. Additional small coils mounted in the dipole correctors [5] will be used for a fine adjustment of the horizontal and vertical steering angle. The map (see Fig. 1) of magnetic field along the ion beam orbit has been measured with typical operational parameters.

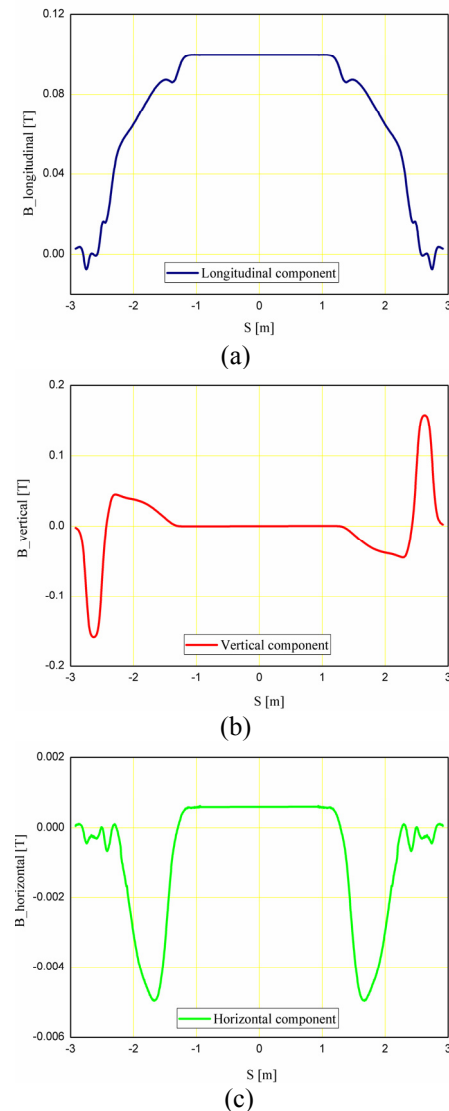


Figure 1: The magnetic field along the ion trajectory in cooler. From top down are shown the longitudinal, vertical and horizontal components. The current value of power supply is 175 A for the solenoid, 500 A for the toroids and the dipole correctors, 200 A for the bending coils. These parameters are half of design value.

#l.mao@fz-juelich.de

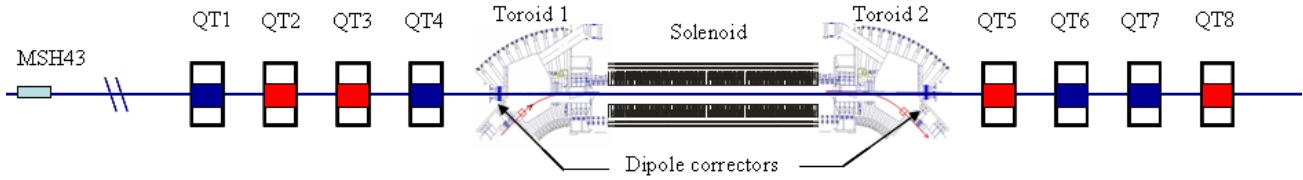


Figure 2: The COSY lattice structure in the 2 MeV electron cooler region. QT1, QT4, QT6 and QT7 are horizontally defocusing quadrupoles, QT2, QT3, QT5 and QT8 are horizontally focusing quadrupoles

## CLOSED ORBIT DISTORTION

The vertical and horizontal components of the magnetic field (see Fig. 1(b) and Fig. 1(c)) cause a horizontal and vertical deflection of the circulating ion beam, respectively. The deflection angle is given by integration:

$$\alpha_{v,h} = \frac{\sum B_{h,v} dz}{B\rho} \quad (1)$$

Here  $B\rho$  is the magnetic rigidity of the ion,  $B_{v,h}$  is the measurement data of magnetic field component and  $dz$  is the measurement step length (5mm for BINP measurement case). As the magnetic field in cooler is fixed and not ramped with the ion energy, this formula reflects the worst case of maximum angles occurring at injection energy and maximum magnetic field. Therefore, the calculations below are performed for 45 MeV (0.98 Tm) proton beam and maximum design magnetic field value of 0.2 T. Since the horizontal magnetic field is determined by the electron energy, the vertical deflection is considered for the maximum electron energy 2.0 MeV.

In order to correct the orbit in both planes, several steerers installed in the quadrupoles near the electron cooler region are used (see Fig. 2). Two horizontal steerers have been installed in quadrupoles QT1 and QT8. Two vertical steerers have been installed in QT4 and QT5. The main parameters of these regular COSY steerers are listed in Table 1 [6]. The location value denotes the distance from centre of electron cooler. The deflection angle is calculated for 45 MeV proton beam. All calculations are made with MAD program for COSY injection optics [7].

Table 1: Main parameters of steerers

Steerer	Location	Max. deflection angle
MSH43	-12.192 m	28.0 mrad
MSH_QT1	-6.398 m	12.0 mrad
MSV_QT4	-3.538 m	12.0 mrad
MSV_QT5	3.538 m	12.0 mrad
MSH_QT8	6.398 m	12.0 mrad

## SCHEME OF CORRECTION

Fig. 3 shows the suggested correction scheme in the horizontal plane. The steerers installed in QT8 together with the toroid and the dipole corrector at the downstream side of the cooler form a three steerer bump. Upstream, due to the lattice structure (DFFD quadrupole sequence instead of FDDF sequence downstream), the strength of the steerer in QT1 is too weak. It is suggested to use the regular steerer MSH43 in addition (2.0 mrad). The accurate matching of the bumps is achieved by the fine tuning coils in the dipole correctors. The maximum displacement 41 mm is located at the dipole correctors in the cooler

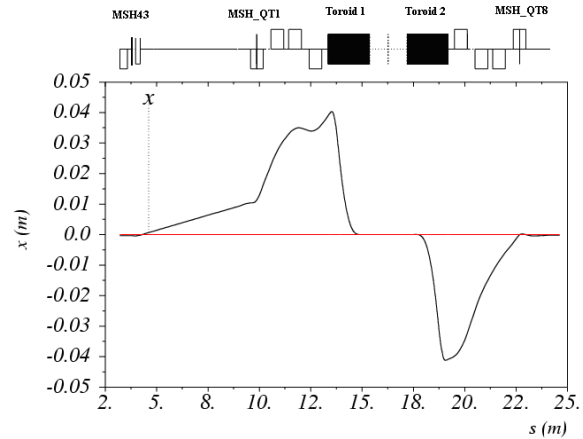


Figure 3: The closed orbit correction scheme in the horizontal plane. The regular COSY steerer magnet MSH43 and the steerers installed in QT1 and QT8 are used for correction on the both sides of cooler.

At COSY stripping injection of  $H^-$  (or  $D^-$ ) ions is applied to fill the ring with protons (or deuterons). For that purpose the COSY orbit is horizontally bumped for a few milliseconds to the edge of the stripping foil which is located in a distance of 16.3 m upstream the centre of the 2 MeV cooler. The last one of the three injection bumper magnets is located just behind QT4. Fig. 4 shows the horizontal orbit during the injection period and how the short term injection bump is superimposed on the steady state cooler bump.

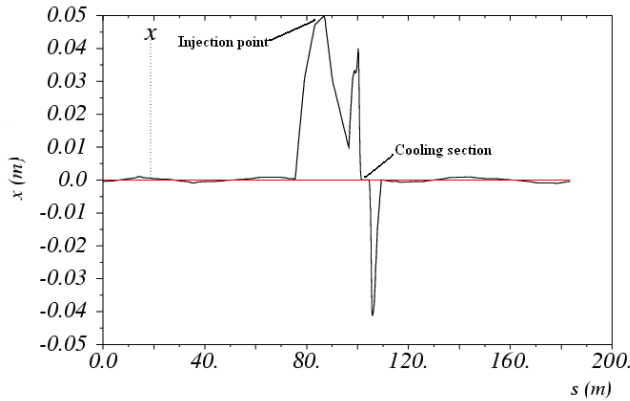


Figure 4: The proton beam trajectory during injection.

Vertically, the deflection due to the electron beam bending field is symmetric. The coils in the dipole correctors and the bending coils in the toroids can be used to form a matched four steerer bump. However will make a remaining offset of about 5 mm in the cooling section (see Fig. 5 (a)). Alternatively, a three steerers bump scheme at each side of the cooler can be applied too when the vertical steerers in QT4 and QT5 are activated (see Fig. 5 (b)). Here, the collinearity with the electron beam is as perfect as in the horizontal plane. The maximum displacement of orbit 5 mm again occurs in the dipole correctors. At higher ion beam energies, all orbit excursions are shrinking proportional to the increasing beam momentum.

The parameters of the closed orbit correction in both planes are listed in Table 2. The steerers EC\_V1 and EC\_V2 are the vertical coils in the dipole correctors upstream and downstream, respectively. The steerers EC\_H1 and EC\_H2 are the horizontal coils in dipole correctors. The values in parentheses are the parameter of the four bump scheme in vertical plane, as shown in Fig. 5(a).

Table 2: Correction scheme in cooler region

Steerer	Deflection angle /mrad	plane
MSH43	2.00	x
MSH_QT1	11.16	x
MSV_QT4	0 (5.06)	y
EC_V1	5.61 (-10.53)	y
EC_H1	10.15	x
EC_V2	5.61 (-10.60)	y
EC_H2	-16.31	x
MSV_QT5	0 (4.82)	y
MSH_QT8	-8.80	x

## CONCLUSION

The closed orbit correction for the new 2 MeV cooler at COSY is investigated. The local bump method is used to

correct the orbit distortion due to the cooler magnetic system. The schemes have been performed by MAD program.

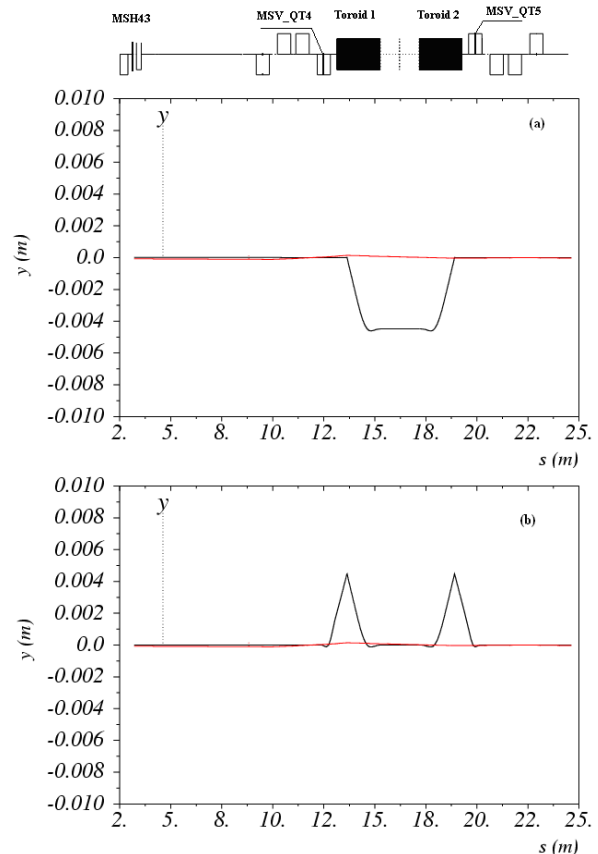


Figure 5: The orbit correction schemes in the vertical plane. (a) Only steerer coils belonging to the cooler are used. (b) The best collinearity is achieved by additionally using the vertical steerers in QT4 and QT5.

## ACKNOWLEDGMENTS

The authors would like to thank the colleagues at BINP for magnetic field measurement.

## REFERENCES

- [1] J.Dietrich et al, "Progress with the 2 MeV Electron Cooler for COSY-Juelich/HESR", Proceedings of RuPAC-2010, Protvino, Russia.
- [2] H.Poth, "Electron Cooling: Theory, Experiment, Application", Physics reports 196, No. 3&4 (1990) 135.
- [3] R.Maier et al, "Acceleration of a Cooled proton Beam in COSY", KFA-IKP Annual Report (1995) 226.
- [4] V.V.Parkhomchuk, BINP, Private communication.
- [5] V.V.Parkhomchuk, "Conceptual Design Report of Electron Cooler COSY 2 MeV", Novosibirsk, 2009.
- [6] Bernd Lorentz, "Orbit Correction for COSY 2MV Electron Cooler" Working draft.
- [7] Bernd Lorentz, FZJ, private communication.

# SIMULATION OF HIGH-ENERGY ELECTRON COOLING AT COSY WITH BETACOOOL PROGRAM

J. Dietrich <sup>a</sup>, L. Mao <sup>a, b, #</sup>

a) Forschungszentrum Juelich GmbH, Juelich 52425, Germany

b) Institute of Modern Physics (CAS), Lanzhou 730000, China

## Abstract

A 2 MeV electron cooling device will be installed at COSY in order to boost the luminosity for future high density internal target experiments, e.g. WASA pellet target experiments. The magnetized electron cooling technique is used to compensate the energy loss and emittance growth due to beam-target interaction. In this article, a numerical simulation of electron cooling process was performed with BETACOOOL program. The cooling time is calculated for variant electron cooling parameters. The intrabeam scattering (IBS) and pellet target effect are essential for prediction of equilibrium beam parameters. The influence of the pellet target on the beam parameters is demonstrated.

## INTRODUCTION

As the requests of high luminosity for future COSY pellet target experiments, an electron cooling system up to 2MeV was suggested to operate at COSY [1]. This device has been developed together with the Budker Institute in Novosibirsk and will be installed in COSY at the end of this year. The magnetized electron cooling technical solution is used to obtain a powerful 6-dimensional phase cooling.

A simulation study of the beam dynamics at COSY taking into account electron cooling in combination with pellet target and intrabeam scattering effects was performed with BETACOOOL program. The BETACOOOL program developed by JINR electron cooling group is oriented to simulation of the ion beam dynamics in a storage ring in the presence of cooling and heating effects [2]. To simulate the short scale luminosity variation in pellet target experiments, an additional algorithm has been implemented into BETACOOOL program recently [3].

In this paper, the cooling time dependences on electron cooler parameters are calculated with RMS dynamics algorithm method. The suggestion for cooler optimization is obtained from the calculation. The momentum distribution of proton beam at equilibrium between electron, IBS and pellet target is simulated with model beam algorithm method. The Landau distribution caused by beam-target interaction is discussed with different cooling efficiency. In the end of this paper, the short-scale and long-scale luminosities for proposed pellet target experiments are analyzed. The main parameters required in simulation are listed in table 1. The lattice structure of zero-dispersion at target point is used in simulation.

<sup>#</sup>l.mao@fz-juelich.de

Table 1: The main parameters of simulation

Proton beam parameters	
ion kinetic	2.0 GeV proton beam
Initial emittance (x/y)	0.2 / 0.2 $\pi$ *mm*mrad
Initial momentum spread (dp/p)	$2.0 \cdot 10^{-4}$
Particle number	$2.0 \cdot 10^{10}$
Electron cooler parameters	
Electron beam radius	5.0 mm
Magnetic field in cooling section	0.2 T
Cooler length	2.69 m
Electron beam current	2.0 A
Electron temperature (trans / longi.)	1.0 / $1.0 \cdot 10^{-4}$ eV
Magnetic field misalignment	$2.0 \cdot 10^{-5}$
Beta function at cooler (hori / vert)	5.5 / 4.5 m
Pellet target parameters	
Effective target thickness	$2.0 \cdot 10^{15}$ atoms/cm <sup>2</sup>
Pellet flux radius	2.5 mm
Pellet velocity	80 m/s
Pellet radius	0.03 mm
Rate of pellet generation	8.0 kHz

## OPTIMIZATION OF COOLER

Electron cooling is a fast process to compress the phase space of charged particle beam in storage ring with low temperature electron beam [4]. The phase space is shrinking up to the equilibrium between electron cooling and heating effects. In order to estimate the electron cooling efficiency, the cooling time dependences were calculated with RMS dynamics algorithm in BETACOOOL program.

The RMS dynamics algorithm is a simplified model that all effects are described by cooling or heating rates. The rates can be calculated with different models. In this calculation, the Parkhomchuk empirical cooling force formula is applied for magnetized electron cooling process [5]. The Martini's model is used for IBS effect calculation and the pellet target effect is presented in the form related to kick of the ion momentum [6]. The initial parameters of proton beam are listed in table.1. The horizontal (or longitudinal) cooling time was defined as

the time it takes for the horizontal emittance (or momentum spread) undergoing exponential shrinking to  $1/e$  times its initial value.

Fig. 1 shows the horizontal and longitudinal cooling time dependence on electron beam current. The cooling time decreases as the current is increased. The decreasing becomes slower while the electron current higher than 2.0A. Meanwhile, the cooling time increases faster as the current becomes lower than 1.0A. It seems that the cooling effect is too weak to compensate the IBS and pellet target heating effects as such low current.

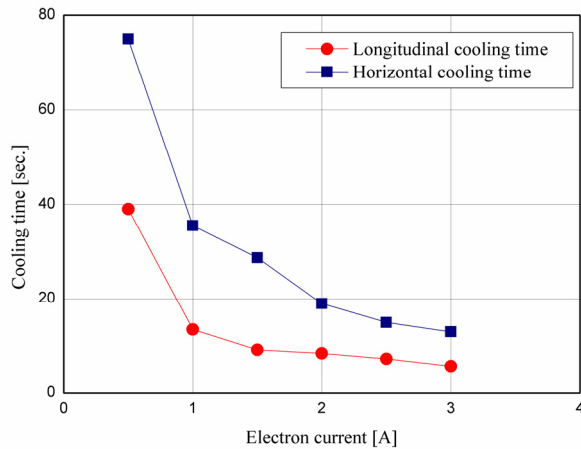


Figure 1: The dependence of cooling time on electron beam current.

The straightness of longitudinal magnetic field in cooling section is one of factors which determine the value of the effective velocity in Parkhomchuk's formula [5]. The cooling time dependence on magnetic field straightness was calculated as shown in Fig. 2. The cooling time increases fast as the magnetic field straightness larger than  $10^{-4}$ .

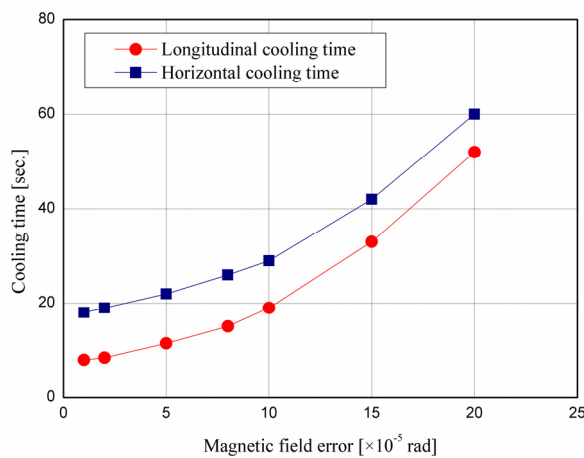


Figure 2: The dependence of cooling time on magnetic field error.

From the calculation of cooling time dependence, it can be seen an electron beam current higher than 1.0A is necessary for compensation of IBS and pellet target

effects. Good longitudinal magnetic field straightness less than  $10^{-4}$  is beneficial for fast cooling process.

## COOLED BEAM EQUILIBRIUM

For a good resolution of the experiments the momentum spread less than  $10^{-4}$  is required [7]. By the simulation with model beam algorithm in BETACOOOL program [6], the equilibrium momentum spread after cooling is plotted as a function of the electron beam current in Fig. 3. The momentum spread is defined as 68% ions enclosed. The calculation result shows that the momentum spread at the equilibrium between electron cooling, IBS and target effect is dominated by intra beam scattering for high electron beam current, as shown in red points in Fig. 3. Moreover, the momentum spread at the equilibrium between electron cooling and IBS only is larger than IBS and target together as electron beam current higher than 1.0A. In addition the heating effect of pellet target is increased dramatically while the electron beam current lower than 1.0A.

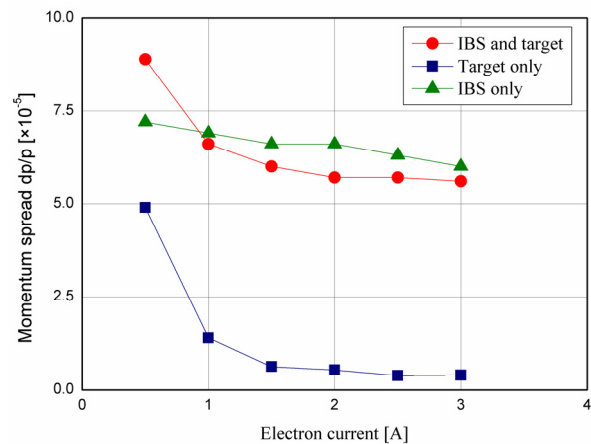


Figure 3: The equilibrium (68%) momentum spread as a function of electron beam current.

Compare with the momentum distribution at various equilibrium in Fig. 4, it can be seen that a momentum distribution with long tail is introduced by the ion-target interaction. The blue line in the figure is the initial momentum distribution before cooling. The red one is the momentum distribution at the equilibrium between cooling and IBS effect only, which is nearly a Gaussian distribution function. The other lines show the momentum distributions at the equilibrium between cooling, IBS and target together. The different cooling rates are obtained by using various electron beam currents. These lines show for proton beam that energy loss straggling in pellet target induced a low energy tail as the Landau distribution [8]. The core part of distribution lies within a narrow momentum interval. For low electron beam current, the cooling efficiency is too weak to compensate the energy loss introduced by beam-target interaction, more and more particles moved to the tail during cooling process,

the momentum spread increases fast as shown in Fig. 3. The particles will be loss since out of acceptance.

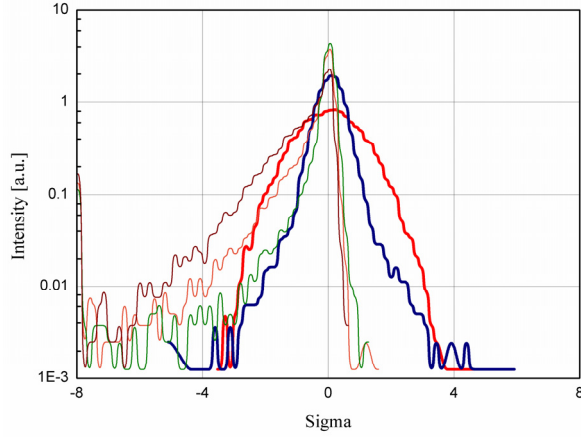


Figure 4: The momentum distribution in equilibrium. The red line is initial distribution before cooling. The blue one is equilibrium distribution of IBS and cooling ( $I_e=2.0A$ ). The other lines are equilibrium distribution of IBS, pellet target and cooling for different electron beam current.

The simulation of momentum variation caused by the beam-target interaction is provided by Urban model in BETACOOOL program. The total energy loss is divided by excitation and ionization of target atoms [6]. Moreover, the energy loss can be calculated by a simplified expression:

$$\frac{dE}{dt} = -4\pi L_c Z_{pellet}^2 Z_{ion}^2 n_{pellet} (atoms/m^3) \gamma_e^2 \beta^{-1} c(m/s) \cdot m_e c^2 (eV) \quad (1)$$

The momentum evolution is described as below:

$$dp(\Delta t) = \frac{1}{E_k} \frac{\gamma}{\gamma+1} \frac{dE}{dt} \Delta t \quad (2)$$

For pellet target thickness listed in table 1, the density is:

$$n_{target} = \frac{2.0 \times 10^{15}}{1.83 \times 10^4} = 1.09 \times 10^{11} (atom/cm^3) \quad (3)$$

The energy loss rate is:

$$\frac{dE}{dt} = -1.74 \times 10^{-5} (eV/s) \quad (4)$$

The comparison on the momentum evolution calculated by BETACOOOL program and simplified formula are shown in Fig. 5. The electron cooling is switched off in simulation. The simulation results are similar obtained by different methods. The momentum shift is larger than  $5 \cdot 10^{-4}$  after 50 seconds. The particles will be loss out of the acceptance. Due to this reason, a powerful electron cooling is necessary to compensate the energy loss and to make particle loss more slowly.

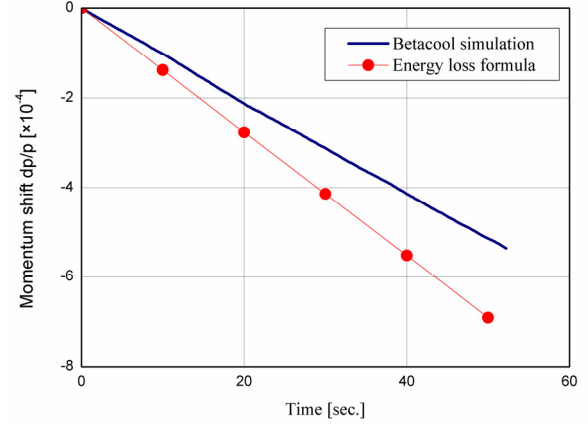


Figure 5: Simulation of the momentum evolution in pellet target experiment. Electron cooling is switched off.

## LUMINOSITY

A new algorithm was developed and implemented into the BETACOOOL program in order to simulate the short scale luminosity variation that comes up with every pellet going through the beam. The short-scale luminosity variation at one step is shown in Fig. 6. The peak signal is produced by collision of ions with each pellet. The repeat frequency is equal to the Rate of pellet generation.

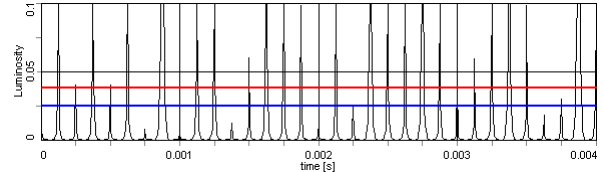


Figure 6: Simulation of short scale luminosity variation. The rate of pellet generation is 80 kHz

The result of long scale luminosity variation shows in Fig. 7. The pellet target is switch on at zero second. The average luminosity depends on the particle number of proton beam and the target thickness, which is show as blue line in Fig. 7. It's nearly constant because the lifetime of proton beam is not considered in the simulation. Usually the detectors are designed for some maximum acceptable event rate. In this simulation an example value of detector limit is given as  $10^{32}$ , which means the count rate value is saturated and equal to the detector limit when it is overloaded ("top-cut" model in simulation) [3]. The event count by the detector is described as the effective luminosity as shown red points in Fig. 7. The effective luminosity increases at the beginning since the phase intensity increased by electron cooling. The equilibrium between cooling, IBS and pellet is obtained around 15 s. The effective luminosity is not changed after 15 s due to the phase intensity is a constant at the equilibrium.

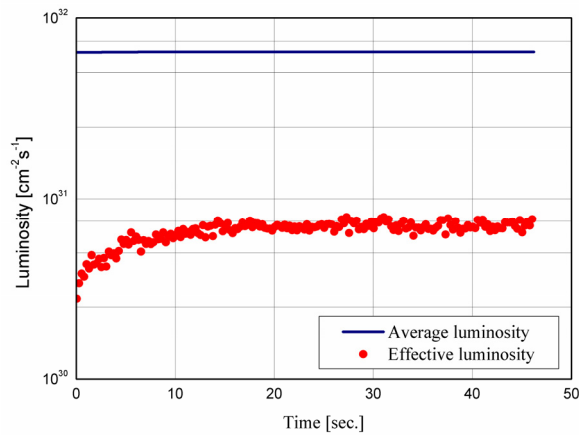


Figure 7: Simulation of long scale luminosity evolution (blue line) and effective luminosity for “top cut” model of detector limit (red point)

### CONCLUSION

Simulation results show that the proton beam can be cooled within several seconds using the high density electron beam produced by the 2 MeV cooler at COSY. The equilibrium momentum spread is dominated by the IBS effect for the high intensity electron beam cooling. But for the low electron beam current, the beam-target interaction produces a core of momentum distribution with long tail and lead particle loss. The high efficiency

electron cooling is necessary to compensate the beam-target interaction. The effective luminosity is less than average luminosity for “top-cut” model detector.

### REFERENCES

- [1] J.Dietrich et al, the proceedings of this conference.
- [2] A.O.Sidorin et al, “BETACOOOL program for simulation of beam dynamics in storage ring”, NIM A 558 (2006) 325.
- [3] A.Smirnov et al, “Effective luminosity simulation for PANDA experiment at FAIR”, Proceedings of COOL09, Lanzhou, China, THPMCP002.
- [4] H.Poth, “Electron Cooling: Theory, Experiment, Application”, Physics reports 196, No. 3&4 (1990) 135.
- [5] V.V.Parkhomchuk, “New insights in the theory of electron cooling”, NIM A 441 (2000) 9.
- [6] I.Meshkov et al, “BETACOOOL physics guide”, <http://lepta.jinr.ru/betacool>
- [7] J.Dietrich et al, “Progress with the 2 MeV electron cooler for COSY-Juelich/ HESR”, the proceedings of RuPAC2010, Protvino, Russia, WECHZ02.
- [8] O.Boine-Frankenheim et al, “Cooling equilibrium and beam loss with internal targets in high energy storage rings”, NIM A 560 (2006) 245.

# ELECTRON GUN WITH VARIABLE BEAM PROFILE FOR COSY COOLER

M. Bryzgunov, A. Buble, A. Ivanov, V. Parkhomchuk, V. Reva, A. Kruchkov, BINP, Novosibirsk, Russia.

## Abstract

Electron gun with variable beam profile is used on COSY 2 MeV cooler to optimize the cooling process. Further development of the gun is achieved with the help of the four-sector control electrode that provides some new features. Combined with BPMs it gives the possibility of the electron beam shape estimation. Application of the gun for stochastic cooling is also discussed in the article.

## INTRODUCTION

The electron gun design is based on the slightly changed gun previously used for CSRe,CSRm [1] and LEIR coolers. The only difference is the four-sector control electrode (fig.1) with separate feeding of all sectors via additional feedthroughs. This small change, nevertheless, opens a new possibility for non-axially modulation of the electron beam profile, which could be used in some applications. Combined with BPMs this feature of the gun provides beam shape monitoring when it passes transport channels.

One more perspective is to use the gun as 3D kicker.

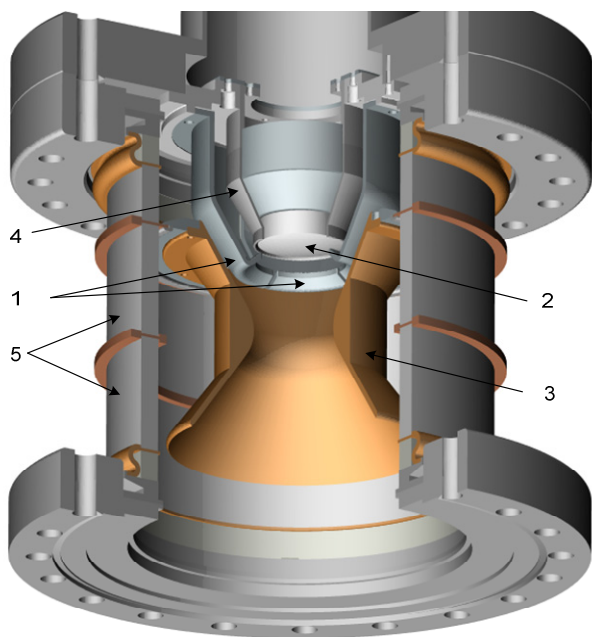


Fig.1 The sketch of the electron gun for COSY 2 MeV cooler.

- 1 – four-sector control electrode, 2 – oxide cathode,
- 3 – anode, 4 – cathode housing, 5 – ceramics.

Since the electron gun of the COSY cooler is embedded in longitudinal magnetic field, its characteristics depend on field strength. Emissive ability of oxide cathode (2) is about 0.5 A/cm<sup>2</sup>, so the maximum possible current is about 3A for 29 mm cathode diameter. Another important characteristic of the gun is the electron transverse temperature, which entirely determines cooling process. One of the tasks for cooler's electron guns design is keeping the transverse temperature as low as possible. On the other hand the electron current density should be increased to provide high efficiency of electron cooling at high energies. Following results of simulations (fig.2), made with UltraSAM code [3], specify the electron beam parameters depending on anode voltage and magnetic field strength.

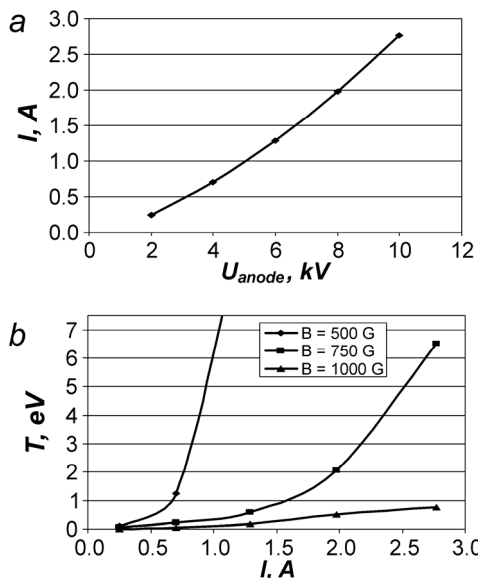


Fig 2: Current (a) and transversal temperature (b) of homogeneous electron beam.

With the current increase the transversal temperature grows also (Fig. 2b). For COSY cooler electron gun 3A current is achievable with few electron-volts transverse temperature at 600 G longitudinal magnetic field and about 10kV anode voltage.

## BEAM PROFILE SIMULATIONS AND MEASUREMENTS

Specification of the electron gun characteristics is very important for further electron cooler operation. Every time when a design of the gun is changed it should be tested before installation on the cooler. For this purpose special test bench was constructed at BINP to perform all

required measurements. Following are current-voltage characteristics of the gun with four-sector control electrode. As it was mentioned above, optics of this gun is similar to previous ones [2], those also provides variable beam profile.

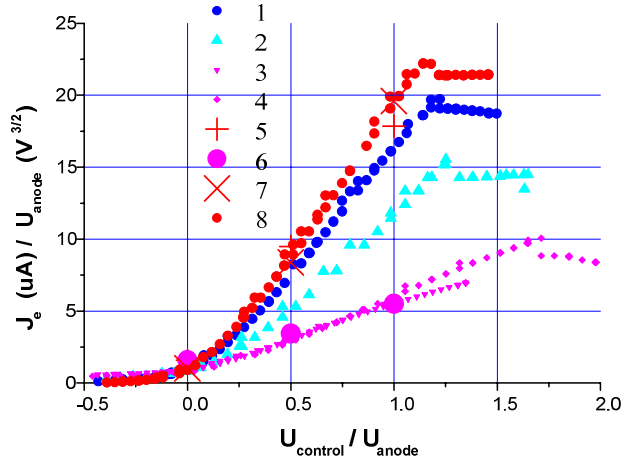


Fig.3. Current-voltage characteristics (perveance) of the gun: 8 – all sectors connected to  $U_{control}$ , 1 –one sector connected to  $U_0$ , 2 – two sectors connected to cathode, 3,4 – three sectors connected to cathode (3 –  $U_{anode}=500$  V, 4 –  $U_{anode}=300$  V. 5,6 – simulations with 3D model, 7 – simulations with 2D axially symmetrical code [3].

Red cycles show data when all four sectors are connected to  $U_{control}$  power supply, blue points – when one sector from four is connected to cathode, triangles up – two sectors from four are connected to cathode potential. Triangles down and diamonds show measurement results when three sectors form four are connected to cathode (for 500 V and 300 V applied to anode).

As one can see, results of the measurements and simulations are in a good agreement.

Another important thing is definition of a correspondence between the electron beam profile and voltages applied to the gun electrodes.

Simulations of beam profiles for the new version of the gun were made with 3D model as well as 2D axial code [3].

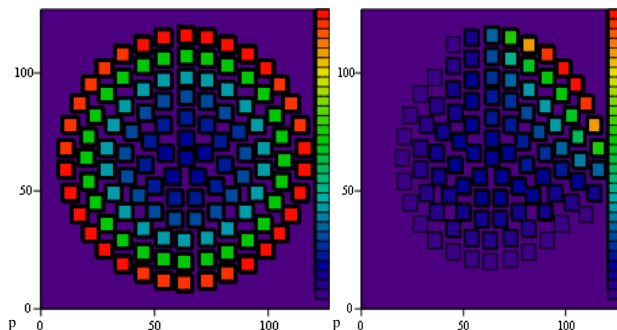


Fig.4. 3D simulation of the electron beam profile for DC current: four sectors on the left, one sector on the right.

Following parameters were chosen for the simulation of the beam profile shown in fig. 4:  $U_{control}=500V$ ,  $U_{anode}=1000V$ . The electron current obtained in this case was 0.3 A and gun microperveance was calculated as  $9.5 \mu A/V^{3/2}$ .

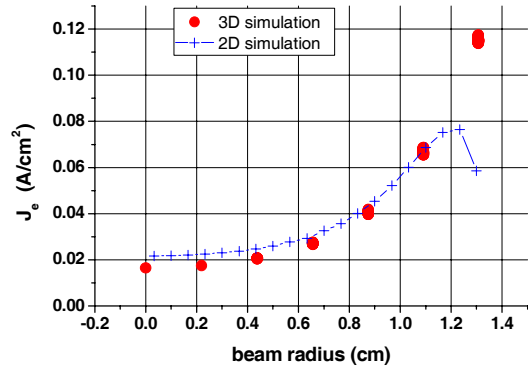


Fig.5. Radial profiles of the electron beam for 3D model (red points), and 2D code simulation.

Difference between two approaches of simulation is shown in fig.5. Results are similar for the main part and rather different for the beam edge. This effect results from lack of accuracy for both methods in area where electron current distribution increases sharply.

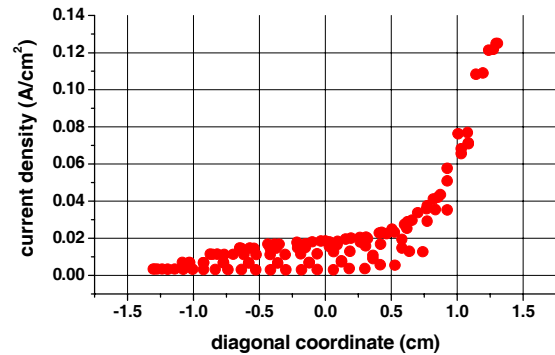


Fig 6. The profile calculation for  $U_{control}=500$  applied to one sector when all other three sectors have the cathode potential.

The electron gun has the perveance which corresponds to simulations made with 2D and 3D codes. It means that predicted profile, based on simulations, corresponds to real electron beam profile.

## ELECTRON GUN AS A PART OF BEAM DIAGNOSTIC

For beam diagnostic purposes the suggestion was made to reject axial symmetry and to divide control electrode into 4 segments. The position of the beam center as well as beam sizes can be measured by applying small potential variation on one of these segments. Beam current modulation decreases at high frequencies of

potential oscillation, thereby to realize this technique the cutoff frequency must be found. The calculation results shown in fig. 7 give 200 Mhz cutoff frequency for this type of the gun.

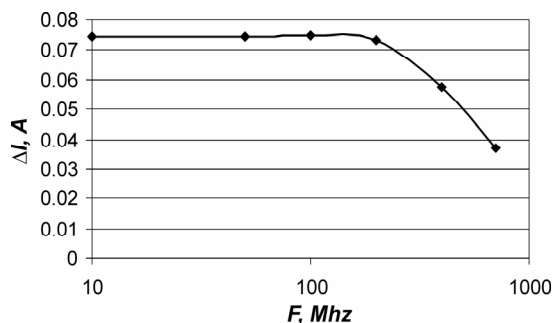


Fig. 7: Electron beam current modulation at oscillation of the control electrode potential ( $\Delta U=50$  V,  $U=600$  V).

To estimate how the of the modulation influences upon beam profile following model was taken. Gun operates in DC mode and small oscillation is applied to one of the segments of the control electrode ( $\pm 5$ V). Results of simulations are shown in figures 8 and 9. On both pictures DC mode is on the left and AC current resulted from modulation in the right (DC current is subtracted).

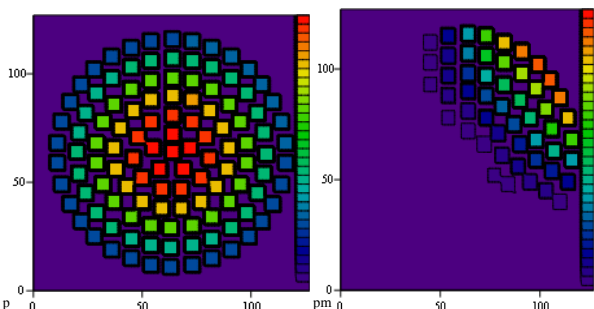


Fig 8. The DC electron beam profile for  $U_{\text{control}}=0$  and  $j_{\text{max}}=19$  mA/cm<sup>2</sup> on the left and AC part with electron beam density 1.4 mA/cm<sup>2</sup> in the right.  $U_{\text{anode}}=1000$ V.

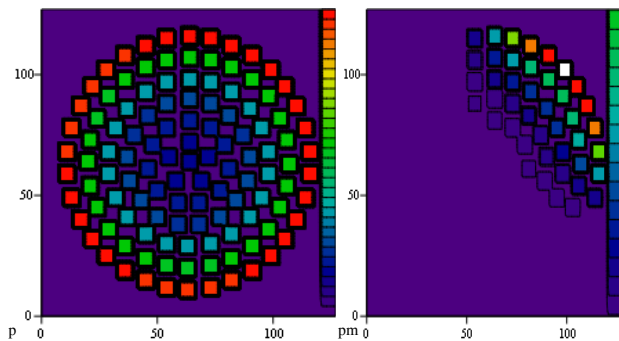


Fig. 9. Profile of the electron beam DC part on the left and AC part on the right for  $U_{\text{control}}=500$  V,  $U_{\text{anode}}=1000$ V.

For the regime represented in fig.8 the integrated current is 50 mA for whole beam and 0.97 mA for the contribution due to modulation. This corresponds to 1cm shift of the beam center of mass from its axis. On the other hand when the DC part of the electron current is

301 mA the AC is only 1.3 mA (fig. 9) that corresponds to the radial shift of 1.2 cm.

While the DC current was changed by six times the AC part and correspondent shift varied slightly (change is about 20%). We can conclude that the beam shift dependence on the gun operation regime is sufficiently weak. This provides us a possibility to monitor the electron beam shape during the cooler operation. The AC current of the beam can be detected with BPMs installed along the transport channels and consequently the beam shift can be measured.

## THE ELECTRON GUN FOR STOCHASTIC COOLING

The idea of combining electron and stochastic cooling in one device was discussed in COOL 07 workshop [4]. The amplified signal of the ion displacement of from pick-up electrode applied to the control electrode of the electron gun. Thus, a wave of the space charge in the electron beam is induced. This wave propagates with the electron beam to the cooling section. The space charge of the electron beam acts on the ion beam producing a kick. The effectiveness of the amplification can be improved with using a structure similar to a travelling-wave tube.

The use of the electron cooler as kicker in the middle range of the energy ( $0.1 \div 1$  GeV/u) may have the following advantages: one device providing 3D kick at the same time; velocity matching of kicking impulse with ion in the wide range; free aperture; using of the existing device; frequency bandwidth may be very high; such type of the kicker doesn't restrict the frequency bandwidth at low value of ion velocity when the time-flight factor becomes the essential [4].

The method, described above, presupposes longitudinal and transversal impacts arisen from electron and ion beams interaction. For longitudinal action the electron beam has axial symmetry. On the other part there is no axial symmetry for the transversal one. Pulse voltage, applied to one of the control electrode sectors, produces transversal kick. Combination of positive and negative pulses gives an opportunity to obtain different types of the influence to the ion beam. Thereby, having four-sector control, one can vary the kick direction (3D kick) as well as its form (dipole, quadrupole).

## SUMMARY

We are looking forward for 2MeV COSY cooler commissioning to start the experiments of cooling at high energies with variable electron beam profile and, as a next stage, for experiments of electron and proton beams interaction when the first one has pulse mode.

## ACKNOWLEDGMENT

Authors thank the head of the ceramic department of the BINP workshop Kosarev A.Y. for the help in production of high quality electron gun.

## REFERENCES

- [1] A. Bublely, A. Goncharov, A. Ivanov, et al., The Electron Gun with Variable Beam Profile for Optimization of Electron Cooling, Proceedings of EPAC 2002, Paris, France.  
<http://accelconf.web.cern.ch/AccelConf/e02/PAPERS/WEPRI049.pdf>
- [2] A.V.Bublely, V.M.Panasyuk, V.V.Parkhomchuk, V.B.Reva, Measuring a hollow electron beam profile, Nucl. Instr. and Meth. A 532 (2004) 413-417
- [3] A. Ivanov, M. Tiunov, ULTRASAM - 2D Code for Simulation of Electron Guns with Ultra High Precision, proceedings of EPAC 2002, Paris, June 2002, WEPRI050, p. 1634 (2002).
- [4] V.V. Parkhomchuk, V.B. Reva, A.V. Ivanov, Electron Beams as Stochastic 3D Kickers, proceedings of COOL 07, Bad Kreuznch, Germany.

# ELECTRON COLLECTOR FOR 2 MEV ELECTRON COOLER FOR COSY

M.I.Bryzgunov, A.V.Bubley, V.A.Chekavinskiy, I.A.Gusev, A.V.Ivanov, M.N. Kondaurov, V.M.Panasyuk, V.V.Parkhomchuk, D.N.Pureskin, A.A.Putmakov, V.B.Reva, D.V.Senkov, D.N.Skorobogatov, Budker INP, Novosibirsk, Russia.

## Abstract

New electron collector for 2 MeV electron cooler for COSY ring is presented. In electron coolers efficiency of collector is important for high voltage power supply. In 2 MeV cooler for COSY it is also important from the point of view of radiation safety because secondary electrons, reflected from the collector go back to accelerating tube. Besides radiation effect it can cause problems with vacuum and electric strength. The collector presented in the article is supplemented with Wien filter which allows increase efficiency of the system by deflection secondary electron flux in crossed transverse electric and magnetic fields. Results of calculation and experimental results achieved on special test bench are presented.

where they can be absorbed. These plates allow to increase efficiency of cooler recuperation from  $10^{-3}$  to  $10^{-6}$ . But in 2 MeV cooler for COSY shape of the magnetic system and high energy of electrons make using of such method very complicated. In this case one should improve collector's efficiency.

In the 2 MeV electron cooler for COSY new construction of collector was proposed. From calculations, its efficiency is about  $10^{-3}$  that is not enough for the high voltage cooler, where maximum electron current is 3 A. In order to increase efficiency of recuperation a Wien filter was installed before the collector for suppression of secondary electron flux reflected from the collector

## INTRODUCTION

Bad efficiency of recuperation in electron cooling systems results in higher current of lost of full energy electrons. It needs higher power of high voltage source that can be difficult technical task. Also electrons reflected from the collector and accelerated in accelerating tube are source of radiation because they hit a wall of vacuum chamber on full energy. Besides the problems, related with the radiation safety, the radiation can cause problems in reaching good vacuum conditions and decrease electric strength of the cooler. In previous coolers produced in BINP for IMP (China) and CERN the efficiency was improved with the help of special electrostatic bending plates installed in the toroid parts of the coolers [1]. Electrons reflected from collector move from collector to gun solenoid and then back to collector

## COLLECTOR

The collector design is shown in Fig. 1. The electron beam coming from the Wien filter (1), passes through collector electrode (2) and suppressor (3) and enters inside the collector (4). Due to magnetic shield (8) and coil (9) with opposite current the beam expands and deposits on cooled collector surface (5). To provide effective pumping from the collector there is a hole with small ion pump (6). To avoid electron flux into this hole in its center a thin electrode is placed.

Adjusting current in coil (9) one can improve collector efficiency by closing in the collector electrons reflected from its surface. Moreover it allows achieve more uniform distribution of electron flux on inner surface of the collector without causing local overheating and to cool the collector more effectively.

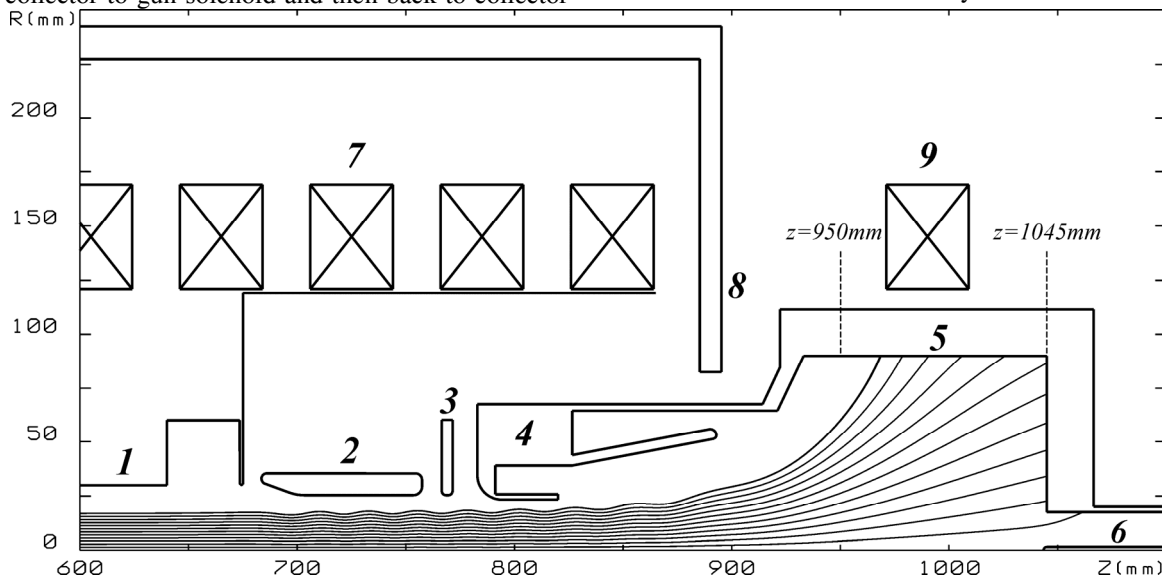


Figure 1: Collector design.

## WIEN FILTER

The idea of the Wien filter is suppression of secondary electrons by crossed transverse magnetic and electric fields (fig. 2). For primary beam Lorenz and electrostatic forces compensate each other and the beam moves along axis of system to the electron collector:

$$F_{\perp} = \frac{e}{c} V_{\parallel} B_{\perp} - eE_{\perp} = 0,$$

where  $V_{\parallel}$  - longitudinal velocity of an electron,  $B_{\perp}$  and  $E_{\perp}$  - transverse magnetic and electric fields.

For secondary beam, reflected from the collector, Lorenz force acts in opposite direction and resulting transverse force is a sum of electrostatic and Lorenz forces:

$$F'_{\perp} = \frac{e}{c} V_{\parallel} B_{\perp} + eE_{\perp} = 2 \frac{e}{c} V_{\parallel} B_{\perp}.$$

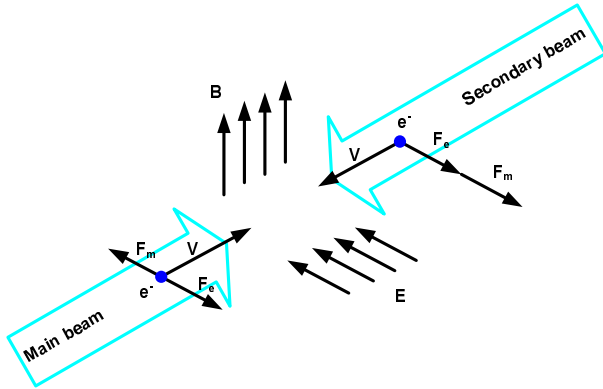


Figure 2: Wien filter.

In longitudinal magnetic field  $B_{\parallel}$  the transverse force courses secondary beam drift in the direction, perpendicular to electric field lines:

$$V_{DR} = c \frac{F_{\perp}}{eB_{\parallel}} = 2V_{\parallel} \frac{B_{\perp}}{B_{\parallel}}.$$

In our system permanent magnets were chosen to produce transverse magnetic field. Using of permanent magnets decreased possibility of tuning the filter, in comparison with additional coils, but it allowed decrease size of the filter and the magnets do not need additional power supplies.

On fig. 3 a sketch of the Wien filter is shown. The permanent magnets (1) are placed on plates of magnetic screen (2) around coils of longitudinal magnetic field (3). Vacuum chamber (4) contains electrostatic plates (5) for production of transverse electric field. The plates are connected to high voltage power supplies via special connectors (6).

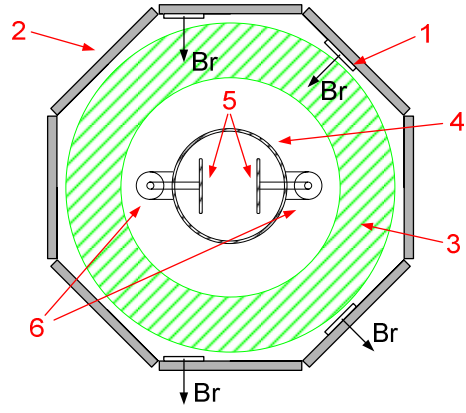


Figure 3: Sketch of Wien filter for 2 MeV cooler.

During entrance to the filter, electron is accelerated or decelerated by edge fields of the plates, that depends on coordinate of an electron. It means that in the filter electrons, flying closer to positive plate, have higher velocity than in the centre of the beam. Since Lorenz force depends on the particle velocity, resulting force for primary beam is not equal to zero for accelerated and decelerated electrons. This results in change of shape of the primary beam and can decrease perveance and efficiency of electron collector.

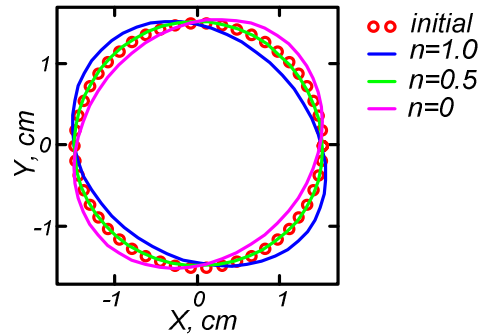


Figure 4: Change of primary beam shape in Wien filter.

In order to avoid this problem transverse magnetic field should have gradient:

$$B_x = B_{\perp} \frac{n}{R} y, \quad B_y = B_{\perp} \left( 1 + \frac{n}{R} x \right),$$

where  $R = \frac{pc}{eB_{\perp}}$ ,  $n = \frac{1}{2\gamma^2}$ ,  $x$  and  $y$  - coordinates in

transverse direction,  $\gamma$  - Lorentz factor. For low energy beam  $n \approx 0.5$ .

On fig. 4 one can see change of main beam shape for different values of  $n$ .

Size, magnetization and positions of the magnets were calculated with the help of the Mermaid program (produced in BINP) in order to produce field with needed parameters. On fig. 5 one can see 3D view of magnetic system of the Wien filter.

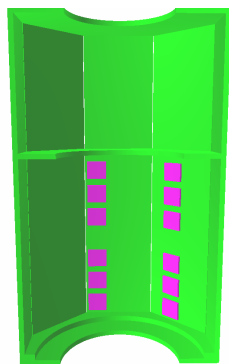


Figure 5: 3D view of magnetic system of Wien filter from Mermaid program.

Total number of magnets is 24 with  $B_r=1.3$  kG. Integral of transverse magnetic field along axis is 1400 G·cm. Length of electrostatic plates is 38 cm.

On fig. 6 the side view of vacuum chamber of the filter is shown.

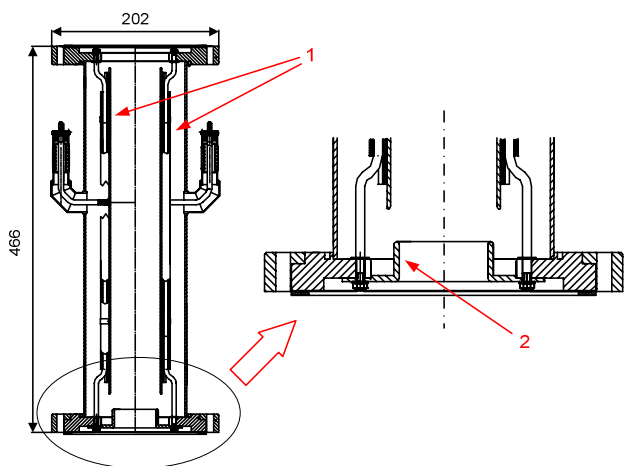


Figure 6: Vacuum chamber of Wien filter.

The chamber includes electrostatic plates (1) and secondary collector (2) which absorbs electrons reflected from the collector and deflected in Wien filter. Inner diameter of the secondary collector is 5 cm. Main beam diameter in this region is about 3 cm.

**TEST BENCH**

In order to test and improve work of the high voltage terminal for the 2 MeV electron cooler for COSY a special test bench was used (fig. 7). It is based on test bench which was built for tests and measurements of electron gun with variable beam profile [2].

The test bench consists of main magnetic system (1), high voltage terminal (2), electron gun (3) and central vacuum chamber (4). High voltage terminal includes magnetic coils of longitudinal magnetic field in gun and in collector (5), collector with Wien filter (6), power supplies and control electronics. It should be noted that in the cooler the gun is placed inside the high voltage terminal but in the test bench we made straight system and gun was placed in the bottom of the system. Control Electron cooling

of the gun was made with the help of electronics of the high voltage terminal.

Measuring the efficiency of the collector in such a straight system is difficult task because reflected electrons fly to cathode region and then return back to collector. In system with Wien filter efficiency of the collector itself can be measured by measuring current which goes to secondary collector  $I_{sec}$ . Supposing that efficiency of the system with Wien filter is much better then without it one can say that all electrons reflected from the collector go to secondary collector and efficiency of collector itself is equal to  $I_{sec}$  divided to main beam current  $I_{coll}$ .

In order to measure efficiency of the collector with Wien filter a ceramic insertion with an electrode was installed under the Wien filter. Inner diameter of the electrode is 4 cm. Supposing that only secondary electrons which deflection in the filter is not enough to go to the secondary collector and electrons reflected from the secondary collector can leave the Wien filter, one can assume that most part of such electrons go to this electrode. It means that efficiency of full system is equal to current of the electrode  $I_{ins}$  divided to  $I_{coll}$ .

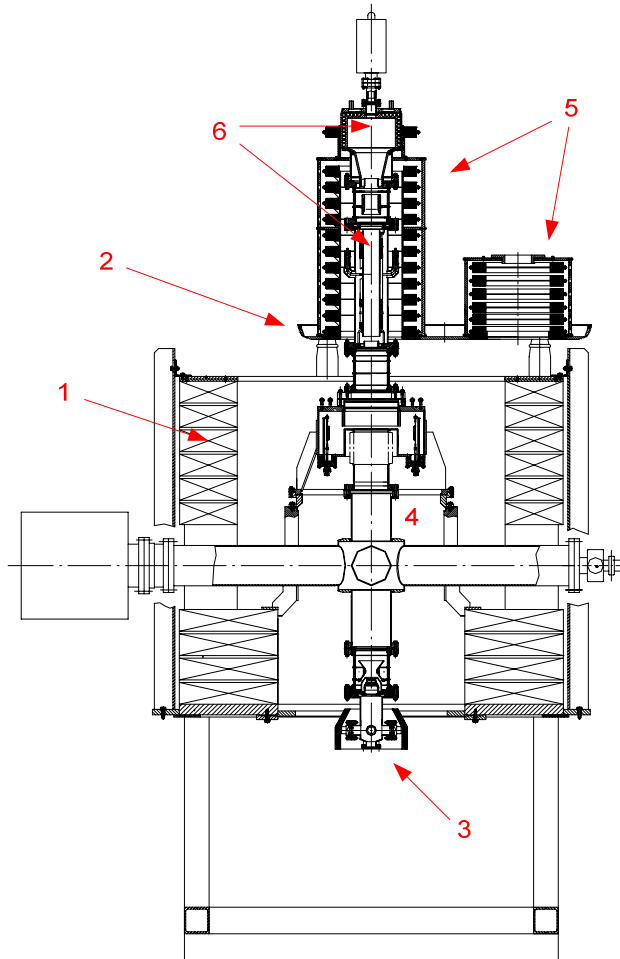


Figure 7: Test bench.

## EXPERIMENTAL RESULTS

Electrons reflected from collector surface have wide energy spectra. The aim of the suppressor electrode is to produce potential barrier in order to close low energy electrons in the collector. But since the electrode is thin, the potential in axis and in edge of electron beam is different. Because of this there must be an optimum in order to close as much reflected electrons in the collector as it possible but to not reflect electrons on the edge of the main beam. Collector electrode is much thicker than suppressor and its potential in axis and in beam edge is equal. Because of this it closes all secondary electrons, which energy is lower than potential of the electrode. On fig. 8 the dependence of collector efficiency on electron beam current for different ratio between voltage of the collector and collector electrode is shown.  $U_{coll}=3.5$  kV.

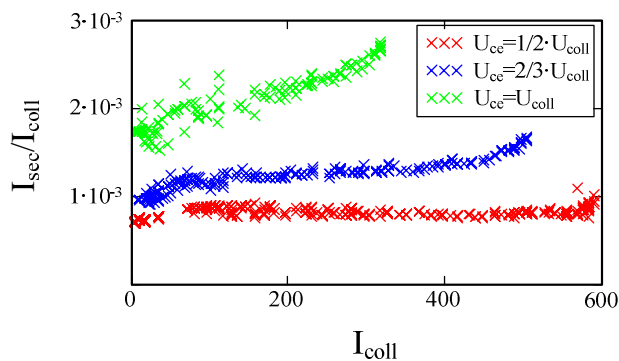


Figure 8: Dependence of efficiency of the collector itself on main beam current.

One can see that decreasing its voltage to  $1/2$  of collector voltage the efficiency of the collector improves to the factor of about 2.

On fig. 9 the dependences of efficiencies on beam current for the collector itself and for collector with Wien filter are shown.

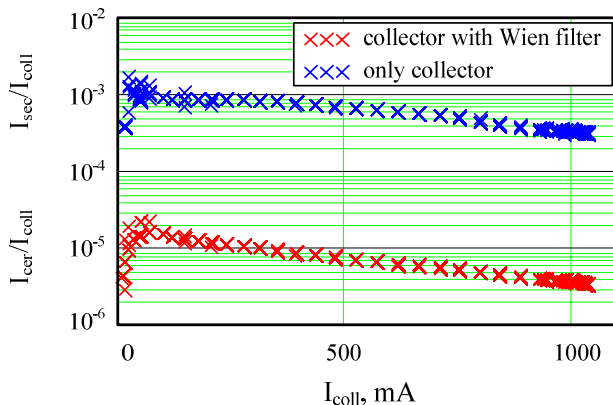


Figure 9: Dependence of efficiency of collector with Wien filter on main beam current.

Efficiency of the collector with Wien filter is about  $3 \cdot 10^{-6}$  for current 1 A. The higher current of beam was limited by power of high voltage source which was used in the test bench.

Electron cooling

It was said above that current in the last coil can be adjusted in order to improve efficiency of the collector. In fig. 10 a dependence of efficiency on coil current for different collector voltage is shown.

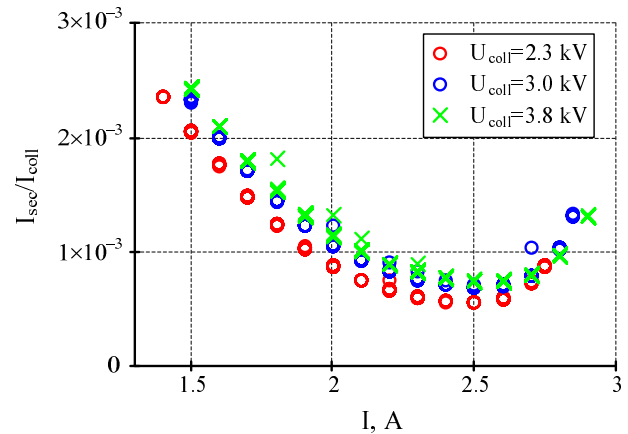


Figure 10: Dependence of efficiency on current in the last coil.

From the figure one can see that adjusting current in the last coil the efficiency of the collector can be improved to a factor of  $\approx 3$ .

## CONCLUSION

Collector with Wien filter can significantly improve efficiency of recuperation of electron cooling system. On system described in the work efficiency  $3 \cdot 10^{-6}$  was reached for main beam current 1 A.

Disadvantages of such system are using of additional high voltage power supplies for electrostatic plates of the filter, increasing of size of the system and complication of magnetic system in order to produce transverse magnetic and electric fields.

## REFERENCES

- [1] V.N. Bocharov, A.V. Bublely, M. Vedenev, et al, "Commissioning of electron cooler EC-300", preprint, Budker INP, Novosibirsk, 2004.
- [2] A. Bublely, V. Panasyuk, V. Parkhomchuk, V. Reva, "Measurements of the profile of an intense electron beam", Instruments and Experimental Techniques. pp. 83-91, Vol. 49, No. 1, 2006.
- [3] A. Konstantinov, V. Parkhomchuk, V. Reva, "Space Charge Oscillation in Electron Cooling Devices", Technical Physics. pp. 85-89, Vol. 48, No 1, 2003.

## SYSTEM FOR MEASUREMENT OF MAGNETIC FIELD LINE STRAIGHTNESS IN SOLENOID OF ELECTRON COOLER FOR COSY

V.N. Bocharov, M.I. Bryzgunov, A.V. Bublely, V.G. Cheskidov, M.G. Fedotov, V.V. Parkhomchuk, V.B. Reva, Budker INP, Novosibirsk, Russia

### Abstract

Construction of measurement system is presented. The system is based on special magnetic sensor (compass) with a mirror attached to the compass needle. The needle with the mirror are suspended on gimbal suspension and can rotate in two directions. Measuring reflected laser beam deflection one can measure field line straightness with accuracy up to  $10^{-6}$  rad. The compass is installed inside vacuum volume of the cooling section on special carriage that moves on rail along the section via special tape. To calibrate the compass special test bench was made. The calibration procedure allows to determine and to diminish compass inaccuracy appeared during manufacture and assembling. Results of calibration of the compass on the test bench are presented.

### INTRODUCTION

Straightness of magnetic field line in cooling section is very important for electron cooling as it increases effective velocity of electrons. For high energy electron cooling it is especially important as the influence increases with energy  $V_{\gamma} = \gamma V \theta$ , where  $\gamma$  – relativistic factor,  $V$  – longitudinal velocity of an electron,  $\theta$  – angle of field line deflection.

Experience with production of electron coolers shows that straightness of magnetic field line degrades with time. Because of this a new device which allows to measure straightness with period of several months without disassembling of vacuum chamber is needed. For 2 MeV cooler for COSY it was proposed to install measuring system based on magnetic compass inside the vacuum chamber of cooling section and toroids. Similar system was used on electron cooler for NAP-M storage ring [1].

The transverse components of the magnetic field of coil can be determined by the magnitude of deviation from the axis of magnetosensitive element of sensor. If it is rigidly connected with the mirror, the angle of deviation can be determined from the shift of the light spot produced by a beam from an external source, reflected by the mirror. Returning a spot in the starting position by the influence of compensating magnetic field from an external source, the magnitude of corresponding component of field of tested solenoid (i.e. misalignment of field line at that point) can be determined.

In the first experiments on determination of the quality of magnetic field in INP [1], an optical automatic autocollimator was used as the measuring system, in which the angle of deflection was determined by the mechanical adjustment of the light in the instrument. As the magnetic sensor it was used a construction composed

of the mirror, laid down in the gimbal suspension with jewels from clock as the bearing supports, and of steel rod penetrating the mirror axis. In a magnetic field of a solenoid with magnitude of about 1 kG field inhomogeneity about  $10^{-5}$  radian was determined. The sensitivity was limited mainly by friction at the nodes of motion in the optical components of the collimator during the rearrangement of its optics.

In 2000, in the BINP a measurement system for a prototype of electron cooling system for the Tevatron (Fermilab, USA) was designed [2]. For operating magnetic field of 50-100 G sensitivity of previous devices was not enough, therefore the measuring system was modernized.

The mirror was fixed on the end of a light frame along which axis a magnet (cylinder of material NdFeB) was inserted. At another end a nonmagnetic counterbalance was attached. With the help of wire, fixed at the center of gravity, the sensor node was suspended in the center of a hollow cylindrical carriage, which had compensating circuits. The carriage was moved along the bottom of a narrow chamber and was stabilized by two strings, stretched along the pipe.

Electronic circuit contained a low power semiconductor red laser as light source, four quadrant photodiode, source of compensating current and the feedback loop, allowing return reflected from the mirror compass beam to the starting position for fixing the value of the compensation current.

This scheme with no significant changes was used in future for setting up solenoids of produced at the BINP coolers for IMP (Lanzhou, China) and for CERN. Only constructions of compasses were improved.

Such constructions of compasses are highly sensitive due to the absence of nodes with the mechanical friction. But they can not be used in the COSY because of limited strength of thin metal suspension wires. This can result in break of the wire especially on curved parts of magnetic system. Such situations are inevitable since the compass need to be removed from a region with homogeneous field to release accelerator's aperture. Increasing the strength of wire by increasing its thickness is also limited because of rapid growth of the elastic forces. Significantly more durable fishing line is not a vacuum material and it does not allow heating to even 100 degrees.

For these reasons for 2 MeV COSY cooler a design (already described above) with setting the magnet to the mirror in a gimbal suspension was chosen (fig. 1).

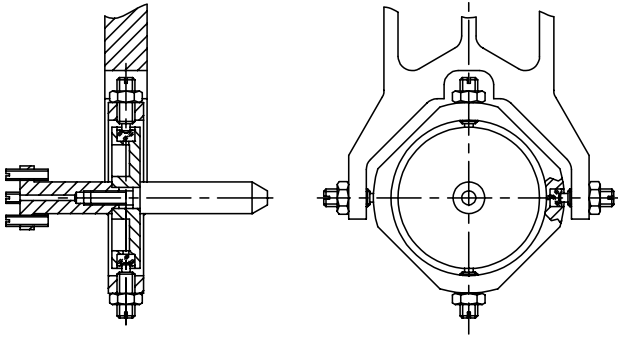


Figure 1: Compass with gimbal suspension.

Since it can rotate in every direction the compass always sets along the field, minimizing the transverse loads from the strong magnetic field.

In the COSY cooler the carriage with a compass is moved along the axis of the solenoid on a massive rail which ensures the stabilization of the carriage in transverse direction (fig. 2).

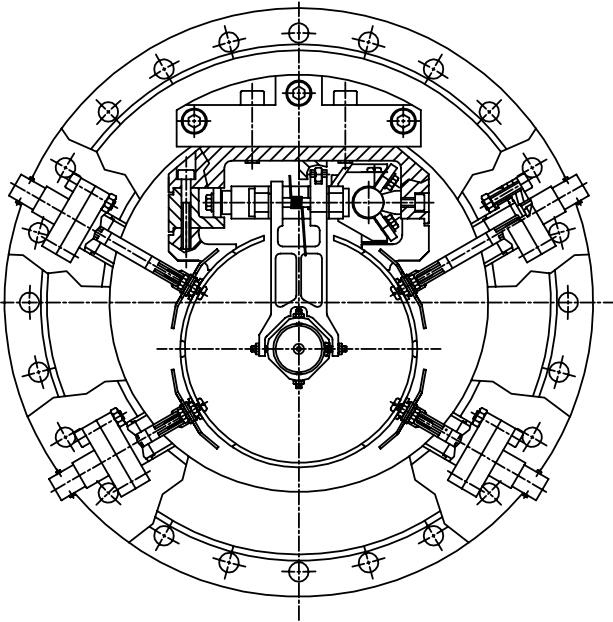


Figure 2: Rail with compass inside the vacuum chamber.

Rail is located at the top of the vacuum chamber, the frame of a compass mounted on a carriage underneath. The carriage is moved along the rail by a closed perforated tape, which moves with a help of a special gear. Near one end of the cooling solenoid the holder goes from vertical to horizontal position, raising the compass, so that the aperture of the accelerator is released.

## TEST BENCH

An important part of the whole complex for the production and regulation of electron cooling is test bench for the magnetic measurements. Such a device as a compass can not be manufactured in a production environment with perfect accuracy. Because of this the

compass is not balanced, and the mirror is not perpendicular to the magnetic axis. Therefore, before installing it in the cooler the compass should be tested and the deviation from the norm of the parameters should be minimized.

The procedure for adjusting the compass is measuring its parameters and possible elimination of distortions. It should be noted that the residual small deflections of parameters don't influence on the quality of measurement of filed line straightness in the cooler, and lead only to consumption of additional compensating currents, resulting in pedestal in results of measurement (systematic error).

On fig. 3 a scheme of the test bench is shown. Compass (1) is installed in center of main solenoid (2), which is powered with a supply (3). The solenoid also contains block of correction and calibration coils (4). Laser beam from source (5) is directed on cube (6) which partly reflects the beam on mirror of the compass. The mirror reflects the beam in opposite direction to prism and then to photodiode (7). By the signals on four sectors of the photodiode, electronic block of feedback system (8) produces signal for correction power supplies (9) in order to place the beam in center of the photodiode. Components of the transverse magnetic field in the compass region are proportional to the currents in correction coils. Another laser (10) is used only for adjustment of the test bench.

The solenoid can be rotated to 180 degrees without correction and calibration coils. It is important for measurements which will be described below.

## EXPERIMENTS

### Measuring parameters of sensor

For measurement of compass parameters we used the same method that was used for previous compasses on another test bench [3]. Briefly, the idea of the method is as follows. The signal recorded by the instrument in some point includes several components. Some of them depend on the solenoid's longitudinal magnetic field  $B_z$ , and the others are field-insensitive. This signal can be represented by the following expression:

$$B_j = B_{1j} + B_{0j} + \delta B_j = B_j [\alpha_j + \beta_j + \gamma_j] + [B_j^{ext} + B_j^{sh} + B_j^{sen}] + \delta B_j$$

where  $j$  is the  $x$  or  $y$  coordinate;  $\alpha_j$  are the imperfections of the solenoid's magnetic field;  $\beta_j$  is the angle between the magnetic axis of the compass and the perpendicular to the mirror;  $\gamma_j$  is the angle between the solenoid's axis and the laser beam,  $B_j^{ext}$  is the external (with respect to the solenoid) magnetic field;  $B_j^{sh}$  is the residual field of the magnetic shield;  $B_j^{sen}$  are the additional  $z$ -independent components due to the magnet's unbalance etc.; and  $\delta B_j$  are the random noises.

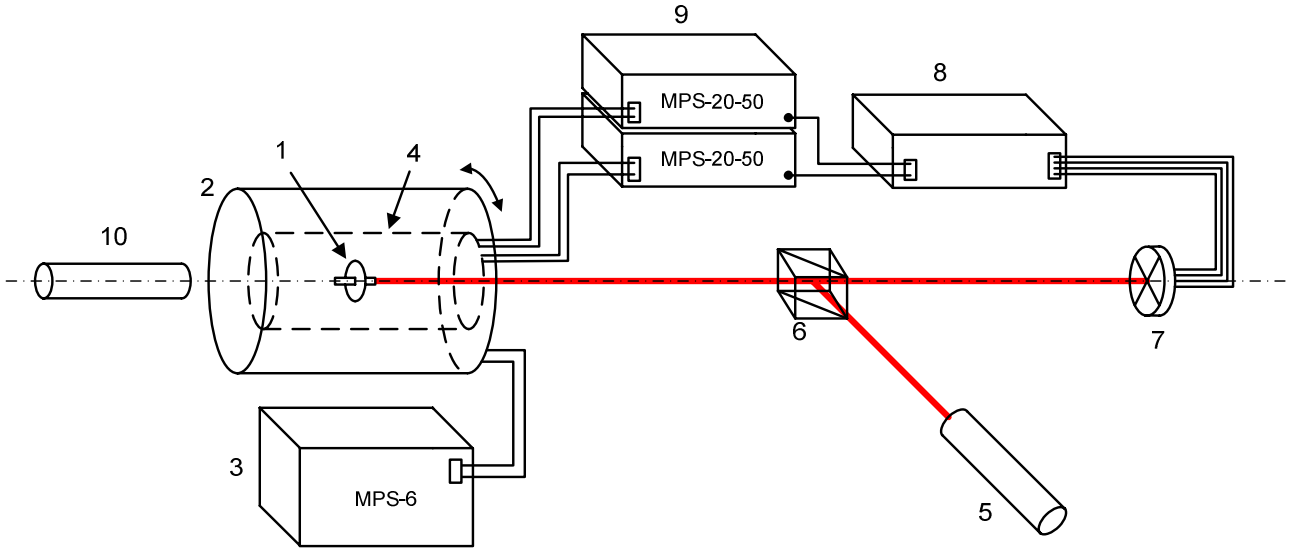


Figure 3: Scheme of the test bench.

The components  $B_{ij}$  and  $B_{oj}$  can basically be found separately by making measurements with different solenoid currents (fields). Parameters  $\beta_j$ ,  $\gamma_j$ , and  $B_j^{sen}$  (as well as  $\delta B_j$ ) are the measurement errors, but they can be reduced to small values by aligning both the compass and the optical channel of the whole measuring system.

If we exclude random factors and take into account that the laser beam can be aligned with the solenoid's axis with deviation  $\gamma_j \sim 1 \cdot 10^{-4}$  rad, the main sources of errors appear to be related to the magnetic sensor's properties. Parameters  $B_j^{ext}$  and  $B_j^{sh}$  can be ignored due to high properties of the magnetic shield. Under these conditions, equation for  $B_j$  becomes simpler and contains only three components:

$$B_j = B_z [\alpha_j + \beta_j] + B_j^{sen}.$$

Rotation of the solenoid about its axis through 180 degrees reverses the signs of its own transverse components. Making three measurements for each of components  $x$  and  $y$  in order to determine  $B_{j1}(B_{z1})$ ,  $B_{j2}(B_{z2})$ , and  $B_{j3}(B_{z3})$  for the fields  $B_{z1}$ ,  $B_{z2} = 2 B_{z1}$ , and  $B_{z3} = -B_{z2}$  (i.e., with the solenoid turned over) allows all of the values characterizing the quality of the compass to be calculated:

$$B_j^{sen} = 2B_{j1} - B_{j2}, \alpha_j = (B_{j2} - B_{j3}) / 2B_{z2}$$

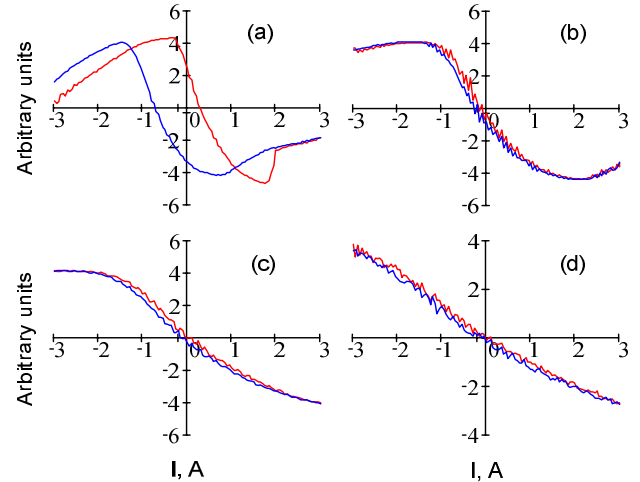
$$\beta_j = (B_{j2} + B_{j3} - 2B_j^{sen}) / B_{z2}.$$

After adjustment of parameters we reached next values:  $B_x^{sen}/B_y^{sen} = 5.4 \cdot 10^{-4} / 4.4 \cdot 10^{-4}$ ;  $\alpha_x/\alpha_y = 1.1 \cdot 10^{-4} / 5.7 \cdot 10^{-4}$ ;  $\beta_x/\beta_y = 8.6 \cdot 10^{-4} / 8.1 \cdot 10^{-4}$ . Such values are appropriate to use the compass for measurement of field line straightness.

### Friction in nodes

It was said above that disadvantage of the gimbal suspension is friction force in jewel bearings which can reduce sensitivity and accuracy of the sensor. In fig. 4 one can see set of curves which were measured by slow changing of current in correction coils without feedback.

There are four pictures with dependence of signal on photodiode on current in the coils, where red lines show results which were measured changing current from -3 A to 3 A, and blue lines – changing current back from 3 A to -3 A. From the figure one can see there is hysteresis related with friction in bearings, but in the same time influence of friction force decreases with increasing of solenoid field.


 Figure 4: Hysteresis due to friction. a)  $B=38$  G, b)  $B=62.5$  G, c)  $B=125$  G, d)  $B=250$  G.

Position of compass is determined by equilibrium between moments of friction force and of magnetic force which acts on magnetic rod of the sensor. In a simple model of the magnetic dipole in longitudinal field the moment of magnetic force is equal to:

$$M_m = q_m B L \alpha$$

where  $B$  – magnetic field,  $L$  – length of the rod,  $\alpha$  – angle between force line and the rod,  $q_m = S \cdot B$  – magnetic charge,  $S$  – sectional area of the rod. Since friction force doesn't depend on magnetic field, the angle  $\alpha$  depends on magnetic field as  $1/B^2$ .

In fig. 5 a dependence of angle between magnetic field line and sensor's rod, calculated from hysteresis, is shown. The blue line is a fitting curve  $\sim 1/B^2$ .

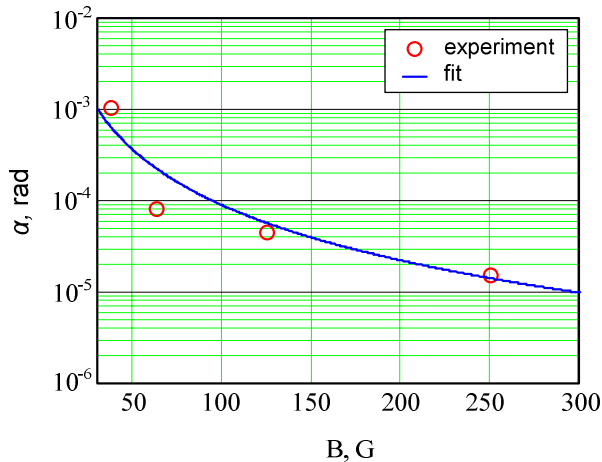


Figure 5: Residual angle due to friction.

Interpolating the results for 2 kG we can get that uncertainty of angle related with friction in bearings is about  $2 \cdot 10^{-7}$ , that is much lower than needed accuracy of measurements  $10^{-5}$ .

### Sensitivity of the compass

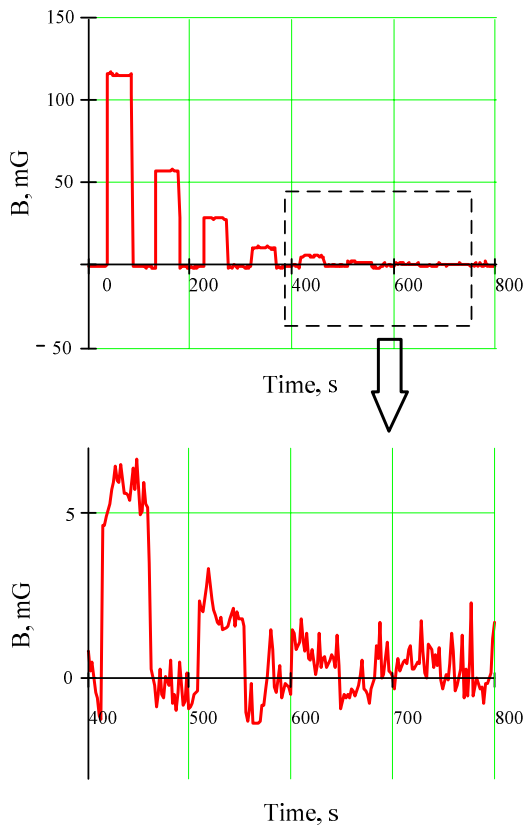


Figure 6: Sensitivity of the compass.

To measure sensitivity the calibration coils were used. On fig. 6 the response of correction coils for the turning on current in calibration coils is shown.

The signal on calibration coils has a step form with decreasing amplitude (from left to right: 2 A, 1 A, 0.5 A, 0.2 A, 0.1 A, 0.05 A, 0.02 A, 0.01 A, 0.005 A, 0.002 A, 0.001 A) and interval with zero signal between two steps. Length of a step and interval between steps are 45 seconds (period 90 sec). 1 A in calibration coil corresponds to field 55 mG in compass region.

From fig. 6 one can see that response from step 0.02 A (region of 600 sec) is the last one that can be distinguished from measurement noise. So sensitivity of the compass is about 1 mG. For field in cooling section 1 – 2 kG such sensitivity means that we can measure angle of field line with accuracy  $(0.5 - 1.0) \cdot 10^{-6}$ .

## CONCLUSION

Measurements of parameters of compass with gimbal suspension, which were made on special test bench, show that it can be used in cooler for COSY to measure magnetic field line straightness with accuracy better than  $10^{-5}$  for field 1 kG and more. At the same time such system has some disadvantages, such as worse sensitivity and accuracy in comparison with compass on wire suspension. However compass with wire is not appropriate to use it in system for measurements without disassembling of vacuum chamber.

## REFERENCES

- [1] L.N.Arapov, N.S.Dikansky, V.I.Kokoulin et al, Proceedings of the XIII international conference on high energy accelerators. Novosibirsk, 1986, p.341-343.
- [2] C. Crawford, E. Mc-Crory, S. Nagaitsev et al, Fermilab Electron Cooling Project: Field Measurements in the Cooling Section Solenoid. Proc. of the 2001 PAC, Chicago.
- [3] V.N. Bocharov, A.V. Buble, S.G. Konstantinov et al, Precision Measurements and Compensation for the Transverse Components of the Solenoids Magnetic Field. Instruments and Experimental Technique, Vol.48, No. 6, 2005, p.p. 772—779.

## LEPTA PROJECT: TOWARDS POSITRONS

E.Ahmanova, M.Eseev\*, V.Kaplin, V.Karpinsky, A.Kobets#\*\*,  
 V.Lokhmatov, I.Meshkov, V.Pavlov, A.Rudakov,  
 A.A.Sidorin, S.Yakovenko, JINR, Dubna

### Abstract

The project of the Low Energy Positron Toroidal Accumulator (LEPTA) is under development at JINR. The LEPTA facility is a small positron storage ring equipped with the electron cooling system. The project positron energy is of 2 – 10 keV. The main goal of the facility is to generate an intense flux of positronium atoms – the bound state of electron and positron.

Storage ring of LEPTA facility was commissioned in September 2004 and was under development up to now. The positron injector has been constructed in 2005 ÷ 2010, and beam transfer channel – in 2011. By the end of August 2011 experiments on electron and positron injection into the ring have been started. The recent results are presented here.

### LEPTA RING DEVELOPMENT

The Low Energy Particle Toroidal Accumulator (LEPTA) is designed for studies of particle beam dynamics in a storage ring with longitudinal magnetic field focusing (so called "stellatron"), application of circulating electron beam to electron cooling of antiprotons and ions in adjoining storage electron cooling of positrons and positronium in-flight generation.

For the first time a circulating electron beam was obtained in the LEPTA ring in September 2004 [1]. First experience of the LEPTA operation demonstrated main advantage of the focusing system with longitudinal magnetic field: long life-time of the circulating beam of low energy electrons. At average pressure in the ring of  $10^{-8}$  Torr the life-time of 4 keV electron beam of about 20 ms was achieved that is by 2 orders of magnitude longer than in usual strong focusing system. However, experiments showed a decrease of the beam life-time at increase of electron energy. So, at the beam energy of 10 keV the life time was not longer than 0.1 ms. The possible reasons of this effect are the magnetic inhomogeneity and resonant behaviors of the focusing system.

### Vacuum system improvements

In old design the distance between kicker plates was off 32 mm that limited the aperture. New kicker design allows us to increase aperture up to 120 mm.

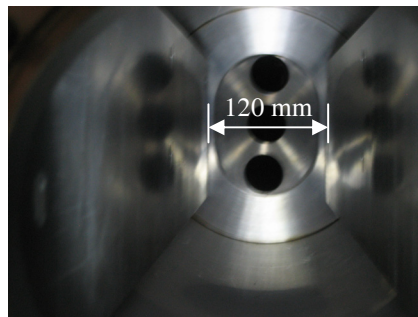


Figure 1: The new kicker

### Testing after upgrading

Typical life time dependence on electron energy,  $\tau_e(E_e)$ , has two slopes (Fig.2). The left one, where  $\tau_e$  increases with  $E_e$ , is defined by electron scattering on residual gas. The right slope, descending with  $E_e$ , relates to violation of electron motion adiabaticity on inhomogeneities of solenoid magnetic field.

The curves 1 and 2 were obtained in 2005, whereas the curves 3, 4 and the point 5 have been measured in June 2008. The curve 6 was measured in August 2009, after all modifications of the ring described above. One can see significant increase of the electron life time. Of the main importance is the increase of the life time (comparing with the values of the year 2005, 2008) in the energy range above 4 keV by 6÷10 times. It proves the necessity of a further improvement of the solenoid field homogeneity. The point 7 (2011) is result of the regime optimization and vacuum improvement.

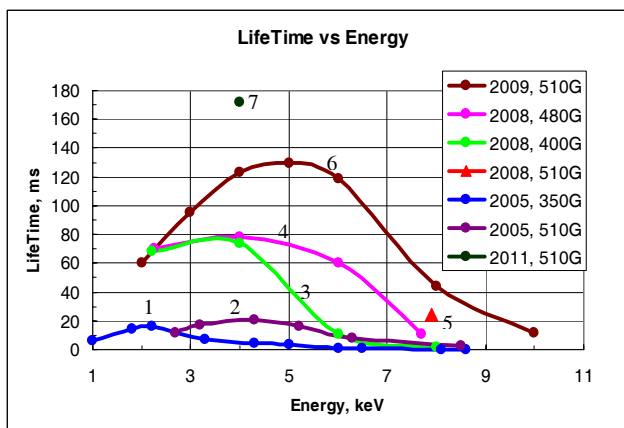


Figure 2: LifeTime vs electron energy.

\* M.V.Lomonosov Pomor State University, Russia.

\*\* Joint Institute for Nuclear Research, Russia,

Institute of Electrophysics and Radiation Technologies, NAS of Ukraine

# kobets@jinr.ru

### Electron cooling system construction

The manufacturing of the system for generation, transportation and energy recovering of single pass electron beam has been completed. Test of the electron beam transportation from the gun to the collector begun in pulsed mode and continued in DC mode of the gun operation. Result is in Table 1.

Table 1. Parameters of electron cooling system

Electron energy	Current		
	$I_e$ , mA	$\Delta I_e$ , $\mu$ A	$\Delta I_e/I_e$
3	20	230	0,011
5	50	290	0,006
7	64	620	0,01
8,7	105	430	0,004

### Positron transfer channel

The channel is aimed to transport positrons extracted from the trap of the injector (see below) and accelerate them up to 10 keV (maximum) in electrostatic field in the gap between the trap and the channel entrance. The designing and manufacturing of the channel elements was completed in 2010. В 2011 году была изготовлена магнитная система канала и инжектор позитронов был присоединен к накопительному кольцу (Fig. 3).

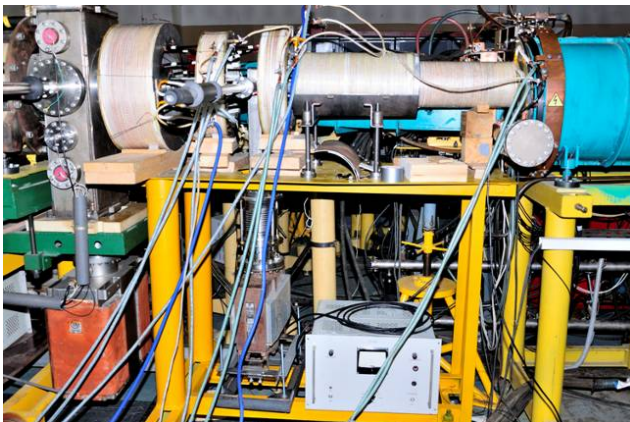


Figure 3. The transfer channel.

### THE POSITRON TRAP

When slow positron beam is formed, it enters the Penning-Malmberg trap where the positron cloud is accumulated [2]. The trap is a device which uses static electric and magnetic fields to confine charged particles using the principle of buffer gas trapping. The confinement time for particles in the Penning-Malmberg traps can be easily extended into hours allowing for unprecedented measurement accuracy. Such devices have been used to measure the properties of atoms and fundamental particles, to capture antimatter, to ascertain reaction rate constants and in the study of fluid dynamics. The JINR positron trap (Fig. 4) was constructed to store

slow positrons and inject positron bunch into the LEPTA ring.

The research of the accumulation process was carried out using electron flux. For this purpose the test electron gun allowing to emit  $dN/dt = 1 \cdot 10^6$  electrons per second with energy 50 eV and spectrum width of a few eV was made. These parameters correspond to slow monochromatic positron beam which we expect from a radioactive source at activity of 50 mCi.

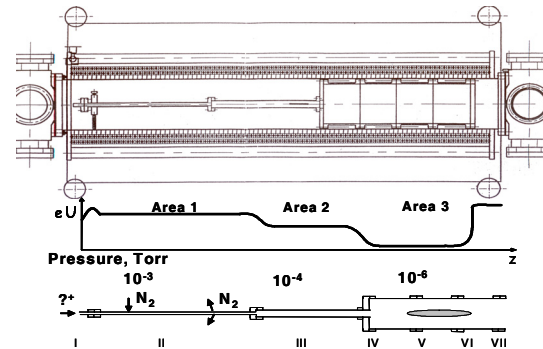


Figure 4: Assembly drawing of the positron trap (upper picture), potential and pressure distributions along the electrode system.

Electron accumulation in the trap with application of rotating electrical field so called "rotating wall" (RW)[3], was studied with electrons during December 2006 and repeated with electrons and positrons in July 2011. The test electron beam shrinking was observed when RW parameters were optimized (Fig.5).

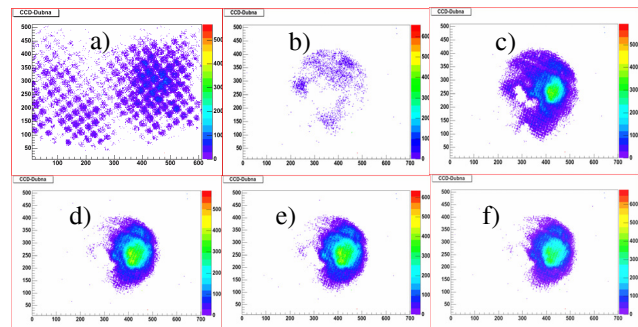


Figure 5: Profiles of the stored test electron beam at different storage time: a) 30s, RF Off; b) 15s, RF On; c) 20s, RF On; d) 30s, RF On; e) 40s, RF On; f) 90s, RF On.

### THE POSITRON INJECTOR

In summer 2010 the slow positron source and the trap have been assembled. The first attempts of slow positron storage were performed (Fig.6) and stored positrons were extracted to the collector.

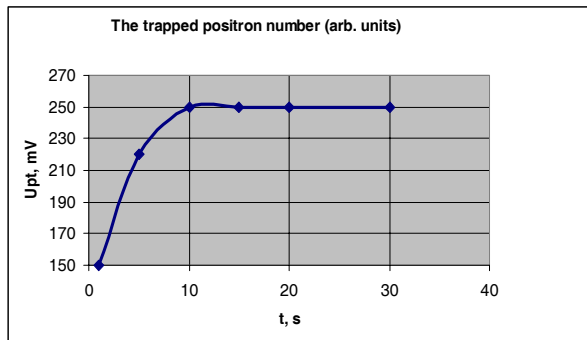


Figure 6: The trapped positron number vs storage time.

Upt is the amplitude of the signal from the phototube (PT), RW amplitude is equal to 0.5 V.

Manufacturing and assembling of the transfer channel from injector to the ring were completed by the end of July 2011. The test of the channel was performed in August 2011, first with test electron beam and later with positrons. Test electron gun was installed at the entrance of positron trap (Fig.7).



Figure 7. The test electron gun.

The ring was disassembled and luminescent screen was placed inside the kicker chamber. The beam images of electron beams both from the test gun and electron gun of the electron cooling system were obtained on the screen (Fig.8). After that positrons were injected into the ring at facility parameters optimized with electron beam.

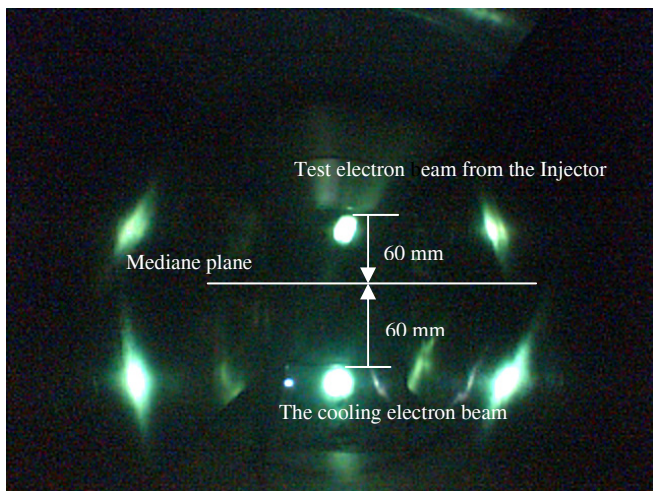


Figure 8. Two beams on luminescence screen.

The registration of positron transportation through the channel and septum section of the ring to the luminescence screen was performed with NaI scintillation counter in counting mode.

### CONCLUDING REMARKS

The development of the LEPTA project is approaching the stage of experiments with circulating positron beam. All main elements of the ring and the injector are ready and have been tested.

All works supported by RFBR, grant №09-02-00084.

### REFERENCES

- [1] A.Kobets, et. al., Status of the LEPTA project, Proc. of COOL'05 AIP Conference Proceedings, 2006, v.821, p.95-102
- [2] M. Amoretti et al., The ATHENA antihydrogen apparatus, Nucl. Inst.Meth. Phys. Res. A 518 (2004) 679-711
- [3] C.M.Surko, R.G.Greaves, Radial compression and inward transport of positron plasmas using a rotating electric field, Physics of plasmas, 8 (2001), 1879-1885.

# MAGNETIC SYSTEM OF ELECTRON COOLER FOR COSY

M. Bryzgunov, A. Bublej, V. Gosteev, V. Panasyuk, V. Parkhomchuk, V. Reva

BINP SB RAS, Novosibirsk.

## Abstract

The magnetic system for the COSY cooler is presented. Electron beam energy range is wide (24keV-2MeV), typical bend's radii of electrons track are near to 1 m, typical magnetic fields are 0.5 – 2kG. Transport channels with guiding magnetic fields for motion of electrons from high voltage terminal of cascade

transformer into cooling section and their return for recuperation under such conditions are discussed. Results of Hall sensors measurements are compared with corresponding computations. Also some steps were taken for improvement of the magnetic field lines straightness in the cooling section.

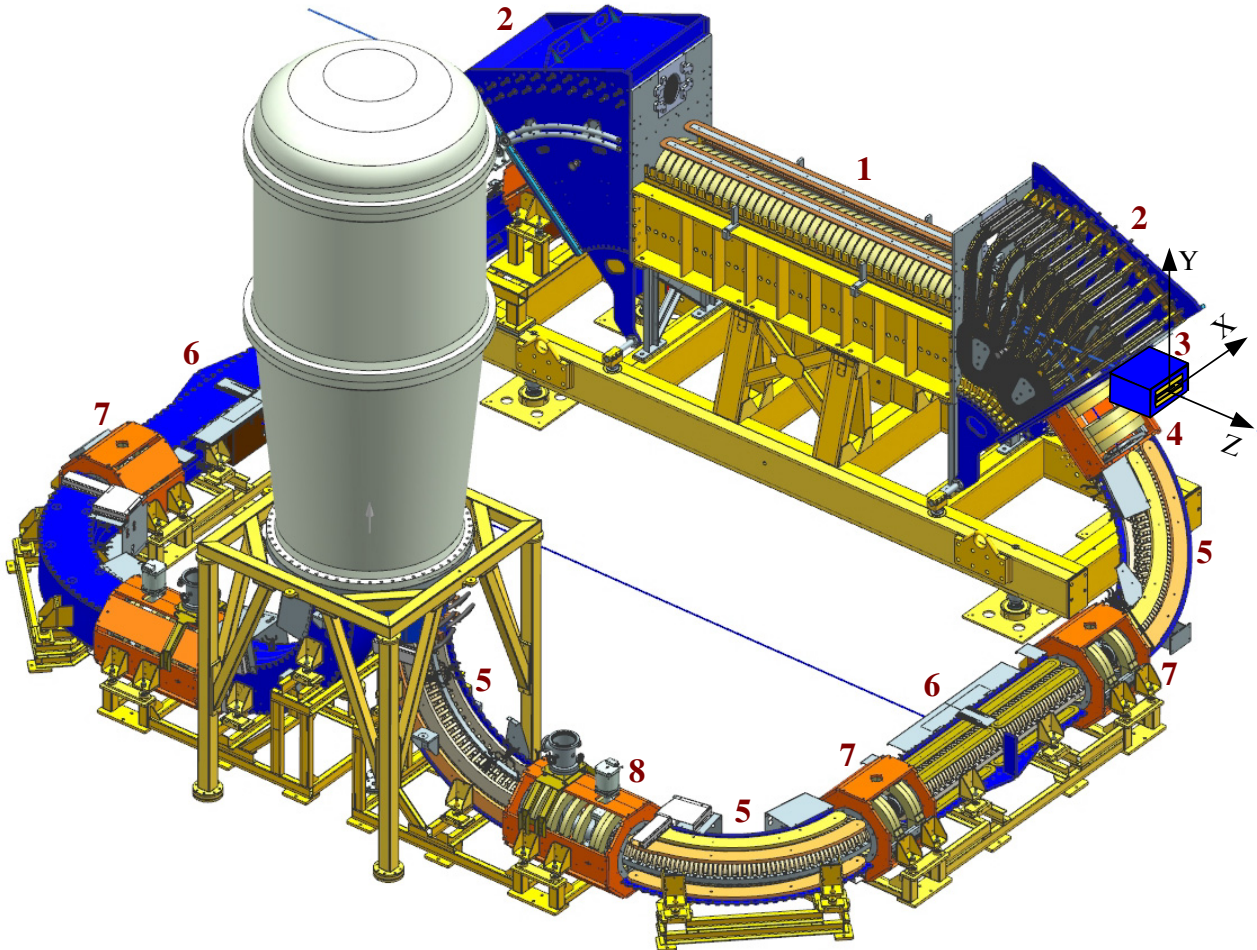


Figure 1: Cooler magnetic system layout: 1 – solenoid and transverse correctors of cooling section, 2 – toroidal and bending coils of 45° toroid, 3 – dipole corrector, 4 – two coil groups of matching section, 5 – toroidal and bending coils of 90° bend, 6 – solenoid and transverse correctors, 7 – coils of short transition section, 8 – coils of long transition section, 9 – coil group of matching section.

## DESCRIPTION

Solenoid consists of 40 pancake moveble coils [1]. Half the coils have right-handed winding, the rest – left-handed winding. Interleaving of such coils minimize field inhomogeneities which arise at commutation of coils. Since cooling by magnetized electrons is used, high straightness of the magnetic field line is required:

$\Delta B_{\perp} / B = \theta < 10^{-5}$ . Coils are installed on ball bearings for adequate correction of position. Magnetic field is aligned by tilting or slewing the coils. Necessary displacements of control screws were found by mathematical treatment of previous compass measurements [2]. Displacements of ~0.01mm were needed in final stage. In addition magnetized electron beam may be tilted by horizontal and vertical correctors

of cooling section ( $B_x=B_y \leq \pm 15G$ ). The values of longitudinal magnetic fields of solenoid  $B_{Zsol}$  and guiding magnetic fields of toroids  $B_{Stor}$  amount to 2kG. Usually  $B_{Zsol} \approx B_{Stor}$ .

High-voltage tank magnetic system includes two solenoids around accelerating and decelerating tubes[1]. The nominal value of the magnetic field is 0.5kG. Electron beam moves from tank to cooling section and comes back for recuperation by identical transport channels. Each channel consists of three 90° bends, two short and one long transition sections and a solenoid with transverse correctors. Guiding magnetic field of channels  $B_S$  amounts to 1kG. Two matching sections are situated at the ends of each channel. These sections ensure passage of electrons through longitudinal gradient of field without heating [3].

Transverse bending field is created by bending coils of bends and toroids. Field index (~0.5) is ensured by coils positioned on the walls of magnetic conductors.

Functionally five power supplies are used for water-cooled coils.

Table 1: Fields and Supplies parameters

Series connection coils	Fields kG	Current A	Power kW
Coils of cooling solenoid	2	330	110
Toroidal coils of 45° toroids	2	1040	180
Toroidal coils of 90° bends	1	320	130
Coils of transition sections	1	300	70
All bending coils	0.1	350	45

Two dipoles are situated on the axis of cooling solenoid outside of toroids. Their vertical field coils may be connected in series with coils of 45° toroids. Two coils of matching section (4) connected in series with coils of cooling solenoid and other three are connected in series with coils of 90° bends.

### HALL SENSORS MEASUREMENTS

Calibrated set of Hall sensors was used for magnetic measurements. Twelve devices are placed on a precise Cross-support so that 3-d components of field are measured, where every component is measured in four points around cross axis. The Cross is installed on a Carriage.

The Carriage moved along rails in one-step operation. Special rigid rails installed in the magnetic system elements ensured movement of the Cross center along the axis in straight sections, or along the arc of 1m radius in bends and toroids. The position of the Cross center along the track was considered as longitudinal coordinate  $s$ .

General assembly consisted of cooling section, toroid, dipole and matching section (1-2-3-4 in Fig. 1). Other eight elements were measured in triads. Each triad consisted of one bend (one of the six 90° bends (5)) in

the center with two neighboring transition straight sections, or one of the two solenoids (6) in the center with corresponding straight sections on sides (7-6-7, 7-5-8 etc). Measurements were carried out with various combinations of four power supplies for the triads' elements.

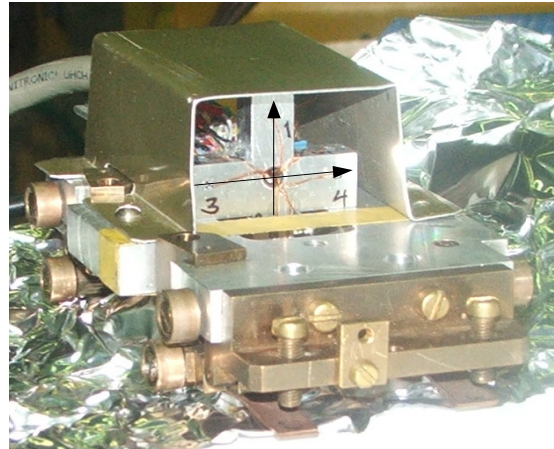


Figure 2: The Cross with Hall sensors on the Carriage.

### MEASUREMENT RESULTS

Results of measurements (dot curves) and results of corresponding computations (solid curves) are presented in next figures.

Measurements on the assembly 1-2-3-4 along straight axis are represented below in Fig. 3 (i.e. measurements in the path of ion beam). The  $z$  origin is fixed in the centre of the cooling solenoid.

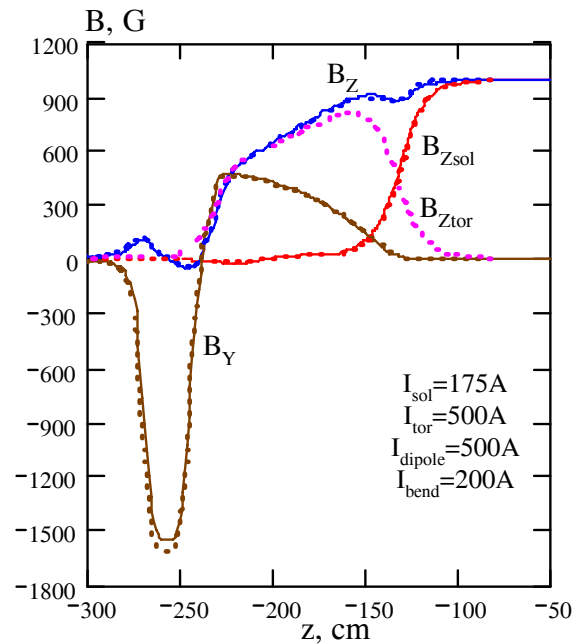


Figure 3: Longitudinal component  $B_z$  and its constituents  $B_{Zsol}$  and  $B_{Ztor}$  and vertical component  $B_y$  along the axis. Dot – measured curves, solid – computed curves.

Here and farther each constituent is powered by its own supply.

Measurements of assembly 1-2-3-4 along travel line (axis-45°arc-straight line) are represented below (i.e. measurements on the path of electron beam). The s origin is fixed also in centre of cooling solenoid.

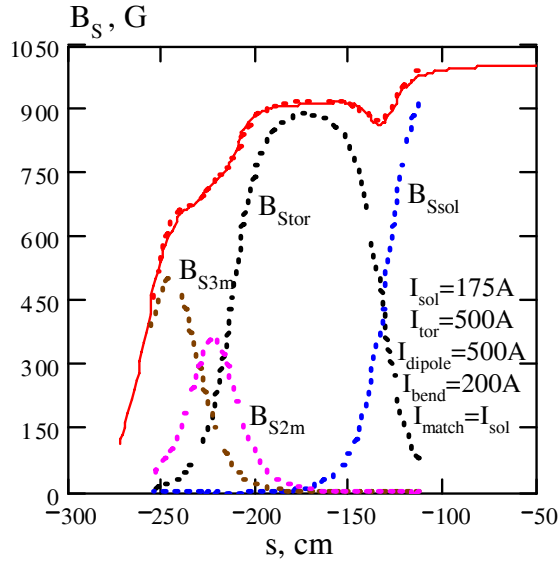


Figure 4: Longitudinal field  $B_S$  and its main constituents  $B_{Ssol}$ ,  $B_{Stor}$ ,  $B_{S2m}$  and  $B_{S3m}$  along travel line  $s$ . Dot – measured curves, solid – computed curve.

Measurements of assembly 8-5-7 along travel line (axis-90°arc-axis) are presented below (i.e. one from six bends measurements). The  $s$  origin is fixed here in centre of the bend.

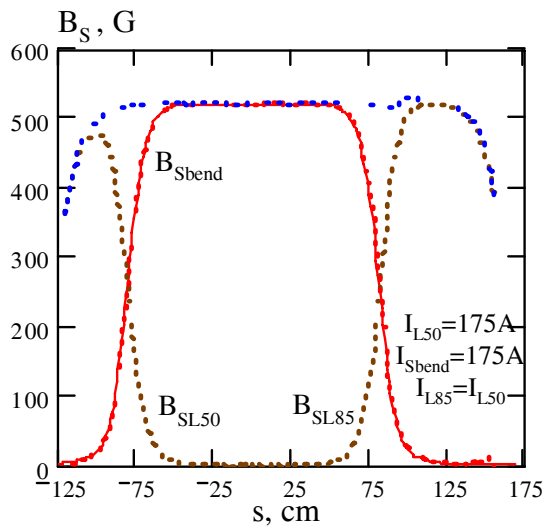


Figure 5: Longitudinal field  $B_S$  and its main constituents  $B_{Sbend}$ ,  $B_{SL50}$  and  $B_{SL85}$  along travel line  $s$ .

Thus:

- Field measurements coincide with field computations.
- Full field equals to its constituents sum, i.e. influence of ferromagnetic nonlinearity is small at stated currents.

Electron cooling

- This allows constructing of field by variation of the constituent currents, for example, constructing the optimal field for electron transit without ‘heating’.

### COMPUTATION OF ELECTRON TRANSIT THROUGH TOROIDS AND BENDS

Profiles of guiding field curvature ( $cur(s)$ ) and bending field  $B_B(s)$  do not coincide. So, the Lorentz force  $F_L(s) = e \cdot \beta \cdot B_B(s)$  counteracts with centrifugal force  $F_C(s) = mc^2 \gamma \beta^2 \cdot cur(s)$  only on average [4]. Normalized profiles are shown in Fig. 6.

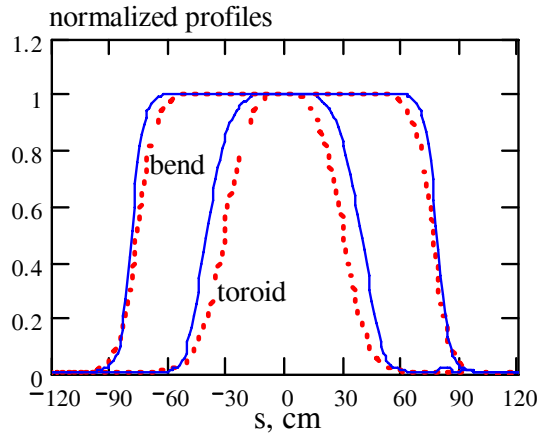


Figure 6: Solid – curvature:  $\max(curv)=0.01cm^{-1}$ . Dot – profiles of bending field.

Electron beam energy range is wide (24keV- 2MeV). Non-adiabatic electrons of major energies are ‘heating’ in such bends and toroids. If electrons make integer number of turns ( $n\omega$ ) around magnetic field  $B_S$  during transit, they leave bend or toroid without ‘heating’.

Since diverging profiles are present, fitting of coils current for  $B_S$  and  $B_B$  is needed. For the beginning we can choose  $B_S$  corresponding to integer number of Larmor’s turns on the bend transit and  $B_B \approx 17\gamma\beta$  (from  $F_L=F_C$ ).

Computations of electron transit through channel fragment 8-5-7-6 are presented on the Fig.7, 8 and 9.

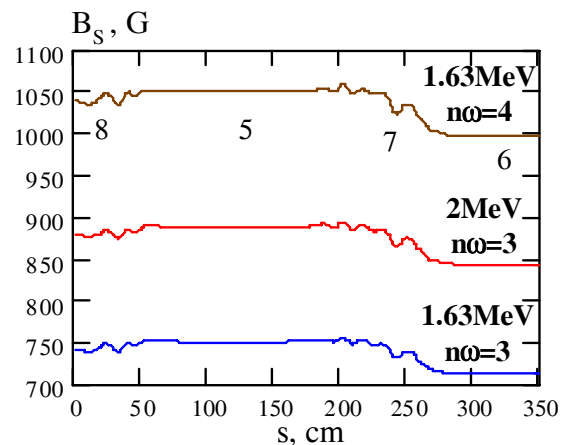


Figure 7. Optimal fields for electron transit through channel fragment 8-5-7-6 without ‘heating’

Electron oscillations relative to central force line are shown below. Here  $\delta r$  is radial displacement in the bend and  $x$  is displacement across bend plane.

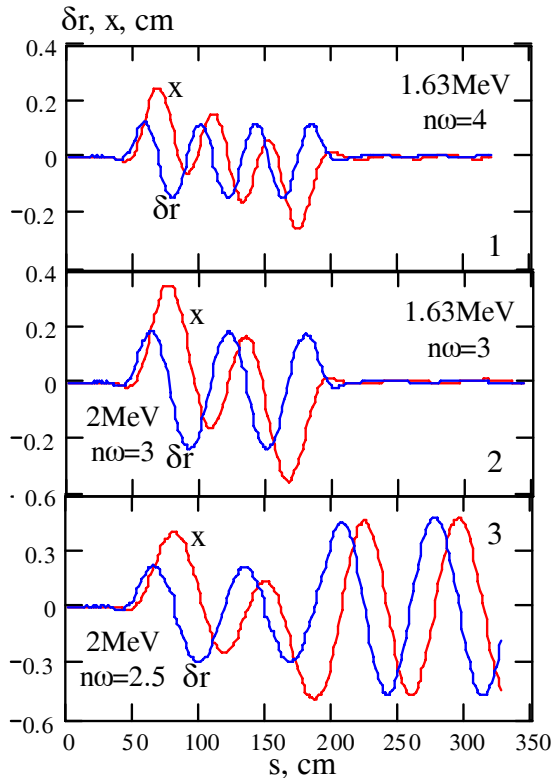


Figure 8: Electron oscillation in optimal fields – 1, 2 and electrons with  $T_e=2\text{MeV}$  in field for  $T_e=1.63\text{MeV}$  – 3.

Larmor's turns of 2MeV electrons into solenoid 6 (i.e. after bend transit) are shown below for different cases.

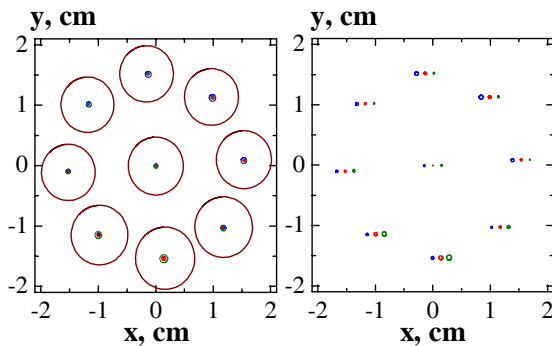


Figure 9: Left graph – Larmor's turns in optimal  $B_s$ ,  $\pm 2\%$  varying relative to optimal  $B_s$  and non-optimal ( $n\omega=2.5$ ). Right graph – Larmor's turns in optimal  $B_B$  and  $\pm 2\%$  varying relative to optimal  $B_B$ .

Optimal fields  $B_s$  at  $T_e=2\text{MeV}$ ,  $n\omega=3$  and at  $T_e=1.63\text{MeV}$ ,  $n\omega=4$  got by fitting. At fixed  $n\omega$  optimal  $B_s$  value varies on energy as  $\gamma\beta$ . At  $T_e=1.63\text{MeV}$  conversion  $n\omega$  from 4 to 3 decreases optimal field by 0.71 instead of 0.75. At electron energy  $T_e=2\text{MeV}$   $\max(B_{B\text{bend}})=84\text{G}$  ( $\max(B_{B\text{tor}})=104.6\text{G}$ ) and varies on energy as  $\gamma\beta$ .

Variation of optimal guiding field  $B_s$  on  $\pm 2\%$  increase 'heating' slightly. Variation of optimal bending field  $B_B$  on  $\pm 2\%$  substantially shifts the beam axis across bend plane on  $\pm 2\text{mm}$ .

Computations were done by MAG3D code [5] in maximal approximation to real design. Steel grade of magnetic conductors is ST10.

### CONCLUSION

The magnet measurement of magnetic elements: cooling section, toroid, bending solenoid and matching section shows good agreement with calculated magnet fields. Beginning of the electron beam orbit optimization for different energy will made according results of  $B_s$  and  $B_B$  computations.

Naturally final positioning of electron beam orbit will made according results of diagnostic measurement. Tools for optimisation exist: system of pick-up and set of the correctors.

### REFERENCES

- [1] Bubley, V. Panasyuk, V. Parkhomchuk, V. Reva, Budker INP, Novosibirsk, 630090, Russia, Optimization of the magnet system for low energy coolers, <http://accelconf.web.cern.ch/AccelConf/d07/PAPERS/THAP04>
- [2] A. Bubley, V. Bocharov, S. Konstantinov, V. Panasyuk, V. Parkhomchuk. Precision Measurements and Compensation for the Transversal Components of the Solenoids' Magnetic Field. Instrum. Exper. Techn. Vol. 48, № 6, 2005, pp.772-779
- [3] M.I. Bryzgunov, V.M. Panasyuk, V.B. Reva. Calculation of electron beam motion in electron cooling system for COSY. Proceeding COOL-09 Conference Lanzhou, China, August 31-September 4, 2009.
- [4] A.V.Ivanov, V.M.Panasyuk, V.V.Parkhomchuk, V.B.Reva, M.A.Tiunov, "Simulation of electron beam dynamics in a high-energy electron cooler", Nuclear Instruments and Methods in Physics Research A 558 (2006) 227-234.
- [5] B. Fomel, M. Tiunov, M. Karliner, "3D simulation of magnets with taking into account the effect of nonlinearity", preprint BINP 83-15, 1983.

# SUPERCONDUCTING SHIELD FOR SOLENOID OF ELECTRON COOLING SYSTEM

N.N. Agapov, D.E. Donets, V.M. Drobin, E.A. Kulikov, H. Malinovski, R.V. Pivin,  
A.V. Smirnov, Yu.V. Prokofichev, G.V. Trubnikov, LHEP JINR, Dubna, Russia  
G.L. Dorofeev, RRC "Kurchatov Institute", Moscow, Russia

## Abstract

The homogeneity of the magnetic field in the straight solenoid of the electron cooling system is the very important task. The superconducting solenoids are planned for electron cooling systems of collider rings of NICA project [1]. To reach the necessary homogeneity in the straight section the superconducting shield was proposed. The design of the superconducting shield, experimental and numerical investigation of the field homogeneity in the solenoid with the superconducting shield are presented.

## INTRODUCTION

Special properties of superconducting materials (Meissner Effect, high current) permits to use these materials for magnetic field screening in different facilities, for example: chambers with magnetic vacuum, current limiters, and tomography. For maximum current density  $5 \times 10^5$  A/cm<sup>2</sup> the magnetic field difference on the thin superconducting layer with the thickness about 20  $\mu$ m can reach a value up to 1000 G. The using of the NbTi superconducting shield for the increasing of the field homogeneity was investigated in the different works [2, 3].

The aim of these investigations is the problem of the field homogeneity in the straight section of the electron cooling system. The price of the straight solenoid with field homogeneity up to value  $\Delta B/B=10^{-5}$  [1] is very high. When the length of the high precision solenoid is 10 m and more than the solenoid is divided on a few sections. This situation leads to the field inhomogeneity between solenoid sections. The using of the superconducting shield can resolve this problem.

For the investigation of the high homogeneity magnetic field in large volumes the experiments with superconducting shields which are placed inside superconducting solenoid were done in Laboratory of High Energy Physics (JINR, Dubna, Russia). The design of the superconducting shield is a multilayer close-coiled winding from the superconducting foil. This article presents the comparison of experimental and numerical results which were done with standard simulation programs and original program code.

## EXPERIMENTS WITH SHORT SOLENOID

Laboratory of High Energy Physics JINR has a large experience in the production of superconducting systems [4]. In first experiment the existing superconducting

solenoid with length 150 mm, outer diameter 130 mm and inner diameter 100 mm was used. The superconducting shield was made from the NbTi foil with thickness 150  $\mu$ m and width 138 mm. The shield was wind on the tube with diameter 78 mm and has 5 layers which have a close-coiled shape and are divided by the isolator paper.

The dependence of the magnetic field homogeneity on different solenoid currents is presented on Fig.1. Initially measurements were done without the superconducting shield then with the shield for the same values of solenoid currents. The field measurements were made with the Hole probe along the solenoid axis with step 5 mm. A sensitivity of the Hole probe was 73 mV/T.

The using of the superconducting solenoid leads to the increasing of the field range with high homogeneity even in the short solenoid (Fig.1). At the same time the value of magnetic field decreases in the solenoid center and increases on the edge. The size of the field range with high homogeneity has a dependence on the absolute value of the magnetic field: the higher field value the smaller range size. This behavior can be explained by the saturation of the superconducting shield. The efficiency of the shield is decreasing when the current in the foil reach the critical value.

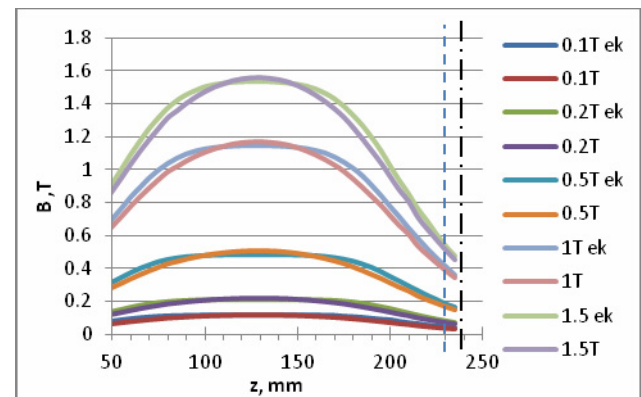


Figure 1: The dependence of magnetic field (arbitrary units) on the longitudinal coordinate for different values of the magnetic field  $B = 0.1, 0.2, 0.5, 1, 1.5$  T) with the superconducting shield (ek) and without it. Vertical lines correspond to boundaries of the solenoid and shield.

## EXPERIMENTS WITH HIGH HOMOGENEITY FIELD

For further investigation of the influence of the superconducting shield on the field homogeneity the solenoid with large ratio of the length and diameter was

constructed. The solenoid has four layers of the NbTi/Cu superconducting ware with diameter 0.5 mm. The length is 480 mm and inner diameter 80 mm. The shield was made from NbTi/Cu foil with the thickness 20  $\mu\text{m}$  and width 80 mm. Each section has 15 layers of the superconducting foil which are divided by the isolator paper. Sections overlap each over with the shift 40 mm. An additional superconducting coil was placed in the center on the shield. It was used for the imitation of the magnetic field unhomogeneity.

The longitudinal magnetic field was measured on the solenoid axis with the Hole probe. The solenoid current was about 30 A. The dependence of the magnetic field with the superconducting shield and without it was presented on Fig.2. The accuracy of the field measurement was about  $\Delta B/B \sim 10^{-3}$  which was mainly defined by the stability of the solenoid power supply. The numerical simulation of the screening effect has only quality agreement with the experiment when the superconducting shield was simulated like the material with zero permeability (Fig. 2).

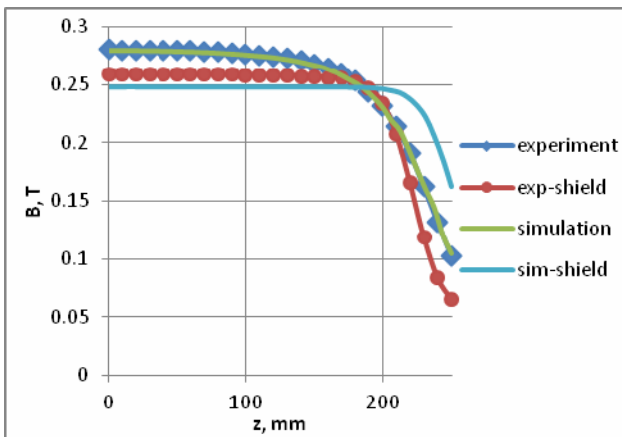


Figure 2: The dependence of the magnetic field on the longitudinal coordinate with the superconducting shield and without it. Zero coordinate corresponds to the solenoid center.

For the investigation of the screening effect the additional coil was used. It was placed in the solenoid center outside of the superconducting shield. The coil has 4 winding from the superconducting ware with diameter 0.5 mm. The coil current was about 10 A. The difference between magnetic fields normalized on the absolute value between measurements with the additional coil and without it are presented on Fig.3. The additional coil increases the absolute value of the magnetic field and does not change the field homogeneity in the solenoid center. It means that non regular winding of the solenoid ware does not destroy the field homogeneity when the superconducting shield is used.

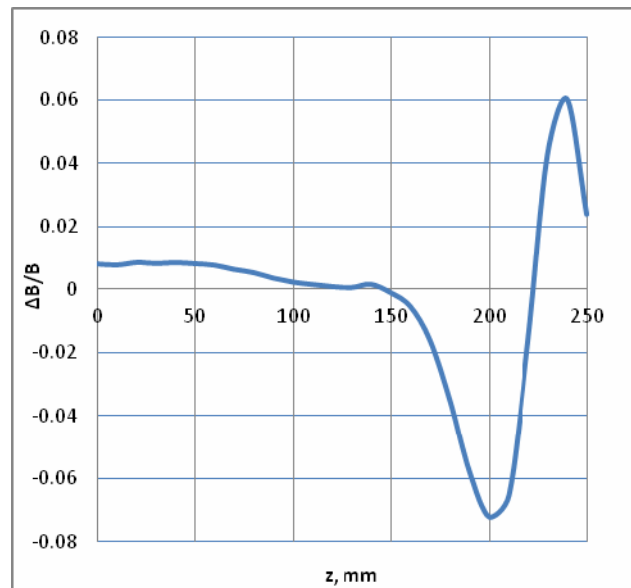


Figure 3: The difference between magnetic fields with the additional coil and without it.

### SIMULATION OF SUPERCONDUCTING SHILED

Standard programs cannot correctly simulate the screening effect from the superconducting solenoid. In the case when the superconducting shield is replaced on the material with zero permeability the simulation result has only a quality agreement with experiments (Fig.2). Then a special program code was proposed for the simulation of the superconducting shield.

In the simple geometry when the superconducting shield is placed inside a solenoid and its axis is parallel the radial component of the magnetic field is perpendicular to the shield surface. It means that the close-coiled shield in the first approximation is equal to the superconducting plate with the perpendicular magnetic field which is correspondents to the radial component of the solenoid field. In the solenoid center the radial component is zero. As result the variable magnetic field leads to the appearance of two closed screening currents in the different part of the plate with opposite directions.

In the superconducting shield the independent currents are screened the radial component of the solenoid magnetic field which has zero value in the solenoid center. Screening currents completely compensate the radial component in the solenoid center and has opposite currents on the solenoid edge. In the accordance with the theory of the critical state of the superconducting materials the current density has to be critical in shield regions where the transverse component of the magnetic field goes through the superconducting shield. This behavior defines the distribution of the screening current and the shield efficiency. Thus the screening currents leads to the increasing the field homogeneity in the solenoid center and decreasing the field homogeneity

(increasing of the radial component of the magnetic field) on the solenoid edge.

For the simulation of the screening effect from the superconducting shield the special program code was used. The influence of shield was simulated with additional coils which were placed in three layers along the solenoid axis. Currents in coils were chosen under conditions that the radial component of the magnetic field leads to zero on the shield surface and current summary is zero in each layers. Simulation results (Fig.4) have a good agreement with experimental results [2]. Thus coil currents have the same direction on the solenoid edge and the opposite direction in the solenoid center.

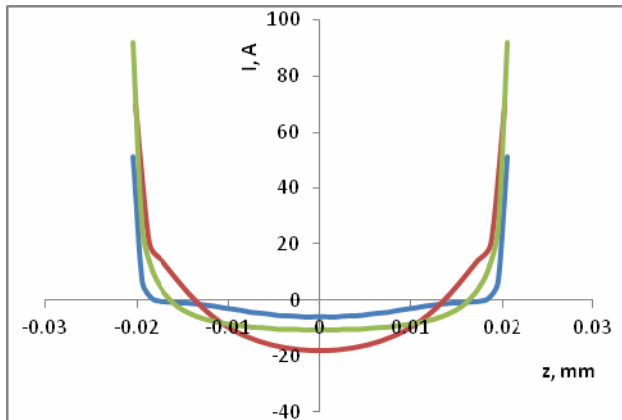


Figure 4: The distribution of currents in additional coils which reproduce the effect of the superconducting shield. Positive values correspond to the same direction of the solenoid current.

## CONCLUSION

Present experimental and numerical investigations show enough high efficiency of the superconducting shield for the increasing of the magnetic field homogeneity in the straight solenoid. The first experiments with the high temperature superconducting materials shows that they can be used for the superconducting shield.

Further investigations will have the aim to the choosing of the optimal material for the superconducting shield (including high temperature superconducting materials) and the technology of the shield winding. For the investigation of the field homogeneity the stability of the power supply and the accuracy of the field measurement have to be improved. For the simulation of the superconducting shield the special algorithms have to be implemented into program code for the optimization of shield parameters. Present experimental and numerical investigations show enough high efficiency of the superconducting shield for the increasing of the magnetic field homogeneity in the straight solenoid. The first experiments with the high temperature superconducting materials shows that they can be used for the superconducting shield.

Further investigations will have the aim to the choosing of the optimal material for the superconducting shield (including high temperature superconducting materials) and the technology of the shield winding. For the investigation of the field homogeneity the stability of the power supply and the accuracy of the field measurement have to be improved. For the simulation of the superconducting shield the special algorithms have to be implemented into program code for the optimization of shield parameters.

## REFERENCES

- [1] I. Meshkov, R. Pivin, A. Smirnov, G. Trubnikov, et al. Application of Cooling Methods to NICA Project // Proceeding of COOL'09 Workshop. Lanzhou, China, 2009.
- [2] Лазарев Б.Г., Лазарева Л.С., Полтавец В.А. О получении однородного постоянного магнитного поля в сверхпроводящих соленоидах при помощи экрана из сверхпроводника с высокими параметрами // ДАН СССР. 1972. Т.203, № 4. С. 810-812.
- [3] Бычков Ю.Ф., Комаров А.О., Хлопков А.К. Изучение факторов, влияющих на эффективность сверхпроводящих экранов, применяемых для повышения однородности магнитного поля // Металлургия и металловедение чистых металлов. М.: Атомиздат, 1980. Вып. 14. С. 53-63.
- [4] Дробин В.М., Малиновски Х. и др. Сверхпроводящая магнитная система с криокулером для источника ионов DECRIS-SC // Письма в ЭЧАЯ. 2006. Т3, №1 (130). С. 45-62.

# OPTICAL ELECTRON BEAM DIAGNOSTICS FOR RELATIVISTIC ELECTRON COOLING DEVICES

T. Weilbach, Helmholtz-Institut Mainz, Germany,  
K. Aulenbacher, KPH Mainz, Germany  
J. Dietrich, FZJ, Germany

## Abstract

For the cooling of proton and ion beams a well established overlap between cooling beam and circulating beam is needed. The new relativistic electron cooling devices, like the one proposed for the High Energy Storage Ring (HESR) at FAIR, have special demands on the diagnostics which can be used to characterize the cooling beam. Due to high voltage breakdowns they only allow a very small beam loss so non-invasive beam diagnostic methods are necessary. A system based on beam induced fluorescence (BIF) was installed at the 100 keV test setup at the Mainzer Mikrotron (MAMI). First results of the measured photon yield as a function of beam current and residual gas pressure will be presented. In addition a Thomson scattering experiment is planned at the same test setup. This method enables the measurement of other observables of the cooling beam like the electron beam energy or the electron temperature. The design of the experiment as well as the challenges will be discussed.

## INTRODUCTION

The cooling beam and the cooled beam have to overlap and propagate with the same velocity to ensure a small cooling time. This matching is done by optimizing the  $H^0$ -signal. In this case the protons of the cooled beam are recombining with the electrons of the cooling beam. The resulting Hydrogen Atoms are neutral they are not deflected by magnetic fields and can be detected after the next bending magnet. This technique is only applicable for protons and positive ions. For the cooling of antiprotons as it is planned in the (HESR) [1] there is no  $H^0$ -signal which could indicate a good cooling rate. Because of this special beam diagnostics of the cooling beam are necessary. The diagnostic has to be non destructive because of the high beam power. It should also not affect the magnetic field flatness of the solenoids inside the cooling section.

There are already several non destructive beam diagnostic methods established. They are used in different accelerators like a scintillation profile monitor [2], [3] or the Laser wire scanner at the synchrotron source PETRA III [4]. These methods can be adapted for the use in relativistic electron cooling devices.

## BEAM INDUCED FLUORESCENCE

For protons and ions beam profile measurement based on beam induced fluorescence is a common technique [5]. The idea is to image the fluorescing residual gas on a photo Electron cooling

detector with a spatial resolution as shown in Fig. 1. There are different types of detectors available, like multi channel plates (MCP), multichannel photo multiplier or intensified ccd (ICCD) cameras.

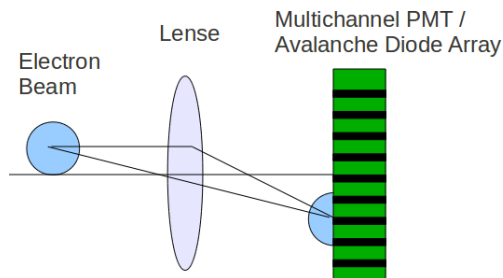


Figure 1: Principle of scintillation profile monitor

The production of the scintillation light depends on the residual gas pressure, the beam current and the composition of the residual gas. Different gases show different excitation spectra and consequential have different fluorescence spectra. But they are also differing in the intensity of the scintillation light.

For electrons and protons with the same velocity the ionization energy loss is very similar. They amount to  $4.4 \text{ MeVcm}^2/\text{g}$  and  $4.3 \text{ MeVcm}^2/\text{g}$  respectively for  $\beta = 0.55$  in  $N_2$ . This should lead to a corresponding light output. From the energy loss and the photo production coefficient from [6] we can therefore estimate the fluorescence rates for electrons in nitrogen gas. For our detection device which has a solid angle  $\Omega = 3.1 \cdot 10^{-2} \text{ sr}$  and a detector efficiency of 0.3 we expect a count rate of  $10^4 \text{ Hz/cm}$  of longitudinal beam extension at a pressure of  $10^{-6} \text{ mbar}$  and a  $100 \mu\text{A}$  beam.

To test this assumption a special vacuum chamber has been designed (Fig. 2) and has been installed at the polarized test source (PKAT) [7] at the Mainzer Mikrotron (MAMI). In this source a NEA-GaAs [8] photo cathode is used which requires  $10^{-11} \text{ mbar}$  for stable operation. Therefore this chamber together with additional turbo molecular pumps acts as a differential pumping stage. This allows local pressure bumps up to  $10^{-5} \text{ mbar}$  while maintaining the UHV condition at the cathode. The main purpose of this experiment is to gain understanding of the different background sources which degrade the signal to noise ratio for the optical beam diagnostics.

The chamber is equipped with a silica window which is transparent down to 200 nm. This allows to image the transverse beam profile by transmitting the UV parts of the spectral lines of  $N_2$ . With the leak valve the residual gas

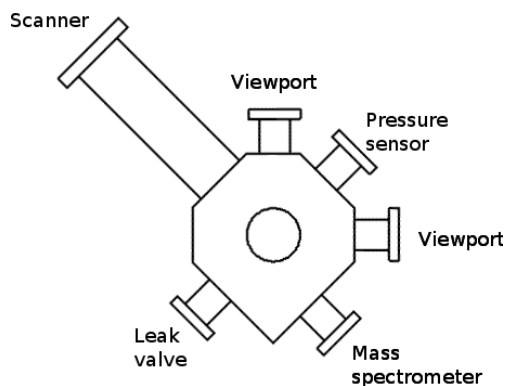


Figure 2: Vacuum chamber for beam induced fluorescence studies. The electron beam goes into the plane of the paper

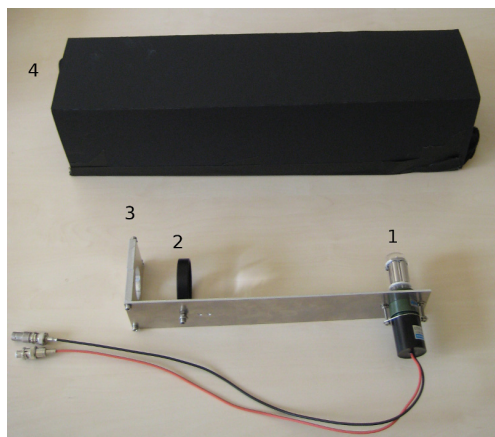


Figure 3: Imaging system consisting of PMT (1), Lens (2) and mounting system (3). Above the shielding against ambient light (4)

pressure can be changed. The pressure sensor monitors the vacuum condition. A mass spectrometer detects the partial gas pressure and enables the analysis of the photon yield of different scintillation gases.

As an imaging system for the fluorescence light a fused silica lens (wavelength range 185-2100nm) with a focal length of 12 cm is used. The distance between the electron beam and the lens is 24 cm the same as between the lens and the detector. A photomultiplier tube (PMT) with a minimal wavelength of 160 nm is used as a detector. The Fig. 3 shows the lens, the PMT and the mounting system which is used to attach the imaging system to the vacuum chamber. This whole system is shielded against light emitted by several sources (e.g. LED) in the lab.

During the first measurement a quite high background, which depended on the residual gas pressure, was observed. This background was caused by the pressure sensor. Different residual gas pressures were established with different settings of the leak valve. The leak valve was connected to a  $N_2$  containing gas bottle. If the gas pressure was stable the pressure sensor was switched off to minimize the background for the measurement of the BIF. After that the

Electron cooling

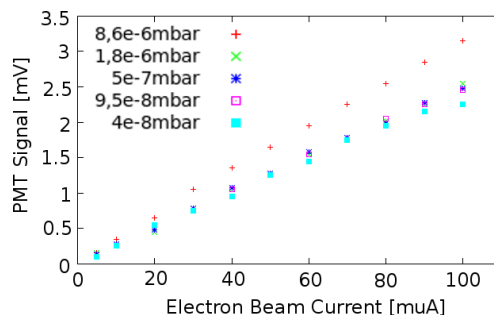


Figure 4: Beam induced fluorescence intensity against electron beam current at different residual gas pressures. The linear dependence on the beam current is clearly visible but the identical curves for pressures below  $10^{-6}$  mbar indicate a background

pressure sensor was switched on to check if the pressure had changed. If the pressure had changed a mean value of the pressure before and after the measurement was evaluated. During the whole measurement the transmission of the electron beam was monitored with two digital volt meters (DVM). One was measuring the emitted beam current of the cathode the other was used to monitor the Faraday cup where the beam was dumped.

The PMT signal was measured against the electron beam current at different residual gas pressures. These measurements are shown in Fig. 4.

One can see clearly the linear dependence on the PMT signal of the beam current. This indicates that the signal is really produced by the electron beam. Furthermore the BIF signal of about 1 mV of a 100 keV electron beam at  $8.6 \cdot 10^{-6}$  mbar (see below) corresponds to a PMT current of 10 nA. With a gain of  $10^7$  and a width of 8 mm of the photo multiplier this equates to  $6 \cdot 10^3$  electrons per second emitted by the PMT cathode. This is a factor of 10 less than the estimated event rate mentioned above. This might be caused by uncertainties in the geometrical alignment, the PMT gain and the residual gas pressure of nitrogen. An investigation and an optimization of these uncertainties is foreseen for the future.

The more or less identical curves for pressures below  $10^{-6}$  mbar indicate a beam induced background which is not caused by fluorescence. This might be x-rays produced in the Faraday cup or other light producing effects inside the beam pipe. Based on this assumption the background signal is 2.4 mV and the beam induced fluorescence signal (at  $8.6 \cdot 10^{-6}$  mbar) is 3.2 mV. The signal to noise ratio then evaluates to 1/4.

For the future our main goal is to increase the signal to noise ratio by background reduction. This can be done with filters which are only transparent for the spectral lines of the nitrogen and by shielding the Faraday cup to get rid of the produced x-rays. A good understanding of the background is not only important for the BIF method but also for the Thomson scattering because this technique suffers from even lower counting rates.

## THOMSON SCATTERING

### Theory

Thomson scattering describes elastic scattering of a photon on a free electron. It is the low energy limit of the Compton scattering process. Figure 5 shows a schematic view of Thomson scattering.

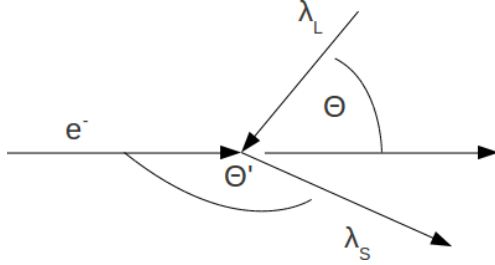


Figure 5: Thomson scattering scheme

A photon  $\lambda_L$  hits the electron beam under an angle  $\Theta$  and is scattered under the scattering angle  $\Theta'$ . The scattered photon  $\lambda_S$  gains energy due to the Doppler shift. The wavelength of the scattered photon as a function of the angle between incident photon and electron and the angle between scattered photon and electron can be evaluated with

$$\lambda_S = \lambda_L \frac{(1 + \beta \cos \Theta')}{(1 + \beta \cos \Theta)} \quad (1)$$

where  $\beta$  is the electron velocity in units of the speed of light. The scattering process is determined by the Thomson cross section

$$\frac{d\sigma}{d\Omega} = \frac{1}{2} r_e^2 (1 + \cos^2 \Theta') \quad (2)$$

with  $r_e$  = classical electron radius. The event rates i.e. how many photons are scattered can be calculated with the following equation

$$R = \frac{1}{2} r_e^2 (1 + \cos^2 \Theta') N_L n_e \epsilon \Delta\Omega l \frac{(1 + \beta \cos \Theta)}{(1 + \beta \cos \Theta')^\gamma} \quad (3)$$

with  $N_L$  = Number of incident photons per Joule,  $n_e$  = Electron density,  $\epsilon$  = Detector system efficiency,  $\Delta\Omega$  = Detector solid angle,  $l$  = Interaction length,  $\frac{(1 + \beta \cos \Theta)}{(1 + \beta \cos \Theta')^\gamma}$  = factor results from Lorentz transformation.

### Beam Diagnostics

In 1987/1988 a pioneer experiment demonstrated the feasibility of Thomson scattering for our purpose [9], [10]. At that time, however, the signal to noise ratio suffered from the low power and repetition rate of the Laser system. We revisit this approach in the light of the enormous developments in Laser technology since that time. The presented setup uses the following angles  $\Theta = 90^\circ$  and  $\Theta' = 180^\circ$  like a Laser wire scanner. In this case the rate of the scattered Electron cooling

photons only depends on the electron density in the electron beam. By moving the Laser beam through the electron beam a profile measurement can be done. Due to the low cross section, mostly dominated by the classical electron radius squared, the necessary Laser power is very high and it is only reasonable for high electron densities. In Tab. 1 the event rates for different setups are shown. For the calculation a 100 W Laser system and an electron beam current of 1 A and a diameter of 3 cm was chosen. The detector system efficiency  $\epsilon = 0.2$  and solid angle  $\Delta\Omega = 100 \text{msr}$ .

Table 1: Scattering Rate for Different Cooling Devices

Electron Energy	$\lambda_L$	$\lambda_S$	Event Rate
100 keV (PKAT)	1.06 $\mu\text{m}$	475 nm	100 $\text{s}^{-1}$
2 MeV (COSY)	10.6 $\mu\text{m}$	220 nm	$6.5 \cdot 10^3 \text{ s}^{-1}$
4.5 MeV (HESR)	10.6 $\mu\text{m}$	50 nm	$1.3 \cdot 10^4 \text{ s}^{-1}$
8 MeV (ENC)	10.6 $\mu\text{m}$	20 nm	$2 \cdot 10^4 \text{ s}^{-1}$

Like the BIF measurements, the Thomson scattering experiment will also be done at the PKAT. As seen in Tab. 2 the gun is capable of delivering peak currents of 60 mA with a diameter of 2 mm so the electron density is the same as in a cooling device with 2 A and 3 cm. To perform this experiment we use the setup shown in Fig. 6. This enables a detection of the scattered photons in forward direction while the electrons are bend by  $270^\circ$  which suppresses the background generated from fluorescent light in the beam dump.

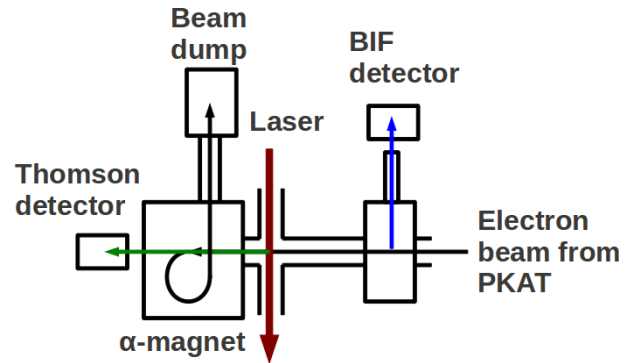


Figure 6: Schematic view of the future diagnostic setup at the PKAT

Table 2: PKAT Parameter Setup

Electron Energy	100 keV
DC current	200 $\mu\text{A}$
Beam diameter	2 mm
Peak current (pulsed)	60 mA
Pulse duration	10 ns
Rep. rate	50 Hz

An other advantage of the Thomson scattering method is the possibility to measure the electron energy. This can

be done in with the same setup which is used for the beam profile measurement. In this case a frequency analysis of the scattered photons is needed instead of the scattering rate. This can e.g. be done with a Fabry-Perot interferometer at an virtual arbitrary accuracy. Since Eq. 1 establishes a well defined relation between the angle and the velocity (i.e. the energy) the error in energy determination is mainly limited by the accuracy of the angle measurement.

This can be very interesting for the cooling of antiprotons. Because of the missing  $H^0$ -signal an energy matching of both beams which is needed for an efficient cooling process is more difficult. With a good energy measurement the adjustment of the electron beam can be done faster and in a more efficient way.

### Challenges

As mentioned above one of the challenges with Thomson scattering is the very low cross section. Because of that very high laser photon fluxes and laser powers are needed. These high power Laser beams have to be transported and focused to the interaction point without significant losses to get high signal rates and avoid a damaging of parts of the beam line. For the beam profile measurements with Thomson scattering the acquisition of a Laser system with the following specifications is planned.

Table 3: Laser System Specifications

Wavelength	1064 nm
Beam diameter	100 $\mu$ m
Pulse power	2 J
Pulse duration	20 ns
Rep. rate	50 Hz

The timing between electron and Laser beam is essential for this experiment. One possibility to solve the timing problem is shown in Fig. 7. A fraction of the Laser pulse will be frequency doubled send to the photo cathode of the PKAT while the main part of the pulse is delayed. The Laser pulse has to be delayed for the time it takes the electron bunch to travel from the cathode to the interaction point. There both beams collide under an angle of  $90^\circ$ . The Thomson scattered photons are detected behind the  $\alpha$ -magnet which bends the electrons by  $270^\circ$ . Mirrors in the Laser beam line allow a transverse shift of the Laser beam and a transverse scanning of the electron beam. The number of scattered photons is proportional to the electron density of the electron beam. If one assumes a Gaussian profile of the electron beam a Gaussian fit to the intensity of the scattered photons as a function of the displacement of the Laser provides the transversal beam profile.

Because of the low scattering rates all kind of background has to be avoided. This includes beam induced fluorescence as well as electron beam loss at the wall of the vacuum chamber or radiation emitted by the beam dump. To decrease the background the photo detector can be syn-

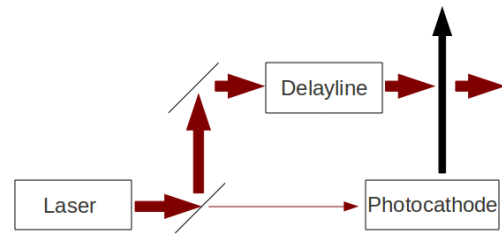


Figure 7: Laser system setup

chronized to the Laser pulses.

### OUTLOOK

We are planning further investigations of the BIF method concerning a further background reduction by using spectral filters and shielding of the Faraday cup. It is also planned to use a detection system with a spatial resolution e.g. a ICCD camera.

For the Thomson scattering further modifications at the PKAT beam line are in preparation and the acquisition of an adequate Laser system is planned for 2011.

### REFERENCES

- [1] T. Bergmark et al., "Status of the HESR Electron Cooler Design Work", TUPSL067, Proceedings of EPAC 2006, Edinburgh, Scotland.
- [2] C. Boehme et al., "Gas Scintillation Beam Profile Monitor at COSY Jlich", TUPSM005, Proceedings of BIW 2010, Santa Fee, New Mexico USA.
- [3] F. Becker et al., "Beam Induced Fluorescence Monitor-Spectroscopy in Nitrogen, Helium, Argon, Krypton, and Xenon Gas", TUPSM020, Proceedings of BIW 2010, Santa Fee, New Mexico USA.
- [4] M.T. Price et al., "Beam Profile Measurements with the 2-D Laser-Wire Scanner at PETRA", FRPMN094, Proceedings of PAC 2007, Albuquerque, New Mexico USA.
- [5] F. Becker, "Beam Induced Fluorescence Monitors", WEOD01, Proceedings of DIPAC 2011, Hamburg, Germany.
- [6] M.A. Plum et al., Nucl. Instr. Meth. A 492 (2002), p. 74.
- [7] P. Hartmann: "Aufbau einer gepulsten Quelle polarisierter Elektronen", Dissertation 1997, JGU Mainz, Germany
- [8] D.T. Pierce et al., Appl. Phys. Lett. 26 (1975) 670.
- [9] C. Habfast et al., "Measurement of Laser Light Thomson-Scattered from a Cooling Electron Beam", Appl. Phys. B 44, 87-92 (1987).
- [10] J. Berger et al.: Thomson Scattering of Laser Light from a Relativistic Electron Beam, Physica Scripta. Vol. T22, 296-299, 1988.

## ELECTRON COOLER FOR NICA COLLIDER

E.V.Ahmanova, A.G.Kobets\*, A.V.Ivanov\*\*, I.N.Meshkov, R.V.Pivin, A.U.Rudakov,  
 A.V.Shabunov, A.V. Smirnov, N.D.Topilin, Yu.A.Tumanova, S.L.Yakovenko#, JINR, Dubna  
 A.A.Filippov, M.P.Kokurkin, N.Yu.Lysov, M.M.Pashin, AREI, Moscow,

### Abstract

The electron cooling system at electron energy up to 2.5 MeV for the NICA collider is under design at JINR. The electron cooler is developed according to the available world practice of similar systems manufacturing. The main peculiarity of the electron cooler for the NICA collider is using of two cooling electron beams (one electron beam per each ring of the collider) that never has been done before. The acceleration and deceleration of the electron beams is produced by common high-voltage generator. The conceptual design of the electron cooling system has been developed. The cooler consist of three tanks. Two of them contain acceleration/deceleration tubes and are immersed in the copper ("warm") solenoids. The third one contains HV generator, which design is based on voltage multiplying scheme.

The magnetic field is formed by a set of straight and toroidal solenoids. The solenoids forming the magnetic field in the region of acceleration/deceleration tubes are placed outside of the tanks that resolve the problem of HV insulation.

### CONCEPTUAL DESIGN OF THE COOLER

The electron cooler (Fig. 1) consists of three tanks filled with SF6 gas under pressure of 8 at. The tanks 1 and 3 contain acceleration tube and electron gun for one of the electron beam and deceleration tube and electron collector for another one. The tank 2 houses the HV generator.

Table 1. Cooler parameters

Electron energy, MeV	0.5 ÷ 2.5
Electron beam current, A	0.1 ÷ 1,0
Beam diameter, cm	1,0
solenoid magnetic field, T	0.1 ÷ 0.2
HV PS current, mA	1
Collector PS, kW	2×2
HV PS stability, ΔU/U	1×10 <sup>-4</sup>
SF <sub>6</sub> gas pressure, at	5 ÷ 8

### ELECTRON BEAM GENERATION AND ENERGY RECUPERATION

Both acceleration and deceleration systems consist of three main subsystems (Fig. 2): acceleration vacuum tube with electron gun or collector mounted on the upper end of the tube, high pressure tank, solenoid forming longitudinal magnetic field. Acceleration vacuum tube with electron gun or collector mounted on the upper end of the tube. Electron gun design (Fig.3) has three main elements: cathode with the Pierce electrode, control (steering) electrode, anode connected with first (upper) flange of acceleration tube. Electron collector (Fig.3) consists of three elements as well: collector anode connected with upper flange of deceleration tube, suppressor ("repeller") electrode, electron collecting vessel. The last one is cooled by water circulating at high potential. The design and construction of collector cooling system is in progress.

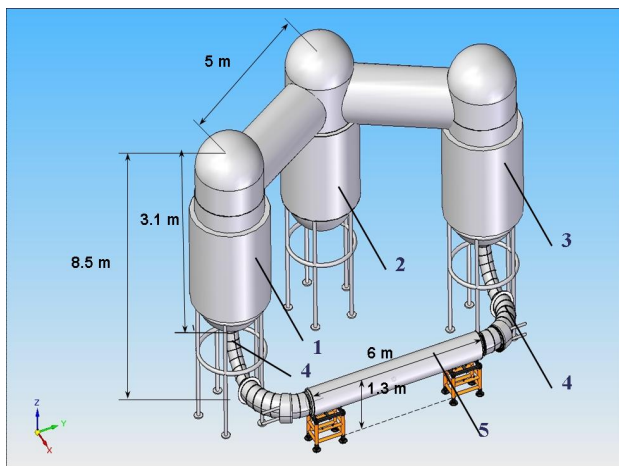


Fig.1. General view of the electron cooler. 1, 3 – tanks with electron gun and acceleration tube and deceleration tube + collector for electron beam of opposite direction, 2 – tank with HV generator, 4 – beam transportation solenoids, 5- electron cooling section.

\* Institute of Electrophysics and Radiation Technologies, NAS of Ukraine

\*\* Budker Institute of Nuclear Physics

# yakoven@jinr.ru



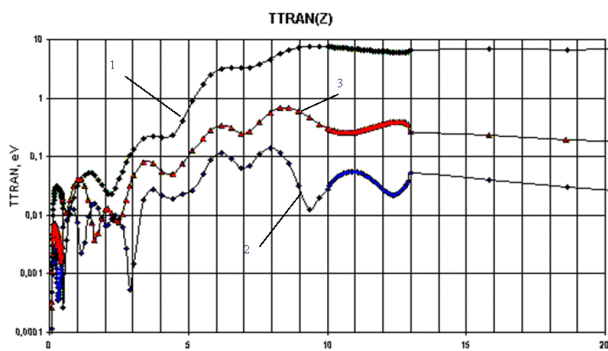


Fig.7. Distribution of electron transverse temperatures TTRAN (Z) along the trajectory of electrons emitted from the cathode on radius R = 0,65 cm; B = 1 (1), 2 (2), 1.5 (3) kG

To enhance the collector efficiency a permanent magnet with opposite field direction is applied. As result magnetic field lines form a magnetic trap reflected electrons are trapped in the collector with a great efficiency. Electron motion in the collector is calculated with the SAM code and results are shown in Fig. 8. The carried out numerical simulation of electron motion in collector with permanent magnet of opposite field direction have shown high efficiency of secondary electron trapping.

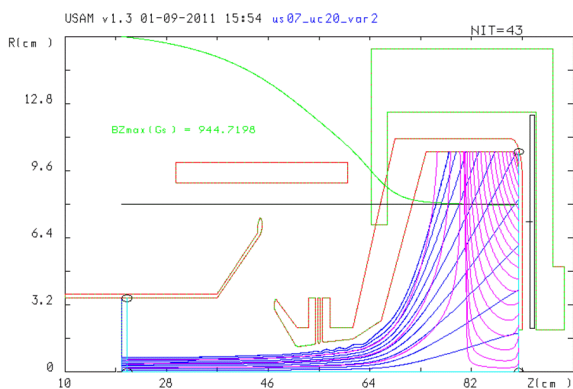


Fig.8. Magnetic field lines in the collector (permanent magnet of opposite field direction is placed on the rear wall of the collector). I = 1A, U<sub>cath-coll</sub> = 2 kV, μP=11.26

### HIGH VOLTAGE GENERATOR

High voltage (HV) generator (Fig.9) is based on the principle of the cascade scheme. The chosen scheme has three diode columns and twelve multiplying levels. At the working frequency of 20 kHz the total number of diodes (type 2I1106Г by Russian standard) is equal to 2500, the total number of capacitors (type C2-29B-2 by Russian standard) is equal to 8316. The HV of U = 2.0 MV is controlled with three-phase autotransformer (AT) of the voltage of 380 V at 50 Hz. The controller transmits the feed-back signal to the three-phase rectifier (V). Smoothed by means of the filter the

control signal comes to the inverter (F) that transforms it into 2 kHz meander. This voltage through resonance throttle (DR) comes to high voltage transformer (HT) with two symmetrical high voltage windings and further to the entrance of the symmetrical cascade generator (CG). It has maximum output voltage of 2.0 MV. For high voltage fluctuations suppression one should add at the exit of CG (Fig. 9) the low-power high voltage triode (T), which operates as a variable resistance controlled by the feedback signal from precise voltage divider (DU) via the feedback chain FB2 at ground level and FB3 at high potential. Operating voltage of triode T has to be higher than 10 kV, operating current – more than 1 mA. For example, if the stray capacity of high-voltage “output” to the ground potential is of 0.1 nF (to be defined later more exactly) voltage “loss” is of 500 V and voltage restoration time is of 0.1 ms, the triode current has to be at least of 0.5 mA.

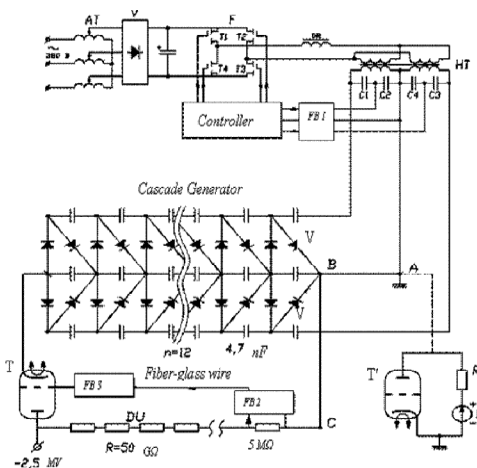


Fig.9. The HV generator electric scheme

The base element of the cascade of capacitors is ceramic capacitor with the following characteristics:

$$C = 1 \text{ nF}; U = 40 \text{ kV}; \phi = 40 \text{ mm}; l = 42 \text{ (65) mm.}$$

The cascade of capacitors consists of 48 series sections. Each section consists of 33 parallel capacitors mechanically fixed between two metal disks of 5÷8 mm thickness and  $\phi \approx 320$  mm that work as intermediate electric shields (Fig. 10). Sections are connected into CG stages: seven sections in series form one stage (280 kV, 4.7 nF).

There are 12 voltage multiplying stages (12x280 = 3360 kV) in each of three CG cascades. The cascade of capacitors is connected into mechanically firm design by means of a plastic tube, which is located in the center hole of metallic shields. The cascades are located inside the tanks and are connected each other by two diode groups (V). The third group (“V”) doesn’t contain diodes and plays the role of mechanical support only.

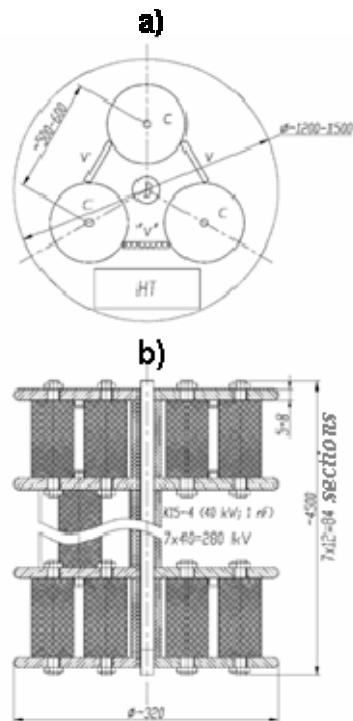


Fig. 10. Design of main elements of power supply of 2.0 MV (a) and cascade of capacitors (b)

Diode groups (V) are designed with the columns of avalanche diodes which may work at  $\text{SF}_6$  gas pressure. Operating voltage is of 150 kV, the current is of 400 mA at 500 Hz frequency. Voltage divider (VD) is used for high voltage measurement and stabilization by means of feedback to triode via controller. It is made of 2500 precise resistors in series ( $20 \text{ M}\Omega$ ;  $\pm 0,25\%$ ; 2 W) with temperature coefficient of  $10^{-6} \text{ }^\circ\text{C}^{-1} = \pm 25 \cdot 10^{-6} \text{ }^\circ\text{C}^{-1}$ . Divider is placed in the main tank axis, where the potential is distributed almost uniformly along the axis by cascade of capacitors. The dimensions of the tank for the generator accommodation are of  $6000 \times 1200 \text{ mm}$ .

## CONCLUDING REMARKS

The scheme of the HV e-cooler has been chosen and construction of 250 kV prototype is in progress. Simulation of magnetic field formation in acceleration columns, electron beam formation and recuperation has been done. Design of the magnetic system, the electron gun and collector has been done. Design of magnetic system the system of power transmission to high potential is in progress.

# THE STOCHASTIC COOLING SYSTEM OF HESR

Rolf Stassen, Hans Stockhorst, FZJ, Jülich,  
Lars Thorndahl, CERN, Geneva, Takeshi Katayama, GSI, Darmstadt

## Abstract

The HESR is the High Energy Storage Ring (1.5 - 15 GeV/c) for antiprotons at the FAIR facility (Facility for Antiprotons and Ion Research) in Darmstadt (GSI). Stochastic cooling in the HESR is necessary not only during the experiments to fulfill the beam requirements, but also during the accumulation due to the postponed RESR. Extensive simulations and prototype measurements have been carried out to optimize the HESR stochastic-cooling system with the new slot-ring couplers. The system design is now in the final construction phase for the mechanical tank layout and all active RF-components. First results of the optical notch-filter with automated frequency control and the 4-6 GHz slot-ring couplers will be presented.

## Stochastic cooling tanks

The main system of the HESR [1] stochastic cooling (SC) system [2] will operate in the frequency range from 2-4 GHz. In total, 5 SC-tanks will be installed, each tank housing 64 slot coupler rings and each ring is coupled out by eight electrodes [3]. Two tanks will be used as pickups, each cryogenically cooled by two cold heads on top of the tank. Support bars and rings connect the combiner-boards with the second stage of the cryopumps. Thus the lowest temperature of about 20 K will be found at the Wilkinson resistors which are the main noise sources.

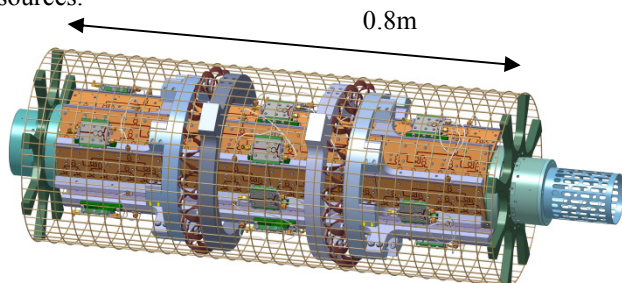


Fig. 1: Inner part of one pickup tank with combiner-boards and support bars for the cryogenic connections.

Each pickup will be used to detect the signals of all three cooling planes (horizontal, vertical and longitudinal). The 16:1 combiners join the electrodes in beam direction, while the 2:1 combiners join neighboring electrode-rows to get the upper, lower, right and left signals for the transverse cooling. These combiners are designed as heat trap for the heat flow coming from the RF lines. The inner part of one pickup tank including all combiner-boards is shown in Fig.1. The design phase of the pickup tanks including the x-y support to adjust the inner structure according to the beam centre is now in the final stage and production can start in 2012.

The kicker-tank layout will be similar to the pickup-tank layout except that no cryogenic cooling system will

be installed and the electrode combination within the tank and thus the number of feed troughs will be adjusted according to the RF power needed for the new accumulation scheme [4, 5]. Here three tanks will be installed, one for each cooling direction. Nevertheless all tanks will be fully installed to ensure that each tank can be used for any cooling plane. This gives a good compromise to meet the necessary phase advance at the different foreseen optics. During the accumulation all tanks will be used for longitudinal cooling, where a higher RF power is needed. A relay-matrix will be used to switch between the different operation modes. This concept provides an installed RF power of about 250 W for each transverse cooling direction (horizontal/vertical) at each tank, or 500 W per tank when used for longitudinal cooling.

## RF components outside the tanks

The combined power of the pairs of 16 electrodes in beam direction are coaxially fed through the vacuum envelope and put in 32 low-noise octave-band pre-amplifiers. These commercial available amplifiers will gain around 20 dB and will work outside the tank at ambient temperature. The compact design of this highly integrated amplifier minimized the fabrication tolerances. Nevertheless each amplifier will be measured and paired to reduce amplitude and phase errors of the corresponding channels. The 16:1 combiner has been optimized for a best signal combination at injection energy ( $\beta = 0.96$ ). Combiner losses at higher energies are negligible while at the lowest HESR energy a loss of 2.5 dB is still tolerable (Fig. 2).

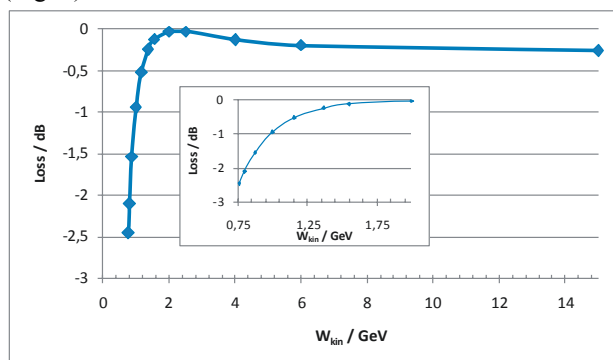


Fig. 2: Losses of the 16:1 combiner at different energies. The shown losses are upper limits occurring at 4 GHz.

The pre-amplified signals will be combined in further 3 layers (Fig. 3). Hereby, switchable delay lines are required to compensate for the energy-dependent beam drift time. The delay lines will be switched in steps of 10 mm of electrical length at the first layer (PV1) and 20 mm at the further layers (PV2, PV4). Each programmable delay-line includes a Wilkinson coupler which combines the two input signals after the switching stage. A

deviation of 10 mm from the ideal length leads to a phase difference between the Wilkinson inputs that causes at 4 GHz an additional attenuation of nearly 0.8 dB. The last Wilkinson layer adds the power of both adjoining tanks. This allows stochastic cooling in the whole energy range of the HESR (0.8 - 14 GeV). To minimize the number of switches, the reference plane is shifted at different energies but this can be easily compensated by adjusting the delay-line between pickup and kicker. Prototypes of each delay line were built and tested and fulfilled all RF requirements.

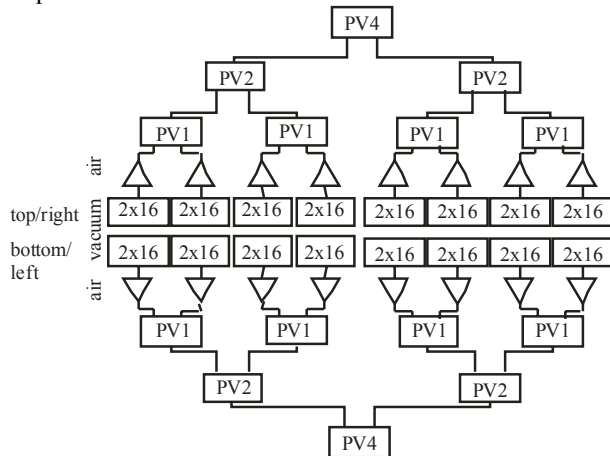


Fig. 3: Pickup section with programmable delay-lines (PV) to provide stochastic cooling in the whole energy range of the HESR (lengths are not to scale).

One important element in the active cooling chain are the high power amplifiers. Power amplifiers in the 2-4 GHz range are nowadays commercially available. But the specific requirements concerning group-delay and phase behavior demands a dedicated design. In collaboration with IMST [6] a first prototype of a 25 W amplifier was built. All requirements have been nearly reached but the modular design with separately housed stages showed some restrictions. The final version will have a compact one-board design with separated caves for each GaN transistor similar to the design of the delay lines.

#### 4-6 GHz System

Besides the main 2-4 GHz system, an additional 4-6 GHz system is planned which is needed to reach the desired momentum spread in the high resolution mode at higher energies. This system will be used for longitudinal cooling only. The higher frequencies required at least 12 electrodes instead of 8. 12 Combiner-boards around the structure are no longer mountable. Thus the circuitry of the electrodes has been changed that 2 electrodes will already be combined within the structure. The combination of the rings is similar to the 2-4 GHz design. Each structure is closed by the next ring which gives the ground plane of the microstrip electrodes. Special mechanical tolerances guarantee the desired connections of the rings.

Simulations have shown that the longitudinal coupling impedance of the 4-6 GHz structure is much lower than

that of the 2-4 GHz one [7]. While the 2-4 GHz structure has a shunt impedance of  $Z_k \approx 36 \Omega$  constant over the whole frequency band, the impedance of the 4-6 GHz structure decreases from about  $Z_k \approx 27 \Omega$  at 4 GHz down to  $Z_k \approx 6.5 \Omega$  at 6 GHz.

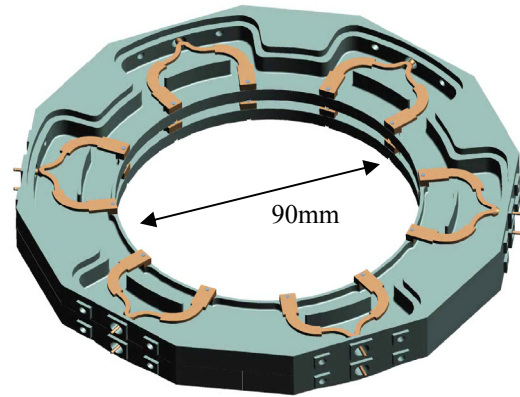


Fig. 4: Two slot coupler rings with combined electrodes for the 4-6 GHz longitudinal cooling.

A part is compensated by the smaller dimension in beam direction. 80 rings instead of 64 in the 2-4 GHz system can be installed in the same tank. The lower sensitivity is tolerable because only longitudinal cooling in the 4-6 GHz range is needed [5]. The first measurements show great resonances above 4.8 GHz. The strongest one can be interpreted as an E31 mode in a corrugated wave guide along the beam direction. This sextupole mode especially interacts with the sixfold electrode structure and degenerates the coupling impedance. We got a partial improvement of the signal transmission by shifting the resonances with metal pieces introduced into the ring slots. The combiner boards contain further error sources. We have chosen to use a substrate with a lower permittivity ( $\epsilon_r = 6$ ) in order to get the nearly the same dimensions of the circuit elements as at the proven 2-4 GHz band ( $\epsilon_r = 9.2$ ). But the signals are less guided and show parasitic ways introducing phase errors. Therefore, we are going to redesign the combiner boards.

#### Optical Notch-Filter with active frequency control

The principle of the notch filter for the HESR is shown in Fig. 6. Similarly to the COSY design [8], both signal paths will operate in the optical range. This eliminates phase noise and amplitude variation from the laser. The fluctuations of each notch frequency over the time must be within 0.5 Hz. The main source for such changes is the high temperature sensitivity of the fibre-optic delay line. An active temperature control of the coil can only minimize the temperature dependence, but not additional sources and is limited by the achievable precision of the temperature control. That's the reason why for the HESR the following control system has been chosen (Fig. 6):

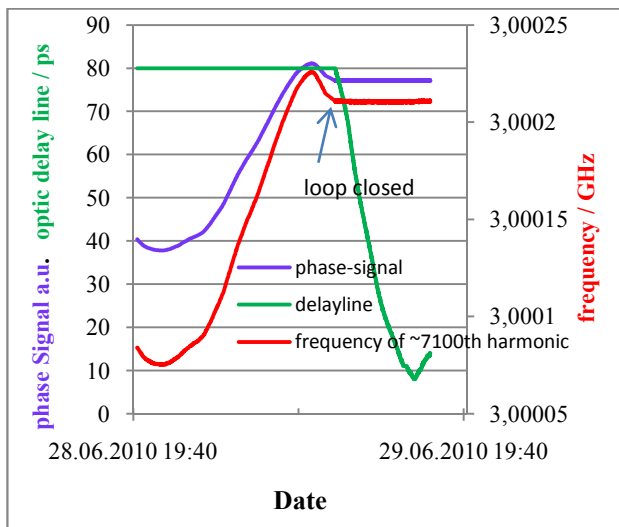


Fig. 5: Frequency change (red) of the 7100th harmonic of the first HESR notch-filter during one night (left part) and after closing the control loop.

Besides the signal from the pickup (In), a fixed frequency pilot signal will be added and transmitted through both optical paths. Directional couplers after the photo-detectors take band-pass-filtered parts of the transmitted signals to a phase detector. Any differences between the lengths of the two signal paths and thus any change of the notch frequencies will be detected by the phase detector. The controller closes this active loop by driving the fibre optic delay line according to the phase change of the pilot signal.

The drift of the 7100th notch frequency over one night is shown in the left part of Fig. 5. This corresponds to a change of the fundamental notch frequency of 25 Hz during the night. This relates to a deviation of  $5E-5$ , which is far too high for the required cooling. At 8:30 in the morning, the phase loop was closed and the frequency-change due to the day's warming up was completely compensated by the phase loop.

The length of the optic delay line (green curve in Fig.5) was changed by about 70 ps (= 21 mm electrical length) during the day. The setting range of the used delay line is 560ps, thus one delay line gives enough margin for a full

compensation. The amplitudes of both optical paths and thus the stability of the notch-depths are automatically controlled by the new optical attenuators. The included power measurements in these attenuators allow a fast control of the amplitudes.

A similar system can be used to control the optical fibre link from pickup to kicker either by sending a portion back via an additional fibre line or by using the BuTis (bunch phase timing) system to generate a phase stable pilot signal at the kicker side.

### REFERENCES

- [1] R. Maier, The high energy storage ring (HESR), Proceedings of PAC2011, New York, USA
- [2] H. Stockhorst, R. Stassen, D. Prasuhn, R. Maier, T. Katayama, L. Thorndahl, Stochastic Cooling for the HESR at the FAIR Facility, PAC09, Vancouver, Canada.
- [3] R. Stassen, P. Brittner, R. Greven, H. Singer, G. Schug, H. Stockhorst, L. Thorndahl, Recent developments for the HESR stochastic cooling system, Cool07, Bad Kreuznach, Germany
- [4] T. Katayama, T. Kikuchi, R. Maier, I. Meshkov, D. Prasuhn, R. Stassen, M. Steck, H. Stockhorst, Beam accumulation with barrier voltage and stochastic cooling, Proceedings of IPAC10, Kyoto, Japan
- [5] H. Stockhorst, R. Maier, D. Prasuhn, R. Stassen, T. Katayama, Status of stochastic cooling predictions at the HESR, to be published, IPAC11, San Sebastian, Spain.
- [6] IMST, www.imst.de Kamp-Lintfort, Germany
- [7] L. Thorndahl, 90mm Full-Aperture Structures with TM01-Mode propagation for 6-8 GHz Stochastic Momentum Cooling in HESR, internal report, 2010
- [8] R. Stassen, F.J. Etzkorn, R. Maier, D. Prasuhn, H. Stockhorst, L. Thorndahl, COSY as ideal Test Facility for HESR RF and Stochastic Cooling Hardware, Proceedings of PAC09, Vancouver, Canada

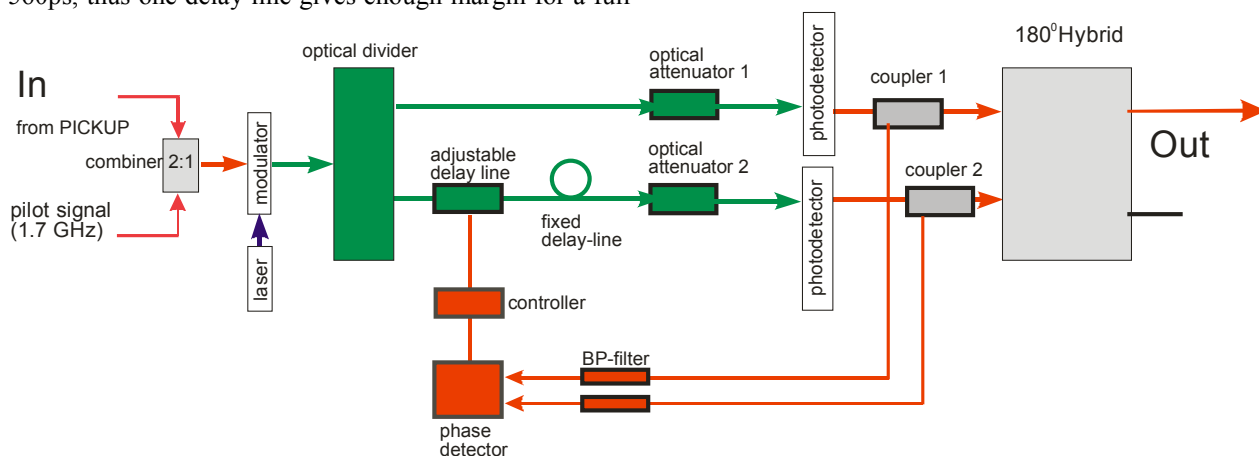


Fig. 6: Optical notch filter with active frequency control

# AN IMPROVED FORWARD TRAVELLING WAVE STRUCTURE DESIGN FOR STOCHASTIC COOLING AT EXPERIMENTAL COOLER STORAGE RING (CSRE), AT THE INSTITUTE OF MODERN PHYSICS (IMP) IN CHINA\*

Yong Zhang<sup>#</sup> and Junxia Wu, IMP, China  
 Fritz Caspers and Lars Thorndahl, CERN, Switzerland  
 Takeshi Katayama and Fritz Nolden, GSI, Germany

## Abstract

An improved forward travelling wave (TW) structure as the pick-up/kicker is designed for the stochastic cooling to match the field wave's (phase) velocity to that of the beam. The theoretical analysis is performed together with the simulations of the propagation characteristics. Using CST Microwave Studio (CST MWS), the simulated results, including phase velocity, characteristics impedance, and distributions of the longitudinal fields, are implemented and compared with the experimented results. The improved forward TW structure can be satisfied the requirements of stochastic cooling project at CSRe, which the phase velocity is closed to 0.70 (matching the desired beam energy of 400 MeV/u) and the characteristics impedance is 17 ohm.

## INTRODUCTION

At the experimental cooler storage Ring, CSRe at the Institute of Modern Physics (IMP) in China, the electron cooler is already equipped and is successfully operated [1]. For the Radio Isotope beam experiment planned at the CSRe, the injected beam emittance will be 20–50  $\pi$  mm. mrad and the momentum spread  $\Delta p/p$  will be  $\pm 0.5 \sim 1.0 \%$ . The pre-cooling of stochastic cooling is quite effective for these RI beam to reduce the emittance to less than  $5\pi$  mm. mrad and  $\Delta p/p$  of 0.05 % within 2 – 20 sec. which is dependent upon the injected RI particle numbers. The energy range of RI beam is expected from 300 MeV/u to 500 MeV/u. The frequency range of the stochastic cooling system is determined as roughly from 0.2 to 0.7 GHz. The structure of pick-up /kicker should have a matched phase velocity, the high coupling impedance and a simple structure to be constructed and installed in the storage ring. In the present CSRe case, the pick-up/kicker should be installed in the bending magnet chamber. The size and the number of pick-up/kicker are severely limited. In this paper, an improved forward travelling wave (TW) structure, based on the electrode designed by Fritz Caspers, as the pick-up/kicker will be shown.

## MODEL OF A FORWARD TRAVELLING WAVE ELECTRODE

A photo and an equivalent representation of the

forward TW structure is shown in Fig. 1. This multi-slot strip-line structure was designed by Fritz Caspers and produced at CERN in 1998 for tests of the concept [2]. In contrast to the conventional travelling wave structures as pick-up/kicker, such as Flatin type slotted transmission line [3] and McGinnis type slotted wave guide structure [4], this structure is very broadband, operating from low frequencies upwards as a forward coupler. We need a structure for the installations in the bending magnet, which has a large bandwidth, which works for the required beta and does not need many feedthroughs and has no significant aperture reduction. Thus this multi-slot strip-line electrode is full of interest to us. As shown in Fig. 1(b), the reduction in phase velocity is a function of slot length  $c$ , slot width  $d$ , electrode thickness, and the spacing between the electrode to ground. From the measurement and simulated results it is evident that up to 1.5 GHz this structure has a very low phase dispersion.

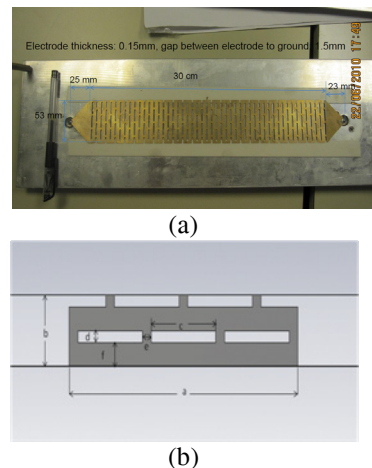


Figure 1: (a) The multi-slot strip-line electrode. The total number of cells in this example is 25. (b) An equivalent representation of this structure ( $a=53\text{mm}$ ,  $b=12\text{mm}$ ,  $c=15\text{mm}$ ,  $d=2\text{mm}$ ,  $e=2\text{mm}$ ,  $f=4\text{mm}$ ).

## Longitude electric field distribution

A quarter cell (of 12mm length in vertical beam direction) model used by CST MWS is shown in Fig. 2(a). The  $xz$  axis and the  $y = 35$  mm planes are magnetic symmetry planes. The beam moves vertically in the  $z$ -direction at  $x=0$  and  $y = 34$  mm. There are strong  $E_x$  fields in the cell mid-plane off the cell centre shown in Fig. 2. There is good agreement with HFSS cell simulations done at CERN as show in Fig. 2 (b).

\*Work supported by NSFC (10705039), HIRFL-CSR

<sup>#</sup>zhangy@impcas.ac.cn

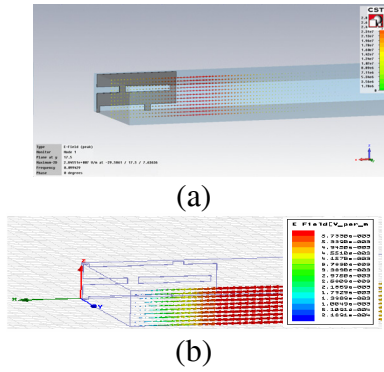


Figure 2: Electric fields distribution along x-axis in the cell mid-plane of the model. (a) CST MWS simulated results was done at CSRe (b) HFSS simulated results was done at CERN.

*Phase dispersion and phase velocity data*

A comparison of measurement and simulation results is shown in Fig. 3. We notice that the phase dispersion is rather small and the deviation from linear phase (displayed in Fig. 3) amounts only 11 degrees at a frequency of 1.5 GHz for a 30 cm long structure (length of the elementary cell  $b = 12$  mm). Fig. 4 shows the simulated results for the phase dispersion when the electrode has 25 cells ( $L = 30$  cm long electrode), 40 cells ( $L = 0.48$  m long electrode) and 80 cells ( $L = 0.96$  m long electrode). The phase deviation is 24 degrees at 1.5 GHz for 80 cells and thus is still not very large. Thus in a frequency range from a few MHz to 1.5 GHz this structure has a phase dispersion acceptable for many applications.

For this type of electrode, the phase velocity is determined by the slot size, thickness of the electrode and the distance from the electrode to ground. When increasing the thickness of the metal strip and its distance to the ground plane the phase velocity rises as well. In the measurement the phase velocity can be deduced from the phase  $\Phi$  of the complex transmission coefficient  $S_{21}$  or alternatively in the time domain from the travel time  $\tau$  (Fig. 4) by the relation given in Equ. (1).

$$\beta = \frac{2L}{c\tau} \quad (1)$$

where  $L$  stands for the electrode length,  $\tau$  is the round-trip travel time. The agreement between both results is good. Minor deviations partly related to the interpretation of measurement data, both in the time and frequency domain.

*Characteristic impedance from time domain measurements and simulation by CST MWS*

Figure 5 shows the step response in real time obtained with a Lecroy sampling scope where the characteristic impedance returns as about 17 Ohm, which is nearly equal to the simulated result obtained from CST MWS (Figure 6). The variation of the characteristic impedance

versus spacing  $s$  between electrode and ground is also depicted in Fig. 7.

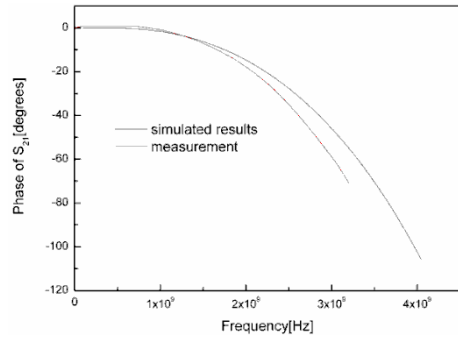


Figure 3: Phase of  $S_{21}$  for 25 cells. The black line shows the simulated and the red line the measured results.

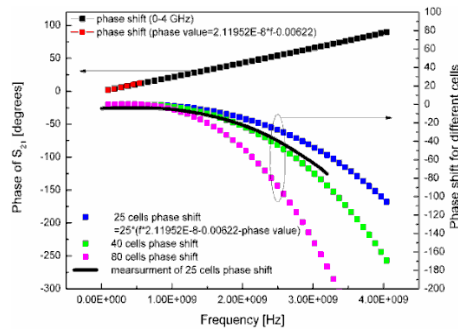


Figure 4: Phase dispersion for 25 cells (blue dots), 40 cells (green dots) and 80 cells (pink dots). Black and red dots mean the phase shift versus frequency when sweeping frequency from 0 to 4 GHz.

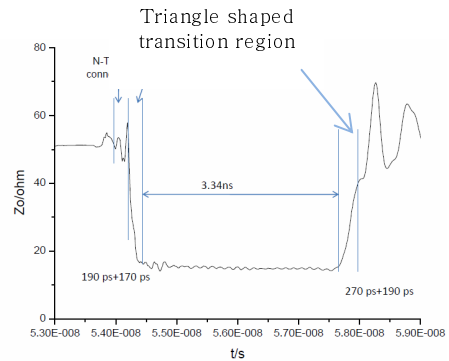


Figure 5: Impedance measurement results using the TDR (Time Domain Reflection) method on a 30 cm long model of 25 cells.

From the simulated and measured results, the phase velocity of this multi-slot strip-line structure doesn't match very well to the beam velocity, which corresponding the energy range of RI beam being expected from 300 MeV/u to 500 MeV/u. Thus we design an improved forward travelling wave (TW) structure as the pick-up/kicker for the stochastic cooling to match the field wave's (phase) velocity to that of the beam.

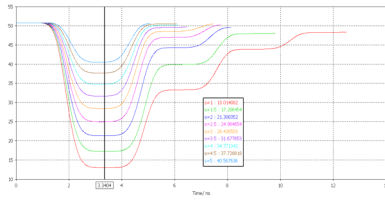


Figure 6: Simulated results of the characteristic impedance in vertical axis [Ω] for different  $s$  = distance electrode to the wall with CST MWS.

### MODEL OF AN IMPROVED FORWARD TRAVELLING WAVE ELECTRODE

#### *A prototype pickup electrode in the vacuum chamber*

A photograph and a technical drawing of an improved forward travelling wave electrode is shown in Fig. 7. Five slots ( $c = 15\text{mm}$  by  $d = 2\text{ mm}$ ) are positioned across the width of the pick-up/kicker metal strip. The unit cell length amounts to  $b = 12\text{ mm}$  and the thickness of the electrode is  $0.4\text{ mm}$ . The electrode which follows the bending of the vacuum chamber inside the bending magnet is  $a = 87\text{ mm}$  wide and about  $L = 1\text{ m}$  long.

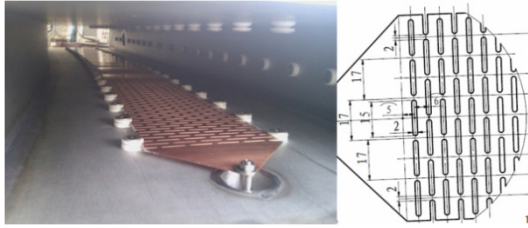


Figure 7: The slotted structure of travelling wave mode with number of cells = 80 and the length  $L \approx 1$  meter.

#### *Simulation and measurement results in the frequency domain*

To ensure the calculation accuracy, the refined mesh for the improved slotted electrode of one period is show in Fig. 8. The phase response of the measurement is shown in Fig. 9. The phase difference from the linear phase (with subtracted delay term) is not more than 45 degrees at 1.5 GHz for the nearly 1 m long electrode. The measured (network analyzer) and simulated results (CST MWS) are compared as well, as shown in Fig. 10. For frequencies below 1.5 GHz the agreement is reasonable.

The phase velocity is measured using the resonant method by replacing the connection of the electrode on both ends to the inner conductor of the measurement lines by (weak) capacitive coupling [5] i.e. positioning the pin of the feed-through very close to the electrode but leaving it unconnected. The measured results (S-parameter data) are depicted in Fig.11

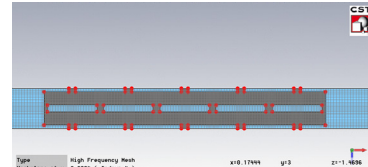


Figure 8: The refined mesh for the improved slotted electrode of one period.

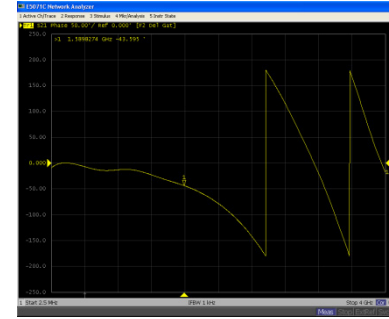


Figure 9: Phase of  $S_{21}$  for the improved slotted electrode of 80 cells.

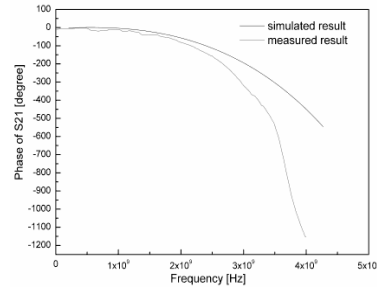


Figure 10: Comparison of  $S_{21}$  for the improved slotted electrode of 80 cells between the measured and the simulated result.

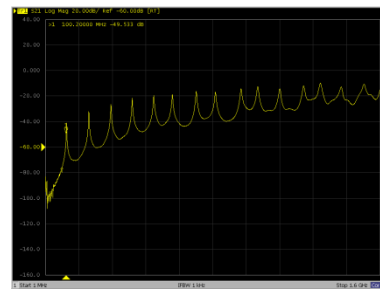


Figure 11: Resonant measurement result of the electrode.

From the resonant frequency and Q value, the phase velocity and the attenuation of the electrode can be calculated using Equ.2 and Equ.3,

$$\beta = \lambda \frac{f}{c} = \frac{2L}{n} \frac{f}{c} \quad (2)$$

$$\alpha = \frac{n}{2L} \frac{\pi}{Q} \left[ \frac{Np}{m} \right] = \frac{n}{2L} \frac{\pi}{Q} 8.686 \left[ \frac{dB}{m} \right] \quad (3)$$

where  $n$  is the resonant harmonic and  $L$  is the electrode length which is 1.03 m. The results for the phase velocity and attenuation are shown in Table 1. The phase velocity is roughly about 0.7, which is not too far away from the simulated result obtained with CST MWS, as shown in Fig. 12. The variation of the characteristic impedance versus spacing  $s$  between electrode and ground is also depicted in Fig. 13.

Table 1: Beta and attenuation result

n	f (MHz)	Q	$\beta$	Attenuation (dB/m)
1	101.66	110	0.69806	0.12036
2	208.36	138	0.71537	0.19188
3	314.20	157	0.71917	0.25299
4	415.80	163	0.71379	0.32490
5	518.48	163	0.71205	0.40613
6	607.66	171	0.69543	0.46455
7	722.04	172	0.70829	0.53883
8	812.94	167	0.69777	0.63424
9	935.06	164	0.71342	0.72657
10	1016.00	145	0.69765	0.91309
11	1120.70	144	0.69959	1.01137
12	1234.00	140	0.70612	1.13484
13	1315.00	113	0.69459	1.52316

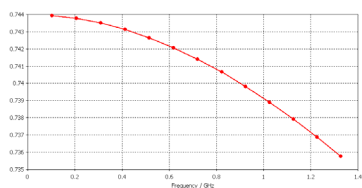


Figure 12: Simulated result for the phase velocity.

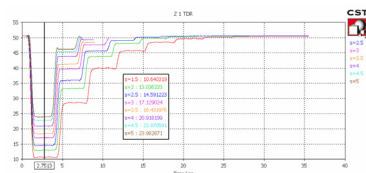


Figure 13: Simulated results of characteristic impedance in vertical axis [Ω] for different  $s$  = distance electrode to the wall.

### CONCLUSION

Based on the analysis of a multi-slot strip-line of travelling mode proposed by Fritz Caspers, an improved structure as the pick-up/kicker is designed for CSRe stochastic cooling project. This kind of structure has the adequate phase velocity of 0.70 which is matched to the operation energy of the stochastic cooling 300 MeV/u - 500 MeV/u (beam velocity  $\beta = 0.654 - 0.759$ ) and has the simple structure. Because the pick-up/kicker should be installed in the bending magnet chamber, the characteristic impedance is 17 ohm when keeping the space of 3 mm between ground and electrode. These

characteristics can be satisfied the requirement of the CSRe stochastic cooling project.

### REFERENCE

- [1] J. W. Xia, et al, Construction and commissioning of the HIRFL-CSR, APAC'04, Indore, India, Feb. 2007, THXMA03, p.534.
- [2] F. Caspers, A novel type of forward coupler slotted stripline pickup electrode for non-relativistic particle beams, CERN-ATS-Note-2011-075 TECH. - 2011. - 8 p
- [3] L. Faltin, Nucl. Instr. And Meth. 148 (1978) 449.
- [4] D. McGinnis, Proceedings of PAC99, New York, 1999, p. 1713
- [5] T. Kroyer, F. Caspers, E. Gaxiola, Longitudinal and transverse wire measurement for the evaluation of impedance reduction measures on the MKE extraction kickers, AB-Note-2007-028

# SIMULATION STUDY OF BARRIER BUCKET ACCUMULATION WITH STOCHASTIC COOLING AT GSI ESR

T. Katayama, C. Dimopoulou, F. Nolden, G. Schreiber, M. Steck, GSI, Darmstadt, H. Stockhorst, FZJ, Jülich, T. Kikuchi, Nagaoka University of Technology, Nagaoka, Niigata

## Abstract

The beam accumulation experiments with use of barrier bucket cavity and stochastic cooling system was performed at the ESR, GSI. Two methods of barrier voltage operation, moving barrier and fixed barrier cases were tried, and for the moving barrier case the electron cooling was additionally employed as well as the stochastic cooling. In the present paper, the beam accumulation processes are simulated with particle tracking code where the cooling force (stochastic and electron cooling), the diffusion force and the barrier voltage force are included as well as the IBS diffusion effects. The simulation results are well in agreement with the experimental results.

## INTRODUCTION

In the original concept of the FAIR project, the function of 3 GeV antiproton accumulation is planned in the RESR ring where the stochastic stacking method is planned. However, the RESR was postponed due to the budgetary limitation as the 2<sup>nd</sup> phase project. Then, a strong demand of the beam accumulation directly from the Collector Ring to the High Energy Storage Ring (HESR) urgently occurred. The barrier bucket accumulation method using the barrier voltage system assisted by the stochastic cooling was proposed as a most promising way. [1, 2]

The concept of beam accumulation with barrier bucket system with beam cooling was already tried in 2007 at the GSI, ESR where the heavy ion beam 40Ar18+, 60 MeV/u was injected into ESR from SIS 18. The experiment was successfully achieved to demonstrate the possibility of beam stacking with BB system assisted by electron cooling. The electron cooling is effective for the low energy and high charge state ions while in the HESR 3 GeV antiproton beam has to be accumulated. In this case the stochastic cooling is exclusively a main cooling means.

To verify the principle of BB accumulation with stochastic cooling, the Proof Of Principle (POP) experiment was performed at ESR, GSI where both the stochastic cooling and electron cooling are available. The experimental results are presented in the accompanied paper in this conference [3]. In the present report the simulation results of BB accumulation are presented and compared to the experimental results to bench-mark the simulation code.

## STOCHASTIC COOLING AT THE ESR

In Table 1 the main parameters for experiment and simulation are tabulated.

Table 1: Parameters of Stochastic Cooling at ESR

Ion species	40Ar18+	Energy	0.4 GeV/u
Ring Circumference	108.36 m	Revolution Period	500 nsec
Number of ions/shot	5e6/shot	Dp/p (rms) of Injected beam	5.0e-4
Bunch length of injected beam	150 nsec (simulation) 60 nsec (exp., cut by kicker)	Ring slipping factor	0.309
TOF from PU to Kicker	0.253e-6 sec	Dispersion at PU & Kicker	4.0 m
Band width	0.9-1.7 GHz	Number of PU & Kicker	8
PU Impedance	50 Ohm	System gain	90-130 dB
Atmospheric temperature	300 K	Noise temperature	40 K

The typical momentum cooling process with this stochastic cooling system is analyzed with the Fokker-Planck code as given in Fig. 1 with 1e6 particles.

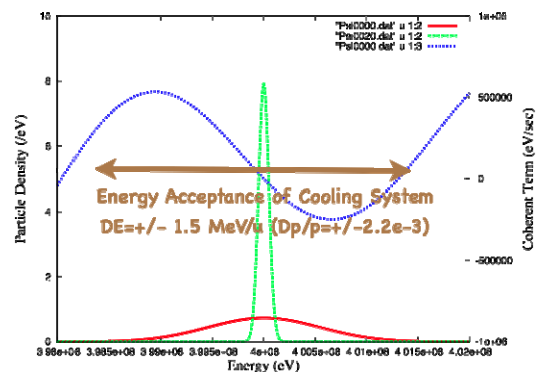


Fig. 1 The evolution of momentum cooling process analyzed with Fokker-Planck code. Red: Initial particle distribution, Green: Particle distribution after 20 sec. Blue: The coherent term of the cooling system. Gold line with arrow: Energy acceptance of the cooling system. Particle number is 5e6 and the cooling system gain is 120 dB.

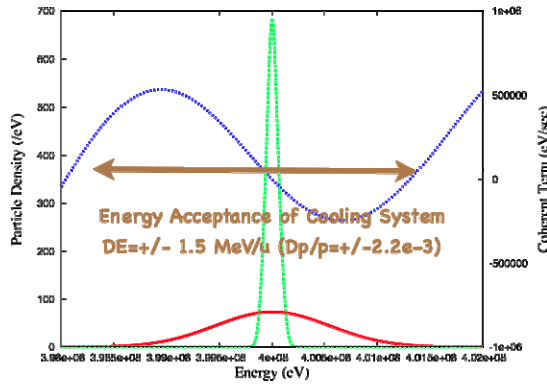


Fig. 2 The same parameters as in Fig. 1 but the particle number is  $1e8$ .

From these results it is confirmed that the present stochastic cooling system could cool the momentum spread well below  $1e-4$  (rms) within 20 sec even when the particle number is as large as  $1e8$ .

### BARRIER BUCKET ACCUMULATION

There are two schemes of barrier bucket accumulation, fixed barrier and moving barrier schemes. In the former one, two half-wave barrier voltages are produced in the one revolution period while in the latter case two full-wave barrier voltages are excited and the timing and amplitude of barrier voltage are controlled in proper way. The fixed barrier scheme is apparently simpler way but concerning the accumulation efficiency we have to carefully compare numerically calculated results for two methods.

The particle tracking code for the BB accumulation has been developed which includes the effects of RF field by barrier voltages, stochastic and electron cooling forces, diffusion forces such as Schottky diffusion, thermal diffusion and Intra-Beam-Scattering effects. If necessary other effects associated with internal target, mean energy loss and multiple scattering, could be included. The details of algorithm are given in [1].

For the barrier voltage accumulation, one of the serious parameters is the separatrix height and the synchrotron tune. It should be noted that at the ESR POP experiment the available voltage was as small as 120 Volt, and then the separatrix momentum height is  $2.6e-4$ . This small separatrix height is the main limitation of the stacked particle number.

### COMPARISON OF SIMULATION & EXPERIMENTAL RESULTS

#### Fixed barrier method

The fixed barrier experiments was performed with following conditions: the barrier voltage is 120 Volt, the frequency of 5 MHz (one wave length is 200 nsec).

Other methods of phase space manipulation

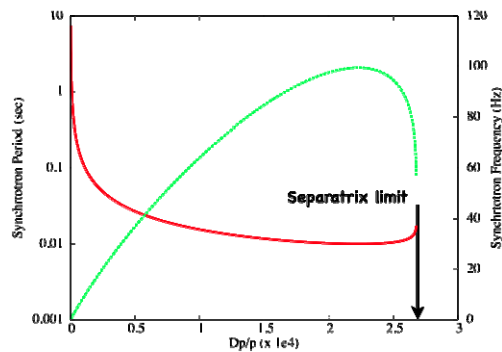
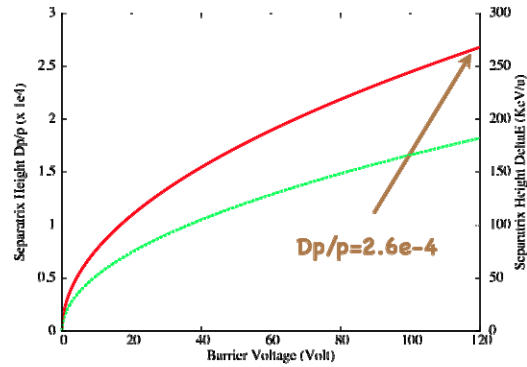


Fig. 3 The separatrix height (top) and the synchrotron tune (bottom) at the ESR POP experiment. The barrier voltage is 120 Volt.

The simulation results is given in Fig. 4, where the cycle time is 13 sec, and the stacking was continued up to 400 sec, 300 times injection. The injected particle number/shot was estimated around  $2e6$ . As the intensity is not so high then the IBS effects did not play important role in the experiments. The un-stacking process means that the beam was not injected but the injection fast kicker magnet was fired. The reduction of the accumulated intensity is due to the fact that the part of accumulated beam is continuously kicked out by the kicker fringing field.

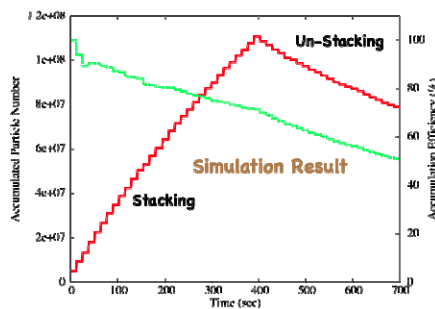


Figure 4 Simulation results of beam accumulation (stacking) and un-stacking at the fixed barrier bucket system.

The experimental results are given in Fig. 5 which is quite well agreement with the simulation results in Fig. 4.

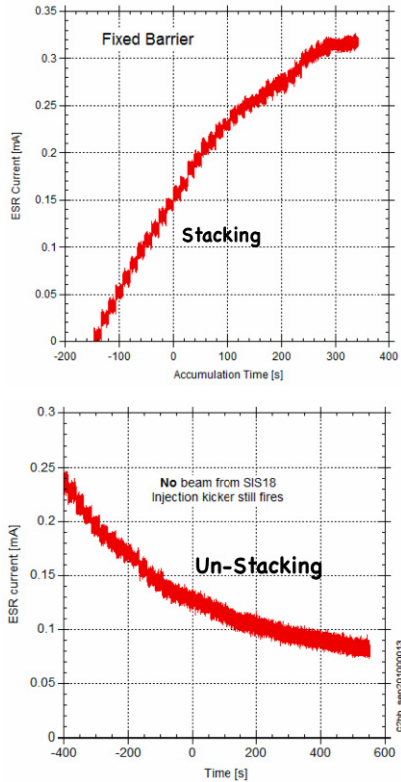


Figure 5 The experimental results of beam accumulation (top) during the period 500 sec with cycle time 13 sec and the un-stacking (bottom). Fixed barrier case.

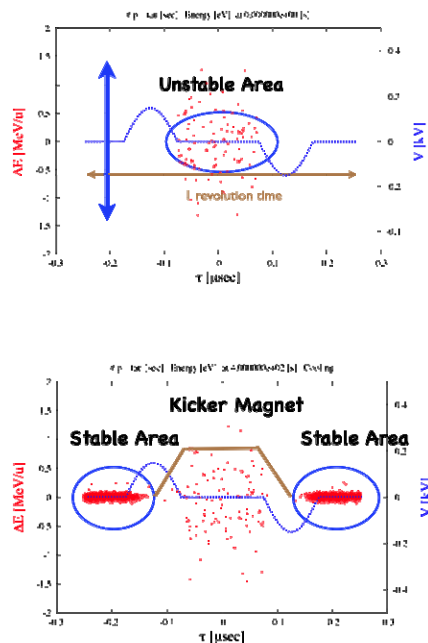


Figure 6 Phase space mapping at the 1<sup>st</sup> injection and 20<sup>th</sup> injection. The fast kicker magnet, of which the magnetic field is illustrated schematically with the pulse length 300 nsec. Particles populated in the kicker magnetic field are labelled as “lost” particles.

Other methods of phase space manipulation

### Moving barrier method

First the moving barrier accumulation experiment was tried with the barrier voltage of 120 Volt and the cooling gain was 120 dB. However we could not observe the any increase of beam current though the accumulation process. From the simulation it is clearly shown that the stochastically cooled momentum spread of the coasting beam is too large and then the beam can not be compressed to prepare the empty gap for the next beam injection. That is a reason for no beam accumulation.

The ESR is equipped with the electron cooler which is able to cool down further the beam momentum spread. The parameters of electron cooler are as follows. length of cooler=2.5 m, electron diameter =5cm, electron current=0.2~0.5 A, effective electron temperature=1e-3 eV, beta function at cooler=15 m. The simulated cooling process is given in Figure 7 where the evolution of  $Dp/p$  (rms) is given as a function of time during two cycles. (Now the cycle time is 20 sec.) The blue line shows the case of only electron cooling, the green line the case of only stochastic cooling and the red line shows the case of simultaneous use of stochastic cooling and electron cooling. It is clearly shown that the electron cooler alone could not give the effective cooling during the cycle time 20 sec as the initial  $Dp/p$  (rms) is as large as  $8e-4$  while with simultaneous use of stochastic and electron cooler, the  $Dp/p$  is reached to around  $2e-5$ .

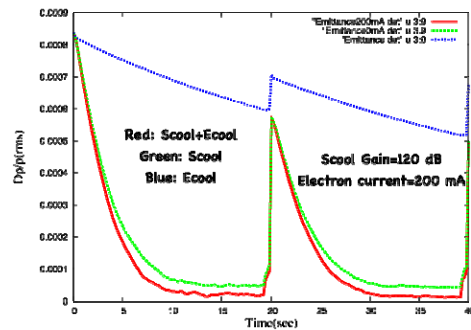


Figure 7 The evolution of  $Dp/p$  (rms) value during two cycles operation of moving barrier. The blue line shows the case of electron cooler alone, the green line the case of stochastic cooling alone and the red line the case of simultaneous use of electron cooler and the stochastic cooler.

The simulation and experimental results of increase of the stacked particle number are given in Fig. 8 where the accumulation efficiency is defined as the accumulated particle number/total injected particle number. The agreement of results are remarkable. At the time 800 sec, after 400 injections, we find the dip in the accumulated particle number in both results. Presently, the reason why both results have such a dip is not clear.

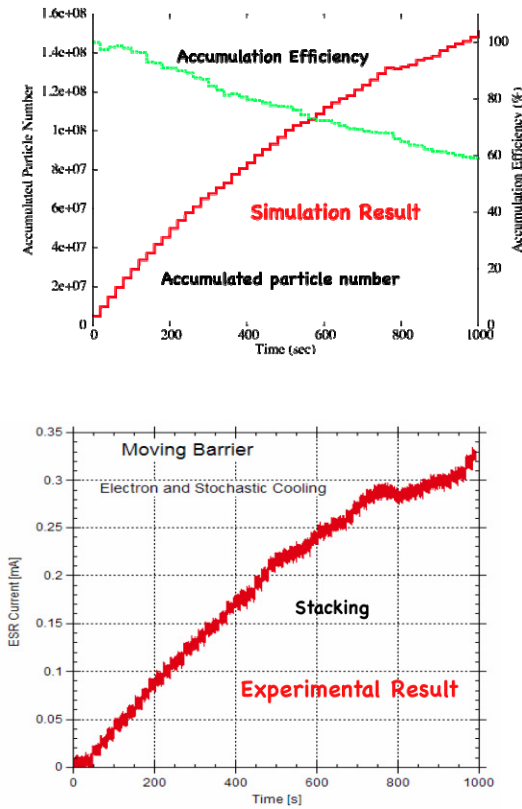


Figure 8 The simulation (top) and the experimental (bottom) results of the moving barrier operation. The red line in the top figure shows the accumulated particle number and the green line the accumulation efficiency.

The timing and amplitude of barrier voltage in the 1<sup>st</sup> cycle are illustrated in Fig. 9 as well as the particle distribution in the phase space for the moving barrier method with stochastic and electron cooling. At  $t=0$  sec, the batch is injected in the gap between two barrier voltages, and shortly after the voltage is switched off and the beam becomes coasting one. After cooling well the coasting beam, two barrier voltages are excited and moved to the original position when the cooled beam is compressed into the accumulation area and the central part is empty for the next beam injection.

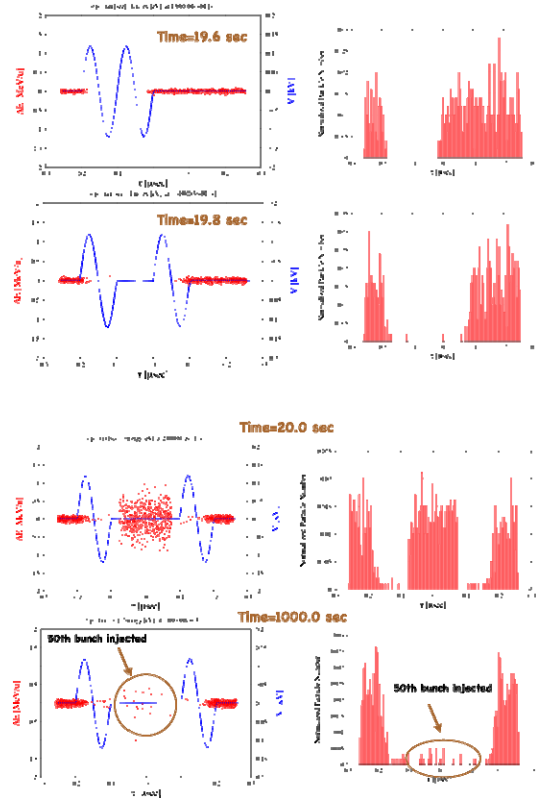
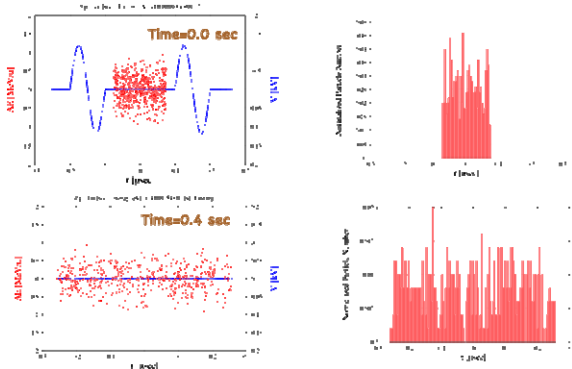


Figure 9 Particle distribution in the longitudinal phase space (left) at  $t=0, 0.4, 19.6, 19.8$  and  $20$  sec for the moving barrier case. The right figures show the particle distribution along the ring. The bottom figure corresponds to  $t=1000$  sec (after 50<sup>th</sup> injection).

## CONCLUSION

We have investigated the barrier bucket accumulation process with stochastic and electron cooling for the POP experiment at the ESR with simulation method. Both for the fixed and moving barrier accumulation process the experimental and simulation results are close in agreement. The particle tracking code developed for the simulation is bench-marked to be reliable. The application of BB accumulation with stochastic cooling to the HESR in FAIR project, and the Collider in NICA project with stochastic and electron cooling are proposed after the analysis with this code.

## REFERENCES

- [1] T. Katayama et al., “Beam Accumulation with Barrier Voltage and Stochastic Cooling”, IPAC10, Kyoto, May 2010.
- [2] H. Stockhorst et al., “Status of Stochastic Cooling Predictions at the HESR”, IPAC11, San-Sebastian, September 2011.
- [3] M. Steck et al., “Demonstration of Longitudinal Stacking in the ESR with Barrier Bucket and Stochastic Cooling”, these proceedings

# DEMONSTRATION OF LONGITUDINAL STACKING IN THE ESR WITH BARRIER BUCKETS AND STOCHASTIC COOLING

M. Steck, C. Dimopoulou, B. Franzke, O. Gorda, T. Katayama

F. Nolden, G. Schreiber, GSI, Darmstadt, Germany

D. Möhl, CERN, Geneva, Switzerland

R. Stassen, H. Stockhorst FZJ, Jülich, Germany

I. N. Meshkov, A. O. Sidorin, G. Trubnikov, JINR, Dubna, Russia

## Abstract

Fast longitudinal beam accumulation has been demonstrated in the ESR at GSI with an  $^{40}\text{Ar}^{18+}$  beam coming from the synchrotron SIS18 at 400 MeV/u. Continuous application of stochastic cooling in all three phase space directions merged the stack with the newly injected bunch. Longitudinal beam compression was achieved either by using short barrier bucket rf pulses or by successive injections onto the unstable fixed point of the rf bucket at  $h=1$ . This recent experiment in the ESR provides the proof of principle for the longitudinal stacking of antiprotons in the FAIR project. It is planned to accumulate pre-cooled antiprotons in the HESR, injected from the CR.

## INTRODUCTION

One of the four pillars of the physics program at FAIR [1] is based on a high production rate of antiprotons for hadron physics with high energy antiprotons, but also on the availability of low energy antiprotons. For optimum production rate it was proposed to have a system of collector and accumulator ring after the antiproton production target in order to have fast collection, stochastic pre-cooling and accumulation of the hot antiprotons emerging from the target. After the accumulator ring the cooled antiprotons then could be sent either to a high energy storage ring (HESR) for experiments with stored antiprotons or to another storage ring (NESR) which constitutes the first stage of deceleration to lowest energy. Due to funding limitations, it was decided to start the FAIR project with high energy antiprotons at reduced intensity.

The first stage antiproton production concept of FAIR now comprises the following ingredients. A high intensity 70 MeV proton beam from a new linac will be injected into the existing synchrotron SIS18 which boosts it to 4 GeV. The new 100 Tm synchrotron SIS100 will accelerate the protons to 29 GeV. The ramping cycle can be as short as 2.5 s, but as the antiproton production rate is limited by the stochastic pre-cooling a repetition cycle of 10 s is foreseen, with an option to upgrade to a 5 s cycle. A single short ( $\approx 50$  ns) bunch of up to  $2 \times 10^{13}$  protons will be extracted towards a nickel target for antiproton production followed by a magnetic horn to focus the divergent antiproton bunch. A magnetic separator selects 3 GeV antiprotons which are subsequently transported to the large acceptance collector

Other methods of phase space manipulation

ring CR [2]. Bunch rotation and debunching transforms the short bunch into a nearly coasting beam with a reduced momentum spread. Stochastic cooling is applied to reduce the longitudinal momentum spread and both transverse emittances. In contrast to the old scheme with a dedicated accumulator ring, the cooled antiprotons will be transferred directly to the high energy storage ring HESR [3], which in the new scheme also serves as accumulator ring.

The HESR cannot support a traditional accumulation system which is based on a ring with large momentum acceptance. The HESR has a momentum acceptance of  $\Delta p/p = \pm 0.25\%$  which is less than twice the momentum spread of the bunch from the CR. On the other hand, the circumference of the HESR is more than double the circumference of the CR. Therefore, a longitudinal accumulation scheme is much more favorable. In addition, the HESR is equipped with a stochastic cooling system and a barrier bucket rf system, thus no significant additional investment is required [4]. It is clear, however, that accumulation in the HESR will reduce the luminosity for experiments with stored antiprotons. A similar scheme for the accumulation of high intensity heavy ion beams is proposed in the frame of the NICA project [5]. At Fermilab, barrier buckets (BB) are being used in many beam manipulations, in particular in combination with stochastic cooling [6]. Efficient antiproton accumulation using the  $h=1$  rf system and stochastic cooling was first demonstrated in ICE [7].

As the usefulness of stochastic cooling in combination with BB is not obvious due to increased coherent signals originating from the time structure of the beam, a proof of principle experiment was proposed. This requires the availability of injected bunches in the receiving storage ring with fast kicker injection, a stochastic cooling system and a BB rf system. All these requirements are met by the ESR [8] storage ring at GSI with the synchrotron SIS18 as injector. Similar accumulation experiments in combination with electron cooling have been performed before [9]. From these experiments two serious limitations are well known. Firstly, the timing of the injection kicker of the ESR is very critical, in particular because of the small ring circumference and the resulting relatively short revolution time. Secondly, the ESR is not equipped with a dedicated BB system, the modified ESR acceleration cavity can provide a maximum voltage of 120 V in the BB mode. Nevertheless, with these known limitations the ESR is useful to study the accu-

mulation process and allows a comparison of experimental observations with the computer codes used to predict the performance of accumulation in the future scenario in the HESR. In particular, this will give better confidence in the estimated parameters of the systems involved in the accumulation process.

## EXPERIMENTAL PROCEDURE

In this frame, different longitudinal beam accumulation schemes in combination with stochastic cooling have been investigated by experiments and benchmarked by simulations [10].

The first method uses short BB pulses provided by a broadband rf system [11]. In the moving BB scheme, two sinusoidal BB pulses are applied. One stays stationary while the other is shifted in phase to compress the beam. Thus, a gap is created where new beam can be injected. In the fixed BB scheme, one prepares a stationary (fixed in phase) distribution consisting of (or similar to) two half sine wave barrier pulses of opposite sign. The resulting stretched rf potential separates the longitudinal phase space into a stable and an unstable region. After injection into the unstable region (potential maximum), the particles are pushed by cooling to the stable region. After some time the unstable region is free again for injection.

The second method uses a  $h=1$  rf system for bunching (adiabatically) of the circulating beam and injection of a new bunch onto the unstable fixed point. Then, the voltage is decreased (rather fast in order to avoid dilution of the new bunch) to let the beam debunch. In both schemes, continuous application of stochastic cooling counteracts heating of the stack during the rf compression and merges the stack with the freshly injected bunch. The required rf voltage for the longitudinal beam compression is moderate since the momentum spread of the cooled stack is small (of the order of a few times  $10^{-4}$ ). However, as shown below, the maximum available voltage of 120 V of the present BB cavity was a limiting factor. The cooled stack is repeatedly subjected to the same procedure until an equilibrium between beam losses and injection rate is reached.

Both options have been tested in the ESR under the same conditions. The experiments were performed with a  $^{40}\text{Ar}^{18+}$  beam at 400 MeV/u injected from the synchrotron SIS. The SIS and ESR rf systems were synchronised to operate at  $f_{rf}=1.97$  MHz, at  $h=2$  and  $h=1$ , respectively, since the SIS has double the circumference of the ESR. One of the two SIS bunches is fast extracted to the ESR. The ESR injection kicker pulse was typically 260 ns long (100 ns rise and fall time, 60 ns flattop), thus affecting about half of the ESR circumference. Well-controlled and precisely synchronised kicker pulses of all three injection kicker modules were essential for the success of the experiment. The total time of one revolution period ( $T_{rev}=507$  ns) had to be shared among the injected beam, the BB pulses (sinusoidal of period  $T_B=200$  ns) and the stacked beam. The short injection kicker pulse restricted the injection efficiency. At

Other methods of phase space manipulation

each injection from the SIS the ESR received on average  $20\mu\text{A}$  of beam current ( $3.5 \times 10^6$  ions) in a pulse with a FWHM of about 60 ns (see Figs. 2 and 3). In the HESR, which has a larger circumference, the revolution period for 3 GeV antiprotons is  $2\mu\text{s}$ , thus a longer kicker pulse can be used, permitting the injection of the single bunch of pre-cooled antiprotons from the CR.

The maximum height of the rf barrier  $\delta_B$  is given by the usual formula for a sinusoidal rf pulse

$$\delta_B = \sqrt{\frac{2QeV_{rf}}{\pi\beta^2\eta h E_{0,tot}}}$$

where  $E_{0,tot} = \gamma A m_u c^2$  is the total energy ( $m_u c^2=931.5$  MeV is the nucleon mass) and  $Q$  the charge state of the ion. The height  $\delta_B$  is defined so that the maximum height of the separatrix is at  $\Delta p/p = \pm\delta_B$ . For the BB pulses of period  $T_B$  a "harmonic" number  $h = T_{rev}/T_B \approx 2.5$  is defined. Hence, at the same voltage the confining potential of the BB system is  $\sqrt{2.5}$  lower than for the  $h=1$  rf.

The time between two successive injections, i.e. the stacking cycle time, depends on the cooling process. The ESR stochastic cooling system [12] is designed for a particle velocity corresponding to 400 MeV/u beams. Cooling in all three dimensions is provided within the band from 0.9 to 1.7 GHz. Measurements of the momentum spread by Schottky noise diagnostics showed that the injected beam had a momentum spread (full width at baseline) of  $1.3 \times 10^{-3}$  and was stochastically cooled down to  $6 \times 10^{-4}$  within 13 s.

## STACKING WITH FIXED BARRIER BUCKETS

Two sinusoidal BB pulses of  $T_B=200$  ns period shifted relative to each other by  $180^\circ$  were used to create the stretched rf potential (Fig.1).

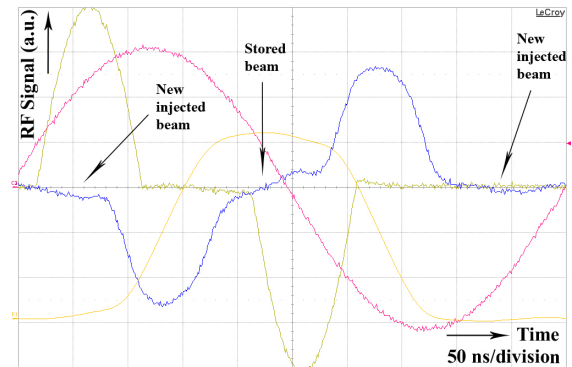


Figure 1: Realisation of fixed BB. Measured rf voltage pulse (blue line) and its potential with opposite sign (orange line). Applied BB voltage (yellow line). Carrier rf wave at  $h=1$  used to synchronise the SIS and ESR rf systems (magenta line).

Fig. 2 shows the  $^{40}\text{Ar}^{18+}$  signal measured in the ESR beam position monitor during the stacking and illustrates the experimental procedure. The after-pulses of the kicker pulse in Fig. 2 are due partly to real jitter and mostly to cable reflections on the signal line. Because of the jitter, the kicker pulse overlaps in time with the tail of the stack. This leads to transverse heating of the particles in the stack and to beam loss from the stack at every injection.

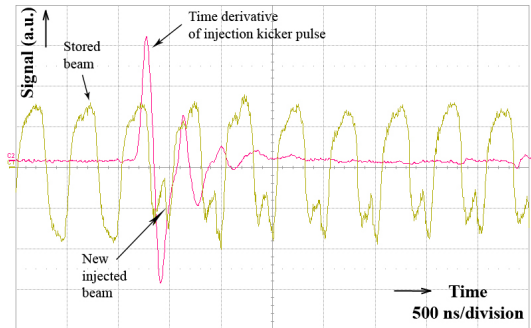


Figure 2: Signals (arbitrary units) of the stored beam at saturation intensity of 0.25 mA and of the injected bunch. The measured time-derivative of the injection kicker pulse is also shown but is not correlated to the beam signal because of different cable delays. The difference between the max. and the min. of the kicker pulse corresponds to  $\sim 3$  flattop=180 ns.

The increase of beam intensity in the ESR during the stacking was measured with the dc beam current transformer. An example is shown in Fig. 3. The losses induced to the tails of the stack by the jitter of the kicker at every injection were observed as follows: After reaching the saturation intensity, the transfer of beam from the SIS was stopped, but operation of the ESR injection kicker continued (Fig. 3).

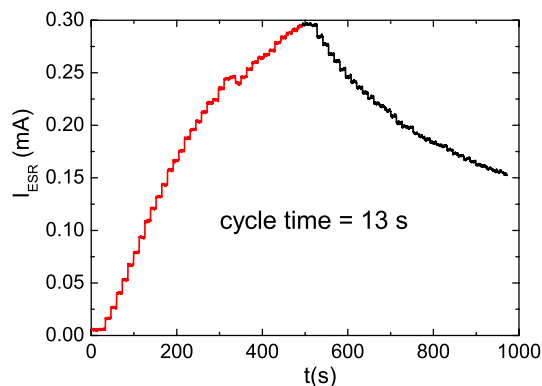


Figure 3: Stacking by fixed BB and antistacking, i.e. kicker operation without injection of new beam, in the ESR. Stochastic cooling continuously applied. A beam current of 0.4 mA corresponds to  $7 \times 10^7$   $^{40}\text{Ar}^{18+}$  ions at 400 MeV/u in the ESR.

In the present case, the main reason for the saturation of the stacked beam current is the following: Within the short time  $T_{rev}=507$  ns, some overlapping of the BB pulses and Other methods of phase space manipulation

of the kicker pulse with the tails of the stacked beam could not be avoided. As the stored beam current and the corresponding bunch length of the stack increase, the particle losses from the stack due to these overlaps also grow, until a saturation is reached.

Fig. 4 shows a qualitative investigation of the cooling performance. Fig. 5 illustrates the importance of good horizontal cooling (in addition to longitudinal and vertical). Without horizontal cooling the horizontal emittance grows because of the disturbance from (i) the injection kicks and (ii) the longitudinal correcting kicks since the longitudinal stochastic cooling kicker is located at high dispersion in the ESR ( $D \approx 6$  m).

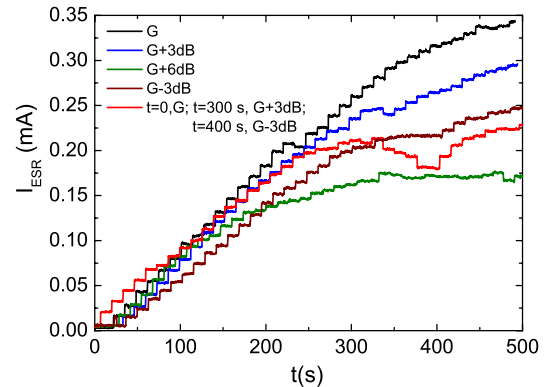


Figure 4: Stochastic cooling performance during stacking with fixed BB, for different gain values relative to an initial value G.

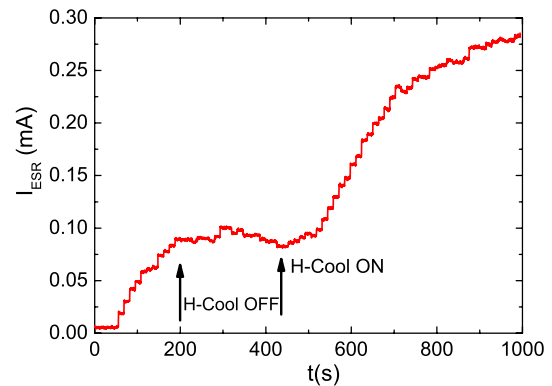


Figure 5: Role of the horizontal stochastic cooling during stacking with fixed BB.

## PROCEDURE WITH MOVING BARRIER BUCKETS

In this scheme, two BB pulses are adiabatically introduced into the cooled coasting beam. One stays stationary while the other is shifted in phase during 0.9 s to compress the beam. At  $t \approx 1.7$  s a new bunch is injected into the gap between the barriers and subsequently debunches because the voltage is not sufficient to capture the particles. Then, the BB pulses are switched off adiabatically, while the beam is being continuously cooled. For 120 V BB voltage, the bucket height  $2\delta_B = 5 \times 10^{-4}$  was not sufficient to maintain the cooled stack with  $\Delta p/p = 6 \times 10^{-4}$  during

the compression (although the moving of the buckets was adiabatic w.r.t. the synchrotron motion of the stack, which occurs at a rate  $\Delta f/f = \eta \Delta p/p \approx 2 \times 10^{-4}$ ). Thus, particles from the stack remained in the gap, got lost at every new injection and no accumulation could be observed. Application of additional electron cooling (at electron beam density of  $6 \times 10^6 \text{ cm}^{-3}$ ) further reduced the momentum spread of the stack, making accumulation possible (Fig. 6).

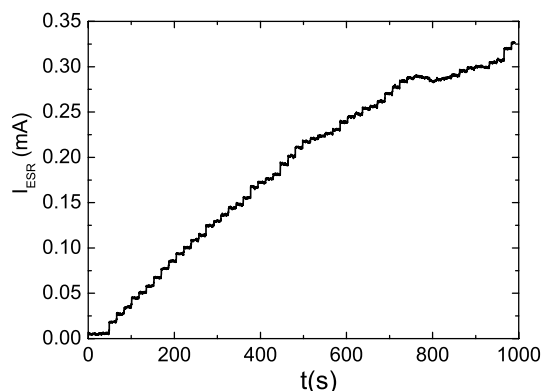


Figure 6: Stacking in the ESR using moving BB. Stochastic and electron cooling continuously applied.

### STACKING WITH THE $H=1$ RF

In this scheme, the standard ESR rf cavity provided higher voltage and thus higher saturation intensities have been reached. Two cases of rf manipulation have been tested, yielding qualitatively similar results: (i) continuous application of the  $h=1$  sine wave i.e. continuous cooling into the bucket and multiple injections onto the unstable fixed point; (ii) isoadiabatic bunching of the beam within 0.2 s, holding the rf voltage constant for 1.3 s in order to cool into the bucket and receive the new bunch on the unstable fixed point, abrupt (within 50  $\mu\text{s}$ ) switching-off the rf voltage to merge the two beam components. Fig. 7 shows the accumulation curves obtained with the procedure (ii).

The option of stacking with the  $h=1$  rf may be advantageous since a longer injection kicker pulse can be used than in the BB schemes. This guarantees high injection efficiency if the incoming bunch is long w.r.t. the ring circumference.

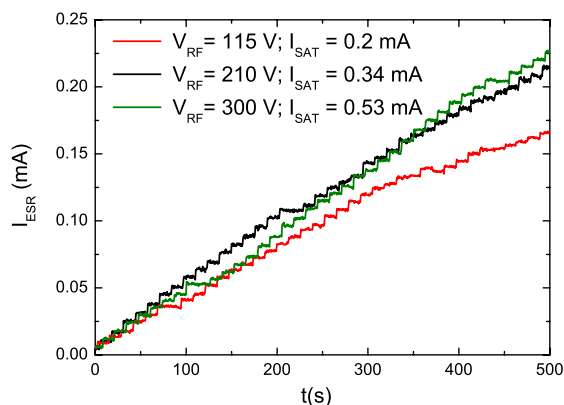


Figure 7: Stacking in the ESR using the  $h=1$  rf. Saturation intensity reached for different peak voltages.

Other methods of phase space manipulation

## CONCLUSIONS AND OUTLOOK

If the revolution period of the beam is long, e.g. for lower beam velocity or for a long ring like the HESR, the injected bunch, the stack, the BB pulses and the injection kicker pulse can be well-separated. Then, the accumulation will continue until the momentum spread of the stack as determined by the equilibrium between stochastic cooling and intrabeam scattering fills the available rf bucket height. An additional limiting factor is the onset of instabilities. These effects have been quantitatively studied in the case of stacking combined with electron cooling in the ESR [13].

For realistic future operation of the longitudinal stacking mode in the ESR, it is planned to install a new dedicated BB cavity, providing a voltage up to 2 kV. Depending on the injection energy, stochastic or electron cooling will support the stacking. Thus, the intensity of low-abundant rare isotope beams can be effectively increased, as requested by in-ring experiments.

The experimental results at the ESR demonstrate the principle and feasibility of the stacking methods. They indicate how the expected luminosity in the HESR will be a trade-off between accumulated intensity, duty cycle and phase space quality. In this respect, flexibility in the choice of the stacking method should be foreseen. These results can be extrapolated to set or confirm the requirements for the HESR systems, namely, (i) faster stochastic cooling or cooling of higher number of particles (larger bandwidth), (ii) a BB cavity with 2 kV peak voltage with the option to operate as  $h=1$  rf system, (iii) an adjustable injection kicker pulse and (iv) powerful beam diagnostics.

## REFERENCES

- [1] FAIR Baseline Technical Design Report, GSI (2006).
- [2] M. Steck et al., PAC'09, Vancouver, Canada, FR1GRI03 (2009). <http://www.jacow.org>.
- [3] R. Maier et al., PAC'11, New York, USA, THOCN2 (2011).
- [4] H. Stockhorst et al., IPAC'11, San Sebastian, Spain, THPS003 (to be published) (2011).
- [5] I. N. Meshkov et al., these proceedings, MOIO02 (2011).
- [6] C. M. Bhat, EPAC'04, Lucerne, Switzerland, THOBCH03 (2004).
- [7] H. Herr, Möhl, Workshop on cooling of high energy beams, Madison, USA, p.41 (1978) and CERN-EP-Note-79-34 (1979).
- [8] B. Franzke, NIM B 24/25, p.18 (1987).
- [9] C. Dimopoulou et al., EPAC'08, Genoa, Italy, THPP048 (2008).
- [10] T. Katayama et al., these proceedings, TUPS19 (2011).
- [11] G. Schreiber, Ph.D. Thesis, Frankfurt University (2006).
- [12] F. Nolden et al., EPAC'98, p.1052 (1998) and EPAC'00, p.1262 (2000).
- [13] C. Dimopoulou et al., COOL'07, Bad Kreuznach, Germany, MOM2C05 (2007).

# THE NONLINEAR TRANSFORMATION OF AN IONS BEAM IN THE PLASMA LENS\*

A.Drozdowskiy, N.Alexeev, S.Drozdowskiy, A.Golubev,  
Yu.Novozhilov, P.Sasorov, S.Savin, V.Yanenko. ITEP, Moscow, Russia

## Abstract

The plasma lens can carry out not only sharp focusing of ions beam. At those stages at which the magnetic field is nonlinear, formation of other interesting configurations of beams is possible. Plasma lens provides formation of hollow beams of ions. Application of the several plasma lenses allow to get a conic and a cylindrical beams. The plasma lens can be used for obtaining a beams with homogeneous spatial distribution. Calculations and measurements were performed for a  $C^{+6}$  and  $Fe^{+26}$  beams of 200-300 MeV/a.u.m. energy. The obtained results and analysis are reported.

## INTRODUCTION

The ion beam focusing in the plasma lens is carried out as shown in Fig.1. The discharge current produces an azimuthal magnetic field. The ions are injected along the lens axis, and the radial Lorentz force focuses the ion beam [1].

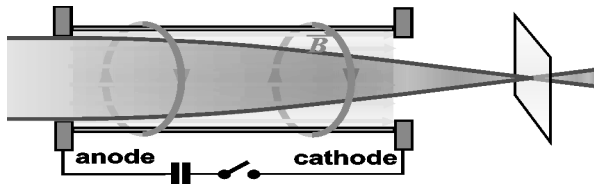


Figure 1: Ion focusing in a plasma lens.

In the current generator (Table 1) cold-hollow cathode

Table 1: Features of discharge current generator

Short pulse mode	
Switch (2 pcs)	Thyratron TDI1-150/25
Discharge current pulse duration	$T = 5 \mu\text{s}$ at $C = 25 \mu\text{F}$
Max discharge current	$I = 200 \text{ kA}$ at $T = 5 \mu\text{s}$
Long pulse mode	
Switch (2 pcs)	Thyratron TDI1-200k/25H
Discharge current pulse duration	$T = 20 \mu\text{s}$ at $C = 160 \mu\text{F}$
Max. discharge current	$I = 400 \text{ kA}$ at $T = 20 \mu\text{s}$

thyratrons (pseudospark switches) TDI1-200k/25H [2] are employed to form a stable discharge with peak current

\* Work supported by the Russian Fed. Min. of Education and Science

up to 250 kA. TDI-thyratrons in plasma lens generator avails to operate in a mode of long energy-intensive pulse. The time sweep of the luminosity of the plasma and the discharge current for short pulse mode and long pulse mode are shown on Fig. 2 and 3.

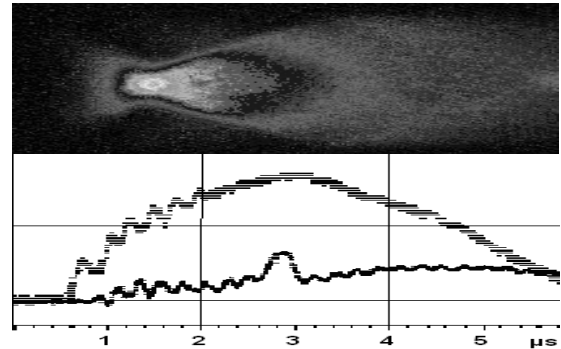


Figure 2: Time scanning of a discharge luminescence and a discharge and beam currents for short pulse mode.

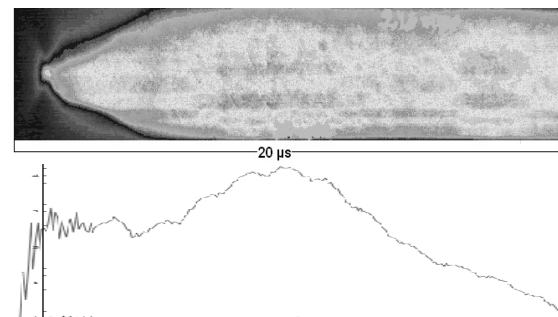


Figure 3: Time scanning of the discharge luminescence and current for long pulse mode.

Hamped shape of the long current due to the fact that part of the capacity ( $25 \mu\text{F}$ ) have low self-inductance. The focusing properties of plasma lenses depend on the current density distribution along the radius of the plasma discharge. The current distribution across the tube changes significantly during the discharge. Therefore, plasma lens, in general, is nonlinear. Uniform current distribution exists for a limited time, so the plasma lens, as a device for sharp focusing, operates for about  $1 \mu\text{s}$  or less. As a non-linear focusing device, the plasma lens can be used to produce beams of special shape. The researches were conducted on the follows parameters: the discharge tube radius  $R = 1 \text{ cm}$  and its length  $L = 10 \text{ cm}$ ,

argon pressure – 1-8 mbar, the ion beam duration – 300ns.

### FORMATION OF THE HOMOGENEOUS BEAM

Usage of ions beams for irradiation of various objects, in particular, in medical purposes, demands creation of a homogeneous field of an irradiation. The initial beam, as a rule, has the gaussian distribution. For alignment irradiation fields use the special filters-absorbers. This solution spoils however quality of irradiation fields and essentially reduces efficiency of beams. The solution of this problem is possible by means of the nonlinear focusing device. A simulation were conducted for to research opportunities of plasma lenses to solve this problem. It appears that it is possible to get homogeneous distribution of ion density for a case of equilibrium distribution of a discharge current. At enough large duration of a current pulse of >10 μs, current distribution is tending to equilibrium one. A similar distribution is the “quasibennett” distribution, was applied in the study of a high-current arc discharge [3]:

$$j = I(1 + \tilde{A}) / \pi R^2 (1 + \tilde{A} (r/R)^2)^2, \quad (1)$$

where  $R$  - plasma lens aperture,  $I$  discharge current. The value  $\tilde{A}$  is a function of the discharge current, the plasma temperature and the plasma conductivity.

The results of the first experiments (beam of ions  $C^{+6}$  with energy 300 MeV/n, current half-wave - 20 μs) are presented in Fig. 4 The density ions distribution was obtained by averaging of the scintillator luminosity over the angle around the beam axis.

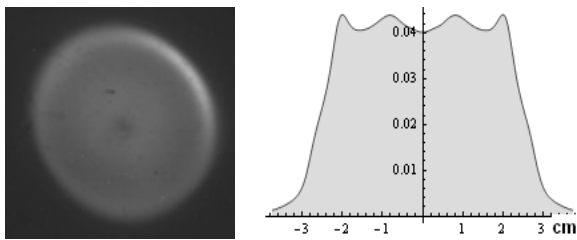


Figure 4: The light output from the scintillator and the density distribution of the ion  $C^{+6}$  at 8.5 μs after beginning of discharge at distances of 110 cm for current of 80 kA. The spot rms diameter is 40 mm.

The calculated distributions of density of ions in a beam of  $C^{+6}$  (300 MeV/n,  $z = 150$  cm) is shown on Fig.5. The initial distribution is adequate to the beam injected into the plasma lens. The transformed distribution was obtained in the plasma discharge which has the “quasibennett” distribution (1) where  $\tilde{A} = 0.85$ .

As we can see, transformation of a gaussian beam into a homogeneous can be carried out effectively, and with observance of the geometrical sizes demanded at a

medical irradiation: the size of a beam spot and drift distance behind the lens.

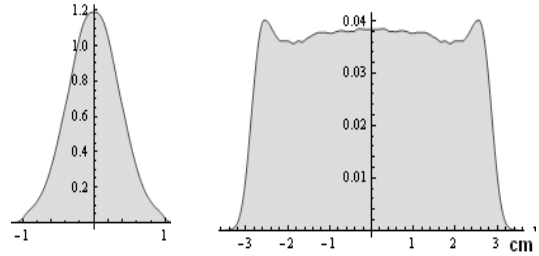


Figure 5: The initial and transformed distributions.

### FORMATION OF HOLLOW BEAMS

Hollow beams can be used for the implosion of thermonuclear targets [4]. Possibility of that transformation of ion beams has been demonstrated experimentally in GSI [5]. Researches carried out on the ITEP plasma lens confirmed this opportunities in a wide range of operating modes lens. [6].

Experimental results concerning formation of a hollow beam of small diameter, less than 1 cm, is shown on Fig.6.

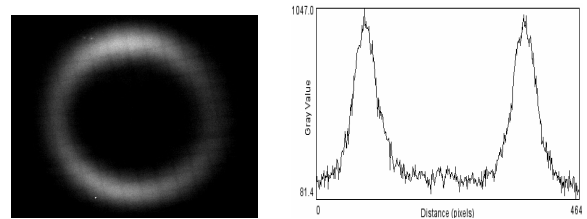


Figure 6: Light output from scintillator and the density distribution of ion  $Fe^{+26}$  at 1.7 μs after beginning of discharge at distances of 30 cm for current of 150 kA. The ring diameter is 9 mm.

The paraxial beam with zero emittance is converted to a tube beam, when the distribution of azimuthal magnetic field in the plasma lens is as follows

$$B = a + br, \quad (2)$$

where  $a$  and  $b$  - constants. This distribution takes place, when distribution of the discharge current density is a superposition of a homogeneous distribution and a singular one, inversely proportional to radius  $r$ :

$$j = I_o / \pi R^2 + I_s / 2\pi Rr \quad (3)$$

Here  $R$  - plasma lens aperture, within which there are a homogeneous current  $I_o$  and a singular one  $I_s$ . In this lens the ion beam is focused into a ring of radius

$$\rho = R I_s / I_o \quad (4)$$

at a distance

$$Z_o = R \mathcal{R} / B_o L, \quad (5)$$

where  $L$  - length of the lens and  $\mathcal{R}$  - rigidity of the beam of ions. Note that  $Z_o$  is equal to the focal length of the lens in the absence of a singular component of the current. The role of the latter is to create a independent from  $r$  component of the field, which causes the coherent deflection of ion trajectories on the angle  $\rho/Z$ . The picture of ions trajectories is shown in Fig. 7.

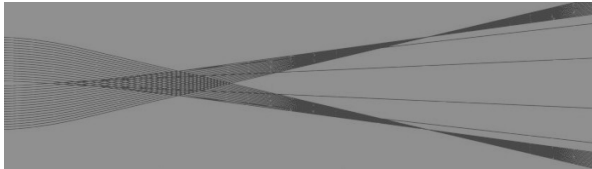


Figure 7: The picture of trajectories of a beam of ions

Our mathematical model gives (fig. 8) adequate ion beam distribution for the described experiment, if  $I_s/I_o = 0.3$ .

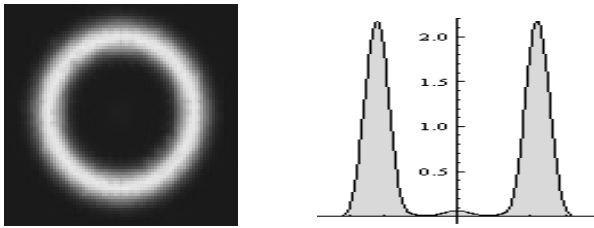


Figure 8: The light output from a scintillator and the distribution of ion  $Fe^{+26}$  density calculated in the model approximation for the experimental condition.

## TWO-STAGE BEAM TRANSFORMATION

Other possible application of a plasma lens is formation a converging conic beam by means of two plasma lens. In this case the problem of an irradiation of certain area is solved in such a way as to not affect the previous adjacent zone. The results of calculations for  $C^{+6}$  (200 MeV/n) beam was focused by two lenses are shown on Fig. 9.

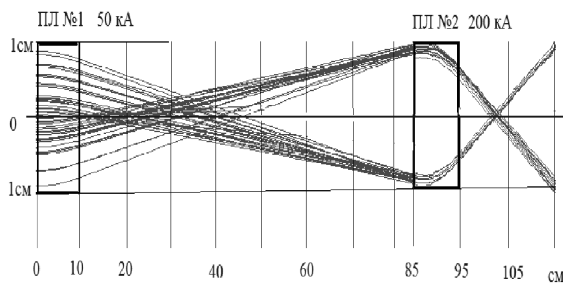


Figure 9: Formation a converging conic beam by means of two plasma lens.

In this case we used the distributions of a discharge currents of close to real ones. We can see that it is possible to get a conic beam and, as a special case, cylindrical one.

## CONCLUSION

The plasma lens can carry out not only sharp focusing of ion beam with considerable reduction sizes of focal spot. At those stages of the plasma discharge at which the magnetic field is nonlinear, formation of other interesting configurations of beams is possible.

The plasma lens can be used for transformation of beams with gaussian distribution of particles density in a beams with homogeneous spatial distribution.

The plasma lens provides formation of hollow beams in a wide range of parameters that allows to consider it as a possible variant of a terminal lens for realization of inertial thermonuclear synthesis.

Application of the several plasma lenses which are in different stages of the plasma discharge, presumes to create some special spatial configurations of ions beams.

Thus, the plasma lens essentially represents the universal device is able to form beams for scientific and technical applications.

## REFERENCES

- [1] E.Bogdash, M.Dornik, D.H.H.Hoffmann, M.de Magistris, W.Laux, A.Tauschwitz, H.Wetzler IEEE Trans. on Plasma Sci. 23, 388-392 (1995).
- [2] V.A.Gribkov, M.Scholz, V.D.Bochkov, A.V.Dubrovsky, R.Miklaszewski, L.Karpinski, S.Lee, Pseudosparks in nanosecond range of its operation: firing, jitter, and disconnection, Journal of Physics D: Appl. Phys. 37 (2004) 2107-2111.
- [3] P.C.Thonemann and W.T.Cowling, The Role of the Self Magnetic Field in High Current Gas Discharges, Proc. Phys. Soc., 64, 345 (1951).
- [4] N.Alexeev, M.Churazov, A.Golubev, D.Koshkarev, B.Sharkov, P.Zenkevich, "Heavy ion fusion energy program in Russia", Nucl. Instr. and Methods in Phys. Res. Sec.A: , 464 (2001), 1-3, pp. 1-5.
- [5] U.Neuner, R.Bock, C.Constantin, D.Hoffmann, M.Geeissel, J.Jacoby, A.Kozyreva, M.Roth, N.Tahir, A.Tauschwitz, and D.Varentsov, "Shepping of intence ion beams into hollow cilindrical form", Phys. Rev. Lett. 85, 4518, (2000).
- [6] A.Drozдовskiy, N.Alexeev, S.Drozдовskiy, A.Golubev, S.Savin, B.Sharkov, V.Yanenko, "Investigation of the formation of a hollow beam in the plasma lens", IPAC'10, Kioto, <http://cern.ch/AccelConf/IPAC10/MOPE040>.
- [7] A.Drozдовskiy, A.Golubev, B.Sharkov, S.Drozдовskiy, A.V.Yanenko, Formation of Hollow Heavy Beams in Plasma Lens, Physics of Particles and Nuclei Letters, 2010, Vol. 7, No. 7, pp. 534-538

# DECELERATION OF CARBON IONS AT THE HEAVY ION STORAGE RING TSR

S. Artikova, M. Grieser, J. Ullrich, A. Wolf

Max-Planck-Institut für Kernphysik, Saupfercheckweg 1, 69117 Heidelberg, Germany

## Abstract

To evaluate the beam quality obtained after deceleration of  $^{12}\text{C}^{6+}$  ions at the heavy ion Test Storage Ring (TSR), considering the possible sources of beam heating is important. In our experiments at the TSR, we inject  $^{12}\text{C}^{6+}$  ions at 73.3 MeV and decelerate them to 9.7 MeV in a cycle that includes two steps in which beam cooling is applied. In this study we discuss the influences of intrabeam scattering (IBS) on the circulating ions during deceleration. We additionally present results on the deceleration efficiency and lifetime measurements of  $^{12}\text{C}^{6+}$  ions in the energy range 9.7 - 73.3 MeV .

## INTRODUCTION

The heavy ion storage ring TSR, at the Max-Planck-Institut für Kernphysik (MPIK) in Heidelberg, operates for accelerator, atomic and molecular physics experiments. The storage ring has a circumference of 55.42 m, and it receives heavy ions from a 12 MV tandem van-de-Graaff and a normal conducting RF linac combination. Light positive ions and negative ions with mass to charge ratio  $\frac{A}{|q|} \leq 9$  are provided by a high current injector. At TSR the experiments mainly performed at the injection energy. In addition, the widely tunable range of the RF resonator enables the possibility to accelerate and decelerate ions. To ramp the magnetic fields at TSR, Digital-Analog Converter(DAC) and DSP driven synthesizer cards developed by MPIK. The generated functions to ramp the magnetics can be calculated from the rigidity by assessing the measured saturation effects of the TSR magnets. With some minor additional corrections to the calculated dipole magnets ramp and one quadrupole family ramp, decelerating a  $^{12}\text{C}^{6+}$  ion beam from 73.3 MeV to 9.7 MeV, corresponding to a rigidity decrease from 0.71 Tm to 0.26 Tm is possible. In the deceleration process, an increase of bunch length, momentum spread and beam emittance occurs. To avoid beam loss during deceleration due to these effects, electron pre-cooling of the injected bunched ion beam is necessary.

## INTRABEAM SCATTERING EFFECTS DURING DECELERATION

To decelerate a heavy ion beam, cooling at the injection energy is required, resulting in a dense ion beam such that IBS effects must be considered. Immediately before starting the deceleration cycle, electron cooling is switched off and the ion beam sizes increase due to IBS. The blow up rate of a bunched beam due to IBS can be expressed by [1]:

$$\frac{1}{\sigma_i} \frac{d\sigma_i}{dt} = c_i \cdot \frac{Z^4 N}{A^2 \beta^3} \frac{1}{\epsilon_x \epsilon_y \Delta p/p \cdot h \cdot l_{eff}}, \quad (1)$$

where  $i$  ( $i=x,y,\frac{\Delta p}{p}$ ) corresponds to the horizontal, vertical and longitudinal coordinates of the beam.  $N$  is the number of ions with charge state  $Z$ , mass  $A$ , and velocity  $\beta$ . The number of bunches in the storage ring is  $h$  and  $l_{eff}$  is the effective bunch length.  $c_i$  are lattice dependent functions which depend slightly on the ion energy. The horizontal emittance and vertical emittance scales are computed as  $\epsilon_x \propto \sigma_x^2$ ,  $\epsilon_y \propto \sigma_y^2$ , where  $\sigma_x$  and  $\sigma_y$  are the horizontal and vertical beam widths, respectively. If in the IBS process  $\sigma_x$ ,  $\sigma_y$ , and the momentum spread  $\Delta p/p$ ,  $l_{eff}$  are proportional to each other as in  $\epsilon_x \epsilon_y l_{eff} \Delta p/p \propto \sigma_i^6$ , we obtain three uncoupled differential equations for all three degrees of freedom [2] [3]:

$$\frac{1}{\sigma_i} \frac{d\sigma_i}{dt} = \frac{D_i}{\sigma_i^\gamma}. \quad (2)$$

In simplified IBS model  $\gamma=6$  [3] for a bunched ion beam and the heating term:

$$D_i \propto c_i \frac{Z^4}{A^2} \frac{1}{\beta^3} \frac{N}{h}. \quad (3)$$

If the velocity of circulating the ion beam is not changed the solution of equation 2 is given by:

$$\sigma_i(t) = (\sigma_{i,0}^\gamma + \gamma D_i t)^\frac{1}{\gamma}, \quad (4)$$

where  $\sigma_{i,0}$  is the initial beam width. In figure 1, the measured horizontal beam width of a  $^{12}\text{C}^{6+}$  bunched ion beam at the injection energy of 73.3 MeV is shown as a function of time. For bunching, a resonator voltage of 186 V was applied. By fitting the experimental data, we obtained  $\bar{\gamma} = 5.9$ , which is approximately close to the theoretical value of  $\gamma = 6$ . As shown in figure 1, the horizontal profile can be described well with simplified IBS model if the ion beam velocity is constant. To investigate the velocity dependence of IBS we make the following ansatz for the heating term:

$$D_i(t) = \frac{\tilde{D}_i}{\beta^\kappa(t)}, \quad (5)$$

where  $\kappa=3$ . In the deceleration cycle the ion velocity is changed linearly:

$$\beta(t) = \beta_0 + \alpha t, \quad (6)$$

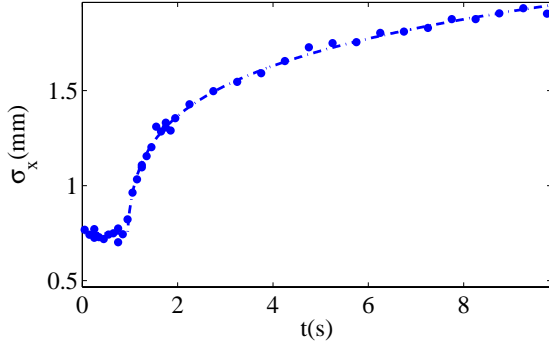


Figure 1: Measured horizontal beam width  $\sigma_x$  of a  $^{12}\text{C}^{6+}$  bunched ion beam (73.3 MeV,  $50\mu\text{A}$ ) as a function of time after 1.5 s. The dashed line through the data is a fit using equation 4 where  $\gamma$  is the fit parameter.

where  $\beta_0$  is the initial velocity of ions. The parameter  $\alpha$  can be determined as follows:

$$\alpha = (\beta_f - \beta_0)/T, \quad (7)$$

where  $T$  is ramping time and  $\beta_f$  is the final velocity of ions. To assess the beam width during deceleration the equation (2) can be solved with (5) and (6):

$$\sigma_i(t) = \left( \sigma_{i,0}^\gamma + \frac{\gamma \tilde{D}_i (\beta_0^{1-\kappa} - (\beta_0 + \alpha t)^{1-\kappa})}{\alpha(\kappa - 1)} \right)^{\frac{1}{\gamma}} \quad (8)$$

In figure 2, the experimental and computed horizontal beam width during deceleration as a function of time is shown. Computed  $\sigma_x$  from equation (8) for different values of  $\kappa$  are shown as red and green lines, measured  $\sigma_x$  are shown as colored dots. After injection, the ion beam was electron cooled, resulting in a horizontal beam width of  $\sigma_x = 0.65$  mm. At the time  $t=4$  s electron cooling was switched off and the ion beam was decelerated in 7 s to the final energy of 9.7 MeV. After reaching the final energy at  $t=11$  s, electron cooling was switched on again, yielding in fast reduction of the horizontal beam width  $\sigma_x$ . Because the IBS heating term  $D_i$  (in equation (3)) is higher at the final energy, the equilibrium beam width at 9.7 MeV is larger comparing to at the initial energy of 73.3 MeV. The heating term  $\tilde{D}_i$  and the parameter  $\gamma$  were both determined by the IBS measurement obtained at the initial energy of 73.3 MeV [3]. As displayed in figure 2, the computed  $\sigma_x$  values are below than the measured beam widths, especially at low velocities. Obviously, some term in equation (8) is missing to describe the real measured beam widths. From equation (8), the conclusion follows that the beam width for very weak intensities ( $\tilde{D}_i \rightarrow 0$ ) would be constant during deceleration, which is, however, not correct. Deceleration of beams can be described by Liouville's theorem, which postulates that the phase space area occupied by noninteracting particles is conserved during deceleration. Thus the theorem leads to an increase of the ion beam

Cooled beam dynamics

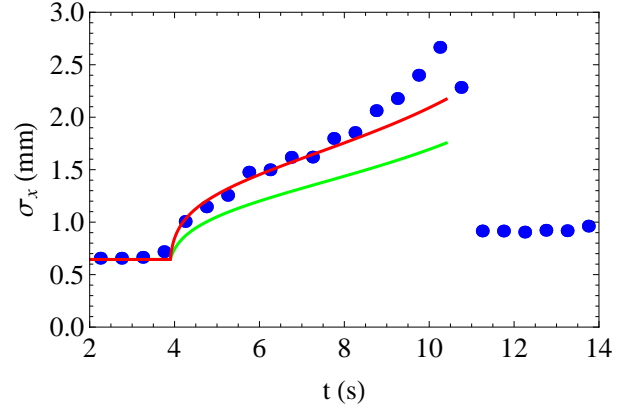


Figure 2: Experimental and computed horizontal beam width  $\sigma_x$  of a  $^{12}\text{C}^{6+}$  ion beam ( $28\mu\text{A}$ ) as a function of time during deceleration. Deceleration starts at  $t=4$  s. Two cooling steps were applied at  $t=0$  s and  $t=11$  s. The final energy is 9.7 MeV. The red and green lines are computed beam width with equation (8) for  $\kappa = 3.25$  and  $\kappa = 3$ , respectively.

size during deceleration even without any IBS effects. Accordingly, in the non-relativistic approach, the change of the ion beam size  $\sigma_i$  is given by:

$$\sigma_i(t) = \tilde{\sigma}_i \sqrt{\frac{\beta_0}{\beta(t)}}, \quad (9)$$

where  $\beta(t)$  is the ion velocity at the time  $t$  and  $\tilde{\sigma}_i$  is the beam width at  $t=0$  s. Equation (9) is the boundary value for  $\tilde{D}_i \rightarrow 0$  of the equation 8, for which we are looking. To consider IBS time dependent beam width  $\tilde{\sigma}_i$  in equation (9) will be replaced by the beam width  $\sigma_i(t)$  in equation (8):

$$\sigma_i(t) = \left( \sigma_{i,0}^\gamma + \frac{\gamma \tilde{D}_i (\beta_0^{1-\kappa} - \beta(t)^{1-\kappa})}{\alpha(\kappa - 1)} \right)^{\frac{1}{\gamma}} \sqrt{\frac{\beta_0}{\beta(t)}}. \quad (10)$$

According to equation (10), the beam width during deceleration was computed. The result is shown in figure 3 as a red line. The IBS heating term  $\tilde{D}_i$  and  $\gamma$  were determined at the injection energy of 73.3 MeV [3]. The equilibrium beam width  $\sigma_{i,0}$  was found from the measured beam widths between  $t=2-4$  s. As demonstrated in figure 3, the calculation of the beam width during deceleration using only IBS data, measured at the injection energy, is now consistent with the observation. As shown in the next section, the number of ions decreases slightly in the deceleration cycle, whereas this particle loss is not considered in equation (10). Further calculation shows that after taking into account the small particle loss during deceleration, there is no significant deviation to equation (10). Assuming the number of particles as a constant, for particle losses which less than 15%, approximating the measured beam width in deceleration cycle with equation (10) is possible.

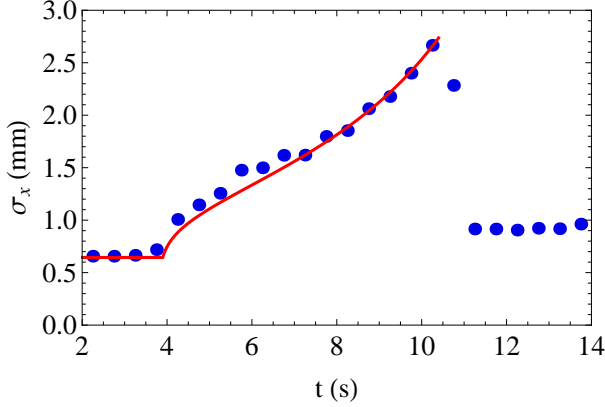


Figure 3: Development of  $\sigma_x$  of a  $^{12}\text{C}^{6+}$  ion beam ( $I=28 \mu\text{A}$ ) as a function of time during deceleration. Computed  $\sigma_x$  for  $\kappa = 3$  is shown as red line.

## DECELERATION EFFICIENCY

To obtain information about the ion loss in the deceleration cycle, the number of ions by measuring the voltage on a capacitive pick-up is determined. The integral of this signal over one RF period scales with the number of ions in the bunch [4]. Because several injections were needed to evaluate the ion number at different time in the deceleration cycle and since the injection intensity fluctuated in the range  $55 \pm 9 \mu\text{A}$ , measuring the number of particles at injection by determining the counting rate of the residual gas beam profile monitor was required. The ratio of the number of particles  $N(t)$  during the deceleration cycle and the number of particles  $N_0$  of the injected ions is shown in figure 4 as a function of time. Beam is injected at  $t=0$  s and electron pre-cooled for 1.5 s. Deceleration starts at  $t=1.5$  s and lasts 7 s. The final energy was achieved at  $t=8.5$  s. During deceleration of the beam the initial intensity was  $55 \pm 9 \mu\text{A}$  and the resonator voltage for bunching was 232.5 V. As shown in figure 4, a small, almost linear particle loss occurs. 83 % of the ions reach the final energy of 9.7 MeV. In the intensity range of  $8 \mu\text{A}$  -  $120 \mu\text{A}$  the  $\epsilon$  of the deceleration process was measured.  $\epsilon$  is defined as the ratio of the final number of particles  $N_f$ , reaching the final energy of 9.7 MeV, to the initial number of particles  $N_0$ :  $\epsilon = \frac{N_f}{N_0}$ . The results has no significant dependency on the injected ion intensity as shown in figure 5. Determined efficiency  $\bar{\epsilon}=87.5\%$  in the intensity range of  $8 \mu\text{A}$ - $120 \mu\text{A}$ .

## LIFETIME

Ion losses occur in the deceleration process. In order to compare these with those resulting from the ion interaction with the residual gas, lifetime measurements were performed in the energy rangy of 9.7-73.3 MeV. In these experiments the ion beam was injected and then decelerated to the various energies where the lifetimes were determined. In all measurements which are shown in figure 6 no Cooled beam dynamics

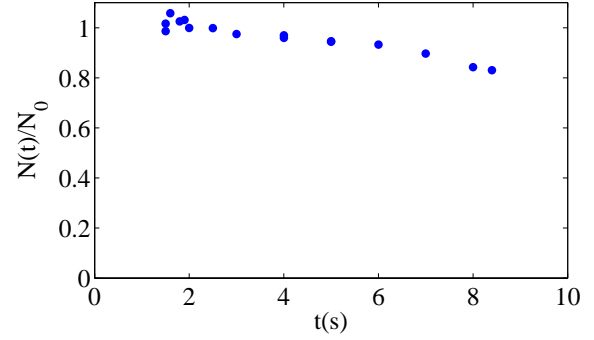


Figure 4: Measured number of particles  $N(t)$ , normalized to the injected particle number  $N_0$ , during deceleration of a  $^{12}\text{C}^{6+}$  ion beam from  $E=73.3$  MeV to  $E=9.7$  MeV. Deceleration starts at  $t=1.5$  s. At  $t=8.5$  s the final energy was reached.

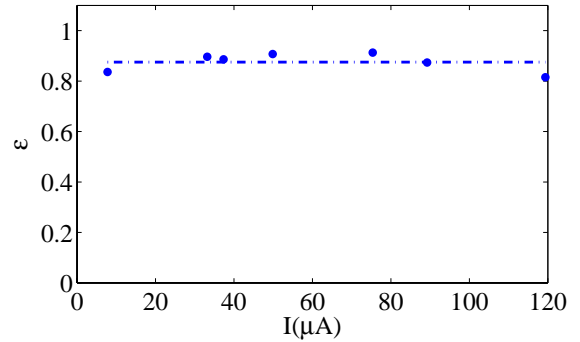


Figure 5: Measured deceleration efficiency as a function of the injected ion intensity.

electron cooling was applied. Obviously, the lifetime decreases with decreasing energy. For uncooled bare  $^{12}\text{C}^{6+}$  ions, we have to consider two loss mechanisms: multiple scattering and electron capture in the residual gas. The partial lifetime  $\tau$  of the beam with respect to a certain process is given by  $\tau^{-1} = \sigma \rho v$ , where  $\sigma$  is the relevant cross section,  $\rho$  the density of the residual gas atoms or molecules of atomic charge number  $Z_{gas}$ , and  $v$  the ion velocity. Because of the loss cross section for electron capture in the residual gas scales with a power of about 4 of  $Z_{gas}$ , the concentration of heavier atoms in the residual gas is most important for the lifetime of the beam. After bakeout of the storage ring to  $250^\circ$ , the residual gas composition is of typically 93 % hydrogen. Other molecules contain 2 % carbon, 1 % nitrogen 6 % oxygen and the heaviest component is 0.3% argon. In figure 6, the partial lifetimes of electron capture and multiple scattering are shown as blue and green dashed lines, respectively, both calculated for  $p=7 \cdot 10^{-11}$  mbar. The total lifetime of these resulting from two processes is displayed with a solid red line. As indicated in figure 6, multiple scattering dominates at higher energies of 70 MeV and at low energies around 10 MeV electron capture is the determining process for the final energy of 9.7 MeV when the lifetime has the minimum value

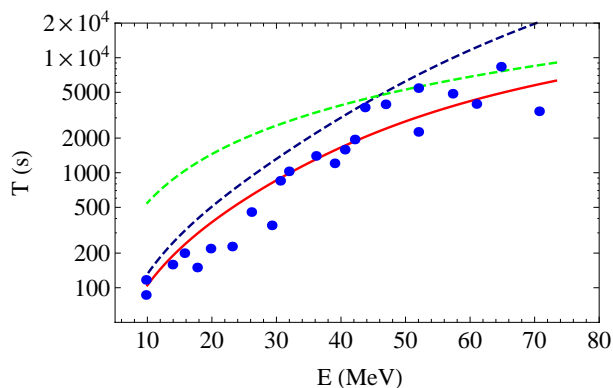


Figure 6: Measured lifetime of the  $^{12}\text{C}^{6+}$  beam for different energies. The green dashed line is the lifetime taken into account multiple scattering, whereas the blue dashed line represents the electron capture lifetime. The red solid line is the total lifetime calculated for  $p=7 \cdot 10^{-11}$  mbar.

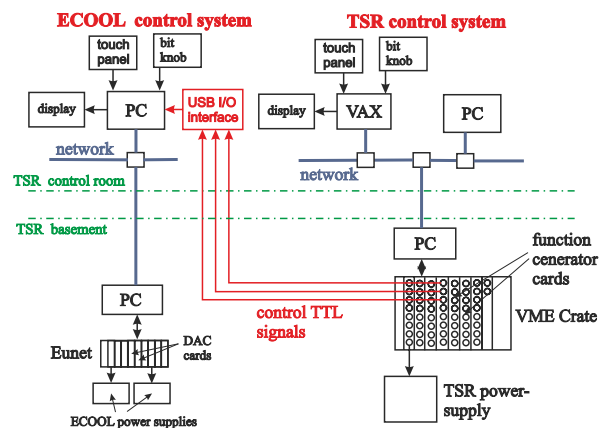


Figure 7: Schematic drawing of the TSR and ECOOL control system modification to enable electron cooling at various energies in the deceleration cycle.

of about 100 s was measured. Consequently, the losses during the deceleration time of 7 s coming from the interaction with the residual gas much less than 1 % and are, thus negligible.

## MODIFICATION OF THE CONTROL SYSTEM

In the deceleration cycle, at least two cooling steps at the initial and final energy, when the experiment takes place, are necessary. This means the electron cooler has to operate at different settings during the deceleration cycle, requiring an extension of the electron cooler control system. To enable a cooler operation at different settings a USB I/O card is added to the ECOOL user interface computer (compare figure 7), containing the database of the electron cooler settings. The I/O card is connected via an USB bus

with the ECOOL computer. An additional three control cables connect the I/O card with three function generators of the TSR control system. Those create the ramps controlling the TSR power supplies and three TTL control signals for the ECOOL computer. If one of the three control signals changes its value, the ECOOL computer loads a new data base, according to the TTL values of the three control signals. Eight different data bases of the electron cooler settings can be loaded because 3 digital control signals are used.

## CONCLUSION

Experiments to decelerate  $^{12}\text{C}^{6+}$  ions from 73.3 MeV to 9.7 MeV (1 MeV/u), which corresponds to a rigidity decrease from 0.71 Tm to 0.26 Tm, were conducted where a reduction of the beam energy was by a factor of  $> 7$ . To achieve an efficiency of 87.5% from deceleration, an electron pre-cooling is required. The cooling results in a dense ion beam where IBS effects have to be taken into account to describe the development of the ion beam width during deceleration. We proposed the approximated equation (10) to explain the beam width during the deceleration process which is consistent with the observation.

## REFERENCES

- [1] M. Martini, CERN PS/84-9(AA) (1984).
- [2] M. Beutelspacher, M. Grieser, K. Noda, D. Schwalm, A. Wolf, Dispersive Electron Cooling Experiments at the Heavy ion Storage Ring TSR. NIM A 512 (2003) 459-469.
- [3] S. Artikova, M. Grieser, J. Ullrich. Investigation of intrabeam scattering in the heavy ion storage ring TSR, proceeding of IPAC11, 2011.
- [4] M. Grieser, S. Artikova, K. Blaum, F. Laux, J. Ullrich. Beam current measurements at the TSR Heidelberg, proceeding of IPAC11, 2011.

## List of Authors

*Italic* papercodes indicate primary authors

### — A —

Agapov, N. N. *TUPS11*  
 Ahmanova, E. V. *TUPS02*, *TUPS09*, *TUPS13*  
 Alexeev, N. N. *TUPS21*  
 Alinovsky, N. *THIOA02*  
 Artikova, S. T. *TUPS22*  
 Asfandiyarov, R. *TUIOA01*, *TUIOA02*  
 Aulenbacher, K. *TUPS12*

### — B —

Batrakov, A. M. *THIOA02*  
 Bedareva, T. V. *THIOA02*  
 Bekhtenev, E. A. *THIOA02*  
 Belikov, O. V. *THIOA02*  
 Bell, G. I. *TUIOC02*  
 Belochitskii, P. *THIOC03*  
 Blaum, K. *WEIOB02*, *TUPS01*, *TUPS22*  
 Bocharov, V. N. *THIOA02*, *TUPS08*  
 Borodich, V. V. *THIOA02*  
 Bruhwiler, D. L. *TUIOC02*, *TUCOC01*  
 Bryzgunov, M. I. *MOIO05*, *THIOA02*, *TUPS06*,  
*TUPS07*, *TUPS08*, *TUPS10*  
 Buble, A. V. *THIOA02*, *TUPS06*, *TUPS07*,  
*TUPS08*, *TUPS10*

### — C —

Caspers, F. *TUCOB01*, *TUPS16*  
 Chai, W. P. *MOIO01*  
 Charman, A. E. *WEIOA01*  
 Chekavinskiy, V. A. *THIOA02*, *TUPS07*  
 Cheskidov, V. G. *THIOA02*

### — D —

Derbenev, Y. S. *TUIOC01*, *TUCOA01*  
 Dietrich, J. *MOIO04*, *MOIO05*, *TUPS03*,  
*TUPS05*, *TUPS12*  
 Dimopoulou, C. *TUIOB02*, *TUPS20*  
 Dolinskii, A. *TUIOB02*  
 Donets, D. E. *TUPS11*  
 Dorofeev, G. L. *TUPS11*  
 Dovzhenko, B. A. *THIOA02*  
 Drobin, V. M. *TUPS11*  
 Drozdovsky, A. A. *TUPS21*  
 Drozdovsky, S. A. *TUPS21*

### — E —

Eriksson, T. *THIOC03*  
 Erokhin, A. *THIOA02*  
 Eseev, M. K. *WECOB01*, *TUPS09*

### — F —

Fatkin, G. A. *THIOA02*  
 Fedotov, M. G. *THIOA02*, *TUPS08*  
 Fellenberger, F. *WEIOB02*  
 Filippov, A. A. *TUPS13*  
 Franzke, B. *TUPS20*  
 Froese, M. W. *WEIOB02*  
 Fujimoto, T. *MOIO06*

### — G —

Gladkikh, P. *TUPS17*, *TUPS18*  
 Golubev, A. *TUPS21*  
 Goncharov, A. D. *MOIO05*, *THIOA02*  
 Gorchakov, K. *THIOA02*  
 Gorda, O. E. *TUPS20*  
 Gosteev, V. K. *THIOA02*, *TUPS10*  
 Grieser, M. *MOIO06*, *WEIOB02*, *TUPS01*,  
*TUPS22*  
 Gusev, I. A. *THIOA02*, *TUPS07*

### — H —

Hao, Y. *TUIOC02*, *TUCOC01*  
 Hu, X. J. *TUPS14*

### — I —

Ivanov, A. V. *THIOA02*, *TUPS02*, *TUPS06*,  
*TUPS07*  
 Iwata, S. I. *MOIO06*

### — J —

Jia, H. *MOIO01*, *TUPS14*  
 Johnson, R. P. *TUCOA01*

### — K —

Kalamayko, A. A. *TUPS17*  
 Kamerdzhev, V. *MOIO05*, *TUPS03*  
 Karnaukhov, I. M. *TUPS17*  
 Karpov, G. V. *THIOA02*  
 Katayama, T. *TUIOB01*, *TUIOB02*, *TUCOB01*,  
*TUPS14*, *TUPS15*, *TUPS16*,  
*TUPS19*, *TUPS20*  
 Kikuchi, T. *TUPS19*  
 Kobets, A. G. *WECOB01*, *TUPS09*, *TUPS13*  
 Koisin, Y. I. *THIOA02*  
 Kondauron, M. N. *THIOA02*, *TUPS07*  
 Krantz, C. *WEIOB02*, *TUPS01*  
 Kruchkov, A. M. *TUPS06*  
 Kryuchkov, A. *THIOA02*  
 Kulikov, S. *TUPS11*  
 Kuznetsov, A. B. *THCOB01*

— L —

Lange, M. WEIOB02  
 Lehrach, A. MOIO04  
 Li, G. H. MOIO01  
 Li, J. MOIO01  
 Li, P. MOIO01  
 Lisitsyn, A. D. THIOA02  
 Litvinenko, V. TUIOC02, TUCOC01  
 Litvinov, Yu. A. TUPS01  
 Lokhmatov, V. I. TUPS09  
 Lopatkin, I. A. THIOA02  
 Lorentz, B. MOIO04, TUPS03

— M —

Ma, X. M. MOIO01  
 Maier, R. MOIO04  
 Malakhov, V. N. TUPS09  
 Mamkin, V. R. THIOA02  
 Mao, L. J. MOIO01, TUPS03, TUPS05  
 Mao, R. S. MOIO01  
 Maury, S. THIOC03  
 Medvedko, A. S. THIOA02  
 Meshkov, I. N. MOIO02, MOIO06, TUIOB01,  
 WECOB01, TUPS02, TUPS13,  
 TUPS20, THCOB01  
 Möhl, D. TUIOB02, TUPS20  
 Morozov, V. S. TUCOA01  
 Mytsykov, A. TUPS17

— N —

Nakao, M. MOIO06  
 Noda, A. MOIO06  
 Noda, K. MOIO06  
 Nolden, F. TUIOB02, TUCOB01, TUPS16,  
 TUPS19, TUPS20  
 Novozhilov, Yu. B. TUPS21

— O —

Okamoto, H. MOIO06

— P —

Panasyuk, V. M. MOIO05, THIOA02, TUPS07,  
 TUPS10  
 Papash, A. I. WECOA01  
 Parkhomchuk, V. V. MOIO05, THIOA02, THIOA03,  
 TUPS06, TUPS07, TUPS08,  
 TUPS10  
 Paul, K. TUIOC02  
 Pavlov, V. TUPS09  
 Penn, G. WEIOA01  
 Peschke, C. TUIOB02  
 Philippov, A. V. THCOB01  
 Pivin, R. TUPS02, TUPS11, TUPS13  
 Pogorelov, I. V. TUIOC02, TUCOC01

Poletaev, I. V. THIOA02  
 Polukhin, V. A. THIOA02  
 Prasuhn, D. MOIO04  
 Prost, L. R. THIOA01  
 Protopopov, A. Yu. THIOA02  
 Pureskin, D. N. TUPS07, THIOA02  
 Putmakov, A. A. TUPS07, THIOA02

— R —

Reiche, S. TUIOC02, TUCOC01  
 Repnow, R. TUPS01  
 Reva, V. B. MOIO05, THIOA02, THIOA03,  
 TUPS06, TUPS08, TUPS10,  
 TUPS07  
 Rudakov, A. Yu. WECOB01, TUPS02, TUPS09,  
 TUPS13

— S —

Sasorov, P. V. TUPS21  
 Savin, S. M. TUPS21  
 Schreiber, G. TUPS19, TUPS20  
 Schwartz, B. T. TUIOC02, TUCOC01  
 Schweikhard, L. WEIOB02  
 Semenov, E. P. THIOA02  
 Senkov, D. V. THIOA02, TUPS07  
 Sessler, A. WEIOA01  
 Shabunov, A. V. TUPS02, TUPS13  
 Shcherbakov, A. A. TUPS17, TUPS18  
 Shemyakin, A. V. THIOA01  
 Shibuya, S. MOIO06  
 Shirai, T. MOIO06  
 Shokin, V. I. TUPS02  
 Shornikov, A. WEIOB02  
 Sidorin, A. A. TUPS09  
 Sidorin, A. O. TUPS02, TUPS20  
 Skorobogatov, D. N. MOIO05, THIOA02, TUPS07  
 Smirnov, A. V. MOIO06, WECOA01, TUPS02,  
 TUPS11, TUPS13  
 Song, M. T. MOIO01  
 Souda, H. MOIO06  
 Stassen, R. MOIO04, TUPS15, TUPS20  
 Steck, M. MOIO03, TUIOB02, TUPS19,  
 TUPS20  
 Stein, H.-J. TUPS03  
 Stockhorst, H. MOIO04, TUPS15, TUPS19,  
 TUPS20  
 Syresin, E. MOIO06

— T —

Telegin, Y. N. TUPS17  
 Thorndahl, L. TUIOB02, TUPS15, TUPS16  
 Tongu, H. MOIO06  
 Topilin, N. D. TUPS02, TUPS13  
 Tranquille, G. THIOC03  
 Trubnikov, G. V. MOIO07, TUIOB01, TUPS11,

Tumanova, Yu. A. **TUPS20**  
**TUPS02**, **TUPS13**

— U —

Ullrich, J. **TUPS22**

— V —

von Hahn, R. **WEIOB02**

— W —

Wang, G. **TUIOC02**, **TUCOC01**  
Weilbach, T. **TUPS12**  
Welsch, C. P. **WECO A01**  
Wolf, A. **WEIOB02**, **TUPS01**, **TUPS22**  
Wu, J. X. **TUCOB01**, **TUPS14**, **TUPS16**  
Wurtele, J. S. **WEIOA01**

— X —

Xia, J. W. **TUCOB01**, **TUPS14**

— Y —

Yakovenko, S. **WECOB01**, **TUPS09**, **TUPS13**,  
**TUPS02**  
Yan, T. L. **MOIO01**  
Yanenko, V. V. **TUPS21**  
Yang, J. C. **MOIO01**  
Yang, X. D. **MOIO01**  
Yin, D. Y. **MOIO01**  
Yoshikawa, C. Y. **TUCOA01**  
Yuan, Y. J. **MOIO01**, **TUPS14**

— Z —

Zapiatkin, N. P. **THIOA02**  
Zelinsky, A. Y. **TUPS17**  
Zhang, W. **MOIO01**  
Zhang, X. H. **MOIO01**  
Zhang, Y. **TUCOB01**, **TUPS14**, **TUPS16**  
Zhao, T. C. **MOIO01**  
zheng, W. H. **MOIO01**  
Zolotorev, M. S. **WEIOA01**



## Institutes List

### AEC

Chiba

- Fujimoto, T.
- Iwata, S. I.
- Shibuya, S.

### Allrussian Electrotechnical Institute

Moskow

- Filippov, A. A.

### BINP SB RAS

Novosibirsk

- Alinovsky, N.
- Batrakov, A. M.
- Bedareva, T. V.
- Bekhtenev, E. A.
- Belikov, O. V.
- Bocharov, V. N.
- Borodich, V. V.
- Bryzgunov, M. I.
- Bubley, A. V.
- Chekavinskiy, V. A.
- Cheskidov, V. G.
- Dovzhenko, B. A.
- Erokhin, A.
- Fatkin, G. A.
- Fedotov, M. G.
- Goncharov, A. D.
- Gorchakov, K.
- Gosteev, V. K.
- Gusev, I. A.
- Ivanov, A. V.
- Karpov, G. V.
- Koisin, Y. I.
- Kondaurou, M. N.
- Kruchkov, A. M.
- Kryuchkov, A.
- Lisitsyn, A. D.
- Lopatkin, I. A.
- Mamkin, V. R.
- Medvedko, A. S.
- Panasyuk, V. M.
- Parkhomchuk, V. V.
- Poletaev, I. V.
- Polukhin, V. A.
- Protopopov, A. Yu.
- Pureskin, D. N.
- Putmakov, A. A.
- Reva, V. B.
- Semenov, E. P.
- Senkov, D. V.
- Skorobogatov, D. N.
- Zapiatkin, N. P.

### BNL

Upton, Long Island, New York

- Hao, Y.

- Litvinenko, V.

- Wang, G.

### CERN

Geneva

- Belochitskii, P.
- Caspers, F.
- Eriksson, T.
- Maury, S.
- Möhl, D.
- Thorndahl, L.
- Tranquille, G.

### DPNC

Genève

- Asfandiyarov, R.

### Ernst-Moritz-Arndt-Universität

Greifswald

- Schweikhard, L.

### FZJ

Jülich

- Dietrich, J.
- Kamerdzhev, V.
- Lehrach, A.
- Lorentz, B.
- Maier, R.
- Mao, L. J.
- Prasuhn, D.
- Stassen, R.
- Stein, H.-J.
- Stockhorst, H.

### Fermilab

Batavia

- Prost, L. R.
- Shemyakin, A. V.

### GSI

Darmstadt

- Dimopoulou, C.
- Dolinskii, A.
- Franzke, B.
- Gorda, O. E.
- Katayama, T.
- Nolden, F.
- Peschke, C.
- Schreiber, G.
- Steck, M.

### HIM

Mainz

- Weilbach, T.

**HU/AdSM**

Higashi-Hiroshima

- Okamoto, H.

**IKP**

Mainz

- Aulenbacher, K.

**IMP**

Lanzhou

- Chai, W. P.
- Hu, X. J.
- Jia, H.
- Li, G. H.
- Li, J.
- Li, P.
- Ma, X. M.
- Mao, L. J.
- Mao, R. S.
- Song, M. T.
- Wu, J. X.
- Xia, J. W.
- Yan, T. L.
- Yang, J. C.
- Yang, X. D.
- Yin, D. Y.
- Yuan, Y. J.
- Zhang, W.
- Zhang, X. H.
- Zhang, Y.
- Zhao, T. C.
- zheng, W. H.

**ITEP**

Moscow

- Alexeev, N. N.
- Drozdovsky, A. A.
- Drozdovsky, S. A.
- Golubev, A.
- Novozhilov, Yu. B.
- Sasorov, P. V.
- Savin, S. M.
- Yanenko, V. V.

**JINR**

Dubna, Moscow Region

- Agapov, N. N.
- Ahmanova, E. V.
- Donets, D. E.
- Drobin, V. M.
- Eseev, M. K.
- Kobets, A. G.
- Kulikov, S.
- Lokhmatov, V. I.
- Malakhov, V. N.
- Meshkov, I. N.
- Pavlov, V.
- Pivin, R.

- Rudakov, A. Yu.
- Shokin, V. I.
- Sidorin, A. A.
- Sidorin, A. O.
- Smirnov, A. V.
- Syresin, E.
- Topilin, N. D.
- Trubnikov, G. V.
- Tumanova, Yu. A.
- Yakovenko, S.

**JINR/DLNP**

Dubna, Moscow region

- Meshkov, I. N.

**JINR/VBLHEP**

Dubna, Moscow region

- Kuznetsov, A. B.
- Philippov, A. V.
- Shabunov, A. V.

**JLAB**

Newport News, Virginia

- Derbenev, Y. S.
- Morozov, V. S.

**Kyoto ICR**

Uji, Kyoto

- Nakao, M.
- Noda, A.
- Souda, H.
- Tongu, H.

**LBNL**

Berkeley, California

- Penn, G.
- Sessler, A.
- Wurtele, J. S.
- Zolotarev, M. S.

**MPI-K**

Heidelberg

- Artikova, S. T.
- Blaum, K.
- Fellenberger, F.
- Froese, M. W.
- Grieser, M.
- Krantz, C.
- Lange, M.
- Litvinov, Yu. A.
- Papash, A. I.
- Repnow, R.
- Shornikov, A.
- Ullrich, J.
- Wolf, A.
- von Hahn, R.

**Muons, Inc**

Batavia

- Johnson, R. P.
- Yoshikawa, C. Y.

**NAFU**

Arkhangelsk

- Eseev, M. K.

**NIRS**

Chiba-shi

- Noda, K.
- Shirai, T.

**NSC/KIPT**

Kharkov

- Gladkikh, P.
- Kalamayko, A. A.
- Karnaukhov, I. M.
- Mytsykov, A.
- Shcherbakov, A. A.
- Telegin, Y. N.
- Zelinsky, A. Y.

**Nagaoka University of Technology**

Nagaoka, Niigata

- Kikuchi, T.

**PSI**

Villigen

- Reiche, S.

**RRC**

Moscow

- Dorofeev, G. L.

**Tech-X**

Boulder, Colorado

- Bell, G. I.
- Bruhwiler, D. L.
- Paul, K.
- Pogorelov, I. V.
- Schwartz, B. T.

**The University of Liverpool**

Liverpool

- Welsch, C. P.

**UCB**

Berkeley, California

- Charman, A. E.

## Participants list

Akhmanova E.	Russia	JINR, Dubna
Asfandiyarov R.	Switzerland	University of Geneva, DPNC
Aulenbacher K.	Germany	Institut fuer Kernphysik der Johannes Gutenberg-Universitaet zu Mainz
Bruhweiler D.	USA	Tech-X Corporation, Boulder, Colorado
Bryzgunov M.	Russia	BINP, Novosibirsk
Bubley A.	Russia	BINP, Novosibirsk
Dietrich J.	Germany	FZ Juelich
Dimopoulou C.	Germany	GSI
Dorofeev G.	Russia	RRC "Kurchatov Institute"
Drozdovskiy A.	Russia	ITEP
Eriksson T.	Switzerland	CERN
Eseev M.	Russia	Northern (Arctic) Federal University, Arkhangelsk
Gladkikh P.	Ukraine	NSC KIPT, Kharkov
Hangst J.	Denmark	Aarhus University
Johnson R.	USA	Muons, Inc.
Kamerdzhev V.	Germany	FZ Juelich
Katayama T.	Germany	GSI
Kobets A.	Russia	JINR, Dubna
Kuzin M.	Russia	BINP, Novosibirsk
Mao L.	Germany	FZ Juelich; IMP Lanzhou
Matyukhina O.	Russia	JINR, Dubna
Meshkov I.	Russia	JINR, Dubna
Moehl D.	Switzerland	CERN
Noda A.	Japan	Institute for Chemical Research, Kyoto University
Panasyuk V.	Russia	BINP, Novosibirsk
Papash A.	Russia	JINR, Dubna
Parkhomchuk V.	Russia	BINP, Novosibirsk
Philippov A.	Russia	JINR, Dubna
Pivin R.	Russia	JINR, Dubna
Pogorelov I.	USA	Tech-X Corporation, Boulder, Colorado
Prasuhn D.	Germany	FZ Juelich
Reva V.	Russia	BINP, Novosibirsk
Rudakov A.	Russia	JINR, Dubna
Seryi A.	GB	J. Adams Institute
Sessler A.	USA	LBNL
Shcherbakov A.	Ukraine	NSC KIPT, Kharkov
Shemyakin A.	USA	Fermilab
Sidorin A.	Russia	JINR, Dubna
Stassen R.	Germany	FZ Juelich

Steck M.	Germany	GSI
Trubnikov G.	Russia	JINR, Dubna
Weilbach T.	Germany	HIM, Mainz
Wolf A.	Germany	MPI
Wu J.W.	China	IMP CAS, Lanzhou
Yakovenko S.	Russia	JINR, Dubna
Yang X.D.	China	IMP CAS, Lanzhou
Zenkevich P.	Russia	ITEP, Moscow
Zhang Y.Y.	China	IMP CAS, Lanzhou
Zhang Y.	USA	JLab
Zhdanova K.	Russia	JINR, Dubna
Zolotorev M.	USA	LBNL